

**OPTIMIZATION OF SURFACE-PROTEIN INTERACTIONS FOR
NEXT GENERATION BIOSENSORS**

A Dissertation
Presented to
The Academic Faculty

by

Eleanor Brightbill

In Partial Fulfillment
of the Requirements for the Degree
Doctorate of Materials Science and Engineering in the
School of Materials Science and Engineering

Georgia Institute of Technology
May 2021

COPYRIGHT © 2021 BY ELEANOR BRIGHTBILL

OPTIMIZATION OF SURFACE-PROTEIN INTERACTIONS FOR NEXT GENERATION BIOSENSORS

Approved by:

Dr. Eric Vogel, Advisor
School of Materials Science and
Engineering
Georgia Institute of Technology

Dr. Ravi Kane
School of Chemical and Biomolecular
Engineering
Georgia Institute of Technology

Dr. Valeria Milam
School of Materials Science and
Engineering
Georgia Institute of Technology

Dr. Craig Nies
AVX Corporation

Dr. Vladimir Tsukruk
School of Materials Science and
Engineering
Georgia Institute of Technology

Date Approved: April 21, 2021

To Snuffles

ACKNOWLEDGEMENTS

While I would love to claim all of my accomplishments are mine alone, my five years at Georgia Tech were full of support and assistance.

I am extremely appreciative of my advisor, Dr. Eric Vogel, for asking me to join his group. You did a great job of helping and guiding, but mostly leaving me to struggle on my own. I continue to simultaneously resent and appreciate learning that way. Additionally, I have been surrounded by fantastic groupmates in the Vogel Lab. Thank all of you for your insightful discussions and friendships, and specifically Dr. Meng-Yen Tsai, Dr. Spyridon Pavlidis, Dr. Katie Young, Dr. Billyde Brown, Bryce Hitchcock, Decarle Jin, and Hilena Gezahagne for collaborating with me. To my committee, thank you for the time you took to discuss and guide my thesis work. To my undergraduate research advisors Dr. Donita Robinson, Dr. Leslie Sombers, and Dr. Scott Warren, thank you for letting an inexperienced undergraduate into your labs. Without those experiences I never would have considered a Ph.D.

I would also like to thank our collaborators at AVX, Tyndall Institute, and Queen's University Belfast for including me in research happening in industry and different fields. I want to express gratitude to the NSF GRFP, GT President's Fellowship, and GT Lamar H. Franklin Fellowship for helping support my time in graduate school. I would also like to issue a quick catch-all thank you for everyone else who has discussed my research with me, except *Langmuir* Reviewer #3.

To my family, thanks for never doubting that getting a PhD was the right move for me. To the Shotkeys, thanks for all the fun and memory-filled wine nights, although

without you I might have graduated earlier. To Sohan, thanks for all the dinners you cooked and lunches you prepared. Because of you this thesis was not fueled by instant ramen and frozen meals.

Last but not least, I have to thank Snuffles, the best doggo I know. He adopted me my first year at GT, and was with me through it all. In fact, with COVID-19 quarantine, he curled next to me while I wrote almost all of this document. Thanks for making sure I took enough “breaks” while writing to pet you.



Snuffles, ‘assisting’ with thesis writing

TABLE OF CONTENTS

ACKNOWLEDGEMENTS	iv
LIST OF TABLES	x
LIST OF FIGURES	xi
LIST OF SYMBOLS AND ABBREVIATIONS	xxxii
SUMMARY	xxxvii
CHAPTER 1. Introduction	1
1.1 Label-Free Biosensing	1
1.1.1 Surface Plasmon Resonance	5
1.1.2 Potentiometric	11
1.2 Protein-Surface Interactions	18
1.2.1 Protein Structure	18
1.2.2 Antibody-Antigen Interactions	23
1.2.3 Non-Selective Adsorption	26
1.3 Thiol-Based Self-Assembled Monolayers	30
1.3.1 SAM History and Uses	30
1.3.2 COOH-SAMs for Biosensing Applications	32
1.3.3 COOH-SAM Structure and Defects	34
1.3.4 SAM Stability and Oxidation	36
1.4 2D Materials	41
1.4.1 Use in Biotechnology	42
1.4.2 Graphene-Based Biosensors	44
1.4.3 Substrate Influence	46
CHAPTER 2. Organization of this Thesis	52
CHAPTER 3. Optimization of COOH-SAM Formation^A	55
3.1 Introduction	55
3.2 Methods	57
3.2.1 Materials	57
3.2.2 COOH-SAM Formation	57
3.2.3 X-Ray Photoelectron Spectroscopy	58

3.2.4 Contact Angle	58
3.2.5 Atomic Force Microscopy	58
3.2.6 Surface Plasmon Resonance	59
3.3 Results	59
3.3.1 Au Film Quality	59
3.3.2 Effect of COOH-SAM Preparation Conditions	60
3.3.3 Protein Adsorption to COOH-SAMS	73
3.4 Conclusions	75
CHAPTER 4. Preblocking Method for COOH-SAM-Based Biosensing^A	77
4.1 Introduction	78
4.2 Methods	79
4.2.1 Materials	79
4.2.2 COOH-SAM Formation	80
4.2.3 Surface Plasmon Resonance	80
4.3 Results	80
4.3.1 Preblocker Selection	80
4.3.2 Preblocked Functionalization and Sensing	83
4.4 Conclusions	87
CHAPTER 5. Inhibition of COOH-SAM Oxidation via Protein Blocking^B	89
5.1 Introduction	90
5.2 Experimental Methods	92
5.2.1 Materials and Storage Conditions	92
5.2.2 X-ray Photoelectron Spectroscopy	94
5.2.3 Cyclic Voltammetry	96
5.2.4 Surface Plasmon Resonance	96
5.3 Results	99
5.3.1 Degradation of COOH-SAMS in Ambient Conditions	99
5.3.2 Affinity Biosensing after Ambient Storage	104
5.3.3 Comparison to Inert Atmosphere Storage	109
5.4 Conclusions	111
CHAPTER 6. Substrate modification of Graphene-Protein Interactions^C	112
6.1 Introduction	113
6.2 Experimental Methods	115

6.2.1 Chemicals and Substrate Cleaning	115
6.2.2 X-ray Photoelectron Spectroscopy	116
6.2.3 Graphene Synthesis and Transfer	117
6.2.4 Ellipsometry	117
6.2.5 Contact Angle	118
6.2.6 Quartz Crystal Microbalance with Dissipation	118
6.3 Results	119
6.3.1 Graphene Transfer and Model System Properties	119
6.3.2 Ex Situ Protein Adsorption	124
6.3.3 In Situ Protein Adsorption	131
6.4 Conclusions	135
CHAPTER 7. Summary and Future Work	137
7.1 Summary	137
7.2 Future Work	140
APPENDIX A. Considerations for Potentiometric Biosensing	143
A.1 Methods	143
A.2 Reference Electrode and Fluidic Tubing	145
A.3 Multi-Channel Detection	146
A.4 Direct Voltage Measurements	149
A.5 Conclusions	150
APPENDIX B. Methods to Confirm Surface-Protein Attachment	152
B.1 Atomic Force Microscopy	152
B.2 Ellipsometry	153
B.3 X-Ray Photoelectron Spectroscopy	154
B.4 Conclusions	156
APPENDIX C. Mass Transport and Sensor Geometry^D	157
C.1 Theory	158
C.1.1 Reaction	158
C.1.2 Diffusion	159
C.1.3 Convection	161
C.1.4 Model Evaluation	164
C.2 Model Results and Discussion	165

C.2.1 Effect of sensor length (radius) on settling time	167
C.2.2 Effect of flow rate on settling time	170
C.2.3 Effect of changing channel height on settling time	171
C.3 Conclusions	172
REFERENCES	174

LIST OF TABLES

Table 4.1	– Preblocking attachment and stability results.	83
Table 6.1	– Parameters of selected graphene substrates.	122
Table A.1	– Input impedance for selected transducers	150
Table C.1	– Dimension dependent parameters used in Equation 19	160

LIST OF FIGURES

- Figure 1.1 – Schematic presentation of the basic types of ELISA (enzyme-linked immunosorbent assay): a) direct, b) indirect, c) sandwich, d) competitive; Ag antigen, Ab antibody, E enzyme, S substrate. Reprinted unmodified under Springer Nature Creative Commons Attribution 4.0 International License from K Boguszewska, M Szewczuk, S Urbaniak, and B Karwowski. Review: immunoassays in DNA damage and instability detection. *Cellular and Molecular Life Sciences*. **76**, 4689–4704 (2019) <http://creativecommons.org/licenses/by/4.0/>. 3
- Figure 1.2 – Schematic representation of label-dependent (left) vs. label-free (right) biosensors 5
- Figure 1.3 – Schematic diagrams illustrating (a) a surface plasmon polariton (or propagating plasmon) and (b) a localized surface plasmon. Reprinted with permission from G Das, M L Coluccio, S Alrasheed, A Giugni, M Allione, B Torre, G Perozziello, P Candeloro, and E Di Fabrizio. Plasmonic nanostructures for the ultrasensitive detection of biomolecules *La Rivista del Nuovo Cimento* 2016, **39**, 547-586. Copyright 2016 Springer Nature. 6

- Figure 1.4 – The most common geometrical setup (the Kretschmann configuration) of SPR. The incoming light is located on the opposite side of the metallic slab than the adsorbate. Reprinted with permission from P Pattnaik. *Surface Plasmon Resonance: Applications in Understanding Receptor–Ligand Interaction Applied Biochemistry and Biotechnology*, 2005, **126**, 79-92. Copyright 2005 Springer Nature. 8
- Figure 1.5 – Typical shape of an SPR-sensorgram. It can be divided into four phases: association phase, steady state or equilibrium phase, dissociation phase, and regeneration phase. Reprinted unmodified under Hindawi Journals Creative Commons Attribution 3.0 License from M Ritzefeld and N Sewald. *Real-Time Analysis of Specific Protein-DNA Interactions with Surface Plasmon Resonance. Journal of Amino Acids* 2012, Article ID 816032 doi.org/10.1155/2012/816032 9
- Figure 1.6 – Prototype portable SPR instrument. The overall sensor (main part) is 480 mm x 150 mm x 180 mm with a weight of 3.09 kg. Reprinted unmodified under MDPI Journals Creative Commons Attribution 4.0 International License from Y Huang, L Zhang, H Zhang, Y Li, L Liu, Y Chen, X Qiu, and D Yu. *Development of a Portable SPR Sensor for Nucleic* 10

Acid Detection. *Micromachines* 2020, **11** (5), 526
doi.org/10.3390/mi11050526

- Figure 1.7 – Schematic representation of the first ISFET device. 11
Reprinted with permission from P Bergveld. Development of an Ion-Sensitive Solid-State Device for Neurophysiological Measurements *IEEE Transactions on Biomedical Engineering*, 1970, **1**, 70-71. © 1970 IEEE
- Figure 1.8 – Illustration of a biological and chemical FET sensor. 13
Reprinted unmodified under Elsevier Creative Commons Attribution-NonCommercial-NoDerivatives 4.0 International License from M Kaisti. Detection principles of protein–antibody interactions. *2D Materials* 2015, **2**, 044009. Copyright 2015 IOP Publishing Ltd.
- Figure 1.9 —Impact of Debye screening on streptavidin sensing. (a) 14
Schematic (not to scale) showing λ_D from the device surface. The blue bar represents the active region of the device, the yellow regions the leads (S = source, D = drain), the gray hashed region the underlying oxide, the purple diamonds are biotin, and the red objects are streptavidin. The negative charges surrounding the protein represent its negative charge. The green “1×” line (also not to scale) represents the screening length (λ_D) from 1× PBS relative to the protein and

the blue and orange lines represent that from 1:10 and 1:100 dilutions of this buffer, respectively. (b) Biotin-functionalized sensor response ($|ISD|$ vs time) to varying buffer ionic concentrations with (red) and without (black) streptavidin addition at time = 0. The blue text gives the PBS buffer concentration [Tris(2-carboxyethyl)phosphine hydrochloride, TCEP, was added in $0.01 \times$ PBS] and the blue arrows represent the onset of solution exchange. The two results derive from different devices. Reprinted with permission from E Stern, R Wagner, F J. Sigworth, R Breaker, T M Fahmy, and M A Reed. Importance of the Debye Screening Length on Nanowire Field Effect Transistor Sensors. *Nano Letters* 2007, **7**, 11, 3405-3409. Copyright 2007 American Chemical Society.

Figure 1.10 – Schematic of EGFET Sensor. Reprinted with permission from A Tarasov, MY Tsai, E M Flynn, C A Joiner, R C Taylor, and E M Vogel. Gold-coated graphene field-effect transistors for quantitative analysis of protein–antibody interactions. *2D Materials* 2015, **2**, 044009. Copyright 2015 IOP Publishing Ltd.**Error! Reference source not found.** 13

Figure 1.11 – BRD detection using EGFET, benchmarked to SPR and ELISA. (a) The application of increasing concentrations of 17

negatively charged antibody shifts the FET gate voltage. The detection limit and sensitivity of EGFET detection of BRD in blood plasma scales with both SPR (b) and standard ELISA (c) analysis. Reprinted with permission from A Tarasov, D W Gray, MY Tsai, N Shields, A Montrose, N Creedon, P Lovera, A O'Riordan, M H Mooney, and E M Vogel. A potentiometric biosensor for rapid on-site disease diagnostics. *Biosensors and Bioelectronics* 2016, **79**, 669-678. Copyright 2015 Elsevier.

Figure 1.12

– Protein structure levels. (a) Primary structure, the amino acid sequence (b) secondary structure, α -helix and β -sheet (c) tertiary structure, and (d) quaternary structure. Reprinted with permission from R Gupta, A Dey, A Vijan, and B Gartia, In *Silico Structure Modeling and Characterization of Hypothetical Protein Y 004590319.1 Present in Enterobacter aerogens. Journal of Proteomics and Bioinformatics* 2017, **10**, 152-170. Copyright 2017 Longdom Publishing.

20

Figure 1.13

– Importance of the hydrophobic effect. (a) optimized structure of a propane clathrate hydrate. Reprinted with permission from G Lanza and M A Chiacchio. The water molecule arrangement over the side chain of some aliphatic amino acids: A quantum chemical and bottom-up

22

investigation. *International Journal of Quantum Chemistry* 2020, **120** (9), e26161. Copyright 1969, John Wiley and Sons

(b) Illustration of the thermodynamics of protein folding, including the contributions of various stabilizing and destabilizing interactions. Reprinted with permission from A Rani and P Venkatesu. Changing relations between proteins and osmolytes: a choice of nature. *Physical Chemistry Chemical Physics* 2018, **20** (31), 20315-20333. Copyright 2018 Owner Societies.

Figure 1.14

– Antibody structure. Human antibodies are composed of four polypeptide chains: two heavy chains (dark blue) and two light chains (light blue). Antigen binding sites are each formed by the variable regions of a light chain and a heavy chain (Fab regions). The constant regions of the heavy chains form the tail (Fc region). The two Fab regions and Fc region are linked by a flexible hinge region that improves the ability of the Ab to bind antigen. Reprinted with permission from N Stevens and A Cowin. Overcoming the challenges of topical antibody administration for improving healing outcomes: a review of recent laboratory and clinical approaches. *Wound Practice & Research: Journal of the Australian Wound*

23

Management Association 2017. Copyright 2017 Cambridge Media.

- Figure 1.15 – Lock-and-key model of antigen-antibody binding. 24
Reprinted with permission from J X Zhang and K Hoshino. *Molecular Sensors and Nanodevices: Principles, Designs and Applications in Biomedical Engineering*. Academic Press: 2018. Copyright 2019 Elsevier Inc.
- Figure 1.16 – Adsorption and denaturation of a protein on a hydrophobic surface, allowing the release of structured water. Reprinted unmodified under MDPI Journals Creative Commons Attribution 4.0 International License from F Poncin-Epaillard, T Vrlnic, D Debarnot, M Mozetic, A Coudreuse, G Legeay, B El Moulaj, and W Zorzi. Surface Treatment of Polymeric Materials Controlling the Adhesion of Biomolecules. *Journal of Functional Biomaterials*. 2012, **3**, 528-543. 27
- Figure 1.17 – Overview of kinetic models. A short scheme of each adsorption mechanism is presented in the middle column. The most important characteristics of the observable adsorption kinetics are depicted in the right column (solid line: adsorption curve; dashed line: desorption curve upon buffer rinsing). Reprinted with permission from M Rabe, D Verdes, 30

and S Seeger. Understanding protein adsorption phenomena at solid surfaces. *Advances in Colloid and Interface Science* 2011, **162** (1-2), 87-106. Copyright 2011 Elsevier B.V.

- Figure 1.18 – Some applications of self-assembled monolayers in nanotechnology. Reprinted with permission from C Vericat, M E Vela, G Benitez, P Carrob, and R C Salvarezza. Self-assembled monolayers of thiols and dithiols on gold: new challenges for a well-known system. *Chemical Society Reviews* 2010, **39** (5), 1805-1834. Copyright 2010 Royal Society of Chemistry. 31
- Figure 1.19 – Schematic diagram of an ideal, single-crystalline SAM of alkanethiolates supported on a gold surface with a (111) texture. Reprinted with permission from J C Love, L A Estroff, J K Kriebel, R G Nuzzo, and G M Whitesides. Self-assembled monolayers of thiolates on metals as a form of nanotechnology. *Chemical Reviews* 2005, **105** (4), 1103-1170. 32
- Figure 1.20 – Protein receptor functionalization of the SAM via amine coupling. Reprinted with permission from E L Brightbill, B Hitchcock, MY Tsai, A Verga, and E M Vogel. Preblocking Procedure to Mitigate Nonselective Protein Adsorption for Carboxyl-SAMs Used in Biosensing. *The Journal of Physical* 34

Chemistry C 2019, **123** (27), 16778-16786. Copyright 2019 American Chemical Society.

Figure 1.21

– Schematic diagram illustrating an oxidation-desorption pathway for the initial degradation of SAMs on gold. Critical structural evolution and morphological changes are included. Reprinted from G Yang, N A Amro, Z B Starkewolfe, and G Liu. Molecular-Level Approach to Inhibit Degradations of Alkanethiol Self-Assembled Monolayers in Aqueous Media. *Langmuir* 2004, 20 (10), 3995-4003. Copyright 2004 American Chemical Society.– COOH-SAM defects on polycrystalline Au, including bilayer formation through hydrogen bonding, striped phase, tangled chains and gauche defects, vacancies, and SAM grain boundaries. Reprinted with permission from E L Brightbill, B Hitchcock, MY Tsai, A Verga, and E M Vogel. Preblocking Procedure to Mitigate Nonselective Protein Adsorption for Carboxyl-SAMs Used in Biosensing. *The Journal of Physical Chemistry C* 2019, **123** (27), 16778-16786. Copyright 2019 American Chemical Society.

35

Figure 1.22

– Schematic diagram illustrating an oxidation-desorption pathway for the initial degradation of SAMs on gold. Critical structural evolution and morphological changes are included.

38

Reprinted from G Yang, N A Amro, Z B Starkewolfe, and G Liu. Molecular-Level Approach to Inhibit Degradations of Alkanethiol Self-Assembled Monolayers in Aqueous Media. *Langmuir* 2004, 20 (10), 3995-4003. Copyright 2004 American Chemical Society.– Schematic diagram illustrating an oxidation-desorption pathway for the initial degradation of SAMs on gold. Critical structural evolution and morphological changes are included. Reprinted from G Yang, N A Amro, Z B Starkewolfe, and G Liu. Molecular-Level Approach to Inhibit Degradations of Alkanethiol Self-Assembled Monolayers in Aqueous Media. *Langmuir* 2004, **20** (10), 3995-4003. Copyright 2004 American Chemical Society.

Figure 1.23

– Mechanism of desorption inhibition of alkanethiol SAMs in amphiphile and water. (a) Schematic diagram illustrates the adsorption of DMF molecules on SAM surfaces, and the preferred attachment to defect sites. (b) Quantitative free energy diagram for the initial desorption process of decanethiol under various environments. Reprinted from G Yang, N A Amro, Z B Starkewolfe, and G Liu. Molecular-Level Approach To Inhibit Degradations of Alkanethiol Self-Assembled Monolayers in Aqueous Media. *Langmuir* 2004,

40

20 (10), 3995-4003. Copyright 2004 American Chemical Society.

- Figure 1.24 – Structure of different 2D materials; Graphene, transition metal dichalcogenides, layered double hydroxides, gC₃N₄, laponite clay, hBN, transition metal dichalcogenides and black phosphorous. Reprinted with permission from A Jayakumar, A Surendranath, M Pv. 2D materials for next generation healthcare applications. *International Journal of Pharmaceuticals*. 2018, **551** (1-2), 309-321. Copyright 2018 Elsevier B.V. 42
- Figure 1.25 – Biomedical applications of 2D materials. Reprinted with permission from D Chimene, D L Alge, and A K Gaharwar. Two-dimensional nanomaterials for biomedical applications: emerging trends and future prospects. *Advanced Materials* 2015, **27** (45), 7261-7284. Copyright 2015 John Wiley & Sons. 43
- Figure 1.26 – Schematic of a typical graphene FET. Reprinted with permission from K Matsumoto, K Maehashi, Y Ohno, and K Inoue. Recent advances in functional graphene biosensors. *Journal of Applied Physics D* 2014, **47**, 094005. Copyright 2014 IOP Publishing LTD. 45

- Figure 1.27 – Water contact angle measurements for Si and Au substrates with and without a monolayer graphene coating. The intermediate graphene layer has no significant impact on the baseline wettability of the underlying substrate. Reprinted with permission from J Rafiee, X Mi, H Gullapalli, A V Thomas, F Yavari, Y Shi, P M Ajayan, and N A Koratkar. Wetting transparency of graphene. *Nature Materials* 2012, **11** (3), 217. Copyright 2012 Nature Publishing Group. 48
- Figure 1.28 – Substrate polarity effect on epitaxial growth through graphene. a,b, EBSD of the exfoliated surfaces of GaN (a) and Si (b). c,d, DFT simulations of a potential fluctuation (meV) map at the epitaxial surface of 1-ML-graphene/GaN (c) and of 1-ML-graphene/Si (d). e,f, DFT simulations of the potential fluctuation at the epitaxial surface from GaN and Si through 1 ML graphene (e) and of the potential fluctuation decay from the GaN and Si surface (f). Reprinted with permission from W Kong, H Li, K Qiao, Y Kim, K Lee, Y Nie, D Lee, T Osadchy, R J Molnar, D K Gaskill, R L Myers-Ward, K M Daniels, Y Zhang, S Sundram, Y Yu, S Bae, S Rajan, Y Shao-Horn, K Cho, A Ougazzaden, J C Grossman, and J Kim. Polarity governs atomic interaction through two-dimensional materials. *Nature Materials* 2018, **17** (11), 999. 50

Copyright 2018 Wei Kong et al, under exclusive license to Springer Nature Limited.

- Figure 3.1 — Au film characterization. XPS survey spectrum of Au surface with inset Si 2p region for (a) SPR Au/Glass Chip and (b) evaporated Au/SiO₂ chip. AFM images with inset RMS roughness (in white) of (c) SPR Au/Glass Chip and (d) evaporated Au/SiO₂ chip. 60
- Figure 3.2 — XPS S 2p spectra with properly and improperly bound peak fitting. a) Relatively far-spaced (1.1 eV) S peaks. b) Relatively close-spaced (0.8 eV) S peaks. 62
- Figure 3.3 — S 2p XPS scans for the 5 mM Air preparation condition. The number denotes the sample, while letters denote different spots on the same sample. 64
- Figure 3.4 — S2p XPS scans for the 5 mM N₂ preparation condition. The number denotes the sample, while letters denote different spots on the same sample. 66
- Figure 3.5 — S2p XPS scans for the 20 μM N₂ preparation condition. The number denotes the sample, while letters denote different spots on the same sample. 68

Figure 3.6	— S2p XPS scans for the 20 μ M N2 AA preparation condition. The number denotes the sample, while letters denote different spots on the same sample.	70
Figure 3.7	— XPS summary results of COOH-SAMs. a) Box and whisker plots of total S and properly bound S density, normalized by the Au signal area. b) Percentages of properly and improperly bound S by area. c) Improperly bound S peak position.	71
Figure 3.8	—DI water contact angle on COOH-SAMs	73
Figure 3.9	— NSA of a model small, medium, and large protein on 5 mM Air and 20 μ M N2 COOH-SAMs.	75
Figure 4.1	– Schematic of functionalized surface with preblocker.	81
Figure 4.2	– Example SPR sensorgram of preblocker screening procedure, with amount bound and stability parameters indicated.	82
Figure 4.3	– a) Example functionalization SPR sensorgram with preblocking steps (vertical step changes are due to solution refractive index). b) Degree of functionalization without preblocking. c) Degree of functionalization after preblocking. d) SPR aHp attachment curve for gelatin preblocked COOH-	85

SAM compared to gelatin adsorbed directly to Au with no treatment, with NHS/EDC activation and ETA blocking treatment, and with NHS/EDC activation only (refractive index change removed for clarity).

- Figure 4.4 – Hp sensing result with kinetic fitting for commercial CM5 sensor compared to COOH-SAM sensors without blocking, with gelatin preblocking, and with gelatin postblocking . b) Amount of attached blocker and blocker stability for preblocked and postblocked sensors c) receptor activity comparison, given by sensor response to 25 $\mu\text{g/mL}$ Hp solution, normalized by the degree of aHp functionalization. 87
- Figure 5.1 – Example S 2p spectrum before and after Savitzky-Golay smoothing. 95
- Figure 5.2 – Example S 2p XPS fitting for oxidized signal. a) Peak fitting on a clearly present peak b) non-zero peak fitting on a spectrum that appears flat 96
- Figure 5.3 – Analysis of C 1s XPS signal. Survey spectra with software-identified peaks for unblocked (a) and blocked (b) COOH-SAMs. Survey C 1s peak area normalized to Au 4f peak area for unblocked (c) and blocked (d) COOH-SAMs during 1 week of storage in ambient conditions. 98

- Figure 5.4 – Inhibition of oxidation by gelatin blocking. a) Schematic of COOH-SAM with common defects before and after oxidation in ambient conditions. Gelatin blocks defective regions and prevents oxidation. b) Example S 2p spectra of unblocked COOH-SAM stored in ambient conditions. Orange peak fitting indicates oxidized S species. c) Example S 2p spectra of blocked COOH-SAM stored in ambient conditions. Blue peak fitting illustrates lack of oxidized S species. 100
- Figure 5.5 —Summary of XPS fitting for unblocked COOH-SAM (orange, square) and blocked COOH-SAM (blue, circle) oxidized S peaks. 101
- Figure 5.6 – AFM images of functional surfaces on 100 nm Au/SiO₂ chips with inset root-mean-square roughness (in white). a) Plain Au b) unblocked COOH-SAM, freshly prepared c) unblocked COOH-SAM, 1 week storage d) unblocked COOH-SAM, 3 months storage e) blocked COOH-SAM, freshly prepared f) blocked COOH-SAM, 1 week storage g) blocked COOH-SAM, 3 months storage. 102
- Figure 5.7 – CV curves showing reductive desorption of COOH-SAMs a) chemical reaction and schematic of reductive desorption b) Example CV for bare Au substrate, unblocked COOH-SAM, and blocked COOH-SAM c) CV of unblocked COOH-SAM 104

before and after 1 week storage in ambient conditions d) CV of blocked COOH-SAM before and after 1 week storage in ambient conditions.

- Figure 5.8 – Functionalization parameters for COOH-SAM samples. a) Example functionalization SPR sensorgram with preblocking steps (vertical step changes are due to solution refractive index). b) degree of functionalization on each sample type c) post-functionalization drift of each sample type. 106
- Figure 5.9 – Label-free detection of Hp via SPR with COOH-SAM aHp functionalized sensor. a) schematic representation of functionalized surfaces b) SPR response for each sensor type with Langmuir isotherm fitting. Inset: unnormalized response. 109
- Figure 5.10 – Comparison of COOH-SAM degradation after 2 months storage in ambient and inert (N₂) conditions. a) CV curves for COOH-SAMs b) oxidized S XPS signal for COOH-SAMs. c) XPS S 2p scans with smallest oxidized S signal for each sample type d) XPS S 2p scans with largest oxidized S signal for each sample type. 110
- Figure 6.1 – C1s XPS spectra. PMMA fitting before (a) and after (b) post-transfer anneal. c) comparison of C 1s scans of freshly 121

cleaved graphite, as-grown graphene, transferred graphene, and graphene after the transfer and cleaning process.

- Figure 6.2 – Example Raman of transferred CVD graphene before (a) 121 and after (b) post-transfer anneal.
- Figure 6.3 — DI H₂O contact angles on the prepared substrates with and 124 without a transferred graphene monolayer.
- Figure 6.4 – Comparison of BSA attachment on Au and Au with 125 graphene with and without grounding of the substrate during protein adhesion. a) schematic of floating BSA adsorption b) schematic of reference-grounded BSA adsorption c) thickness of BSA layer attachment as measured by ellipsometry.
- Figure 6.5 – Summary of protein surface layer thickness by ex situ 128 ellipsometry. Fibrinogen (a), Lysozyme (b), and BSA (c), attachment to SiO₂, Si, Au, and TaN substrates with and without a transferred graphene monolayer.
- Figure 6.6 – BSA attachment vs measured substrate contact angle. A 128 general positive correlation is seen regardless of the presence of graphene

Figure 6.7	– XPS using normalized N 1s or S 2p signal as an indication of protein adsorption levels. Lysozyme, BSA, and Fibrinogen attachment to SiO ₂ (a), Si (b), Au (c) and TaN (d) substrates with and without a transferred graphene monolayer.	130
Figure 6.8	– Comparison of BSA attachment on Au/Graphene to Graphite	131
Figure 6.9	– Frequency and Dissipation QCM curves a) frequency overtone 5 and b) dissipation overtone 5 for Lysozyme attachment to Au and Au/graphene sensors. c) frequency overtone 5 and d) dissipation overtone 5 for Lysozyme attachment to Si and Si/graphene	132
Figure 6.10	– Kinetic fitting of QCM frequency protein attachment curves. Langmuir fitting of Lysozyme adsorption to Au (a) and Au/graphene (b) sensors. Two-state fitting of Lysozyme adsorption to Si (c) and Si/graphene (d) sensors.	134
Figure A.1	– EGFET sensor layout and characterization. (a) Schematic of the potentiometric sensing device, consisting of two parts: a sensor for signal generation and a transducer for signal amplification and readout. (b) A typical transistor transfer curve showing that the drain current I_d can be modulated by sweeping the voltage at the reference electrode V_{ref} . The	144

same curve is shown on linear scale (left axis) and semi-log scale (right axis). (c) Image of a disposable sensing chip. (d) sensor chip in contact with solution via PDMS wells and connected using a test clip shown in to the gate of the transducer. Adapted with permission from A Tarasov, D W Gray, MY Tsai, N Shields, A Montrose, N Creedon, P Lovera, A O'Riordan, M H Mooney, and E M Vogel. A potentiometric biosensor for rapid on-site disease diagnostics *Biosensors and Bioelectronics* 2016, **79**, 669-678. Copyright 2016 Elsevier.

Figure A.2	– Comparison of post-functionalization drift in PBS	146
Figure A.3	– Multi-channel sensing interference a) schematic of 2-channel, 1-well sensing b) Measured voltage on CH1 with applied voltages on the reference and CH2	148
Figure A.4	– Multi-channel coupling from cables a) Schematic of multi-channel sensing b) Coupled response c) Schematic of coaxial and triaxial cables	148
Figure A.5	– Sensor surface voltage changes due to pH measured with high (a, Keithly 4200) and low (b, HP 4245) input impedance instruments. Spikes in (b) due to pump noise.	150

Figure B.1	– AFM images of functional surfaces on 100 nm Au/SiO ₂ chips with inset RMS roughness (in white). a) 20 μM COOH-SAM b) 20 μM COOH-SAM/Gelatin Preblocking c) 20 μM COOH-SAM/Gelatin Preblocking/aHp Functionalization d) 20 μM COOH-SAM/Gelatin Preblocking/aHp Functionalization/50 μg/mL Hp	153
Figure B.2	– Protein layer thickness as measured by ellipsometry.	154
Figure B.3	– N 1S peak intensity of NTA-SAM only, after HSA functionalization, and after aHSA attachment.	
Figure C.1	– (a) Comparison of the model (line) with numerical solutions from the literature (symbols) of the purely diffusive case ³⁰⁷ The inset shows example sensors with planar and radial geometry. (b) Channel geometry. (c) Comparison of the model (blue symbols) to COMSOL simulation data (lines) for the diffusion-convection case. ³⁰⁸ The red triangles mark the conditions associated with the model validation provided in Figure C.2.	161
Figure C.2	– Comparison of model to data from literature. (a) SPR data of binding of myoglobin ³¹¹ (b) Data from simulations of binding of a model protein in a transport limited regime ¹¹⁰ (c-d) Data from simulations of binding of a model at different	165

flow rates with $N_0 = 8.6 \times 10^{10} \text{ cm}^{-2}$ and $N_0 = 8.6 \times 10^{11} \text{ cm}^{-2}$.
2. 312 (e) Experimental SPR data of binding of fusion protein GST-Lcyt-YF at different flow rates.³¹²

Figure C.3 – Modeling (a) a transient binding curve and (b) settling time 167
at different concentrations to a microplanar and nanowire sensor. $L = 50 \text{ } \mu\text{m}$ (planar), 50 nm (radial), $Q = 10 \text{ } \mu\text{l/min}$, $N_0 = 2 \times 10^{12} \text{ cm}^{-3}$, $k_a = 10^6 \text{ M}^{-1}\text{s}^{-1}$, $k_d = 10^{-3} \text{ s}^{-1}$, $c = 10 \text{ fM}$, $D = 10^{-7} \text{ cm}^2/\text{s}$, $H = 100 \text{ } \mu\text{m}$, $W_c = 200 \text{ } \mu\text{m}$

Figure C.4 – (a) and (b) Effect of the sensor length (radius) on the 168
settling time at two different flow rates. (c) and (d) Effect of the flow rate on the settling time at two different sensor sizes. (e) and (f) Effect of the channel height on the settling time at two different flow rates.

LIST OF SYMBOLS AND ABBREVIATIONS

2D	Two-dimensional material
Å	Angstrom
AA	Acetic acid
AmA	Amino acid
Ab	Antibody
AFM	Atomic force microscopy
Ag	Antigen
AbAg	Antibody-antigen complex
aBSA	Antibody bovine serum albumin
aHp	Antibody human haptoglobin
aHSA	Antibody human serum albumin
BE	Binding energy
BRD	Bovine respiratory disease
BSA	Bovine serum albumin

CNT Carbon nanotube

COOH-SAM Carboxylic-acid-terminated self-assembled monolayer

CV Cyclic voltammetry

CVD Chemical vapor deposition

DC Direct current

DI Deionized water

DMF Dimethylformamide

DNA Deoxyribonucleic acid

e-beam Electron beam

EDC 1-Ethyl-3-(3-dimethylaminopropyl) carbodiimide

EDTA Ethylenediaminetetraacetic acid

EGFET Extended-gate field-effect transistor

EIA Enzyme immunoassay

EIS Electrochemical impedance spectroscopy

ELISA Enzyme-linked immunosorbent assay

ETA Ethanolamine

Fab Fragment antigen-binding

Fc Fragment crystallizable

FET Field-effect transistor

FWHM Full-width-half-maximum

gFET Graphene field-effect transistor

hBN Hexagonal boron nitride

HEPES 4-(2-hydroxyethyl)-1-piperazineethanesulfonic acid

HIV Human immunodeficiency virus

Hp Human haptoglobin

HSA Human serum albumin

Ig Immunoglobulin

ISFET Ion-sensitive field-effect transistor

k_a Association rate constant

K_A Affinity constant

k_d Dissociation rate constant

K_D Dissociation constant

KE	Kinetic Energy
MOS	Metal-oxide-semiconductor
NHS	N-Hydroxysuccinimide
NSA	Non-selective adsorption
NTA	Nitrilotriacetic acid
PBASE	1-Pyrenebutyric acid N-hydroxysuccinimide ester
PBS	Phosphate buffered saline
PEG	Poly-ethylene glycol
PEG-SAM	Poly-ethylene glycol-terminated self-assembled monolayer
pI	Isoelectric point
PMMA	Poly(methyl methacrylate)
QCM	Quartz crystal microbalance
QCM-D	Quartz crystal microbalance with dissipation
RD	Reductive desorption
RF	Radio frequency
RU	Response unit

SAM Self-assembled monolayer

SEM Scanning electron microscopy

SP Surface plasmon

SPR Surface plasmon resonance

vdW van der Waals

VM Voltmeter

SUMMARY

Currently, diagnosis for serological diseases such as Ebola, HIV, and Lyme disease relies on enzyme-linked immunosorbent assays (ELISAs), which require centralized laboratories and several-day timescales to complete. However, emerging technologies such as potentiometric and electrochemical impedance biosensing can be developed into portable, label-free, point-of-care devices that require only hour timescales. Specifically, potentiometric sensing platforms can be miniaturized through cost-effective microfabrication, lend themselves to multiplexed and parallel sensing, and are easily integrated with other electronics.

Despite the promise of these new label free technologies, device reliability inhibits commercialization and adoption. This work focuses on improving potentiometric sensing, primarily through understanding erroneous behavior at the sensor-solution interface. During biomolecular sensing, biomolecules in solution interact with the sensor surface. Ideally, protein recognition mechanisms are leveraged to allow only target proteins to attach to the surface, imparting signal selectivity. However, unwanted protein interactions with sensor surfaces cause signal instability and increase false-positive rates. Although commonly used to functionalize the sensing surface, carboxyl-terminated thiol self-assembled monolayers (COOH-SAMs) can have large defect densities, which in turn leads to large non-selective adsorption of proteins to hydrophobic surfaces exposed by these defects. A procedure is developed where the surface of COOH-SAMs is treated before functionalization to improve the reliability and quality of receptor attachment to the sensor surface.² In this method, a preblocking protein orthogonal to the immunological system of

interest is used to cover hydrophobic, non-selective sites on the sensor surface while still leaving carboxylic acid headgroups available for covalent functionalization. This methodology is advantageous when compared to standard blocking, where the receptor protein must be attached to the sensor prior to the blocking step. With traditional postblocking, non-selective adsorption and degradation of the receptor protein itself can occur, and the storage stability of the receptor must be considered since the sensor cannot be functionalized after blocking. Additionally, COOH-SAMs oxidize when exposed to ambient conditions. The impact of this degradation of sensing, as well as methods to prevent degradation, are explored.³

Beyond SAM-based sensors, there has been significant interest in biomedical applications of 2D materials, including potentiometric sensing. The inert basal plane of certain 2D materials, such as graphene, could lead to larger biosensing signals due to a decrease in surface pH response. However, there is conflicting literature on to what extent interaction from the substrate are transmitted through a 2D monolayer, and the subsequent effect on biomolecule interactions are unknown. Therefore, the degree to which the substrate influences graphene-protein interactions is explored.⁴ Finally, a section is dedicated to non-surface-layer sources of signal unreliability, including presentation of a model for sensor response time.⁵

The work presented in this thesis demonstrates initial steps towards reliable control over sensor-solution interfaces. Despite the current challenges facing label-free, portable biosensors, the work presented here provides a step towards reliable biosensing.

CHAPTER 1. INTRODUCTION

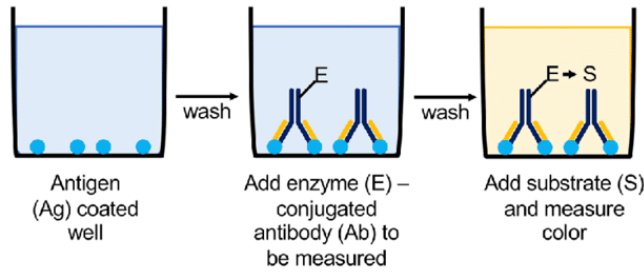
Biomarker detection is critical for applications including disease diagnosis, human health and performance monitoring, food safety, environmental monitoring, and drug development. Early detection of cancer through biomarkers including nucleic acids, proteins, and sugars significantly decreases cancer mortality rates.⁶ Identification and removal of food contaminated by pathogenic bacteria such as *Escherichia coli* or *Salmonella typhimurium* could eliminate transmission of approximately 90% of all food borne diseases.⁷ Many less obvious, but equally interesting, applications of biomarker detection also exist. Amino acid detection in soil samples on Mars would provide evidence of extraterrestrial life.⁸ Rapid *in vivo* detection of the neurotransmitter dopamine can be used to better understand, and develop treatments for, addiction.⁹ A biosensor for any of these applications generally consists of at least two functional components. The first is an element that gives the device selectivity to the target biomarker, such as an antibody to a target protein. The second is an element that converts the bio-recognition of the first element into a readable signal (i.e. electrical, optical, mass change). This chapter will focus on current efforts to produce state-of-the-art sensors capable of detecting biomarkers across the diverse conditions illustrated above.

1.1 Label-Free Biosensing

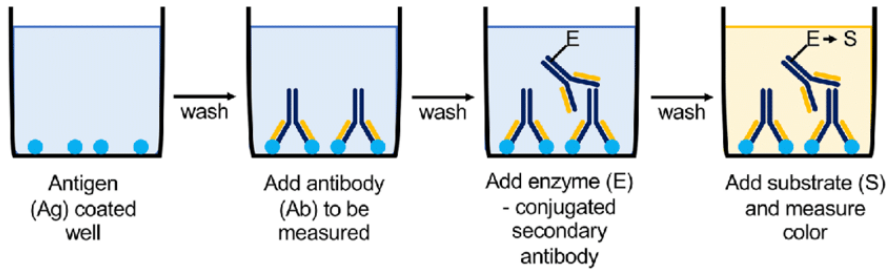
Nearly 60 years after its initial demonstration in 1960,¹⁰ our modern healthcare system continues to rely on enzyme immunoassays (EIA), typically enzyme-linked

immunosorbent assays (ELISA), for trustworthy detection of infectious diseases such as human immunodeficiency virus (HIV), Lyme disease, Zika virus, and Rocky Mountain Spotted Fever.¹¹ Developed concurrently but independently by Peter Perlmann and Eva Engvall at Stockholm University and by Anton Schuurs and Bauke van Weemen in The Netherlands, these assays are based on using an enzyme as a reporter label.¹² While several varieties of EIA/ELISA are used today (Figure 1.1), all methods involve attaching an enzyme to the sensing target, and then using the enzyme's activity to indirectly detect the sensing target.¹³ For example, a sandwich ELISA (Figure 1.1c) is used to detect a pathogen in a blood sample by first adding a primary antibody (Ab) to the well of a microtiter plate, which sticks to the plastic through hydrophobic interactions. Afterwards, the well is washed and blocking protein is added to cover any non-specific binding sites in the well. When the sample is added to the well, if antigens (Ag) from the pathogen are present, they will selectively bind to the Ab. After the binding occurs, an enzyme conjugated to a second Ab that also binds to the target Ag is added to the well. In this way, the enzyme only attaches to the well if the target Ag is present. Finally, the substrate of the enzyme is added and any enzyme activity is measured. Usually, the enzyme substrate is colorless and, in the presence of the enzyme, is converted into a colored end product. The degree of color change can then be related to the amount of bound target Ag.

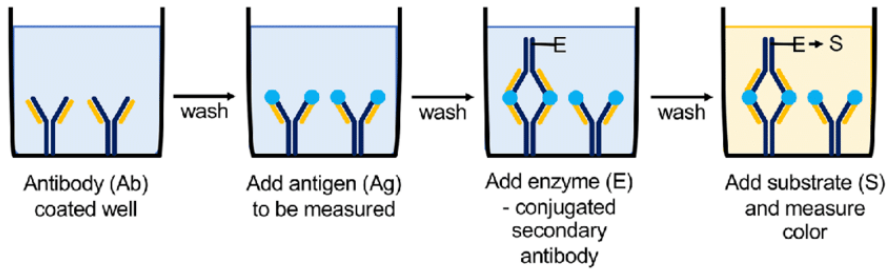
(a) Direct ELISA



(b) Indirect ELISA



(c) Sandwich ELISA



(d) Competitive ELISA

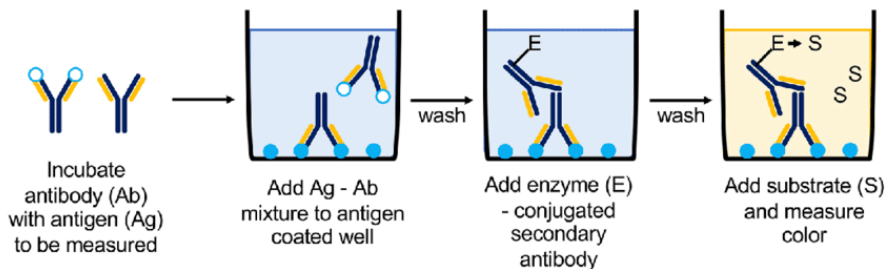


Figure 1.1 – Schematic presentation of the basic types of ELISA (enzyme-linked immunosorbent assay): a) direct, b) indirect, c) sandwich, d) competitive; Ag antigen,

Ab antibody, E enzyme, S substrate. Reprinted unmodified under Springer Nature Creative Commons Attribution 4.0 International License from K Boguszewska, M Szewczuk, S Urbaniak, and B Karwowski. Review: immunoassays in DNA damage and instability detection. *Cellular and Molecular Life Sciences*. 76, 4689–4704 (2019) <http://creativecommons.org/licenses/by/4.0/>.

Although this methodology is currently required for diagnosis, the use of enzymes and optical adsorption equipment for EIAs require that they are done in a centralized laboratory, and results are generally returned on a multiple-day timescale. The ability to detect biochemical species rapidly and without complicated sample preparations in a centralized laboratory would allow for significant improvements in medical care, disease diagnosis, food safety, and environmental monitoring. Moreover, the use of a label can decrease the reliability of the assay. Labeling a secondary Ab can block the protein active site and alter the binding properties.¹⁴ Degradation of the enzymatic label can also be caused by changes in pH, temperature, pressure, exposure to UV radiation, detergents, organic solvents or certain chemicals, resulting in low enzymatic activity even in the present of the target Ag.¹⁵

Label-free biosensing has attracted attention because the absence of indicator molecules or conjugated enzymes allows for direct detection of the biomolecule of interest, reduces sample complexity and thus preparation time and analytical cost, allows for real-time detection of binding events, and indicates these systems are amenable to point-of-care and field applications (Figure 1.2).¹⁴ Label-free biosensing has already been demonstrated in a large range of sensing platforms, including evanescent wave sensing,¹⁶ fluorescence spectroscopy,¹⁷ colorimetric sensing,¹⁸ Raman spectroscopy,^{19, 20} photonic micro-

resonators,^{21, 22} nanoplasmonics,²³ quartz crystal microbalance,^{24, 25} cantilever resonance,^{26,}
²⁷ surface plasmon resonance (SPR),^{28, 29} electrochemical impedance,^{30, 31} and
 potentiometric sensing.^{31, 32} Further discussion below into SPR and potentiometric
 biosensing methodologies highlights the benefits and challenges of these label-free
 techniques over EIA methods.

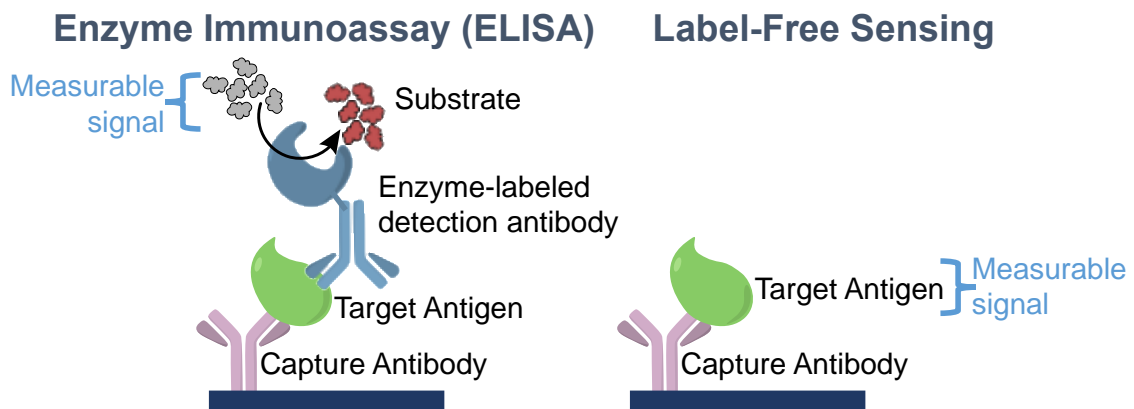


Figure 1.2 – Schematic representation of label-dependent (left) vs. label-free (right) biosensors.

1.1.1 Surface Plasmon Resonance

SPR biosensing, while still an optical technique like EIAs, offers label-free sensing as the result of changes at a metal-dielectric interface.³³ Surface plasmons (SPs) were first predicted by Ritchie in 1957,³⁴ and can be described as coherent electron oscillations at the interface of two materials, given that the real part of the dielectric function changes across the interface.³⁵ Harnessing the SP for sensing allows for a surface-sensitive technique, since the electron oscillations decay exponentially into the materials on each side of the interface and the wavelength of SP resonance is extremely sensitive to any change at the

material interface.³³ SPR biosensing generally involves a metal-water interface, where the SP penetration into the metal and water is on the order of 10s and 100s of nms, respectively.³⁶ Conventionally, SPR refers to SPs on planar surfaces (Figure 1.3a) while localized SPR (LSPR) is used to describe the same effect in nanoparticles and nanostructures (Figure 1.3b).³⁷

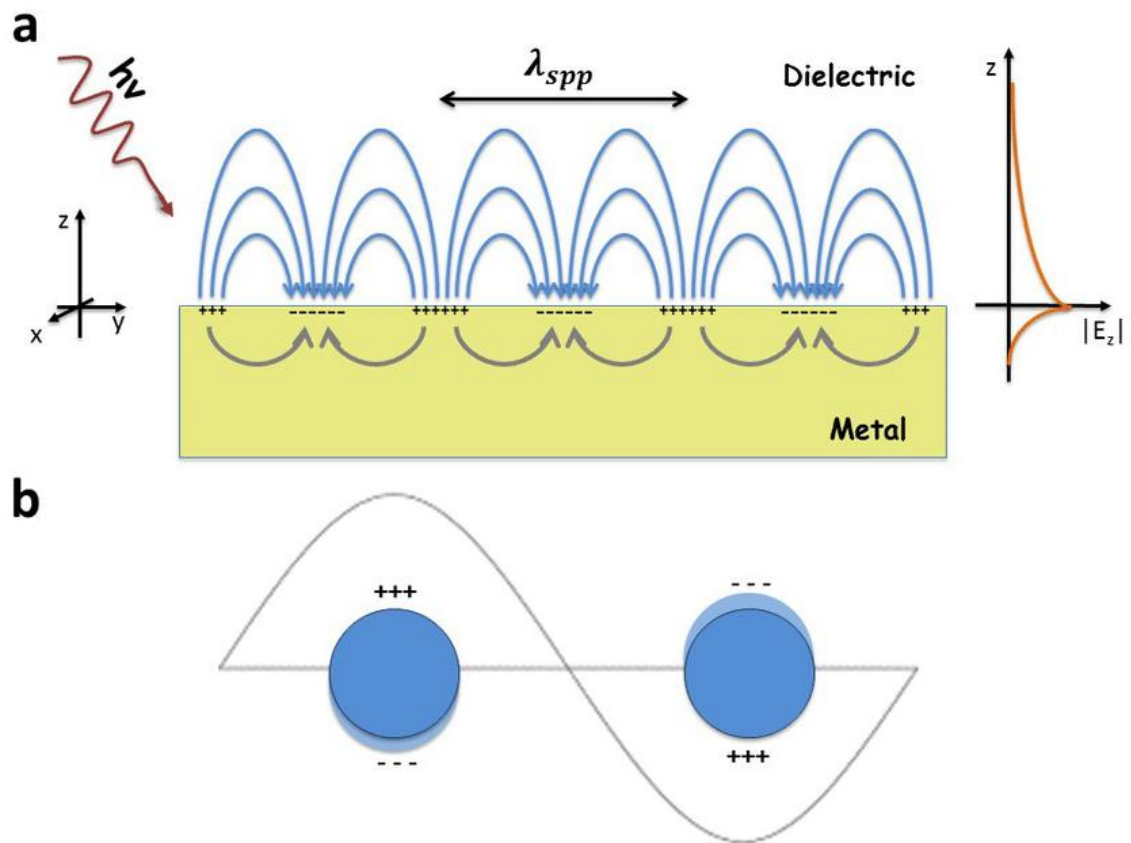


Figure 1.3 – Schematic diagrams illustrating (a) a surface plasmon polariton (or propagating plasmon) and (b) a localized surface plasmon. Reprinted with permission from G Das, M L Coluccio, S Alrasheed, A Giugni, M Allione, B Torre, G Perozziello, P Candeloro, and E Di Fabrizio. Plasmonic nanostructures for the ultrasensitive detection of biomolecules *La Rivista del Nuovo Cimento* 2016, 39, 547-586. Copyright 2016 Springer Nature.

In practice, the most common setup for SPR is the Kretschmann configuration (Figure 1.4).³⁸ A thin film of metal (typically gold) is directly deposited on a prism. The SP is excited from photons on the prism side of the metal, while the opposite surface is allowed to contact the measurement solution. The angle at which the SP is excited can be measured by a decrease in intensity of the of the reflected light. The exact angle of SP excitation is strongly dependent on the refractive index of the media in contact with the metal surface. Therefore, as biomarkers (i.e. proteins) adsorb to the metal surface, the difference between the refractive index of the biomarker and liquid solution results in a shift in the SP angle. If the refractive index of both the solution and biomarker are known, the shift in SP excitation angle can be converted to mass of adsorbed biomarker. A typical SPR system has a detection limit on the order of 10 pg/mL.³⁹

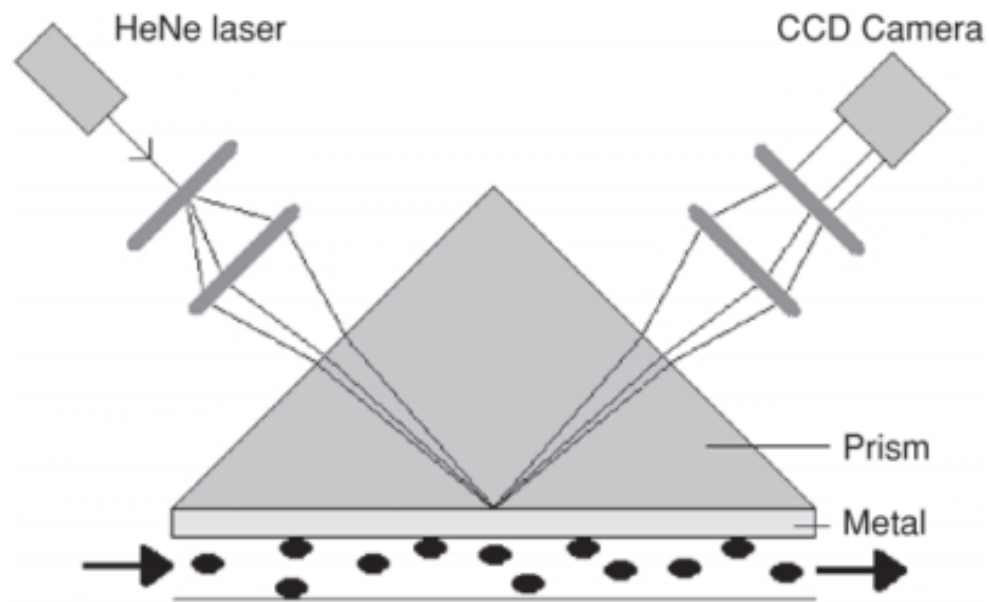


Figure 1.4 – The most common geometrical setup (the Kretschmann configuration) of SPR. The incoming light is located on the opposite side of the metallic slab than the adsorbate. Reprinted with permission from P Pattnaik. Surface Plasmon Resonance: Applications in Understanding Receptor–Ligand Interaction *Applied Biochemistry and Biotechnology*, 2005, 126, 79-92. Copyright 2005 Springer Nature.

SPR data is generally presented in the form of a sensorgram, where the change in the SP excitation angle is plotted vs time. Often, instead of directly plotting the angle change, response units (RU, also called refractive index units or resonance units), where 1000 RU corresponds to an angle change of 0.1° , are used for readability.⁴⁰ Since a typical hydrated protein has a refractive index of about $n = 1.45$, the approximation that 1000 RU is equivalent to 1 ng/m^2 of protein adsorption can then be used to convert SPR output to mass change.⁴¹ The typical shape of a sensorgram showing the association and dissociation of a target molecule is shown in Figure 1.5.⁴² As the solution containing the target is introduced to the sensor, the signal increases, indicating target adsorption to the surface. Eventually, a steady state is reached where the target is adsorbing and desorbing at equivalent rates.³⁸ At this point, if the solution containing target is replaced by plain running buffer, the target will start to dissociate from the surface, resulting in a signal decrease. The association and dissociation curves can be fit to elucidate kinetic parameters of the interaction.⁴³ Often, after the sample injection and dissociation, a solution is used to remove any remaining target from the surface, regenerating it for the next sample.⁴⁴

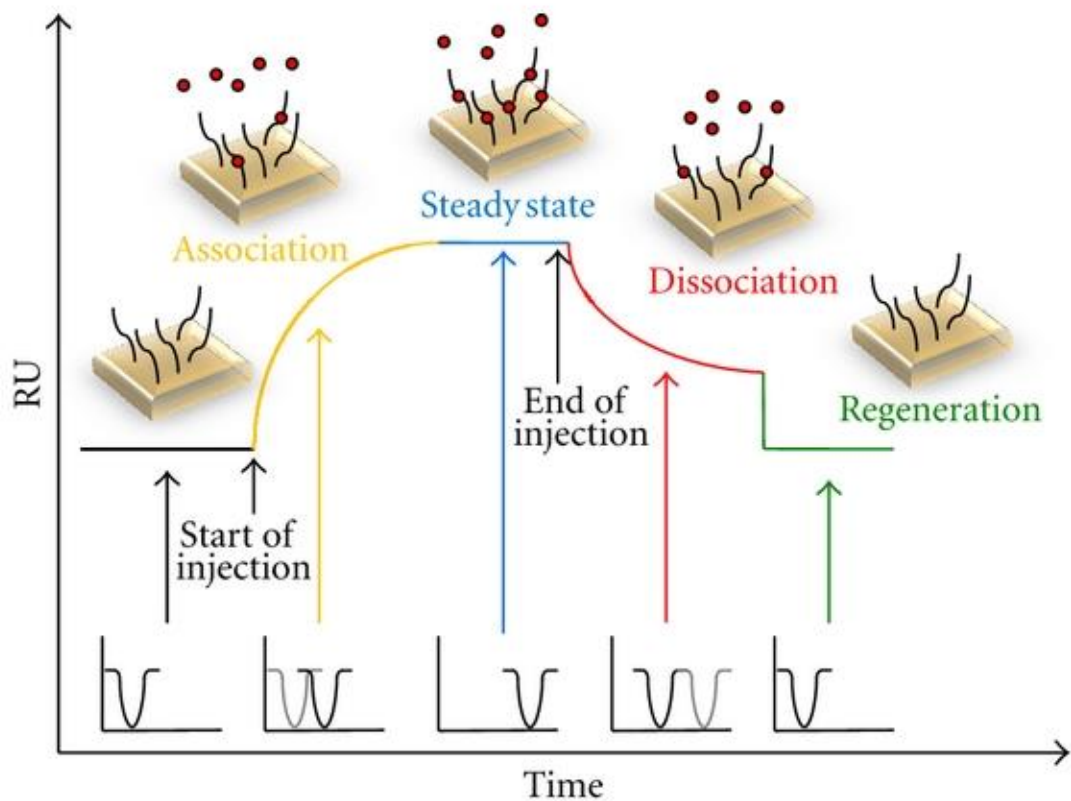


Figure 1.5 – Typical shape of an SPR-sensorgram. It can be divided into four phases: association phase, steady state or equilibrium phase, dissociation phase, and regeneration phase. Reprinted unmodified under Hindawi Journals Creative Commons Attribution 3.0 License from M Ritzefeld and N Sewald. Real-Time Analysis of Specific Protein-DNA Interactions with Surface Plasmon Resonance. *Journal of Amino Acids* 2012, Article ID 816032 doi.org/10.1155/2012/816032

While SPR is a label-free technique, the necessary optical, vibration stabilization, temperature control, and liquid handling components make the system difficult to miniaturize.⁴³ However, there are examples of miniaturized Kretschmann SPR systems for laboratory and field use in the literature.⁴⁵⁻⁴⁹ One such work miniaturized the system to only 480 mm × 150 mm × 180 mm while successfully detecting target DNA at a

concentration of 0.01 $\mu\text{mol/mL}$ (Figure 1.6).⁴⁵ Other SPR configurations are more amenable to miniaturization, such as optical fiber-based SPR probes.⁵⁰⁻⁵² However, the resolution of such sensors is insufficient compared to prism-based systems, and they suffer from increased noise due to the probe stretching and bending.⁵³ Overall, SPR systems are extremely useful in laboratory environments due to the assay's label-free, real-time detection of binding activity.³⁶ However, due to the optical component required for the detection mechanism, miniaturized, cost-effective, portable SPR units for field use are not an obvious direction.

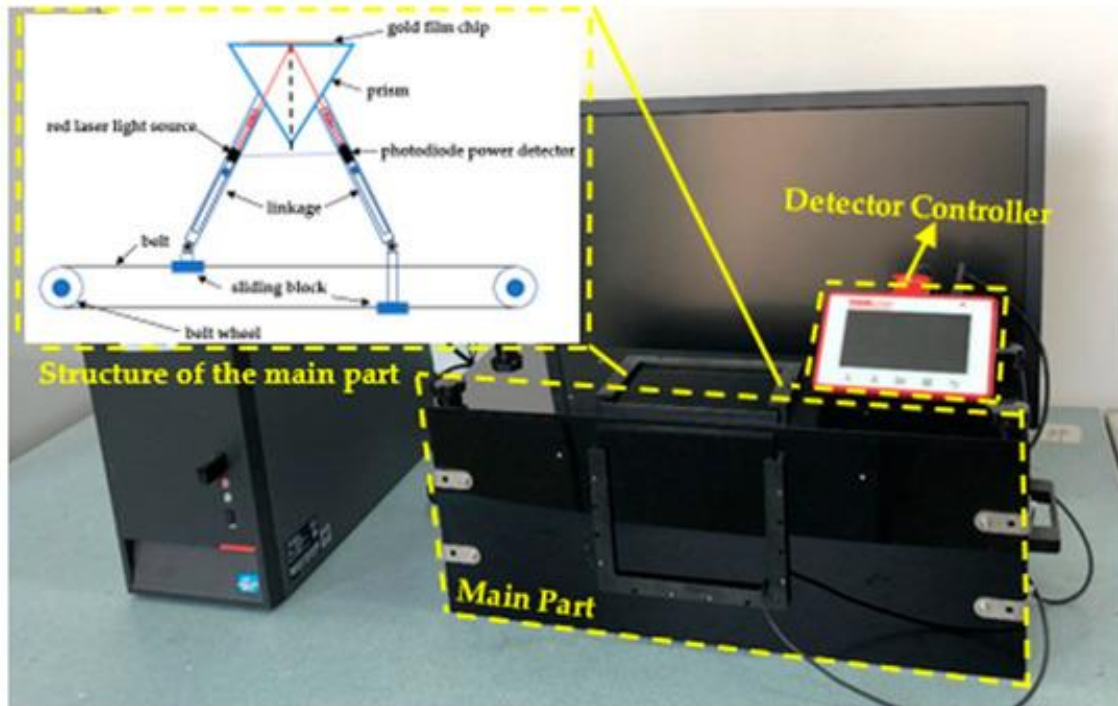


Figure 1.6 – Prototype portable SPR instrument. The overall sensor (main part) is 480 mm x 150 mm x 180 mm with a weight of 3.09 kg. Reprinted unmodified under MDPI Journals Creative Commons Attribution 4.0 International License from Y Huang, L Zhang, H Zhang, Y Li, L Liu, Y Chen, X Qiu, and D Yu. Development of a

1.1.2 Potentiometric

Unlike biomarker detection based on optical interrogation, electrical label-free biosensors can be miniaturized through cost-effective microfabrication. The sensors lend themselves to multiplexed, parallel sensing, and are easily integrated with other electronics. Due to these characteristics, potentiometric sensors are a promising platform both for rapid, in-hospital testing and as transportable sensors for health monitoring. Specifically, potentiometric biosensors detect the change of surface potential due to the attachment of charged target biomolecules to the probes on the sensing surface and are most commonly implemented in the form of ion-sensitive field effect transistors (ISFETs).

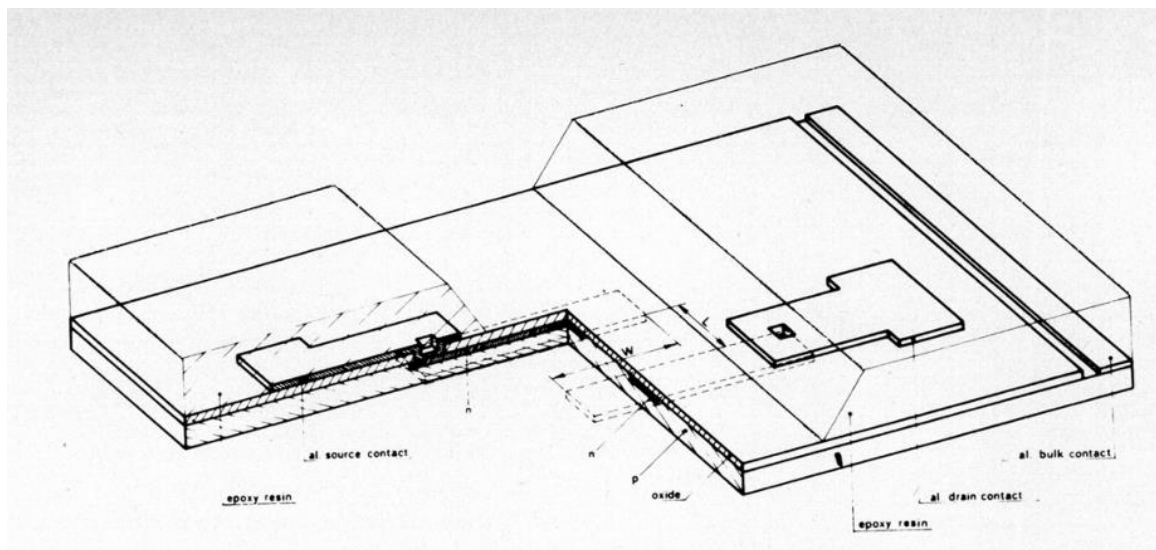


Figure 1.7 – Schematic representation of the first ISFET device. Reprinted with permission from P Bergveld. Development of an Ion-Sensitive Solid-State Device for Neurophysiological Measurements *IEEE Transactions on Biomedical Engineering*, 1970, 1, 70-71. © 1970 IEEE

The first ISFET sensor was reported by Bergveld as a tool to measure ion activities without the use of a reference electrode.⁵⁴ The device, shown schematically in Figure 1.7, was essentially a n-channel metal-oxide-semiconductor (MOS) transistor with the gate oxide exposed to solution. In this sensing setup, activity of ions in solution influence the double layer at the silicon dioxide-solution interface. This field induces a field at the oxide-silicon interface, which in turn induces a mobile surface charge at the silicon surface. The conductance between the drain and source contacts thus serves as a measure of the double layer in solution. Additionally, a potential can still be applied to the ISFET through solution via a reference electrode, where the gate threshold voltage shifts in response to ion activity changes.

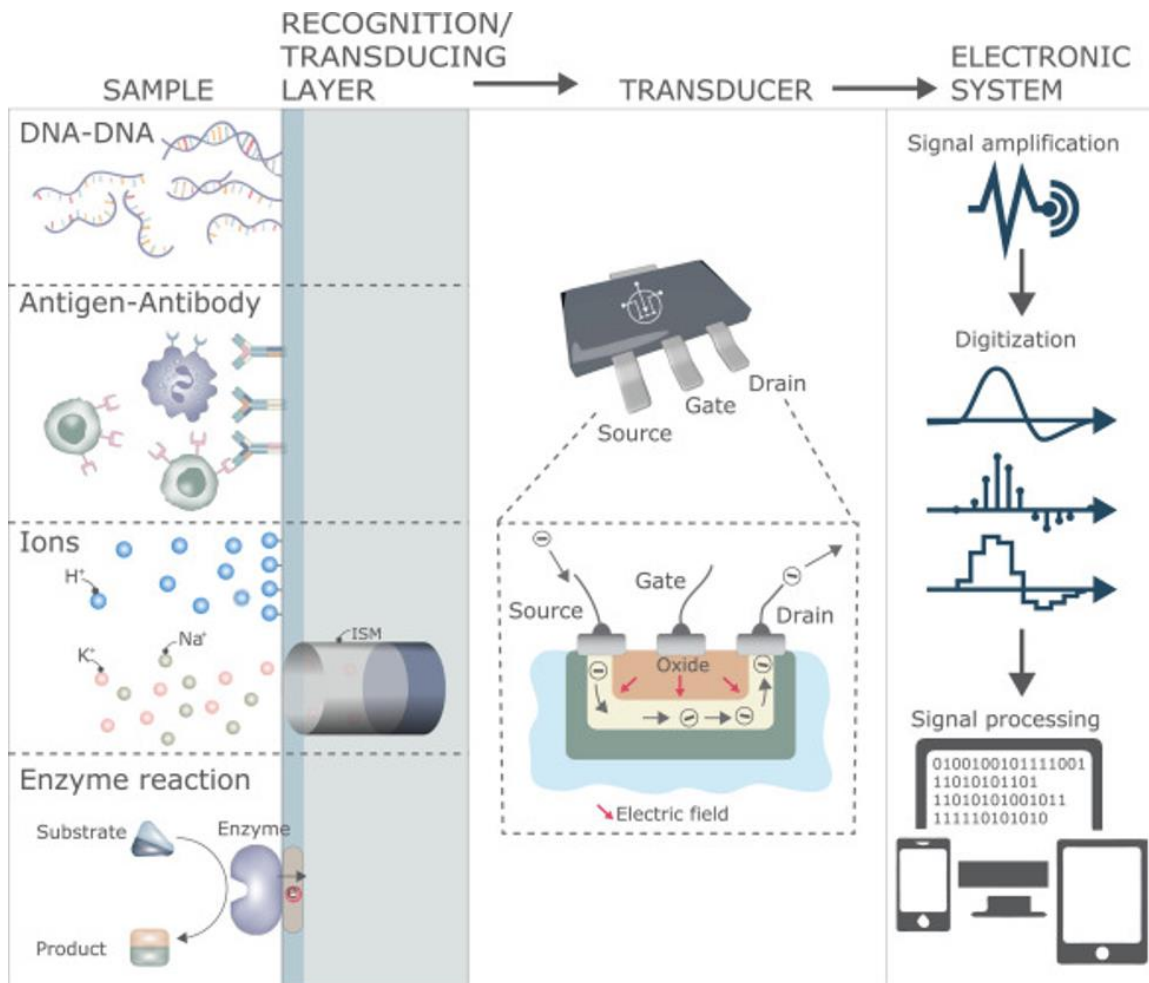


Figure 1.8 – Illustration of a biological and chemical FET sensor. Reprinted unmodified under Elsevier Creative Commons Attribution-NonCommercial-NoDerivatives 4.0 International License from M Kaisti. Detection principles of protein–antibody interactions. *2D Materials* 2015, 2, 044009. Copyright 2015 IOP Publishing Ltd.

While ISFET research initially focused on the detection of the H^+ ion, the literature has more recently shifted to emphasize gate-modification techniques that allow this sensor technology to detect biomolecular interactions.¹ FET-based sensors are now one of the most commonly reported classes of electronic sensors for biomolecular detection in the

literature,⁵⁵ and device design has expanded to include Au-gated SiO₂,^{32, 56, 57} silicon nanowires,⁵⁸ graphene,^{59, 60} carbon nanotubes,⁶¹ and MoS₂.⁶² However, despite the diversity, all FET-based biosensors follow the basic structure illustrated in Figure 1.8, where a recognition layer selectively interacts with a biomolecule of interest, a FET transduces the signal, and that signal is read out by an electronic system.^{1, 63}

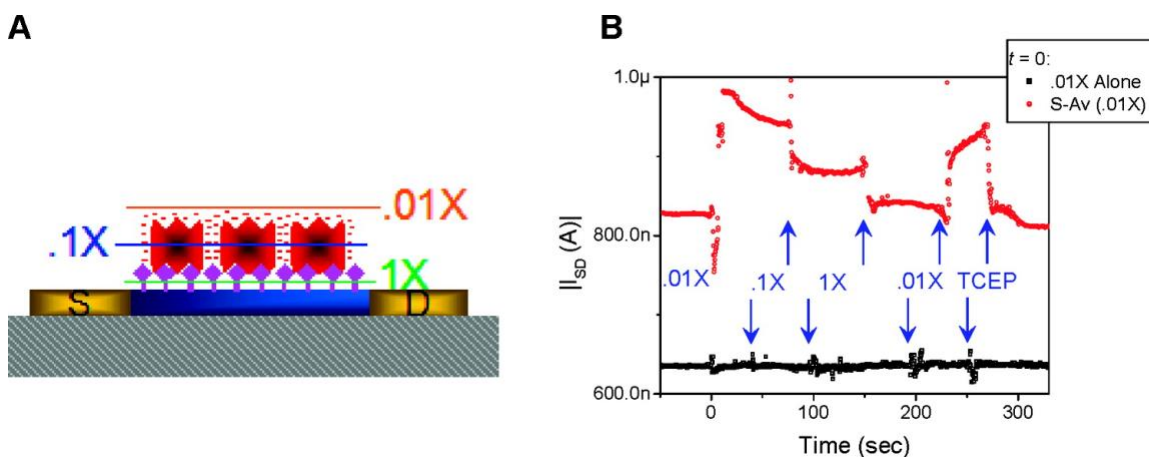


Figure 1.9—Impact of Debye screening on streptavidin sensing. (a) Schematic (not to scale) showing λD from the device surface. The blue bar represents the active region of the device, the yellow regions the leads (S = source, D = drain), the gray hashed region the underlying oxide, the purple diamonds are biotin, and the red objects are streptavidin. The negative charges surrounding the protein represent its negative charge. The green “1×” line (also not to scale) represents the screening length (λD) from 1× PBS relative to the protein and the blue and orange lines represent that from 1:10 and 1:100 dilutions of this buffer, respectively. (b) Biotin-functionalized sensor response ($|I_{SD}|$ vs time) to varying buffer ionic concentrations with (red) and without (black) streptavidin addition at time = 0. The blue text gives the PBS buffer concentration [Tris(2-carboxyethyl)phosphine hydrochloride, TCEP, was added in 0.01× PBS] and the blue arrows represent the onset of solution exchange. The two results derive from different devices. Reprinted with permission from E Stern, R Wagner, F J. Sigworth, R Breaker, T M Fahmy, and M A Reed. Importance of the Debye Screening Length on Nanowire Field Effect Transistor Sensors. *Nano Letters* 2007, 7, 11, 3405-3409. Copyright 2007 American Chemical Society.

The detection mechanism of potentiometric sensing is generally modeled as a controlled modification of gate potential through the binding of a charged biomolecule.⁶⁴ However, since biomolecule (for simplicity, protein) attachment occurs in solution, ionic screening can limit the sensitivity of the device.^{65, 66} The redistribution of ionic charge at the sensor interface due to the presence of a charged protein is generally described by electric double layer theory.⁶⁷ In short, the thickness of the diffuse layer of counter ions can be described by the Debye length (κ^{-1}), which is the distance from the surface where the electrostatic field has decreased by the multiple $1/e$ of the initial value. As seen below in Equation 1, the Debye length can be described by the permittivity of vacuum (ϵ_0), the dielectric constant (ϵ), Boltzmann's constant (k), temperature (T), the elementary charge (q), and the solution ionic strength (I).⁶⁴ The Debye length is often considered to be the sensing length; charge beyond this distance will not significantly perturb the screening layer. Figure 1.9a shows the issue pictorially, where the Debye screening length in solutions of physiological strength are often too short (<1 nm) to expect detection of large biomolecules.⁶⁸ For instance, the length of an IgG Ab often used as a receptor in potentiometric sensors is on the order of 5-10nm.⁶⁹ Due to this screening, sensing procedures often include measurement in lower ionic strength solution in order to increase sensitivity (Figure 1.9) or the device is measured dry.⁷⁰ There is also evidence that modification of the surface, such as the addition of polyethylene glycol (PEG), allows detection beyond the expected Debye limit, potentially by increasing the dielectric constant near the interface.⁷¹ Moreover, the exact mechanism of FET-based sensing is still debated,

with many devices showing sensitivity in physiological strength solutions, despite Debye screening.^{32, 57, 66, 72, 73}

$$\kappa^{-1} = \left(\frac{\epsilon_o \epsilon kT}{2q^2 I} \right)^{\frac{1}{2}} \quad \text{Equation 1}$$

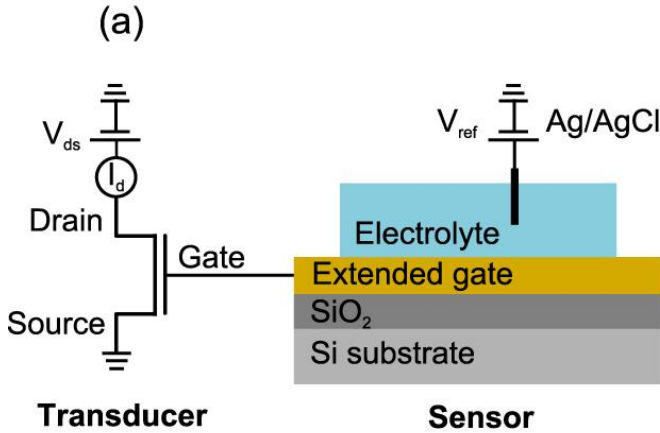


Figure 1.10 – Schematic of EGFET Sensor. Reprinted with permission from A Tarasov, MY Tsai, E M Flynn, C A Joiner, R C Taylor, and E M Vogel. Gold-coated graphene field-effect transistors for quantitative analysis of protein–antibody interactions. *2D Materials* 2015, 2, 044009. Copyright 2015 IOP Publishing Ltd.

Despite screening challenges, the literature is replete with proof-of-concept potentiometric sensing. However, repeatability and stability are crucially lacking, preventing potentiometric sensors from gaining commercial success. Despite the broad range of FET biosensor designs, it has been shown that the sensitivity of a potentiometric biosensor is essentially independent of the choice of the transducer and instead relies on the sensing surface.⁵⁷ Therefore, much of what is learned from one sensor system can be

generalized across FET sensing platforms. Additionally, while most ISFET designs require a sophisticated encapsulation scheme to protect the semiconductor device from exposure to the liquid environment that can hamper reliability and stability, extended-gate FET (EGFET) biosensors do not.³² In this scheme, as shown in Figure 1.10, the sensing chip (or extended gate) is separated from the readout transducer to provide a simpler and a more robust design for liquid phase sensing while simultaneously lowering cost by simplifying fabrication. Additionally, EGFET sensing with Au electrodes has been demonstrated both in model systems and applied to real-blood detection, as shown in Figure 1.11 for the detection of Bovine Respiratory Disease (BRD) in serum.^{32, 57} The sensor responds to changes in surface potential as charged antibody binds to the sensor surface, which subsequently alters the channel current inside the FET (Figure 1.11a).³² The EGFET sensor, when benchmarked against SPR and standard ELISA technology, shows a comparable detection limit and detection range (Figure 1.11b,c).³² These results indicate that EGFET sensors could be a more versatile, next-generation counterpart to ELISA.

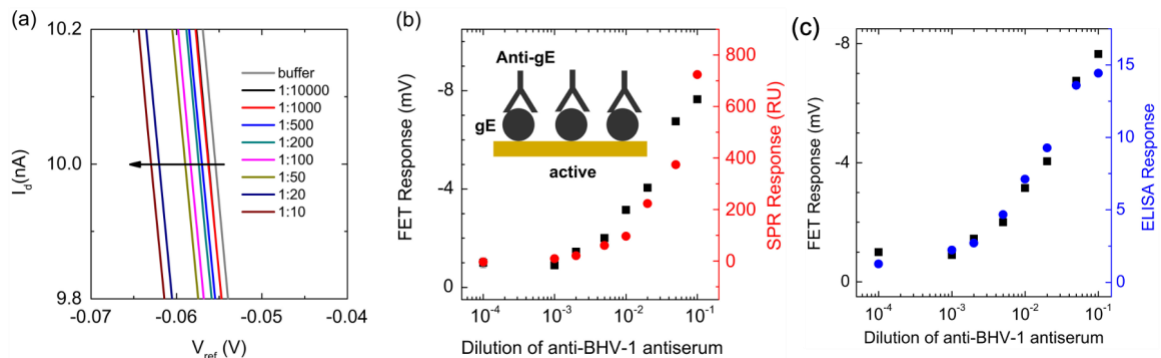


Figure 1.11 – BRD detection using EGFET, benchmarked to SPR and ELISA. (a) The application of increasing concentrations of negatively charged antibody shifts the

FET gate voltage. The detection limit and sensitivity of EGFET detection of BRD in blood plasma scales with both SPR (b) and standard ELISA (c) analysis. Reprinted with permission from A Tarasov, D W Gray, MY Tsai, N Shields, A Montrose, N Creedon, P Lovera, A O'Riordan, M H Mooney, and E M Vogel. A potentiometric biosensor for rapid on-site disease diagnostics. *Biosensors and Bioelectronics* 2016, 79, 669-678. Copyright 2015 Elsevier.

1.2 Protein-Surface Interactions

During biomolecular sensing, biomolecules in solution interact with the sensor surface. Ideally, protein recognition mechanisms are leveraged to allow only target proteins to attach to the surface, imparting signal selectivity. However, unwanted protein interactions with sensor surfaces (non-selective adsorption, NSA) cause signal instability and increase false-positive rates.⁷⁴⁻⁷⁶ Additionally, unexpected interactions between the selective receptor and the sensor can cause denaturation of the receptor protein, causing false negative results.⁷⁷⁻⁷⁹

1.2.1 Protein Structure

In order to discuss protein adsorption behavior, it is important to understand basic protein structure. A protein is a complex copolymer composed of amino acids (AmA), which are attached end-to-end through covalent peptide bonds, forming a polypeptide chain.⁸⁰ All AmAs have the general structure $H_2N-CHR-COOH$, in which the R group identifies one of 20 different AmAs.^{81, 82} The identity of the R-group further gives the residue specific functional characteristics, such as hydrophilicity, polarity, charge, and hydrogen bonding capability. A typical protein is composed of 100s of AmAs, where the order of those AmAs determines the protein sequence, which is also called the primary

structure (Figure 1.12a).⁸³ The polypeptide chain arranges into three main types of secondary structure: α -helices, β -sheets, and loops that connect the structured sections (Figure 1.12b).⁸⁴ These secondary structures are largely formed through hydrogen bonding. The secondary structures then organize into tertiary structure (Figure 1.12c). If there is more than one AmA chain in a protein structure, the complex is referred to as quaternary structure (Figure 1.12d). The final structure of a folded protein creates bioactive domains that allow for biological function and selective interactions with other biomolecules.^{85, 86}

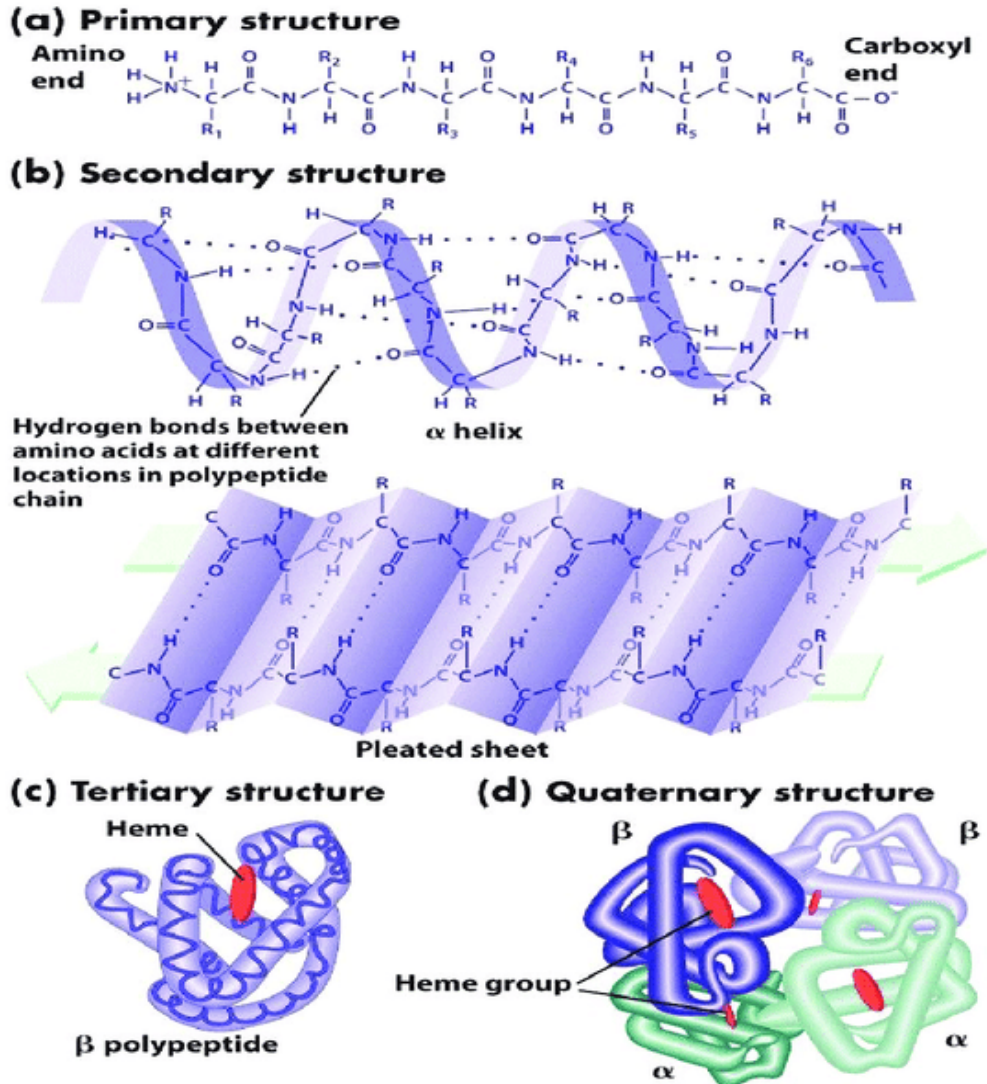


Figure 1.12 – Protein structure levels. (a) Primary structure, the amino acid sequence (b) secondary structure, α -helix and β -sheet (c) tertiary structure, and (d) quaternary structure. Reprinted with permission from R Gupta, A Dey, A Vijan, and B Gartia, In Silico Structure Modeling and Characterization of Hypothetical Protein Y 004590319.1 Present in *Enterobacter aerogenes*. *Journal of Proteomics and Bioinformatics* 2017, 10, 152-170. Copyright 2017 Longdom Publishing.

Proteins fold into a compact form that generally corresponds to the lowest conformational energy.⁸⁷ The lowest energy conformation is determined by AmA characteristics through steric hindrance; ionic, hydrogen, and van der Waals (vdW) interactions; and the hydrophobic effect.⁸⁸ The formation of ionic, hydrogen, and vdW interactions decrease the conformational energy through favorable enthalpic interactions. However, entropic effects also play a crucial role in the stabilization of protein structure. Although the polypeptide chain conformational entropy decreases upon folding, the entropy of the system increases due to the hydrophobic effect.⁸⁹ Water retains short-range order in the liquid state as a result of hydrogen bonding between adjacent water molecules.⁹⁰ X-ray diffraction and thermochemical data indicates that liquid water maintains hydrogen bonds with 4 neighboring molecules, but deformations in the tetrahedral structure are common, causing loss of long-range order.^{91, 92} When hydrophobic residues are exposed to solution, the local ordering of water is interrupted.⁹³ Around small hydrophobic molecules, highly-ordered cages of water, called clathrates, are formed (Figure 1.13a).⁹⁴ The energy loss associated with clathrate formation is generally explained by a decrease in entropy, due to a retardation in the rotational and translational motion of water molecules in the hydration shell.^{92, 95, 96} When a protein folds, hydrophobic AmA residues can be hidden in the interior of the structure, resulting in a release of ordered water.⁹⁷ The cumulative effect of negative entropic interactions of ionic, hydrogen, and vdW bonds, as well as the positive enthalpic contribution of the hydrophobic effect, leads to a net stabilization for the folded protein state (Figure 1.13b).⁹⁸

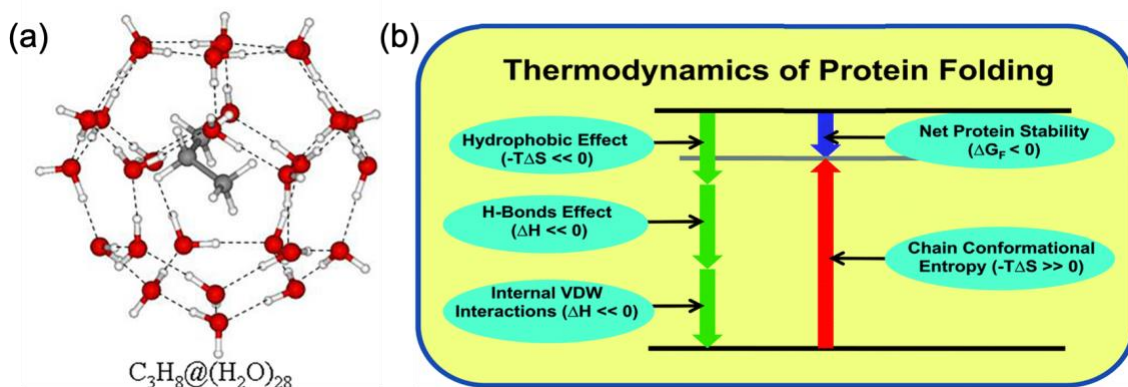


Figure 1.13 – Importance of the hydrophobic effect. (a) optimized structure of a propane clathrate hydrate. Reprinted with permission from G Lanza and M A Chiacchio. The water molecule arrangement over the side chain of some aliphatic amino acids: A quantum chemical and bottom-up investigation. *International Journal of Quantum Chemistry* 2020, 120 (9), e26161. Copyright 1969, John Wiley and Sons (b) Illustration of the thermodynamics of protein folding, including the contributions of various stabilizing and destabilizing interactions. Reprinted with permission from A Rani and P Venkatesu. Changing relations between proteins and osmolytes: a choice of nature. *Physical Chemistry Chemical Physics* 2018, 20 (31), 20315-20333. Copyright 2018 Owner Societies.

A specific subgroup of proteins useful in biosensing applications are antibodies (Ab). These proteins, also called immunoglobulins (Ig), are part of the body's immune system. The quaternary Ab structure is composed of 4 amino acid chains, 2 heavy and 2 light chains that form a Y-shape.^{99, 100} Ends of the Y (the Fragment antigen-binding, Fab) are highly variable and give an antibody specificity for one target, or antigen (Ag). The stem of the Y (the Fragment crystallizable, Fc) is constant within a class of Ab, and determines immune response after the antibody binds to an antigen in the body.¹⁰¹ The structure of a Human IgG Antibody is shown in Figure 1.14.¹⁰²

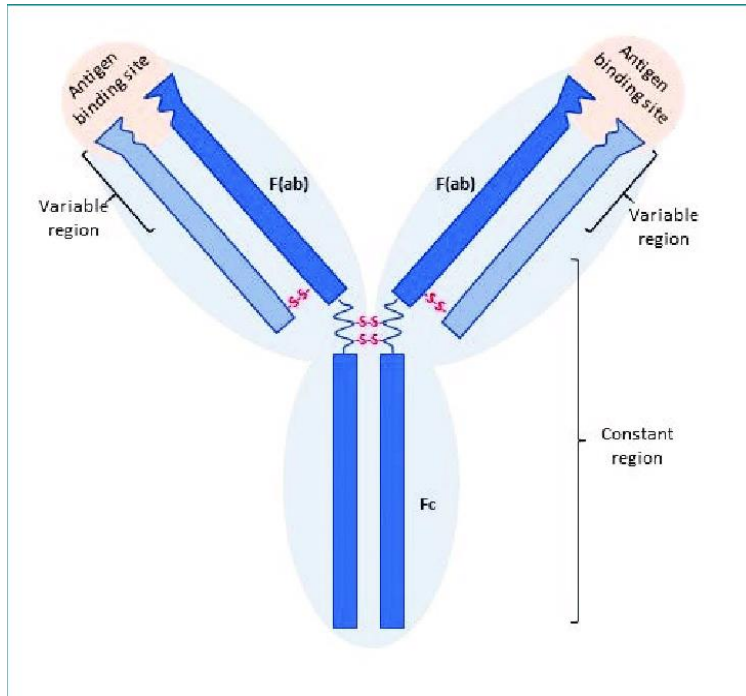


Figure 1.14 – Antibody structure. Human antibodies are composed of four polypeptide chains: two heavy chains (dark blue) and two light chains (light blue). Antigen binding sites are each formed by the variable regions of a light chain and a heavy chain (Fab regions). The constant regions of the heavy chains form the tail (Fc region). The two Fab regions and Fc region are linked by a flexible hinge region that improves the ability of the Ab to bind antigen. Reprinted with permission from N Stevens and A Cowin. *Overcoming the challenges of topical antibody administration for improving healing outcomes: a review of recent laboratory and clinical approaches. Wound Practice & Research: Journal of the Australian Wound Management Association 2017. Copyright 2017 Cambridge Media.*

1.2.2 Antibody-Antigen Interactions

Because Abs contain highly selective binding sites for their respective Ags, Ab-Ag binding is a useful recognition mechanism for biosensing.¹⁰³ The “lock-and-key” model, originally used to describe enzyme-substrate interactions, is also employed to illustrate the selectivity of an Ab for a specific Ag (Figure 1.15).^{103, 104} Generally, the binding event is

driven by enthalpic factors and often involves minor structural changes in the binding sites.¹⁰⁴

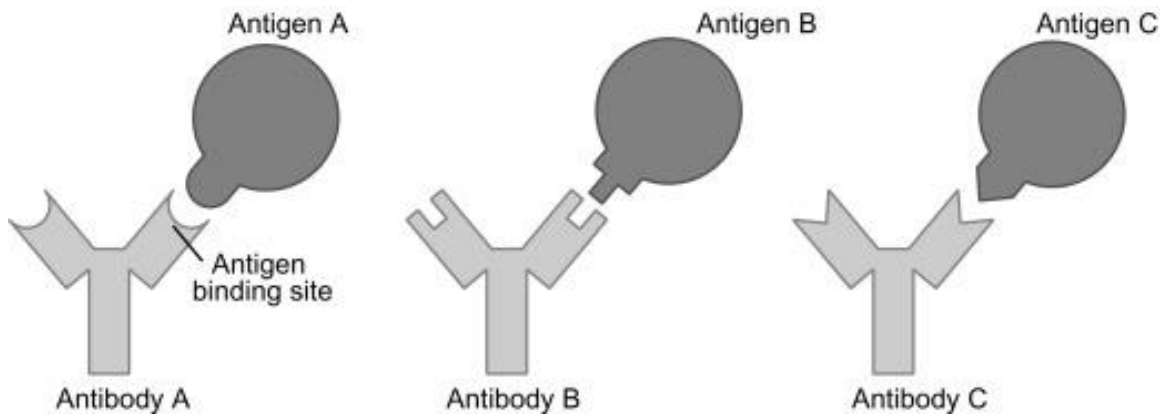


Figure 1.15 – Lock-and-key model of antigen-antibody binding. Reprinted with permission from J X Zhang and K Hoshino. *Molecular Sensors and Nanodevices: Principles, Designs and Applications in Biomedical Engineering*. Academic Press: 2018. Copyright 2019 Elsevier Inc.

Kinetic modelling allows for quantification of the Ab-Ag affinity. The simplest model considers rate equations for Ab-Ag binding where one active site is present per Ab.^{105, 106} The reversible reaction can be expressed as shown in Equation 2, where AbAg is the Ab-Ag complex. The forward and reverse reaction rates are identified by k_a (association) and k_d (dissociation), respectively.



In equilibrium, $k_a=k_d$. Under these conditions, K_a , the association binding constant, can be written as shown in Equation 3, where brackets indicate concentration.¹⁰⁷

$$K_a = \frac{k_a}{k_d} = \frac{[AbAg]}{[Ab][Ag]} \quad \text{Equation 3}$$

K_a , with units of M^{-1} , will be large for high-affinity interactions ($k_a \gg k_d$). However, it is often convenient to discuss the dissociation equilibrium constant instead, where units are simply M (Equation 4). The dissociation constant corresponds to the concentration at which 50% of the Ab in solution is bound to an Ag at equilibrium. A stronger affinity interaction corresponds to a smaller K_d .

$$K_d = \frac{1}{K_a} = \frac{[Ab][Ag]}{[AbAg]} \quad \text{Equation 4}$$

For a biosensor, Ab - Ag binding occurs on a sensor surface. There is a finite number of available binding sites which dictate the saturation signal of the sensor. In this situation, the most commonly used attachment model is Langmuir adsorption.^{108, 109} This model assumes adsorption to and desorption from distinct surface sites and ignores adsorbate/adsorbate interactions. During adsorption (Equation 5) the amount of adsorbed protein (q) is determined by the adsorption (k_a) and desorption (k_d) reaction rates as well as the total number of available surface sites (Q), protein concentration (C) and time (t). For desorption only (Equation 6) the expression can be simplified.¹¹⁰

$$q(t) = Q(1 - e^{-t(k_a C + k_d)}) \quad \text{Equation 5}$$

$$q(t) = Q(e^{-tk_d}) \quad \text{Equation 6}$$

Modifications to Langmuir binding kinetics can improve model performance in systems where the Langmuir assumptions do not hold, such as instances of 2:1 binding, Ag-Ag interactions, or mass transport limitations.^{108, 111, 112}

1.2.3 Non-Selective Adsorption

Protein adsorption to surfaces is a common, and complicated, phenomenon.^{84, 113} Specifically for biosensing applications, non-selective adsorption (NSA) to the device generally results in degradation of the sensor. Unlike rigid, small molecules, proteins have complex structure that may change during adsorption, resulting in phenomena such as cooperativity, size exclusion, and changing surface affinities. Properties of the protein, surface, and solution all effect the protein-surface interaction.¹¹³ For proteins themselves, size and structural stability tend to influence adsorption phenomena.¹¹⁴ Smaller, ‘hard’ proteins such as lysozyme do not generally undergo any structural alterations upon adsorption, while larger ‘soft’ proteins such as albumin undergo complex conformational rearrangement upon interaction with a surface.¹¹⁵⁻¹¹⁷

As with protein folding, a major driving force for protein-surface interaction is the hydrophobic effect.¹¹⁸ As such, NSA of proteins increases with increasing surface hydrophobicity,¹¹⁹ where the hydrophobic effect stabilizes the interaction with an energy of approximately $45\text{-}60 \text{ cal/mol}\cdot\text{\AA}^2$.^{120, 121} Often, upon hydrophobic adsorption, proteins deform or partially unfold to achieve the most stable interaction.⁷⁷⁻⁷⁹ This unfolding is common enough to be known in hydrophobic interaction chromatography as a denatured peak,^{77, 78} and can render the protein inactive and thus useless as a biosensor functional

unit. Figure 1.16 shows a protein adsorbing to a hydrophobic surface, where the initial interaction and subsequent denaturation is entropically favored due to the release of water.¹²² Although surface energy, polarity, charge, and morphology all influence protein adsorption behavior, engineering methods for the development of anti-biofouling materials generally focus on hydrophilicity.^{119, 123, 124}

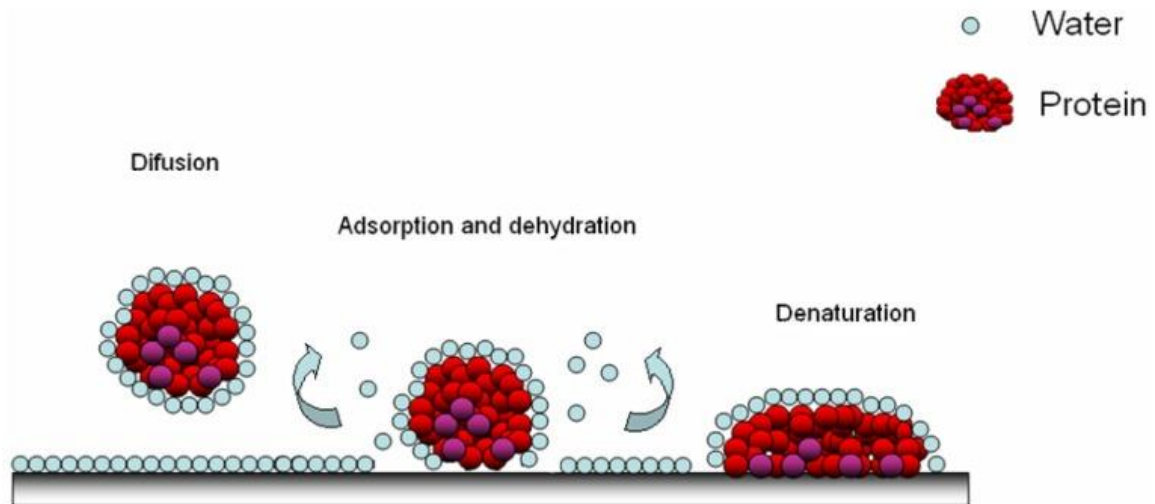


Figure 1.16 – Adsorption and denaturation of a protein on a hydrophobic surface, allowing the release of structured water. Reprinted unmodified under MDPI Journals Creative Commons Attribution 4.0 International License from F Poncin-Epaillard, T Vrlinic, D Debarnot, M Mozetic, A Coudreuse, G Legeay, B El Moualij, and W Zorzi. Surface Treatment of Polymeric Materials Controlling the Adhesion of Biomolecules. *Journal of Functional Biomaterials*. 2012, 3, 528-543.

Temperature, pH, and buffer ionic strength can all influence protein adsorption to a given surface.¹¹³ Temperature generally has the effect of increasing adsorption by accelerating diffusion of protein to the surface.^{113, 125} pH alters the charge of the protein. When the pH of solution is equivalent to the isoelectric point (pI) of the protein, larger amounts of adsorption are possible due to a lack electrostatic protein-protein repulsion on

the surface. Moreover, if the substrate at protein are electrostatically attracted, increased adsorption is expected.^{126, 127} Ionic strength of the solution can also effect protein adsorption, by altering the Debye screening length and therefore the electrostatic interactions between charged species in solution.¹²⁸ As such, in a high ionic strength solution, adsorption of proteins to oppositely-charged substrates is diminished while adsorption to like-charged substates is enhanced.¹²⁹

Different kinetic models have been proposed to describe observed protein adsorption behavior. Generally these models are derived from rate equations and build from the Langmuir model (Equation 5, Equation 6) with additional terms to describe phenomena such as irreversible adsorption and lateral interactions.¹³⁰⁻¹³² A schematic overview of some of the most common kinetic models is shown in Figure 1.17.¹¹³ Although generally insufficient to properly describe free protein adsorption to a surface, the Langmuir model remains the most-applied model, mostly due to its simple mathematical format.¹¹³

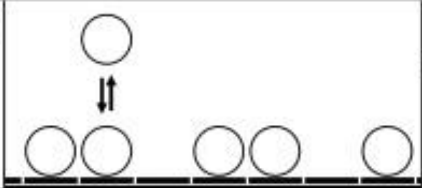
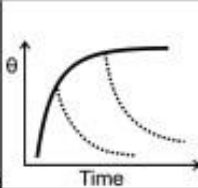
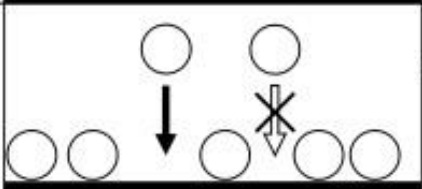
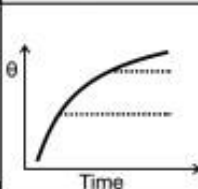
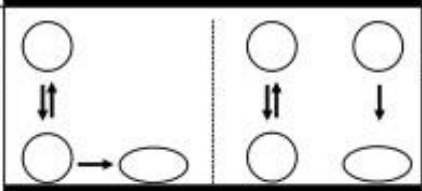
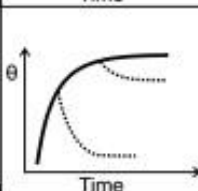
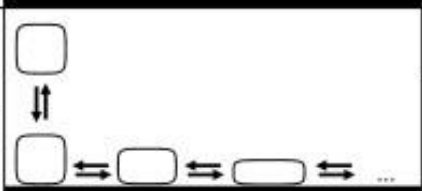
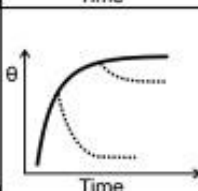
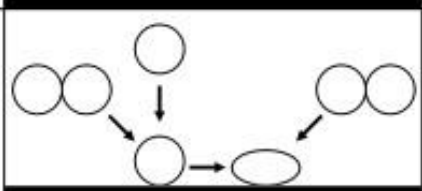
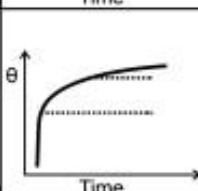
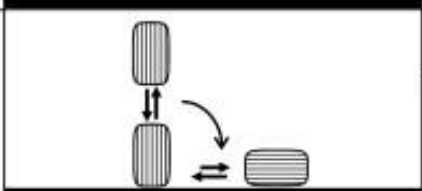
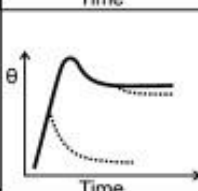
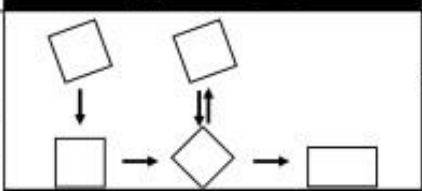
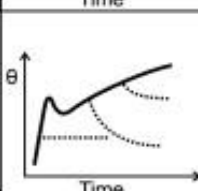
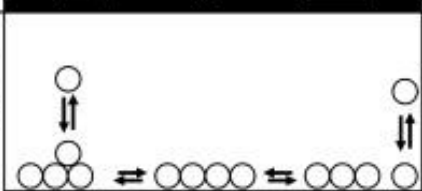
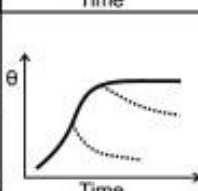
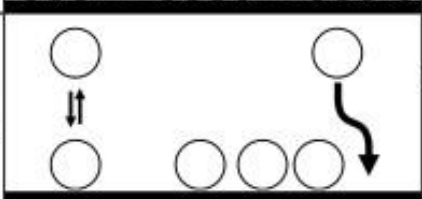
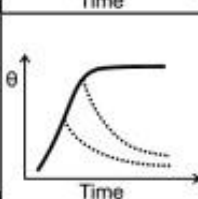
<p>A Langmuir Model adsorption to distinct available surface sites</p>		
<p>B RSA Model adsorption to random available surface sites</p>		
<p>C Two-states Model conformational changes upon adsorption lead to increasing affinity - transition model (left) - two-path model (right)</p>		
<p>D Multiple-states Model transition into states of increasing footprints</p>		
<p>E Monomer/dimer exchange dimers in the bulk solution can replace adsorbed monomers</p>		
<p>F Rollover Model reorientation of end-on adsorbed proteins into side-on adsorbed proteins leads to overshooting kinetics</p>		
<p>G Three-states Model transition of irreversible state into reversible state leads to overshoot</p>		
<p>H Surface clusters 2-dimensional clusters grow via the piggyback pathway (left) or via diffusional addition of monomers (right)</p>		
<p>I Tracking Model cooperative adsorption due to the tracking of proteins to binding sites close to other pre-adsorbed proteins</p>		

Figure 1.17 – Overview of kinetic models. A short scheme of each adsorption mechanism is presented in the middle column. The most important characteristics of the observable adsorption kinetics are depicted in the right column (solid line: adsorption curve; dashed line: desorption curve upon buffer rinsing). Reprinted with permission from M Rabe, D Verdes, and S Seeger. Understanding protein adsorption phenomena at solid surfaces. *Advances in Colloid and Interface Science* 2011, 162 (1-2), 87-106. Copyright 2011 Elsevier B.V.

1.3 Thiol-Based Self-Assembled Monolayers

1.3.1 SAM History and Uses

Monolayer self-assembly was first discovered in the 1940s,¹³³ but the potential of the technology was not immediately recognized and SAMs did not become a significant research focus until the 1980s.¹³⁴ However, since then, many self-assembly systems have been studied and applied in various fields, with thiol SAMs on Au coming to the forefront.^{134, 135} For example, as summarized in Figure 1.18,¹³⁶ thiol SAMs have been used as anti-stiction coatings in micromechanical devices,¹³⁷ to study protein adsorption to surfaces,¹¹⁹ for soft lithography patterning through microcontact printing,¹³⁸ as interlayers in organic electronics,¹³⁹ and, of course, for biosensing.¹⁴⁰ In previous EGFET sensing, self-assembled monolayers (SAMs) of thiols on Au were utilized to link receptor molecules to the sensing surface and thus create a selective biosensor.^{32, 57}

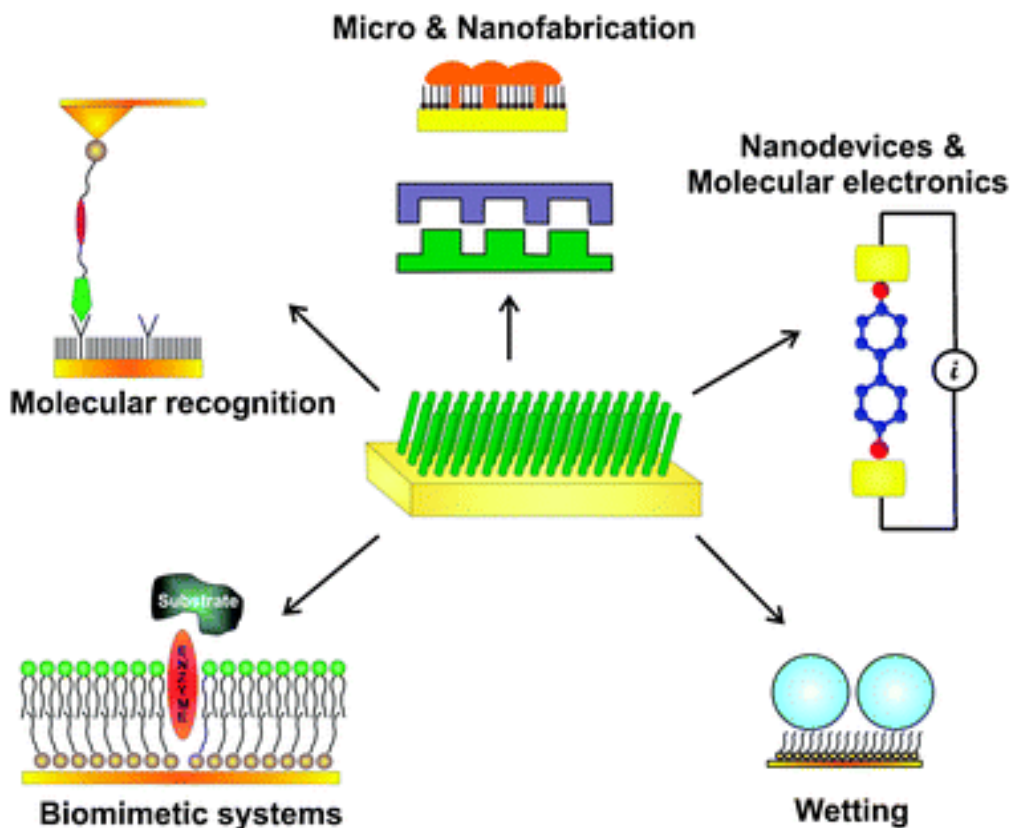


Figure 1.18 – Some applications of self-assembled monolayers in nanotechnology. Reprinted with permission from C Vericat, M E Vela, G Benitez, P Carrob, and R C Salvarezza. Self-assembled monolayers of thiols and dithiols on gold: new challenges for a well-known system. *Chemical Society Reviews* 2010, 39 (5), 1805-1834. Copyright 2010 Royal Society of Chemistry.

Thiol SAMs spontaneously order on Au from solution, with ethanol being the most common solvent.¹³⁴ First, the S chemisorbs to the Au surface; the sulfur-gold interaction is on the order of 45 kcal/mol.¹⁴¹ This strong interaction is about half the strength of a typical C-C covalent bond, which is on the order of 100 kcal/mol.¹⁴² Secondly, the alkane chains interact with one another through vdW forces, driving the thiol molecules to form an ordered layer.¹⁴³ Due to a packing mismatch between the S and Au atoms, the thiol chains

tilt approximately 30° from normal to maximize the hydrocarbon chain vdW interactions.^{141, 144} The resulting monolayer is illustrated in Figure 1.19, where the S head group is bound to the Au surface, the spacer alkane chains are tilted to maximize interaction, and a customizable terminal functional group at the end of the alkane chain is exposed to solution.

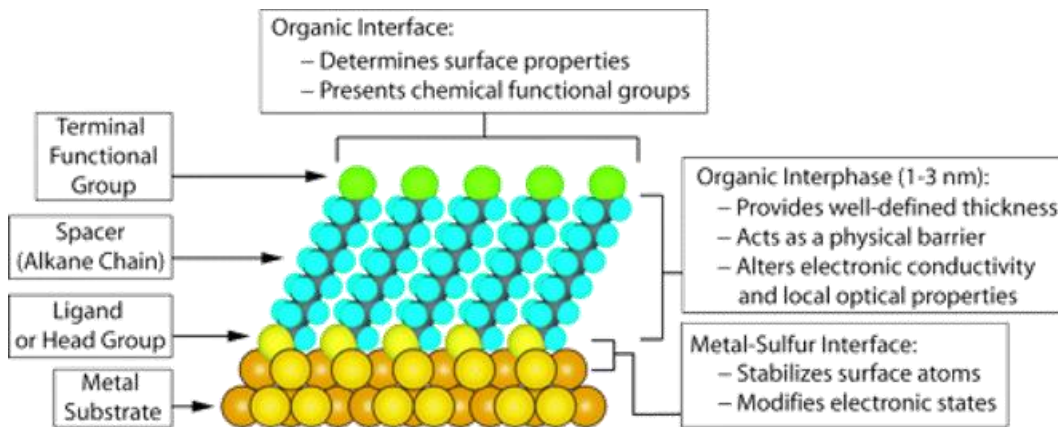


Figure 1.19 – Schematic diagram of an ideal, single-crystalline SAM of alkanethiolates supported on a gold surface with a (111) texture. Reprinted with permission from J C Love, L A Estroff, J K Kriebel, R G Nuzzo, and G M Whitesides. Self-assembled monolayers of thiolates on metals as a form of nanotechnology. *Chemical Reviews* 2005, 105 (4), 1103-1170.

1.3.2 COOH-SAMs for Biosensing Applications

When used for biosensing, protein immobilization is accomplished through amine coupling to carboxyl head groups on the SAM, as seen in Figure 1.20.¹⁴⁵⁻¹⁴⁷ The carboxylic acid (COOH) is activated with a mixture of 1-Ethyl-3-(3-dimethylaminopropyl) carbodiimide (EDC) and N-Hydroxysuccinimide (NHS). The EDC reacts first with the carboxylic acid to form an unstable o-acylisourea intermediate, which further reacts with

NHS to form a semi-stable ester. Displacement of the NHS by a primary amine on the target protein affords the stable amide linkage. Generally, ethanolamine (ETA) is used to react with remaining NHS esters. Carboxyl-terminated thiol self-assembled monolayers (COOH-SAMs) on Au are a common choice for amine coupling, and researchers have utilized them for potentiometry,^{32, 57} electrochemical impedance spectroscopy (EIS),^{56, 148} SPR^{32, 149} amperometry,¹⁵⁰⁻¹⁵² voltammetry,^{153, 154} piezoelectricity,¹⁵⁵ and QCM^{156, 157} based sensors. These linker molecules are particularly important in potentiometric sensing where Debye length considerations restrict the properties of the linker molecule, rendering high signal matrices like dextran utilized in modern SPR unusable.^{32, 68, 158, 159}

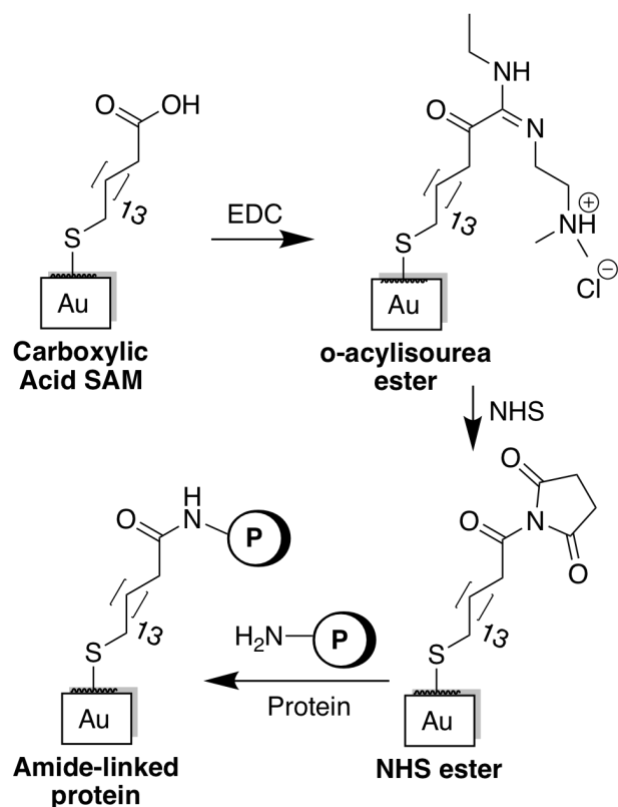


Figure 1.20 – Protein receptor functionalization of the SAM via amine coupling. Reprinted with permission from E L Brightbill, B Hitchcock, MY Tsai, A Verga, and E M Vogel. Preblocking Procedure to Mitigate Nonselective Protein Adsorption for Carboxyl-SAMs Used in Biosensing. *The Journal of Physical Chemistry C* 2019, 123 (27), 16778-16786. Copyright 2019 American Chemical Society.

1.3.3 COOH-SAM Structure and Defects

While well-defined surface functionalization is crucial for the development of a reliable biosensing system, many studies using COOH-SAMs assume a well-ordered monolayer.^{32, 57, 149, 151-153, 155, 156, 160} However, work that has included characterization of the COOH-SAM^{148, 150, 154, 157} indicates far from ideal monolayers are common: EIS and

cyclic voltammetry show that the surface is not completely blocked by the SAM,^{148, 150, 154} with the percentage of defects and pinholes reported as high as 48.8%.¹⁵⁰

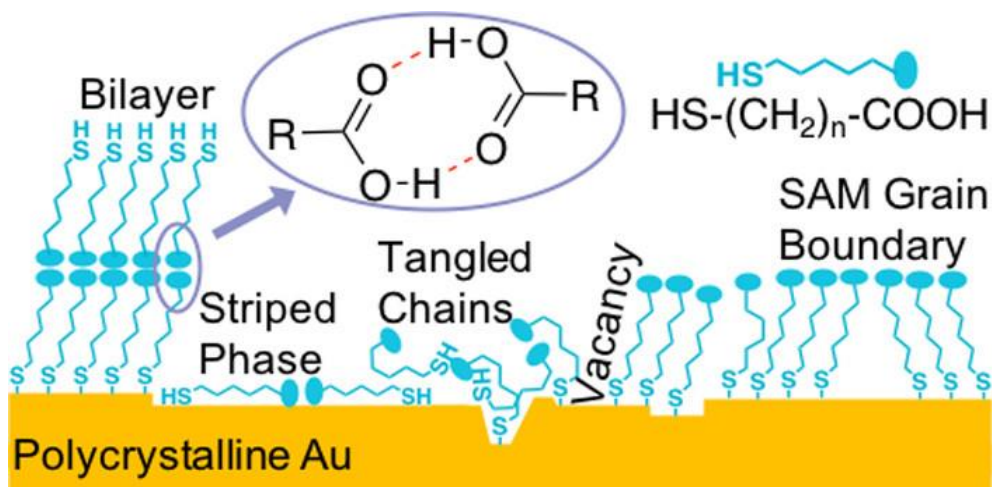


Figure 1.21 – COOH-SAM defects on polycrystalline Au, including bilayer formation through hydrogen bonding, striped phase, tangled chains and gauche defects, vacancies, and SAM grain boundaries. Reprinted with permission from E L Brightbill, B Hitchcock, MY Tsai, A Verga, and E M Vogel. Preblocking Procedure to Mitigate Nonselective Protein Adsorption for Carboxyl-SAMs Used in Biosensing. *The Journal of Physical Chemistry C* 2019, 123 (27), 16778-16786. Copyright 2019 American Chemical Society.

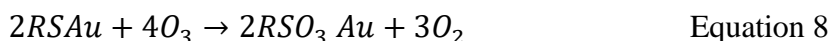
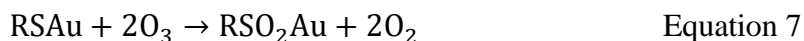
The common assumption of well-formed COOH-SAMs also overlooks literature outside of the biosensor realm which discuss SAM defects; a schematic of possible defects is illustrated in Figure 1.21.¹⁶¹⁻¹⁶⁴ Defects common in all SAMs include laying-down, “striped” phases, gauche defects in alkyl chains interrupting the chain-to-chain vdW interactions, and grain boundaries in the SAM structure due to the tilt of chain alignment from normal.^{135, 165} In addition to these defects, the bulky carboxylic acid head-group decreases the density of packing and ordering of the SAM.¹⁶² Moreover, carboxylic acids can cooperatively hydrogen bond into a resonance stabilized dimer.^{161, 164} This hydrogen

bonding occurs dynamically in the SAM incubation solution, increases the likelihood of tangled chains (gauche defects), and allows bilayer formation where the functional carboxylic acid head groups are buried.¹⁶⁶ Additionally, practical applications require the COOH-SAM used for biosensing to be grown on polycrystalline gold, where the roughness, grain boundaries, and step edges can all further interrupt the structure of the SAM.^{135, 147} Previous studies have investigated process parameters to minimize the hydrogen bonding, focusing on the addition of acids and lowering of the thiol concentration in the incubation solution to minimize COOH-dimer formation.^{161, 164}

There is a gap in the literature investigating what degree of defects exist in COOH-SAMs used for biosensing, and how those defects influence protein adsorption and denaturation on the surface. Defects in COOH-SAMs are of particular importance in biomarker detection since defects expose hydrophobic surfaces to the solution. Previously, NSA to a short (COOH(CH₂)₂SH) and long (COOH(CH₂)₁₀SH) chain COOH-SAM was investigated as a function of incubation time and surface roughness.¹⁶⁷ While this previous work revealed large NSA to these surfaces, only short, few-second incubation times were tested. The SAM was therefore only allowed to partially order, and large areas of hydrophobic striped phase are expected.^{135, 165} While literature indicates that defects can cause significant issues for biosensing, the effect of those defects in fully-formed COOH-SAMs on biosensing is largely unexplored.

1.3.4 SAM Stability and Oxidation

In addition to initial COOH-SAM structure, changes to the monolayer with time also have the potential to detrimentally influence biosensing measurements. Specifically, the S-Au bond has been shown to oxidize through reaction with ozone,¹⁶⁸ as shown in Equation 7 and Equation 8,¹⁶⁹ in both ambient conditions and aqueous solutions with and without exposure to light.^{136, 168, 170} Moreover, this oxidation occurs very quickly, with oxidation observed in as little as 2 hours in some SAM systems.¹⁶⁸



Once oxidation occurs, the thiol molecule is no longer chemisorbed to Au, allowing it to desorb from the surface.^{136, 169} As seen in Figure 1.22, oxidation generally begins at thiol grain boundaries and defect sites and leads to disordered regions.¹⁶⁹ It is obvious that SAM oxidation is injurious to sensing applications. For one, the creation of disordered SAM regions due to oxidation creates more areas of high defect density that contribute to NSA signals. Moreover, once the SAM begins to desorb, areas of plain Au may be left to adsorb protein directly. Additionally, any changes in order will affect the density and availability of COOH end groups. If this oxidation occurs before functionalization, less protein may be functionalized and a less sensitive sensor therefore formed. If this oxidation occurs after functionalization, receptor protein may desorb from the sensor surface with the thiol molecule, leading to erroneous signals.

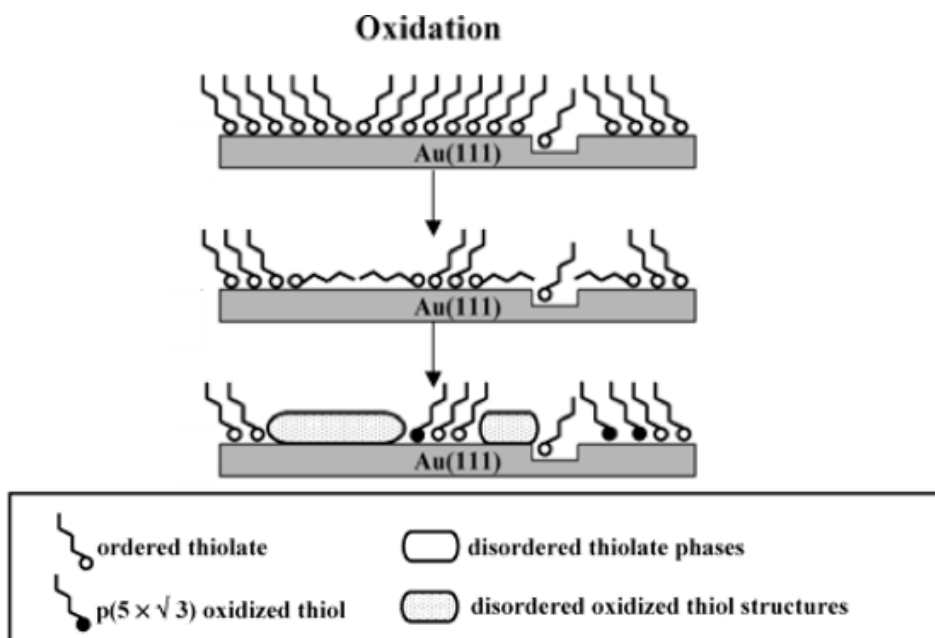


Figure 1.22 – Schematic diagram illustrating an oxidation-desorption pathway for the initial degradation of SAMs on gold. Critical structural evolution and morphological changes are included. Reprinted from G Yang, N A Amro, Z B Starkewolfe, and G Liu. Molecular-Level Approach to Inhibit Degradations of Alkanethiol Self-Assembled Monolayers in Aqueous Media. *Langmuir* 2004, 20 (10), 3995-4003. Copyright 2004 American Chemical Society.

Both the rate and effect on biosensing of COOH-SAM oxidation should be studied to ensure reliable sensing systems. Previous work has investigated substrate structure effects on SAM oxidation and methods to increase SAM lifetime. Specifically, Lee et al. showed that the rate of SAM oxidation increased with the decrease in substrate Au grain size, which is rationalized by an increase in SAM defects and grain boundaries on Au with smaller grains.¹⁷¹ Yang et. al. went on to show that certain surfactant molecules will adsorb preferentially to defect sites of the SAM, effectively decreasing the oxidation rate by inhibiting the start of the oxidation process.¹⁶⁹ However, somewhat in contrast, Vericat et

al. showed a decrease in oxidation rate for SAMs with high defect density on nanostructured Au compared to a relatively low defect density on planar Au.¹⁷² Here, the stronger thiol-substrate adsorption at lower coordination sites was credited as a defense against oxidation. Together, these results indicate that a combination of adsorption strength and overall film quality contribute to the decomposition rate of the SAM. This initial research into thiol SAM oxidation indicates the high rates of oxidation generally observed will limit the shelf life and commercialization of COOH-SAM based sensors. In order to address this, the rates of oxidation in defect-prone COOH-SAMs used for biosensing need to be specifically recorded. Moreover, the effect of this oxidation on the biosensing signal, and the potential of a preblocking protein to slow sensor degradation by protecting oxidation initiation at defects, is yet to be explored.

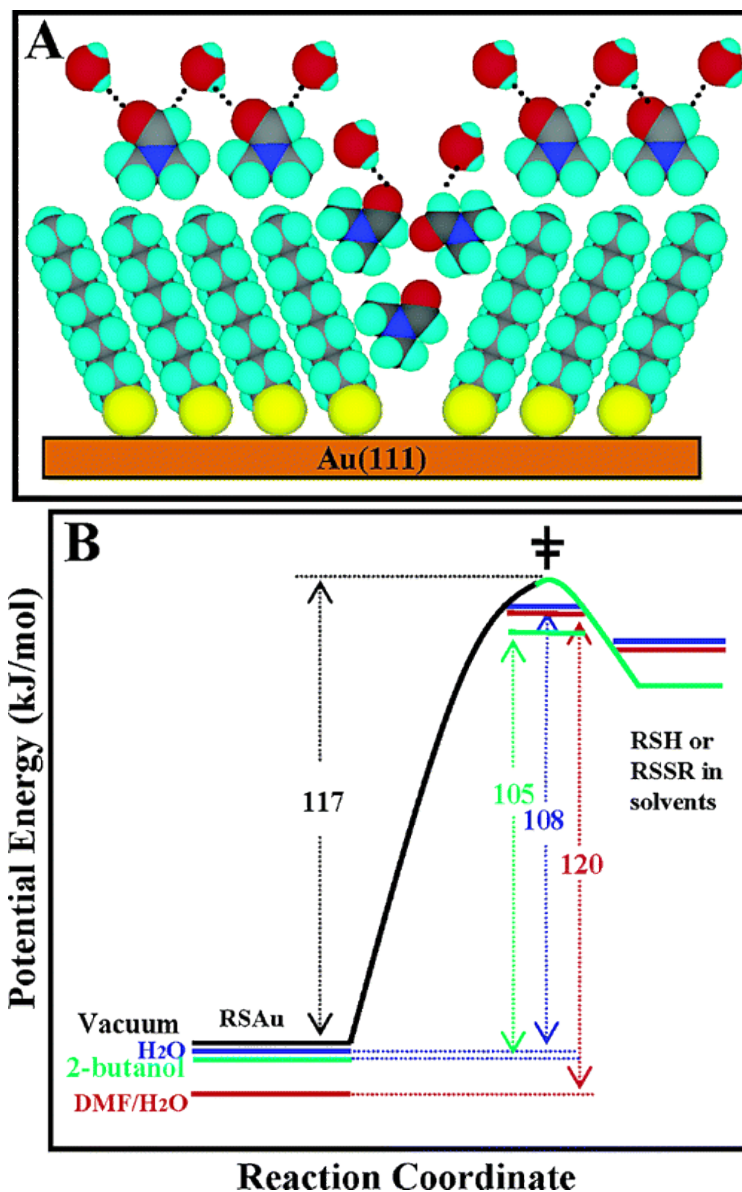


Figure 1.23 – Mechanism of desorption inhibition of alkanethiol SAMs in amphiphile and water. (a) Schematic diagram illustrates the adsorption of DMF molecules on SAM surfaces, and the preferred attachment to defect sites. (b) Quantitative free energy diagram for the initial desorption process of decanethiol under various environments. Reprinted from G Yang, N A Amro, Z B Starkewolfe, and G Liu. Molecular-Level Approach To Inhibit Degradaions of Alkanethiol Self-Assembled Monolayers in Aqueous Media. *Langmuir* 2004, 20 (10), 3995-4003. Copyright 2004 American Chemical Society.

1.4 2D Materials

The successful exfoliation of graphite into monolayer graphene produced the world's first 2D material: a one-atom thick, zero-gap semiconductor with high surface area, mechanical strength, and lateral conductivity.¹⁷³ The result was a global explosion into graphene research, and subsequent interest in alternative 2D materials. Electronic, magnetic, optical, and mechanical properties of 2D materials have been investigated for applications in catalysis, electronics, optoelectronic and spintronic devices, sensors, high performance electrodes, and nanocomposites.¹⁷⁴ The library of known 2D materials has grown rapidly,¹⁷⁵ with new techniques allowing for the systematic discovery of more.¹⁷⁶⁻¹⁷⁸ An overview of the diverse chemical structures of known 2D materials is shown in Figure 1.24.¹⁷⁹

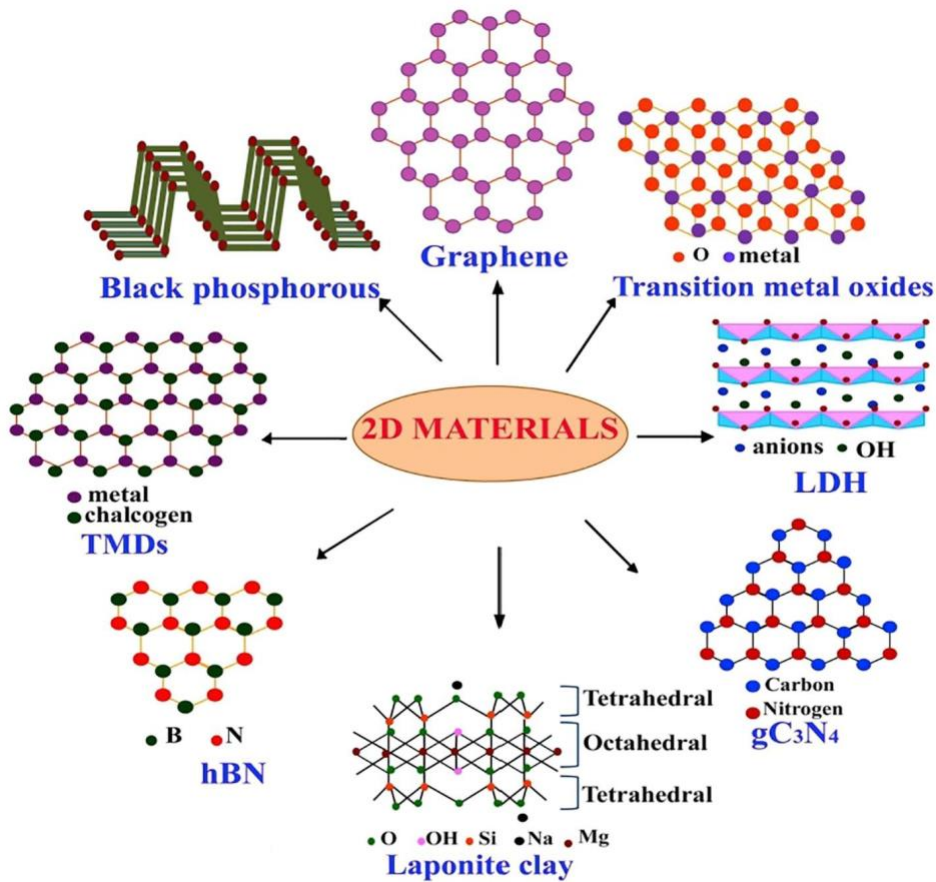


Figure 1.24 – Structure of different 2D materials; Graphene, transition metal dichalcogenides, layered double hydroxides, gC_3N_4 , laponite clay, hBN, transition metal dichalcogenides and black phosphorous. Reprinted with permission from A Jayakumar, A Surendranath, M Pv. 2D materials for next generation healthcare applications. *International Journal of Pharmaceuticals*. 2018, 551 (1-2), 309-321. Copyright 2018 Elsevier B.V.

1.4.1 Use in Biotechnology

Potential applications of 2D materials in biotechnology have been widely explored.

Figure 1.25 shows an overview of potential biomedical applications,^{180, 181} including biosensing,^{60, 62, 182-185} cell growth scaffolds,¹⁸⁶ drug delivery,¹⁸⁷⁻¹⁸⁹ and bioimaging.^{189, 190}

Additionally, proteins and other biomolecules have been investigated for the possible directed self-assembly of 2D nanocomposites.¹⁹¹ For most of these applications, 2D materials are exposed directly to biological solutions, and thus, understanding the interactions between biomolecules and 2D materials is of high importance.¹⁸²

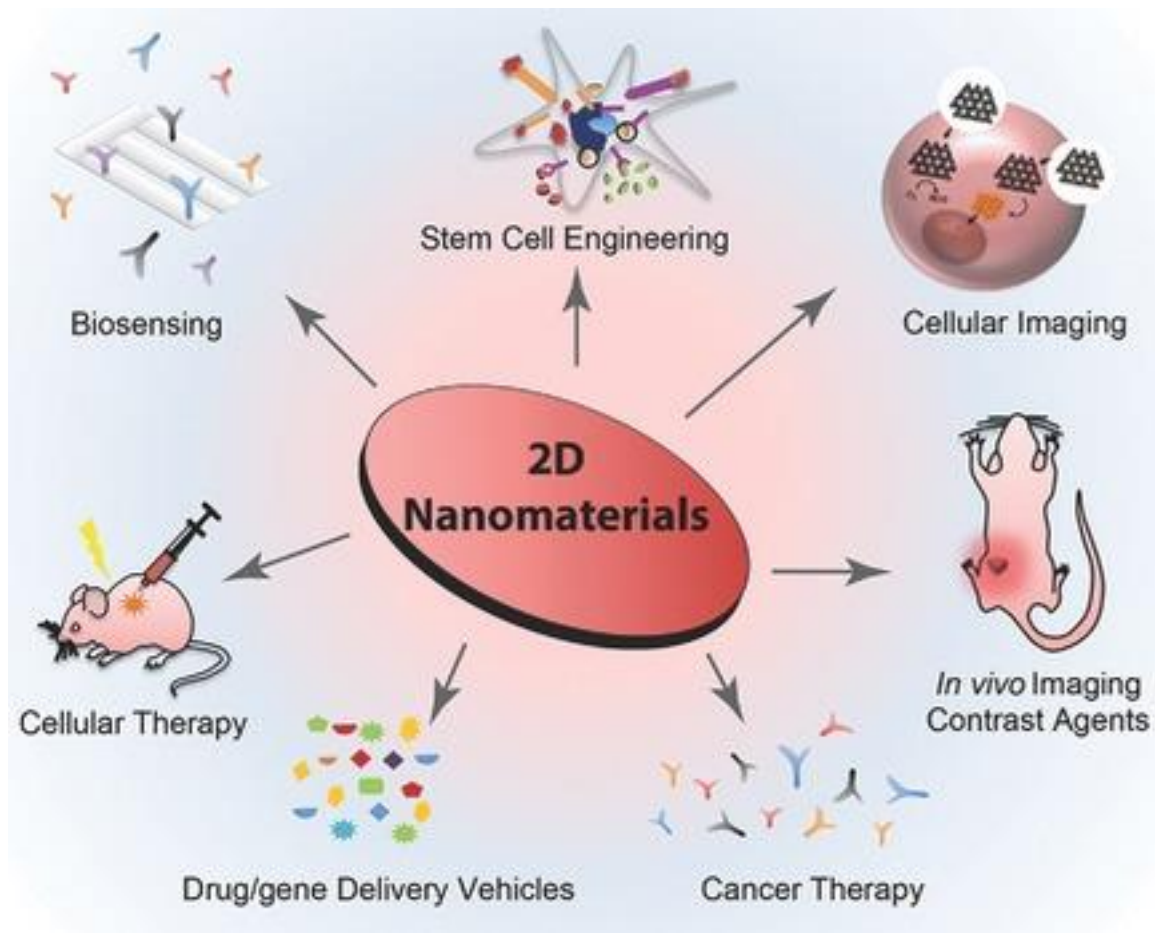


Figure 1.25 – Biomedical applications of 2D materials. Reprinted with permission from D Chimene, D L Alge, and A K Gaharwar. Two-dimensional nanomaterials for biomedical applications: emerging trends and future prospects. *Advanced Materials* 2015, 27 (45), 7261-7284. Copyright 2015 John Wiley & Sons.

Many of these molecular interactions between 2D materials and biomolecules have been studied due to the interest in composite materials.¹⁹¹ Hydrophobic, π - π electron interactions, hydrogen bonding, and charge interactions have been used to self-assemble graphene/protein composite materials.¹⁹¹ These solution-based studies give insight into what intermolecular interactions dictate adhesion between different material and biomolecule classes. A few studies also highlight the importance of understanding these interactions for biosensing applications. For instance, theoretical and experimental work has shown that proteins can unfold in order to maximize their interaction with graphene, thus denaturing and losing biological activity for sensing.^{120, 192} The adsorption of deoxyribonucleic acid (DNA) on graphene has been shown to increase its biostability relative to DNA dispersed in solution ¹⁹³. The DNA-graphene interaction effectively prevents enzymatic cleavage of the DNA by DNase I, but is still weak enough to allow pairing with a complementary strand ¹⁹³.

1.4.2 Graphene-Based Biosensors

Graphene has dominated scientific interest in the incorporation of 2D materials into electrochemical biosensors.^{185, 194-196} Carbon is likely the most widely-used material in electroanalysis,^{185, 197, 198} and graphene's fast electron transport, high thermal conductivity, excellent mechanical flexibility, and good biocompatibility make it advantageous when compared to other carbon materials such as nanotubes (CNTs).^{183, 199} Additionally, Graphene's surface is chemically inert and does not contain metallic impurities detrimental to applications of CNTs.^{199, 200}

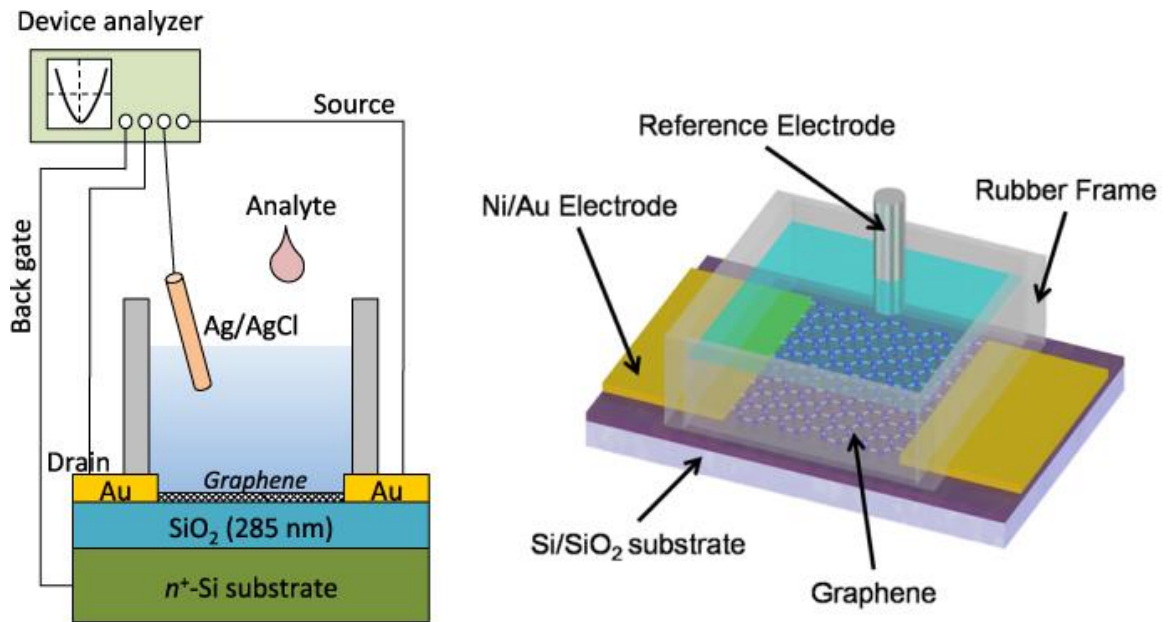


Figure 1.26 – Schematic of a typical graphene FET. Reprinted with permission from K Matsumoto, K Maehashi, Y Ohno, and K Inoue. Recent advances in functional graphene biosensors. *Journal of Applied Physics D* 2014, 47, 094005. Copyright 2014 IOP Publishing LTD.

Graphene has been utilized in electrochemical,²⁰¹⁻²⁰⁶ magnetic,²⁰⁷ and optical²⁰⁸ sensors to detect small molecules,^{203, 209} proteins,²¹⁰ DNA,^{201, 207} viruses,²¹¹ and bacteria.²¹² A typical graphene FET (gFET) is shown in Figure 1.26.²¹⁰ In this sensor, graphene interacts directly with the biological solution, while a reference electrode is used to modulate the gate potential of the gFET. As in other biosensing devices, the graphene is functionalized to impart specificity, typically through an enzyme or receptor protein.^{209, 213} This receptor may be allowed to adsorb directly to the graphene,^{205, 207, 213} or may be attached through a linker that interacts with the graphene via pi-pi stacking, such as PBASE (1-Pyrenebutyric acid N-hydroxysuccinimide ester).^{201, 202, 212}

1.4.3 Substrate Influence

Many of the aforementioned biomedical applications are inherently solution-based processes. Biosensing applications, however, generally require the 2D material, most commonly graphene,^{185, 194-196} to be deposited on a support substrate. Since monolayer graphene is only a single atom thick, protein-graphene interactions may be influenced by the support substrate. A gap in the literature still exists in understanding substrate-graphene-protein interactions.

Although not yet extended to protein interactions, there is evidence of substrate effects on graphene properties. There is a debate in the literature regarding the “wetting transparency” of graphene, or the ability of the substrate’s wetting properties to transmit through a graphene monolayer.²¹⁴⁻²¹⁹ As seen in Figure 1.27, Rafiee et al. showed that the addition of a single monolayer of graphene did not significantly affect the contact angle of water on Si and Au.²¹⁸ While reports conflict on the degree of wetting transparency, the majority of reports indicate that the substrate’s wetting properties at least partially transmit through a graphene monolayer.²¹⁴⁻²¹⁹ A substrate’s effect on graphene’s hydrophobicity is likely to have a subsequent effect on protein adsorption. It is commonly shown that proteins have a stronger affinity for hydrophobic surfaces than hydrophilic ones.^{79, 119, 220, 221} This increased adsorption can be explained by both the favorable entropic loss of structured water at the substrate and protein surfaces when attachment occurs, as well as a favorable increase in the adsorbing protein’s conformational entropy if partial unfolding occurs.^{79, 118, 222} Modification of graphene’s contact angle by the substrate therefore suggests that the

substrate can modify the affinity of graphene-protein interactions. Indeed, one previous study shows this to be the case, where agglomerations of avidin molecules are observed on graphene when the substrate is modified to be hydrophobic.²²³

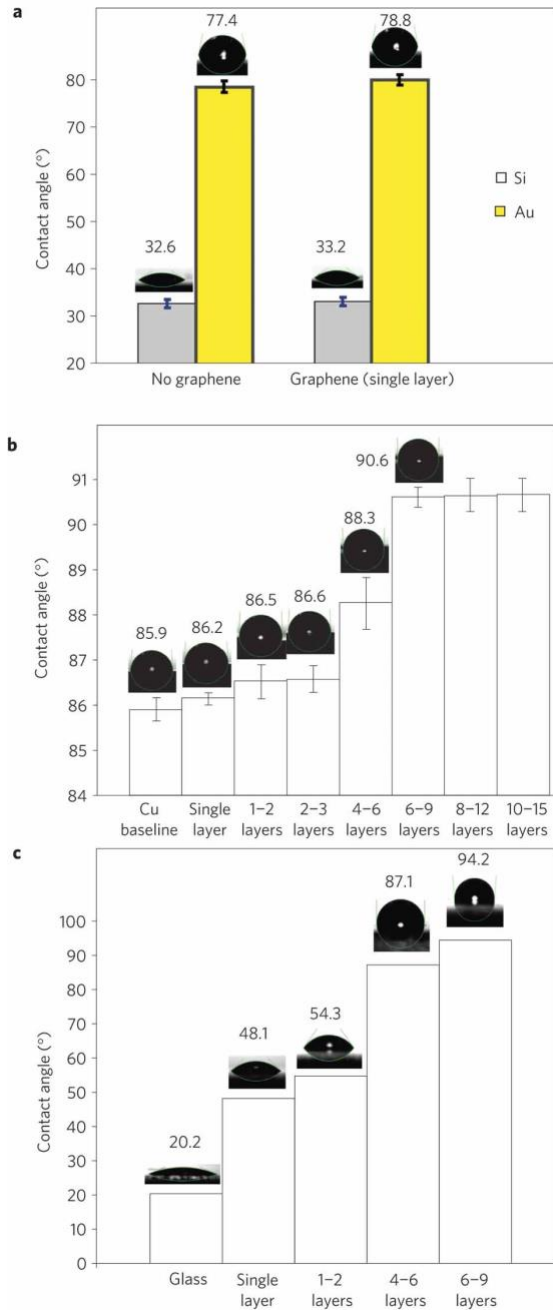


Figure 1.27 – Water contact angle measurements for Si and Au substrates with and without a monolayer graphene coating. The intermediate graphene layer has no significant impact on the baseline wettability of the underlying substrate. Reprinted with permission from J Rafiee, X Mi, H Gullapalli, A V Thomas, F Yavari, Y Shi, P

M Ajayan, and N A Koratkar. Wetting transparency of graphene. *Nature Materials* 2012, 11 (3), 217. Copyright 2012 Nature Publishing Group.

In addition to substrate hydrophobicity, substrate surface polarity may also be important to determine protein adhesion properties to graphene. Kong et al. showed that the polarity of the substrate determines whether or not epitaxial growth is successful across a graphene intermediating layer (Figure 1.28).²²⁴ More specifically, epitaxial growth on polar GaN was shown to be successful despite the presence of a graphene layer, while epitaxial growth of non-polar Si was not.²²⁴ This indicates that the potential fields of non-polar materials can be screened by a graphene monolayer, while the potential field of an ionic-bonded, polar material generally has the ability to penetrate through a graphene layer. Similarly, substrate polarity may influence the degree to which substrate-protein interactions are able to permeate through the graphene where substrates with larger bond polarity have a larger effect on protein adhesion. Overall, the substrate influence of protein interactions with graphene, especially as it relates to biosensor development, is an open area of exploration.

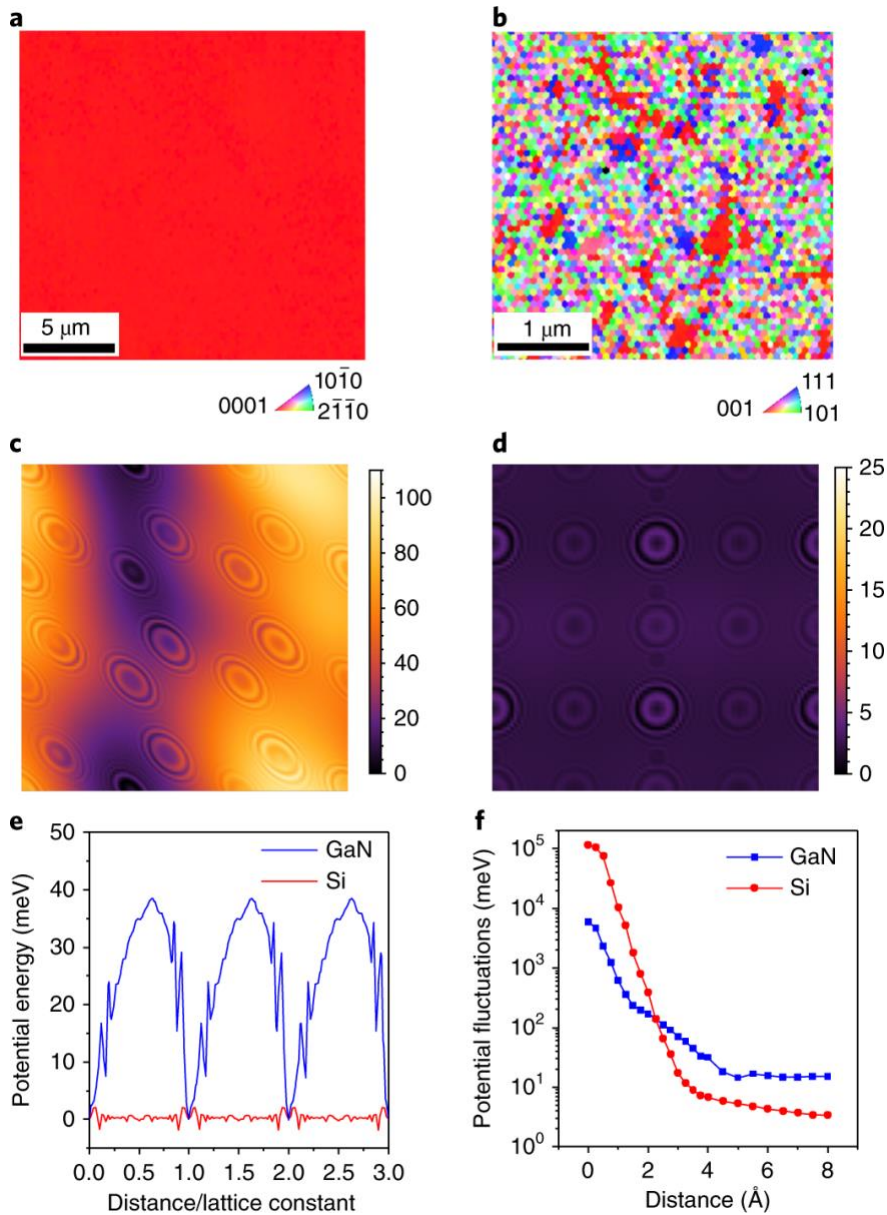


Figure 1.28 – Substrate polarity effect on epitaxial growth through graphene. a,b, EBSD of the exfoliated surfaces of GaN (a) and Si (b). c,d, DFT simulations of a potential fluctuation (meV) map at the epitaxial surface of 1-ML-graphene/GaN (c) and of 1-ML-graphene/Si (d). e,f, DFT simulations of the potential fluctuation at the epitaxial surface from GaN and Si through 1 ML graphene (e) and of the potential fluctuation decay from the GaN and Si surface (f). Reprinted with permission from W Kong, H Li, K Qiao, Y Kim, K Lee, Y Nie, D Lee, T Osadchy, R J Molnar, D K

Gaskill, R L Myers-Ward, K M Daniels, Y Zhang, S Sundram, Y Yu, S Bae, S Rajan, Y Shao-Horn, K Cho, A Ougazzaden, J C Grossman, and J Kim. Polarity governs atomic interaction through two-dimensional materials. *Nature Materials* 2018, 17 (11), 999. Copyright 2018 Wei Kong et al, under exclusive license to Springer Nature Limited.

CHAPTER 2. ORGANIZATION OF THIS THESIS

This work focuses on the fundamental science and engineering of surfaces used for label-free biosensing. Specifically, the first portion of this work focuses on carboxylic-acid-terminated self-assembled monolayers (COOH-SAMs), which are commonly used as the functional sensor surface. CHAPTER 3 describes in detail the formation procedure for COOH-SAMs, focusing on parameters that improve monolayer quality. X-ray photoelectron spectroscopy, contact angle, and protein non-selective adsorption are used to probe COOH-SAM surface structure.² Inert atmosphere and low-concentration thiol solution is shown to provide the most reliable COOH-SAM formation. Improvement of COOH-SAM quality decreases, but does not eliminate, non-selective protein adsorption.

Since non-selective protein adsorption cannot be eliminated through COOH-SAM formation procedures alone, CHAPTER 4 presents a preblocking procedure that can be used to improve reliability of COOH-SAM-based biosensors.² Conventional blocking techniques occur after functionalization (postblocking) and fail to prevent non-selective receptor adsorption to the sensor surface during functionalization, which can cause receptor denaturation and allow the receptor to wash off the surface during later sensing. In the preblocking procedure, the surface of COOH-SAMs is pre-treated by a blocking agent before functionalization. Preblocking can improve baseline stability and prevent receptor denaturation. Amine functionalization of receptor is successfully completed after gelatin preblocking. Additionally, label-free sensing with a preblocked sensor is shown to perform

similarly to conventional postblocking, while demonstrating improved baseline stability and receptor activity. Preblocking can also inhibit oxidation of COOH-SAMs, as shown in CHAPTER 5.³ With preblocking, no surface degradation is observed via X-ray photoelectron spectroscopy nor reductive desorption for 21 days, compared to observable degradation in only one day for an unblocked COOH-SAM. These blocked sensors are shown to maintain biosensing performance for at least one week. Additionally, the blocking technique for degradation prevention is shown to even outperform COOH-SAM storage in N₂.

Due to the challenges associated with COOH-SAMs, CHAPTER 6 is dedicated to a different type of sensor surface, namely, graphene. CHAPTER 6 describes how graphene-protein interactions can be influenced by the substrate used to support the atomically thin graphene layer.⁴ Protein adhesion of model proteins is presented, where monolayer graphene is supported by substrates of varying hydrophobicity and surface polarity. The results indicate that not only the equilibrium attachment, but also the kinetics of interaction, can be affected by the substrate. Overall, a more hydrophobic substrate leads to a larger amount of adsorption to graphene. Moreover, the effect is only observed with monolayer graphene, where no substrate effect is observed with the addition of a second graphene layer.

CHAPTER 7 provides a summary of this work as well as recommendations for future work. In particular, label-free affinity biosensors are an exciting area of scientific

development, but one that will require careful engineering to design robust sensors that produce reliable sensing results.

Broadening from the sensor surface, APPENDIX A is dedicated to practical considerations for potentiometric biosensing, or more generally any developing label-free biosensing technology. Sources of unreliability in potentiometric sensing, including drift due to reference electrodes, drift due to fluidics, multi-channel interference, and voltmeter input impedance is discussed. In APPENDIX B, methods that can independently confirm protein attachment to a label-free sensor are presented. In APPENDIX C, a general model for mass transport to a sensor surface, allowing estimation of sensor response time, is described.⁵

CHAPTER 3. OPTIMIZATION OF COOH-SAM FORMATION^A

CHAPTER 3 describes in detail the formation procedure for COOH-SAMs, focusing on parameters that improve monolayer quality. Section 3.1 provides a brief overview of literature methods for growing minimally defective COOH-SAMs, and highlights how defects in the monolayer may be detrimental to biosensing applications. Section 3.2 describes the methods used to compare COOH-SAM quality, namely XPS, DI H₂O contact angle, and protein NSA. Section 3.3 presents the results, indicating that an inert atmosphere and low-concentration thiol solution leads to the most reliable COOH-SAM formation. Improvement of COOH-SAM quality decreases, but does not eliminate, protein NSA. Section 3.4 concludes the best practices for COOH-SAM formation.

3.1 Introduction

While carboxyl-terminated thiol self-assembled monolayers (COOH-SAMs) on Au are perhaps the most common route to surface functionalization via amine coupling, formation of a well-ordered monolayer is generally assumed. However, it is crucial that the structure of COOH-SAMs and subsequent surface functionalization is well-defined for the development of reliable biosensing systems. COOH-SAMs are subject to range of possible defects, as discussed in section 1.3.3. Previous studies have investigated process parameters to minimize the hydrogen binding defects specific to COOH-SAMs, focusing

^A Adapted in part with permission from E L Brightbill, B Hitchcock, MY Tsai, A Verga, and E M Vogel. Preblocking Procedure to Mitigate Nonselective Protein Adsorption for Carboxyl-SAMs Used in Biosensing. *Journal of Physical Chemistry C* 2019, **123**(27), 16778–16786. Copyright 2019 American Chemical Society.

on the addition of acids and lowering of the thiol concentration in the incubation solution to minimize COOH-dimer formation.^{161, 164} However, these procedures are not commonly used in the biosensing literature and their effectiveness has not been repeated either in the experiments presented here nor in the literature.^{161, 164}

Defects in COOH-SAMs are of particular importance in biomarker detection since they change the characteristics of the surface exposed to solution, and thus effect how proteins interact with the surface. Protein adsorption is a complicated process where protein properties (size, structural stability, composition) as well as surface properties (surface energy, polarity, charge, morphology) all influence the degree to which adsorption occurs.¹¹³ However, despite the wide variety of factors, the non-selective adsorption (NSA) of a variety of proteins has been shown to increase with increasing surface hydrophobicity (see 1.3.3).^{119, 120} Defects in COOH-SAMs expose hydrophobic surfaces to the solution, and therefore NSA due to hydrophobic adsorption is expected. Not only can these interactions lead to false signals from analyte solutions, but they can lead to the denaturation of the receptor protein itself. Often, upon hydrophobic adsorption, proteins deform or partially unfold to achieve the most stable interaction.⁷⁷⁻⁷⁹ This unfolding is common enough to be known in hydrophobic interaction chromatography as a denatured peak,^{77, 78} and can render the protein inactive and thus useless as a biosensor functional unit.

This work highlights the importance of understanding SAM quality used in biosensing, particularly those containing hydrogen-binding moieties. XPS is presented as

a powerful tool to study COOH-SAM quality. Further, SPR is used to analyze the NSA of proteins on the unfunctionalized sensor surface.

3.2 Methods

3.2.1 Materials

16-Mercaptoundecanoic acid [HS(CH₂)₁₅COOH] (99.9%), 1-Ethyl-3-(3-dimethylaminopropyl) carbodiimide (EDC), N-Hydroxysuccinimide (NHS), ethanolamine (ETA), Phosphate Buffered Saline Pellets (PBS), Acetic Acid (AA), Anhydrous Ethanol, Bovine Serum Albumin (BSA), antibody Bovine Serum Albumin (aBSA), Human Haptoglobin (Hp), antibody Human Haptoglobin (aHp), Fibrinogen, and Lysozyme, were purchased from Sigma-Aldrich (St. Louis, MO). Desorb kit and Gold Substrates (SIA kit Au) for SPR were purchased from GE Healthcare Bio-Sciences (Pittsburgh, PA). 100 nm thick Gold surfaces for XPS measurements were e-beam evaporated on a substrate consisting of 280 nm of SiO₂ on silicon.

3.2.2 COOH-SAM Formation

The Au surfaces were cleaned with acetone, methanol, and isopropanol rinses and dried with a N₂ stream, followed by a two-minute O₂/Plasma treatment (200 mTorr, 50 W RF, 25 sccm O₂). The substrates were then placed in ethanolic solutions of thiol in piranha-cleaned (3:1 96% H₂SO₄:H₂O₂) glass petri dishes. After 24 hours, the SAM-covered substrates were sonicated for five minutes in fresh ethanol, followed by drying in a stream of N₂. All measurements on COOH-SAMs began within 30 minutes of drying and

completed within 8 hours. N₂ atmosphere was provided by a Labstar Pro glovebox (MBRAUN), with H₂O and O₂ both <1ppm.

3.2.3 X-Ray Photoelectron Spectroscopy

Measurements were conducted using a K-Alpha X-ray Photoelectron Spectrometer System (Thermo Scientific, Waltham, MA) with a monochromatic Al K α source (KE = 1486.6 eV), a 180° double focusing hemispherical analyzer, and a 128-channel detector. Survey spectra were acquired at a pass energy of 200 eV and a spot size of 400 μ m, and Thermo Scientific Advantage software was used to identify the elemental composition of survey scans. High-resolution elemental spectra were acquired at a pass energy of 50 eV and a spot size of 400 μ m. Au 4f spectra were fit with 2 peaks (spin-orbit splitting of 3.7 eV, 3:4 area ratio), with the 4f_{7/2} peak position used as a reference at 83.95 eV. S 2p spectra were fit with 4 peaks, corresponding to 2 binding states (spin-orbit splitting of 1.16eV, 1:2 area ratio). The full-width-half-maximum (FWHM) of all peaks pertaining to one element were constrained to match. A variable Lorenz-Gauss ratio and Shirley-type background were used for all spectra.

3.2.4 Contact Angle

A Ramé-hart Model 250 goniometer was used for contact angle measurements. 0.6 μ L drops of DI water were placed on the leveled substrate surface, and the resulting static contact angles were measured by the drop tangent in the Ramé-hart software.

3.2.5 Atomic Force Microscopy

Atomic force microscopy (AFM) was performed using a Bruker Icon Scanning Probe Microscope (Billerica, MA) with AppNano (Mountain View, CA) SPM Si probes having a tip radius of <10 nm.

3.2.6 Surface Plasmon Resonance

A Biacore T200 (GE Healthcare Life Sciences; Chicago, Illinois) was used for all SPR measurements. A 30 $\mu\text{L}/\text{min}$ flow rate and PBS running buffer were used unless otherwise stated. Protein solutions were diluted in PBS.

3.3 Results

3.3.1 Au Film Quality

A continuous, low-roughness Au film is necessary for the growth of COOH-SAMs. The 100nm e-beam deposited Au film used for all samples in this thesis is expected to be continuous on both oxidized Si wafer and glass substrates.²²⁵ XPS survey spectra of the Au films show only signals from the Au with small O and C contributions from adventitious species (Figure 3.1a). The lack of Si signal across the 400 μm spot size indicates, in both cases, that the substrate is fully coated with gold. AFM scans of the substrates show reasonably smooth surfaces with similar roughness (RMS roughness <1.5 nm in both cases), which is significantly smaller than the 100 nm Au thickness (Figure 3.1b).

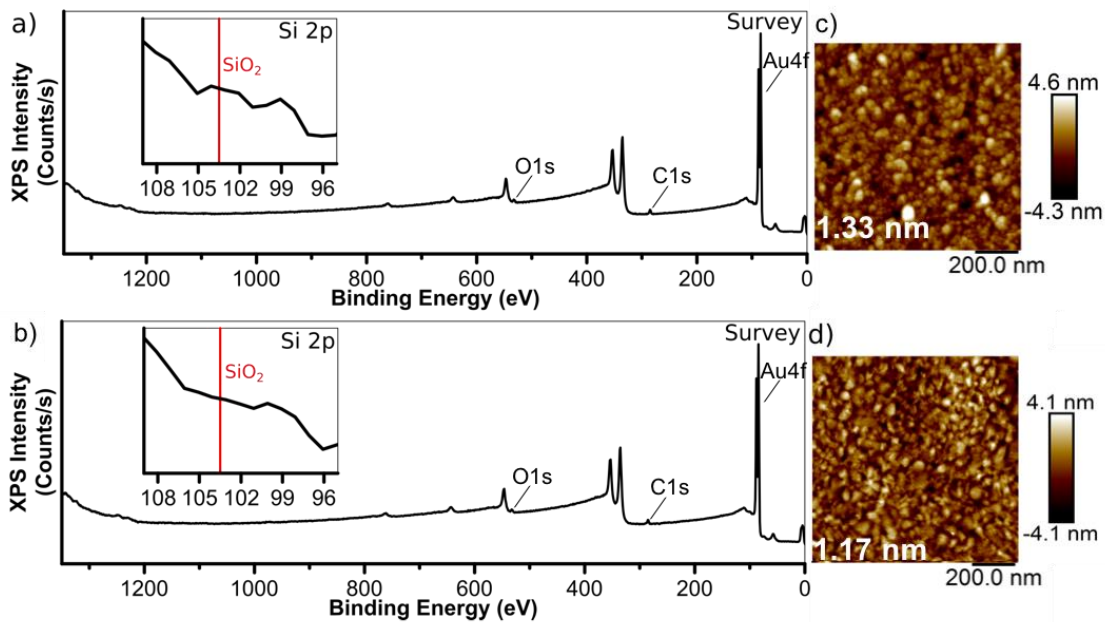


Figure 3.1— Au film characterization. XPS survey spectrum of Au surface with inset Si 2p region for (a) SPR Au/Glass Chip and (b) evaporated Au/SiO₂ chip. AFM images with inset RMS roughness (in white) of (c) SPR Au/Glass Chip and (d) evaporated Au/SiO₂ chip.

In addition to surface roughness, contamination can influence the quality of a resulting SAM. To minimize any effects of unknown contamination, Au substrates were cleaned with acetone/methanol/isopropanol rinses followed by a O₂ plasma treatment immediately before incubation in the thiol solution. Additionally, all glassware used for COOH-SAM formation was cleaned for 15 min in a piranha bath to eliminate any organic residue that could impact COOH-SAM formation.

3.3.2 Effect of COOH-SAM Preparation Conditions

Unbound sulfur present on the Au surface (bilayer formation, tangled chains) is one of the major defect modes of SAMs. XPS is, therefore, a powerful tool capable of probing

the bonding and degree of defect sites on the Au sensor surface by analyzing the percentage of bound S present and the density of that bound S. Due to the variation in the analysis of SAM XPS data across the literature, careful detail of our analysis is included here, which most closely follows the protocol reported by Shaporenko et al.²²⁶ First, the Au 4f_{7/2} signal at each sample spot was used as a reference energy of 83.95 eV. Second, the S spectra was fit with 2 chemical states, S-Au and S-H. The 2p_{3/2} peak corresponding to bound sulfur (S-Au) is reported across literature in the range of 161.8-162.0 eV.^{136, 161, 164, 226-233} Therefore, the bound peak position was allowed to optimize position in that range. The position of the unbound peak (S-H), however, is reported over a much larger range of 163-164.2 eV.^{136, 161, 164, 228-233} Therefore, the position of the unbound peak was allowed to freely float. The analysis returned extremely large sample-to-sample variation in unbound peak position, from 162.7-163.5 eV. In subsequent analysis, the peak at 162.7-163.5 eV is regarded as “improperly bound” thiol, regardless of position (Figure 3.2). This designation was made, despite part of the range falling outside the previously reported positions, for three main reasons. First, the large 1.2 eV range reported in literature indicates that the position is very sensitive to thiol type and preparation conditions. Second, contaminants were not the cause of the peak position shift. Survey scans showed only the presence of the expected Au, S, C, and O. In addition, since the signal-to-noise ratio of the S peak in the survey is only 4:1, the NIST XPS database was used to identify any peaks in the correct range involving an element with a lower sensitivity factor than S, returning no results.^{234, 235} Third, the only other peak, after S-Au and S-H fit to thiol-SAM XPS data found in literature is a peak at

approximately 161 eV, labeled as either atomic S, where the S-C bond has been cleaved, or “differently bound” thiol, such as striped phase.^{136, 226, 231, 232} Since no peaks other than unbound thiol have been designated above the S-Au peak, the peak is identified as unbound, or “improperly bound”, thiol.

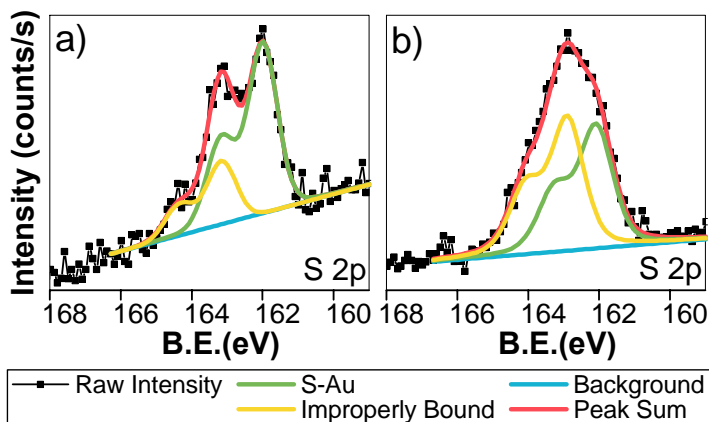


Figure 3.2— XPS S 2p spectra with properly and improperly bound peak fitting. a) Relatively far-spaced (1.1 eV) S peaks. b) Relatively close-spaced (0.8 eV) S peaks.

XPS is used to analyze the relative quality of COOH-SAMs prepared with different thiol solution concentration and/or incubation environment, which is summarized as the following four conditions: (1) 5 mM solution in ambient as previously used (Figure 3.3),^{32, 57} (2) 5 mM solution in N₂ atmosphere (glovebox) to improve reproducibility (Figure 3.4),^{135, 236, 237} (3) a lower thiol concentration of 20 μM in N₂ to decrease bilayer formation (Figure 3.5),¹⁶¹ and (4) 20 μM in N₂ with 10% acetic acid (AA) to further prohibit hydrogen bonding (Figure 3.6).¹⁶⁴ It should be noted that the low 20 μM concentration is still well above the minimum 1 μM necessary to form a dense SAM.¹³⁵

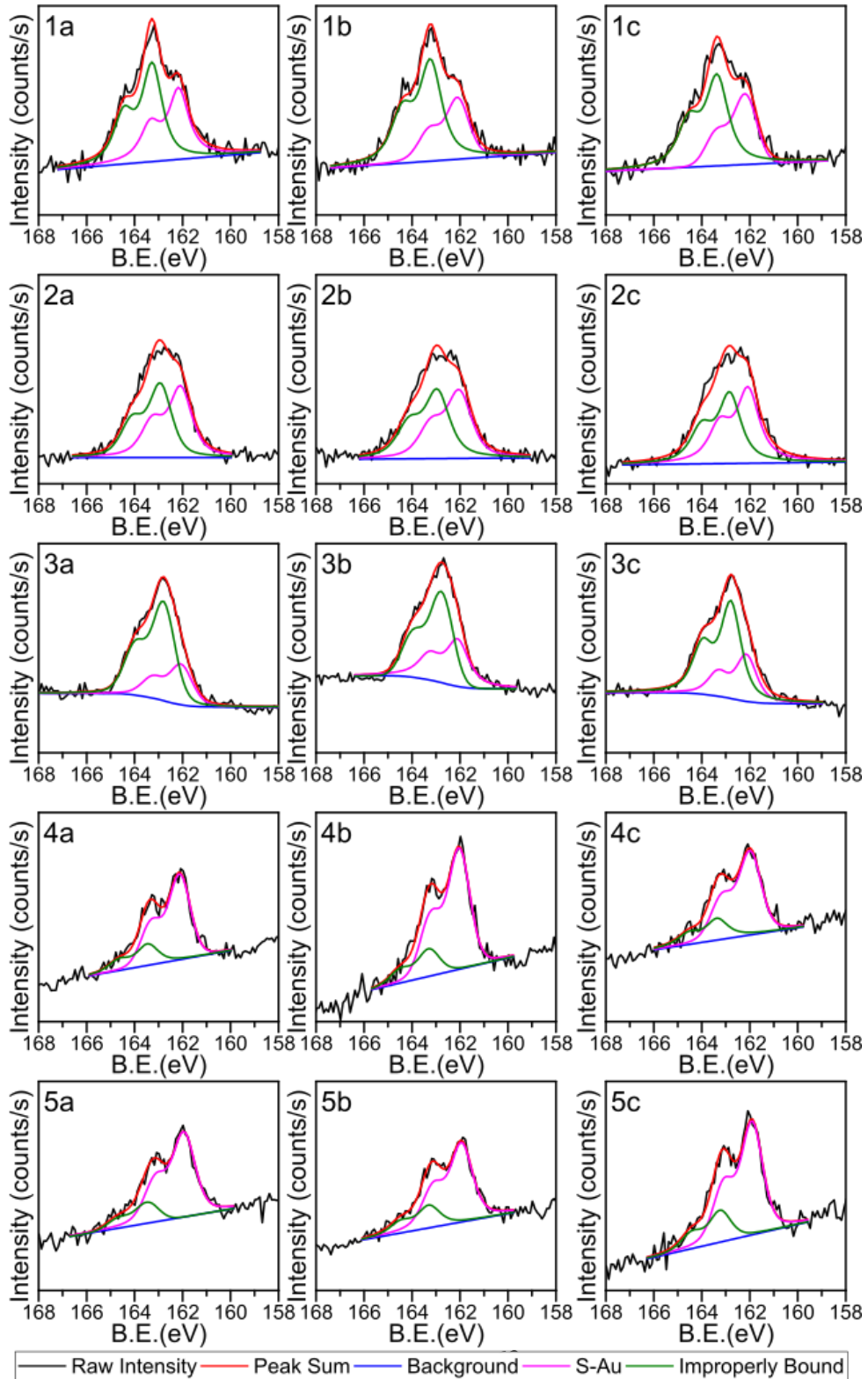


Figure 3.3— S 2p XPS scans for the 5 mM Air preparation condition. The number denotes the sample, while letters denote different spots on the same sample.

Figure 3.3 shows the S 2p XPS spectra for COOH-SAMs prepared with 5mM thiol in ethanol on the bench, which are standard parameters for a SAM preparation.^{32, 57} While the amount of improperly bound thiol is small on some samples (4, 5), the improperly bound peak is larger than the desired S-Au peak on several of the samples (1, 2, 3). The large variability between samples is undesirable, since XPS is not sufficiently fast to be amenable to confirming the quality of every COOH-SAM formed before it is used in a biosensor.

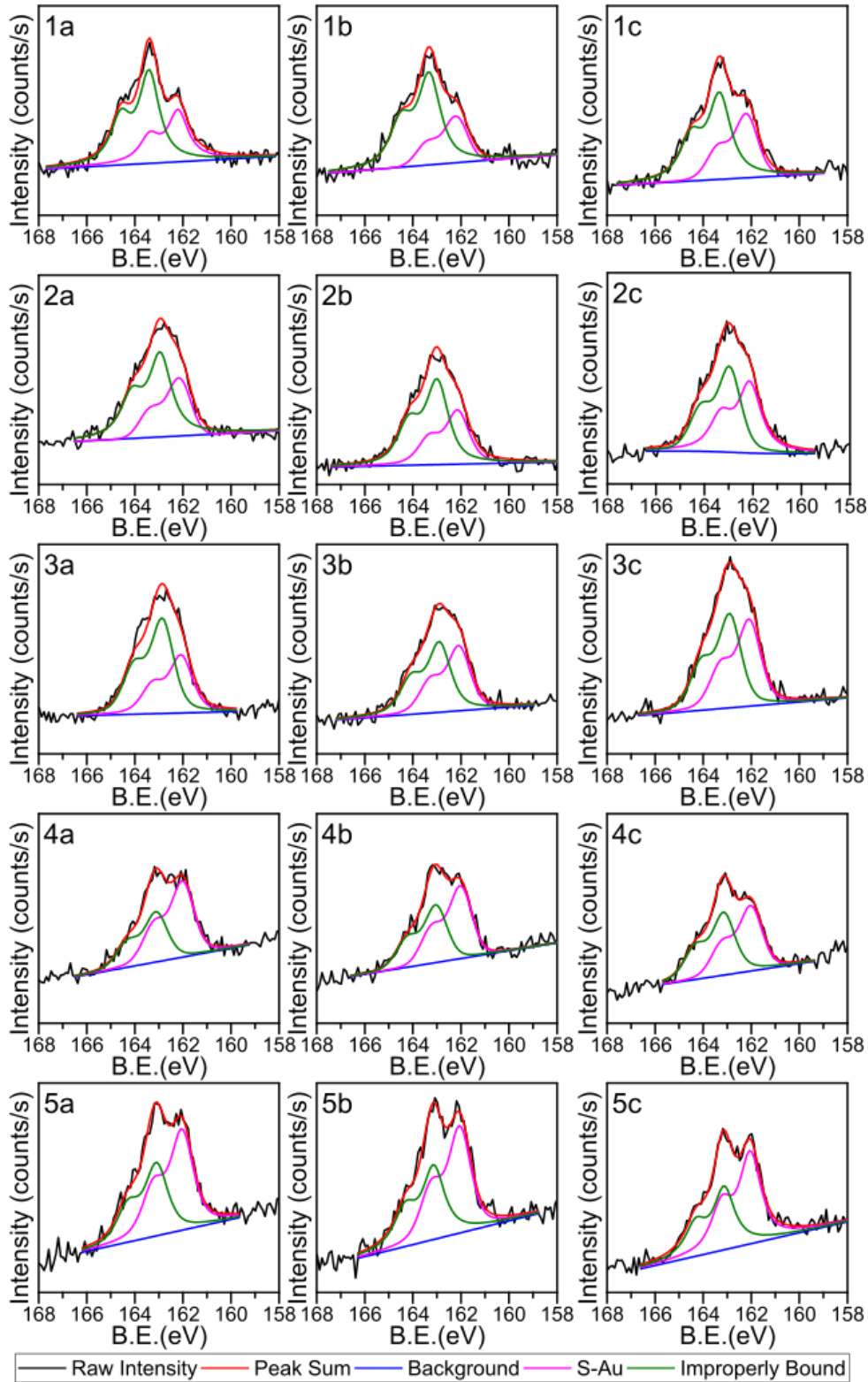


Figure 3.4— S2p XPS scans for the 5 mM N₂ preparation condition. The number denotes the sample, while letters denote different spots on the same sample.

In order to address sample-to-sample variability, some studies have indicated that SAM preparation in an inert atmosphere is beneficial.^{135, 236, 237} Figure 3.4 shows the S 2p XPS spectra for COOH-SAMs prepared with 5mM thiol in ethanol in an N₂ atmosphere. Although there may be decreased sample-to-sample variability, there is a large amount of improperly bound thiol detected on all samples.

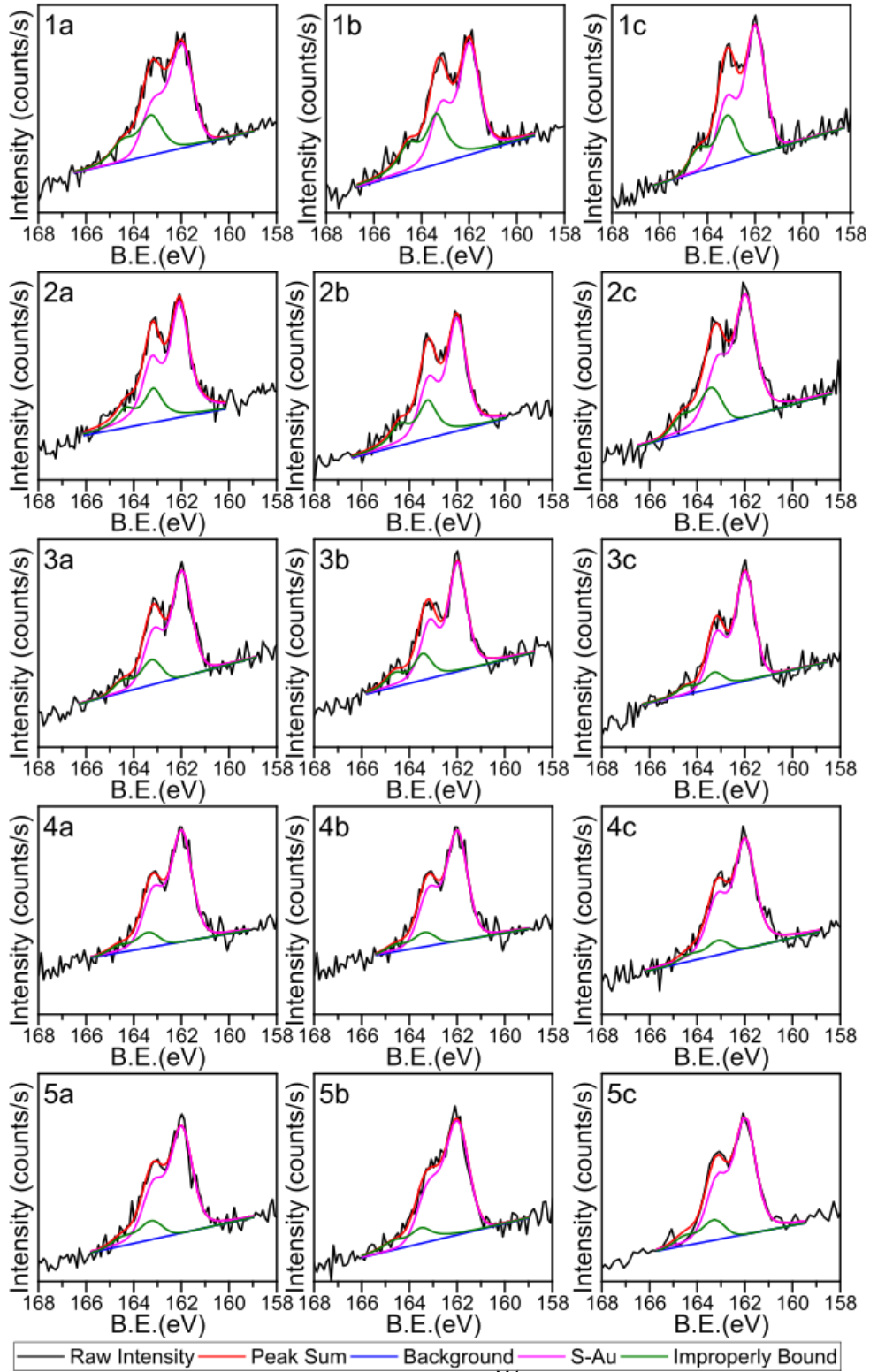


Figure 3.5— S2p XPS scans for the 20 μM N_2 preparation condition. The number denotes the sample, while letters denote different spots on the same sample.

Due to the ability of COOH-terminated thiols to cooperatively hydrogen-bond with one another, it is likely that a large amount of the improperly bound thiol observed in the 5mM incubations is due to bilayer on the surface.¹⁶⁶ A previous study has shown that decreasing the concentration can decrease the presence of bilayer,¹⁶¹ and the result of lowering the thiol concentration to 20 μM is shown in Figure 3.5. Unlike the 5mM preparation conditions, all S 2p spectra show less improperly bound than properly bound thiol.

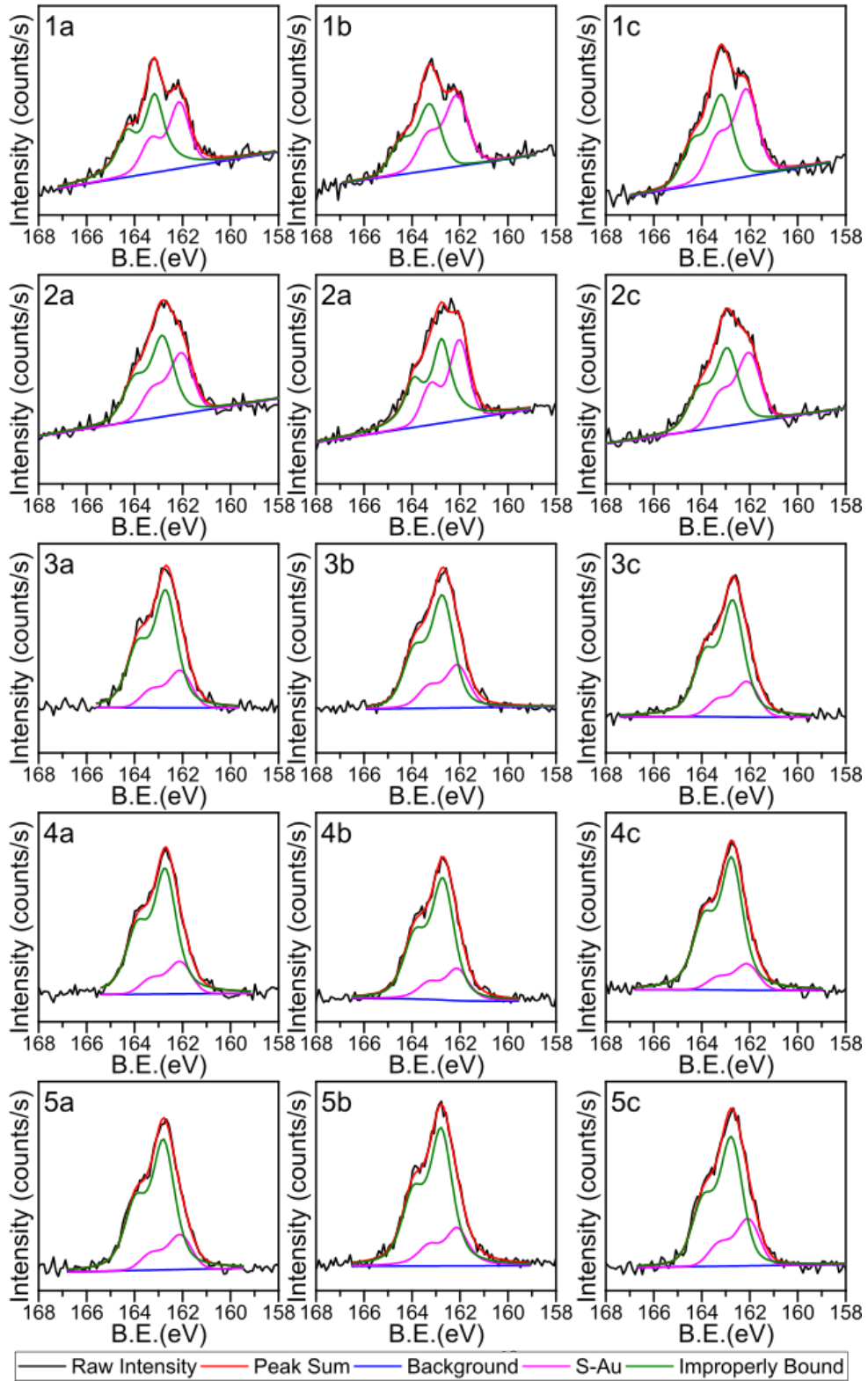


Figure 3.6— S2p XPS scans for the 20 μ M N₂ AA preparation condition. The number denotes the sample, while letters denote different spots on the same sample.

Since bilayer formation through hydrogen bonding is a challenge for COOH-SAMs, it is reasonable that an incubation solution additive that can form the same hydrogen bonds with the thiol molecules would improve the resulting monolayer quality. Indeed, a previous study indicate this was the case, using AA as an additive to interrupt thiol-thiol hydrogen-bonding and decrease the improperly bound thiol signal as seen via XPS.¹⁶⁴ Figure 3.6 shows the S 2p XPS spectra for COOH-SAMs prepared with 20 μ M thiol in ethanol in an N₂ atmosphere with 10% AA added to the incubation solution. Compared to preparation without AA, the observe improperly bound thiol peaks are significantly larger, indicating a poorer quality COOH-SAM. This result does not replicate the literature and is discussed in more detail below.

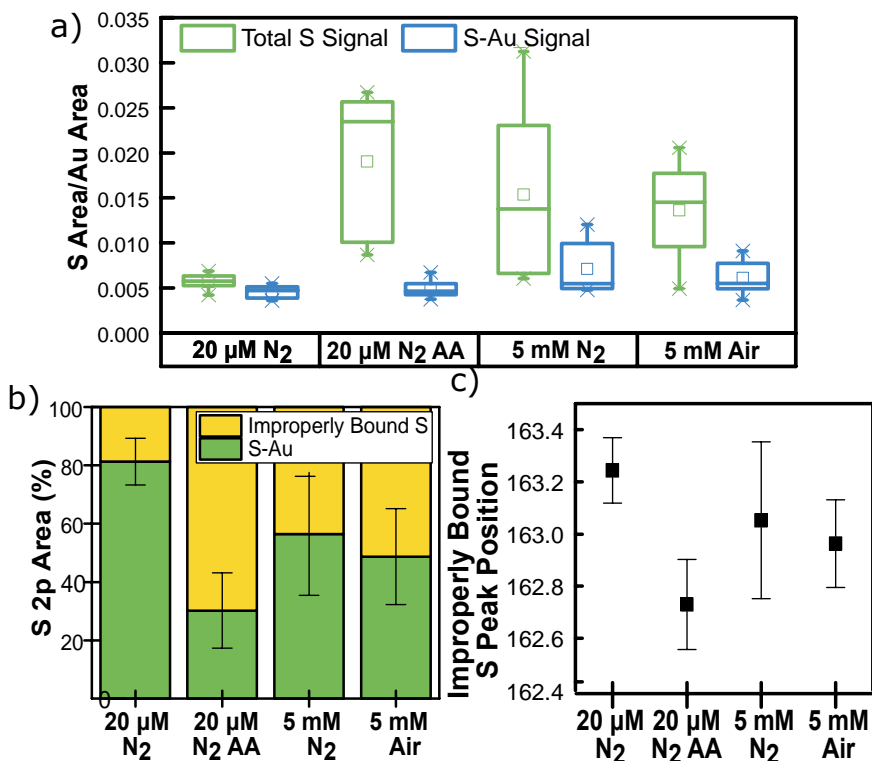


Figure 3.7— XPS summary results of COOH-SAMs. a) Box and whisker plots of total S and properly bound S density, normalized by the Au signal area. b) Percentages of properly and improperly bound S by area. c) Improperly bound S peak position.

The data presented in Figure 3.7 is a summary of the previous XPS results, including 15 spots across 5 samples for each sample type, with error bars indicating the standard deviation of those 15 data points. The total amount of thiol on the surface under each condition can be compared by normalizing the S signal area to the Au 4f_{7/2} peak area (Figure 3.7a). COOH-SAMs formed using a concentration of 20 μM thiol without acetic acid have a lower, and more consistent, total amount of thiol on the surface when compared to all other preparation conditions. However, when comparing only bound thiol, the amount of thiol present across all four conditions is comparable. This indicates that the large

differences in total thiol amount shown in Figure 3.7a are from unbound thiol, and is likely primarily from bilayer formation since the bound amount is not lowered in conditions with large unbound amounts. The percentage of bound thiol was found using the areas of the properly and improperly bound S peaks (Figure 3.7b). The data indicates that, in agreement with previous literature, decreasing the thiol concentration decreases the amount of improperly bound thiol, which can be explained by a lower amount of hydrogen-bonded thiol dimers. However, unlike a previous study, the addition of 10% AA decreased rather than increased the bound thiol percentage.¹⁶⁴ Additionally, the data indicates that even in the best preparation condition (20 μM in N_2), at least 18% of the SAM is improperly bound. Figure 3.7c shows that the position of the improperly bound peak also varies across sample type. Specifically, the addition of AA appears to shift the improperly bound peak to lower BE. This shift decreases the properly and improperly bound peak separation, and may explain the discrepancies in this work showing an increase in improperly bound thiol with the addition of AA and the previous work arguing that AA eliminates the unbound thiol.¹⁶⁴ With the improperly bound peak in some cases only 0.6 eV away from the bound peak, the two chemical states are difficult to resolve and may have been previously identified as a single peak. Additionally, the data presented here shows significant variability across not only samples made in the same laboratory, but on different spots of the same sample; the standard deviation in properly bound thiol percent from the 20 μM AA samples was 13%. Since only a single XPS spectra for each condition is presented in the previous work, a particularly well-formed spot may have been selected by chance.

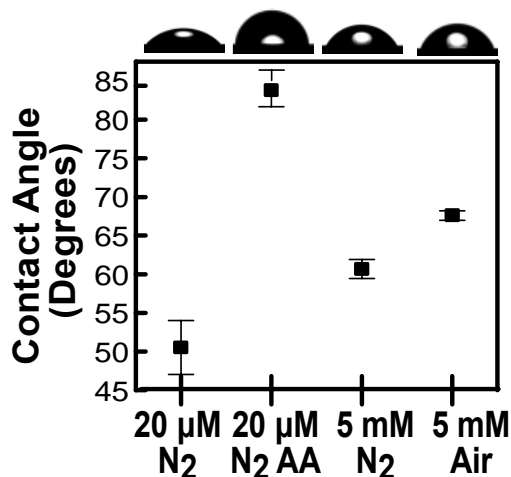


Figure 3.8—DI water contact angle on COOH-SAMs

DI H₂O contact angle can also be used as a measure of COOH-SAM quality, as a perfectly formed COOH-SAM would only have hydrophilic COOH-groups on the surface, resulting in a hydrophilic surface. Any defects in the COOH-SAM, including pinholes, striped phase, and bilayer, exposes hydrophobic Au or hydrocarbon chain to solution, decreasing the surface hydrophilicity. DI H₂O contact angles for COOH-SAMs prepared under the four conditions described above is shown in Figure 3.8. The contact angle hydrophobicity matches with the XPS results, where samples with a larger degree of unbound thiol have a larger (more hydrophobic) contact angle. This data also further supports our designation of unusually low (BE <163 eV) S peaks as improperly bound, as the 20 μ M AA samples have both a low BE of the secondary peak and a more hydrophobic contact angle.

3.3.3 Protein Adsorption to COOH-SAMS

Defects present in the COOH-SAM surface are detrimental to biosensing applications because the proteins in the solution tend to adhere to the exposed hydrophobic surfaces nonspecifically.^{119, 120} Previously, NSA to a short (COOH(CH₂)₂SH) and long (COOH(CH₂)₁₀SH) chain COOH-SAM was investigated as a function of incubation time and surface roughness.¹⁶⁷ While this previous work revealed large NSA to these surfaces, only short, few-second incubation times were tested. The SAM was therefore only allowed to partially order, and large areas of hydrophobic striped phase are expected.^{135, 165} Here, we instead investigate NSA on fully formed (24 hour incubation) COOH-SAM layers, comparing the 20 μ M N₂ and 5 mM air preparation conditions due to their consistent differences in bound thiol percentage as measured by XPS (Figure 3.7b). Since XPS results indicate that more improperly bound thiol is present in the 5 mM SAM, more NSA is expected on this surface. To measure NSA, model small (Lysozyme, 14.4 kDa), medium (BSA, 66.4 kDa), and large (Fibrinogen, 340 kDa) proteins were introduced to the sensor surface in SPR for two 600 s injections with an intermediate 300s PBS wash. The refractive index shift at the end of the second injection is taken as a measure of NSA.

The NSA measurement was completed in triplicate for each model protein, and the results are summarized in Figure 3.9. While this data does not conclusively show that the protein is adsorbing only to defective areas in the SAM, the least defective (20 μ M) SAM adsorbs less of all three proteins, showing that defects do increase NSA. Additionally, a large (>1000 RU) degree of adsorption is still observed in the 20 μ M sample. Because protein solutions interact strongly and non-specifically with the as-formed COOH-SAMs,

this interaction will negatively impact both protein functionalization and sensing. The results indicate that COOH-SAMs alone, even those formed under previously-published optimized conditions, are insufficient for reliable biosensing applications.^{161, 164} The development of a robust blocking procedure will be necessary to ensure accurate sensing results.

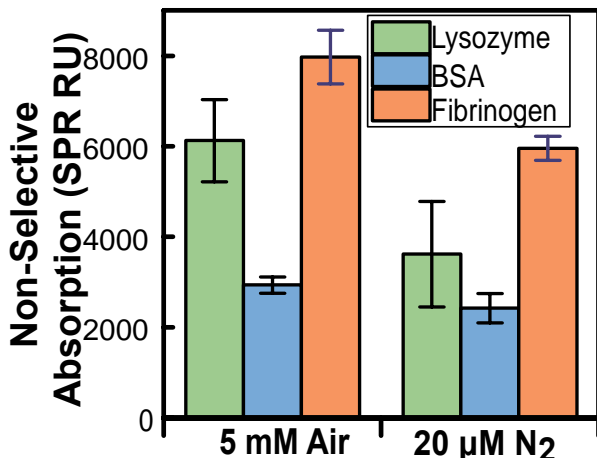


Figure 3.9— NSA of a model small, medium, and large protein on 5 mM Air and 20 μM N₂ COOH-SAMs.

3.4 Conclusions

COOH-SAMs, while commonly used in biosensing literature without characterization, show large NSA of proteins across a wide size range. This work proposes that the NSA is largely the result of defects in the COOH-SAM that expose hydrophobic surfaces to solution, which are exacerbated by the use of polycrystalline Au and the cooperative hydrogen bonding of the carboxylic acid head groups. Best practices for COOH-SAM formation include careful cleaning of the Au surface and incubation

glassware, as well as incubation in a low concentration (20 μM) ethanolic solution of thiol
in inert atmosphere for 24 hours.

CHAPTER 4. PREBLOCKING METHOD FOR COOH-SAM-BASED BIOSENSING^A

CHAPTER 4 discusses a preblocking procedure that can be used to improve reliability of COOH-SAM-based biosensors. Due to the large NSA to COOH-SAMs discussed in CHAPTER 3, blocking is necessary for sensor reliability. Section 4.1 provides a brief overview of literature blocking techniques. However, conventional blocking techniques occur after functionalization (postblocking) and fail to prevent receptor NSA to the sensor surface during functionalization, which can cause receptor denaturation and allow the receptor to wash off the surface during later sensing. Section 4.2 details the experimental methods. Section 4.3 presents the preblocking procedure, where the surface of COOH-SAMs is pre-treated by blocking agents before functionalization. Preblocking can improve baseline stability and prevent receptor denaturation. In this method, a preblocking protein orthogonal to the immunological system of interest is used to cover hydrophobic, non-selective sites on the sensor surface while still leaving carboxylic acid headgroups available for covalent functionalization. Amine functionalization of BSA, antibody BSA, and antibody Haptoglobin (aHp) is successfully completed after gelatin preblocking. Haptoglobin detection via SPR with a preblocked aHp sensor is shown to

^A Adapted with permission from E L Brightbill, B Hitchcock, MY Tsai, A Verga, and E M Vogel. Preblocking Procedure to Mitigate Nonselective Protein Adsorption for Carboxyl-SAMs Used in Biosensing. *Journal of Physical Chemistry C* 2019, **123**(27), 16778–16786. Copyright 2019 American Chemical Society.

perform similarly to conventional postblocking, while demonstrating improved baseline stability and percentage of active receptors. Section 4.4 closes with discussion on how the preblocking procedures offers a route to reliable label-free biosensing on COOH-SAMs by covering NSA sites.

4.1 Introduction

In order to address NSA to COOH-SAMs, we present a new preblocking method. In biosensing studies, a blocking step is sometimes included to decrease NSA to the sensor surface, and thus mitigate false positive signals from the attachment of analytes to the sensor surface via hydrophobic interaction.³⁹⁻⁴¹ This commonly used method, referred to here as postblocking, involves the addition of some agent to the sensor surface after receptor functionalization and before the introduction of analyte. Common post-blocking agents include BSA,^{39-40, 42-44} Casein,^{39, 42, 44} Gelatin,⁴⁵ serum,⁴⁴ poly-ethylene glycol,⁴² and other polymers and proteins orthogonal to the sensing system. While post-blocking is repeatedly shown to reduce false positive and background signals, it only addresses NSA from the analyte solution. Therefore, NSA of the receptor protein is not considered, with receptor attachment instead assumed to be only covalent. However, if COOH-SAM surfaces are highly defective, hydrophobic adsorption of the receptor molecule itself will take place, which may cause the receptor to denature to maximize hydrophobic interactions or wash off the surface during sensing. A blocking protein applied before functionalization, a preblocker, could prevent adsorption of the receptor to defective sites. Additionally, while a postblocker can interfere with the antigen-antibody interaction by covering receptor

active sites, leading to false negative signals,⁴⁶ a preblocker cannot block receptor active sites since the functionalization step occurs after blocking. For these reasons, preblocking, where the hydrophobic sites are covered prior to receptor functionalization, is explored here.

A preblocking method is presented, where NSA sites are covered before amine coupling by a protein orthogonal to the biological system of interest. Preblocking resolves NSA before any active biological agent is applied to the sensor, minimizes wasted receptor protein, and allows blocker drift to be characterized before functionalization.

4.2 Methods

4.2.1 Materials

16-Mercaptoundecanoic acid [HS(CH₂)₁₅COOH] (99.9%), 1-Ethyl-3-(3-dimethylaminopropyl) carbodiimide (EDC), N-Hydroxysuccinimide (NHS), ethanolamine (ETA), Phosphate Buffered Saline Pellets (PBS), Acetic Acid (AA), Anhydrous Ethanol, Bovine Serum Albumin (BSA), antibody Bovine Serum Albumin (aBSA), Human Haptoglobin (Hp), antibody Human Haptoglobin (aHp), Fibrinogen, Lysozyme, Casein, and Gelatin were purchased from Sigma-Aldrich (St. Louis, MO). Desorb kit, Gold Substrates (SIA kit Au) and CM5 chip for SPR were purchased from GE Healthcare Bio-Sciences (Pittsburgh, PA). Blocker Casein in PBS was purchased from Thermo Fisher Scientific (Waltham, MA). 100 nm thick Gold surfaces for XPS measurements were e-beam evaporated on a substrate consisting of 280 nm of SiO₂ on silicon. The deposited Au

film is continuous,⁵¹ and both the Au/SiO₂ substrates and SPR Au substrates have an RMS roughness <1.5 nm, as shown in Figure 3.1.

4.2.2 COOH-SAM Formation

The gold surfaces were cleaned with acetone, methanol, and isopropanol rinses and dried with a N₂ stream, followed by a two-minute O₂/Plasma treatment (200 mTorr, 50 W RF, 25 sccm O₂). The substrates were then placed in ethanolic solutions of 20 μM thiol in piranha-cleaned (3:1 96% H₂SO₄:H₂O₂) glass petri dishes in an N₂ atmosphere. After 24 hours, the SAM-covered substrates were sonicated for five minutes in fresh ethanol, followed by drying in a stream of N₂. All measurements on COOH-SAMs began within 30 minutes of drying and completed within 8 hours. N₂ atmosphere was provided by a Labstar Pro glovebox (MBRAUN), with H₂O and O₂ both <1ppm.

4.2.3 Surface Plasmon Resonance

A Biacore T200 (GE Healthcare Life Sciences; Chicago, Illinois) was used for all SPR measurements. A 30 μL/min flow rate and PBS running buffer were used unless otherwise stated. Protein solutions were diluted in PBS. 0.1 M EDC, 0.1 M NHS, and 1 M ETA solutions were prepared with deionized water.

4.3 Results

4.3.1 Preblocker Selection

In order to create a reliable sensor with COOH-SAMs, NSA must be controlled and minimized during functionalization. While blocking the sensor surface after functionalization to prevent NSA from sample solutions is common in literature, it does

not address the issue of the receptor molecule adsorbing to the surface. The large degree of NSA on the COOH-SAM surface (cf. Figure 3.9) indicates that a large amount of extra protein is necessary to saturate both NHS/EDC activated carboxylic acid sites for covalent protein attachment and hydrophobic sites during functionalization. In many systems, realizing a large concentration of receptor is extremely difficult, expensive, or both. Even in cases where the receptor concentration is sufficient to cover the NSA sites, the stability of such adsorption may be poor, allowing the receptor to be washed off the surface during sensing. Additionally, many proteins partially unfold upon hydrophobic adsorption, which can alter the activity of the protein rendering it insensitive to the target antigen.⁷⁷⁻⁷⁹ As a result, the amount of functionalized protein will be much larger than the amount of active protein, resulting in variable and unpredictable device sensitivity.



Figure 4.1 – Schematic of functionalized surface with preblocker.

This report proposes a preblocking technique to block the hydrophobic sites on the COOH-SAM with a protein orthogonal to the biological system of interest in order to mitigate the negative effects of NSA before functionalization and sensing, shown schematically in Figure 4.1. Preblocking with a protein will prevent NSA during

functionalization and sensing since multiple layers of protein attachment is not observed.¹¹⁹ After preblocking, the properly oriented, hydrophilic carboxylic acid heads of thiol molecules are still accessible for later covalent functionalization, since any NSA to these hydrophilic end-groups is expected to be much weaker and thus can be removed during the washing step. This method allows a high concentration of an inexpensive protein to cover NSA sites, the preblocker's adsorption stability to be determined before functionalization, and a more expensive, functional protein receptor to be conserved.

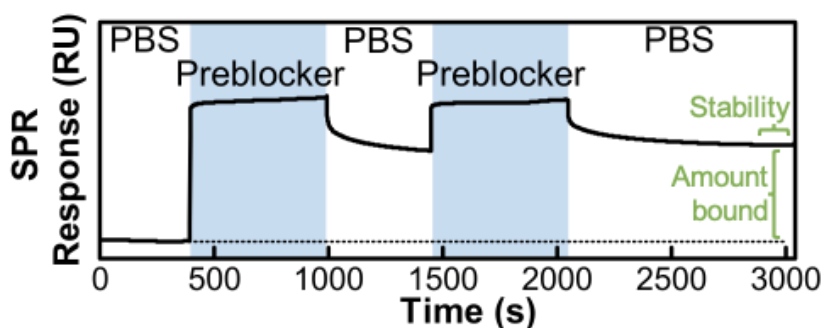


Figure 4.2 – Example SPR sensorgram of preblocker screening procedure, with amount bound and stability parameters indicated.

Three commonly used postblocking agents are investigated for preblocking: BSA, Gelatin, and Casein; each of which is known to adsorb well to hydrophobic surfaces. In order to compare these three agents, two 600 s injections of 1% blocker solution are washed over the sensor surface using a Biacore SPR system. Two PBS wash steps (300 s, 900 s) are incorporated to assess the stability of preblocker attachment following the first and second injections, respectively (Figure 4.2). The injections are completed at the 30 $\mu\text{L}/\text{min}$ flow rate used in the rest of this study, but the washing steps are completed at 50 $\mu\text{L}/\text{min}$.

The high wash flow rate serves two purposes. First, the aggressive washing should remove any weak NSA to hydrophilic areas of the sensor, such as COOH end groups. Indeed, there is an initial decrease in the preblocker attachment before stabilization as seen in Figure 4.2. Second, since the wash is more aggressive than a typical sensing protocol, it is a strong indicator of stability. As summarized in Table 4.1, the result shows a similar degree of preblocker adsorption in terms of RU across all three agents. However, the Gelatin preblocker shows superior adsorption stability compared to BSA and Casein. Due to its superior stability under washing, Gelatin was selected for further investigation.

Table 4.1 – Preblocking attachment and stability results.

Preblocker	BSA	Gelatin	Casein
Preblocker Attachment (RU)	2452	2636	2461
Preblocker Stability (RU/s)	-3.81	-0.02	-0.14

4.3.2 Preblocked Functionalization and Sensing

As the preblocker should only adsorb strongly to hydrophobic sites, the hydrophilic carboxylic acid groups will still be available for amine functionalization. To show this, functionalization of a 20 μ M COOH-SAM with three different receptors with and without preblocking is demonstrated. Figure 4.3a shows an example SPR sensorgram of preblocking functionalization, where the preblocker is first introduced to the sensor in two 600 s injections, followed by a 900 s wash with PBS. After, standard amine functionalization is completed (Figure 1.20), and ETA is used to block leftover activated carboxylic acid groups. Figure 4.3b and Figure 4.3c show the normal receptor protein

immobilization and preblocking assisted receptor protein immobilization, respectively. With all three proteins, the functionalization was successful regardless of the use of gelatin preblocker, showing that preblocking does not prevent amine functionalization by covering COOH endgroups (Figure 4.3b,c). Additionally, the amount of bound receptor decreases with the Gelatin preblocker in all three cases as expected (Figure 4.3b,c). This observation supports the hypothesis that the receptor can only bind to carboxylic acid functional groups while the preblocker proteins occupy hydrophobic NSA sites, and this decreased functionalization does not experimentally affect the accuracy of the biosensor (Figure 4.4a). Additionally, to show that the receptors are not interacting with the preblocker itself, preblocked aHp functionalization is compared to aHp interactions with gelatin adsorbed directly onto gold (Figure 4.3d). While functionalization on the gelatin-blocked COOH-SAM is successful as shown by an increase in SPR response, aHp does not attach to gelatin, gelatin that has been treated with NHS/EDC to activate any COOH-groups on the gelatin surface, or gelatin that has been treated with NHS/EDC followed by ETA to block any COOH-groups on the gelatin surface. If unwanted NHS/EDC activated attachment to the preblocker does occur in other systems, the preblocker could be treated before it is applied to the surface.

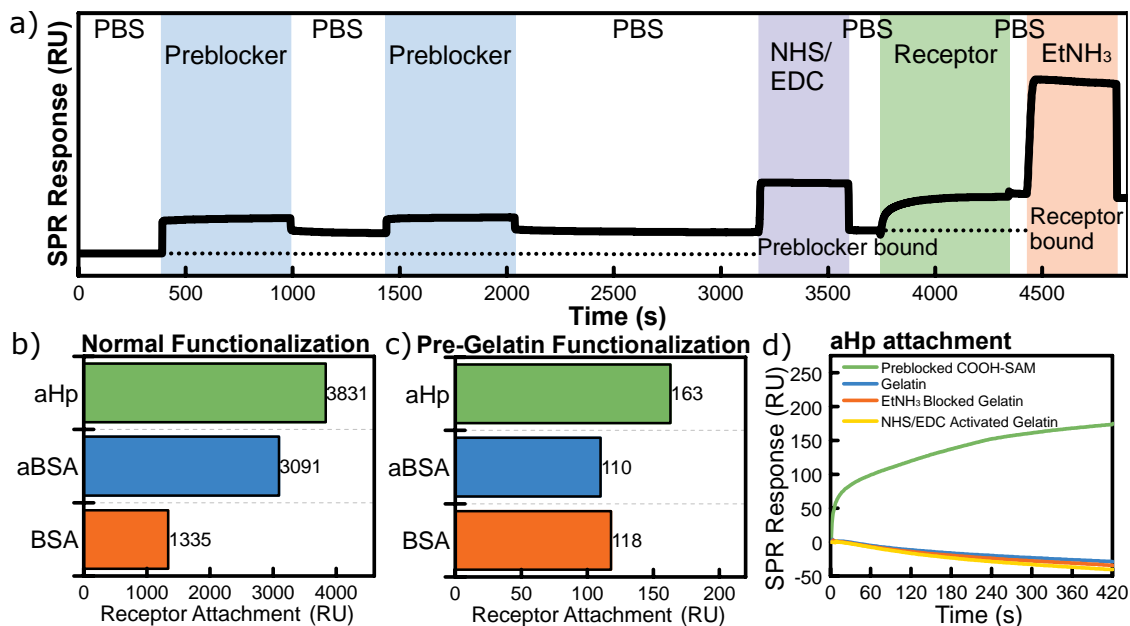


Figure 4.3 – a) Example functionalization SPR sensorgram with preblocking steps (vertical step changes are due to solution refractive index). b) Degree of functionalization without preblocking. c) Degree of functionalization after preblocking. d) SPR aHp attachment curve for gelatin preblocked COOH-SAM compared to gelatin adsorbed directly to Au with no treatment, with NHS/EDC activation and ETA blocking treatment, and with NHS/EDC activation only (refractive index change removed for clarity).

In addition to preventing receptor NSA during functionalization, preblocking improves the accuracy of subsequent biosensing on par with conventional postblocking methodology. Figure 6 shows SPR analysis of Hp detection with an aHp functionalized surface. Results from a 20 μ M COOH-SAM with gelatin preblocking, gelatin postblocking, and no blocking are compared to a commercial CM5 (dextran matrix) SPR chip (Figure 4.4a). The results clearly show that blocking is necessary to achieve accurate results: while the pre and postblocked sensors agree with the CM5 data, the no blocking case overestimates the binding affinity, likely due to NSA of the Hp. Additionally, while the pre

and postblocking sensors give similar results, the postblocked sensor has improved baseline drift (Figure 4.4b). The difference in stability is most likely due to some NSA sites being occupied by the aHP receptor which is releasing from the surface, as the preblocked sensor surface saw the addition of 2636 RU Gelatin to the surface, while the postblocked surface saw only 791 RU. Please note that, due to the variable structure and chain length of gelatin prepared from collagen no assumptions about percent surface coverage, only relative surface coverage, of preblocker is made here. Furthermore, a higher percentage of the aHP on the Gelatin preblocked surface is active compared to the no blocking and postblocking cases (Figure 4.4c). The RU response of the sensor after a 300 s injection of 25 ug/mL Hp is normalized to the functionalization RU response as a measure of receptor activity. Although it is not a direct percentage, the larger these proportions, the larger percentage of receptor molecules are responsive to Hp. The preblocked sensor shows over double the amount of active receptor compared to the postblocked and control sensors, since the preblocking gelatin covered the NSA sites and prevented denaturation of the aHP upon adsorption, while these sites were available to the aHP during the preblocking procedure. Control of denaturation may be of particular importance in some kinetic studies, where it is necessary to carefully control the density of active receptor on the surface.⁶⁵ Overall, the pre-blocking technique outperforms the as-grown COOH-SAM and matches the accuracy of postblocking methods employed in previous literature, while potentially offering the important benefits of decreased baseline drift and control over receptor denaturation in certain biosensing platforms.

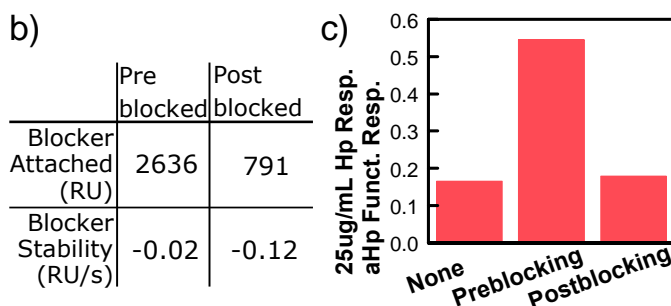
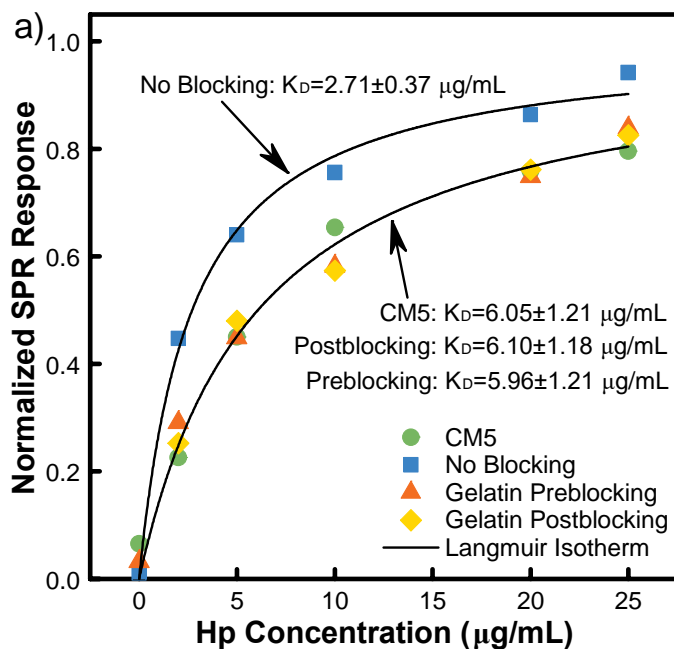


Figure 4.4 – Hp sensing result with kinetic fitting for commercial CM5 sensor compared to COOH-SAM sensors without blocking, with gelatin preblocking, and with gelatin postblocking . b) Amount of attached blocker and blocker stability for preblocked and postblocked sensors c) receptor activity comparison, given by sensor response to 25 µg/mL Hp solution, normalized by the degree of aHp functionalization.

4.4 Conclusions

Blocking procedures offer a route to reliable COOH-SAM biosensing by covering NSA sites. While postblocking the sensor surface does increase the specificity of the sensor, the postblocker can interfere with the activity of the receptor protein, and does not

prevent against NSA of the receptor protein itself. This work shows that preblocking offers a simple and easily implemented method of stabilizing the chip before covalent functionalization while preserving the activity of the sensing surface and the protein receptors. A protein orthogonal to the system of interest can be used to cover the hydrophobic NSA sites prior to amine functionalization, preventing NSA of the receptor and conserving its activity. Experimentally, the preblocked channel showed increased receptor activity and decreased baseline drift when compared to the postblocked sensor. This methodology is particularly important in certain sensing platforms such as potentiometric sensing, where Debye length considerations limit possible linker molecules for sensor design. More work is necessary to optimize COOH-SAM quality and thus decrease NSA. However, a preblocking protein can mitigate many of the concerns with COOH-SAMs.

CHAPTER 5. INHIBITION OF COOH-SAM OXIDATION VIA PROTEIN BLOCKING^B

CHAPTER 5 describes the use of a simple protein blocking procedure prior to receptor functionalization to inhibit the oxidation of carboxylic-acid-terminated thiolate self-assembled monolayers (COOH-SAMs) in ambient conditions. Section 5.1 provides a quick overview of how COOH-SAMs degrade via oxidation, and how this degradation inhibits biosensing. Section 5.2 describes the methods used to both track and prevent oxidation of the COOH-SAMs. Section 5.3 presents data showing that, with gelatin blocking, no surface degradation is observed via XPS nor reductive desorption for 21 days, compared to observable degradation in only one day for an unblocked COOH-SAM. Additionally, unlike a traditional postblocking method that requires the sensor to first be functionalized with active receptor, this blocking procedure occurs directly after COOH-SAM formation and does not prevent the subsequent functionalization of the biosensor. These blocked sensors are shown to maintain surface-plasmon-resonance-based sensing performance for at least one week. Additionally, the blocking technique for degradation prevention is shown to even outperform COOH-SAM storage in N₂. Section 5.4

^B Adapted with permission from E L Brightbill, H F Gexahagne, D S Jin, B Brown and E M Vogel. Protein blocking inhibits ambient degradation of self-assembled monolayers for affinity biosensing. *Applied Surface Science* 2021, **557**, 149843. Copyright 2021 Elsevier B.V.

summarizes the findings and implications for the engineering and design of point-of-care and field affinity biosensors.

5.1 Introduction

Due to the use of label-free biosensors for point-of-care and field sensing, sensor stability and shelf life are crucial considerations for a final device.²³⁸ Despite the popularity of COOH-SAMs in the affinity biosensor literature, few studies have considered their long-term stability. SAMs are known to degrade via oxidation; specifically, the S-Au bond has been shown to oxidize through reaction with ozone into sulfate and sulfite species,^{168, 169} in both ambient conditions and aqueous solutions with and without exposure to light.^{136, 168, 170, 239, 240} This reaction can proceed quickly, with oxidation observed in as little as 2 hours in some SAM systems (see 1.3.4).¹⁶⁸

It is obvious that COOH-SAM oxidation is injurious to sensing applications. Firstly, the creation of disordered, defective COOH-SAM regions due to oxidation results in increased non-selective adsorption (NSA) of proteins due to the hydrophobic effect.² Moreover, once the SAM begins to desorb, areas of plain Au may be left to non-selectively adsorb protein directly.²⁴¹ Secondly, any changes in COOH-SAM structure will affect the density and availability of COOH end groups for receptor functionalization. If oxidation occurs before functionalization, less protein may be functionalized, resulting in a less-sensitive device. If oxidation occurs after functionalization, receptor protein may desorb from the sensor surface with the thiol molecule, leading to lower sensitivity, a drifting baseline, or false-negative signals. One previous study has demonstrated the negative

effects of COOH-SAM oxidation on sensing.²⁴² COOH-SAMs were allowed to oxidize in various storage conditions, while x-ray photoelectron spectroscopy (XPS) and SPR were used to track oxidation and protein adsorption, respectively. As XPS indicated COOH-SAM oxidation increased, SPR indicated that unwanted NSA to the sensor surface increased.²⁴² Also, as the COOH-SAM degraded, the amount of receptor protein attached to the surface during amine functionalization decreased, reducing sensitivity.²⁴²

However, as discussed in CHAPTER 4, preblocking COOH-SAMs with a protein before receptor functionalization improves sensing outcomes.² Preblocking is possible due to the higher adsorption affinity on defective, hydrophobic areas of the COOH-SAM as compared to the hydrophilic COOH end-groups, which remained accessible for sensor functionalization.² Therefore, since SAM oxidation begins at defect sites and grain boundaries, the preblocker should also slow sensor degradation by serving as a physical barrier. Indeed, a previous study measuring SAM oxidation in liquid media shows this mechanism is likely. It was demonstrated that, when an amphiphilic surfactant is added to solution, that surfactant will adsorb to the SAM's defect sites and inhibit the onset of oxidation.¹⁶⁹ While it is reasonable to hypothesize that postblocking will inhibit oxidation via the same mechanism, postblocking requires functionalization of the sensor surface with a receptor protein first, causing two distinct disadvantages as compared to preblocking. First, if the selective receptor is attached to the sensor surface before storage, stability of that receptor must also be considered. While possible degradation of a blocker can be studied and then applied to a wide range of sensing targets, degradation of a receptor would

have to be independently determined for each and every sensing target. Moreover, degradation of the blocker is most likely not of concern, since the blocker, unlike a receptor, does not contain any specific active sites that are necessary for the selectivity and function of the affinity biosensor. Second, if the sensor is functionalized before storage, the sensing target must be predetermined. With preblocking, when it is time for the sensor to be used, it can still be functionalized with any receptor. Due to these advantages, here it is investigated if preblocking, a technique already useful in the development of COOH-SAM-based sensors, also inhibits sensor degradation via oxidation.

This chapter demonstrates the use of a gelatin blocker to prevent COOH-SAM degradation via oxidation in ambient storage conditions. Although SAM oxidation is well established in the literature, very few studies consider the implications of this degradation for point-of-care and field applications of biomarker detection. Specifically, in the case of COOH-SAMs, although oxidation is known to decrease biosensing reliability, appropriate sensor storage conditions have not been established. In this study, the degradation of a COOH-SAM functional surface in ambient storage conditions with and without gelatin blocking is tracked via XPS and reductive desorption. The blocking technique still allows subsequent receptor functionalization for selective biosensing, as demonstrated by the SPR detection of human Haptoglobin. Additionally, the degradation of biosensing response due to oxidation and the limits of harder-to-implement inert atmosphere storage are presented.

5.2 Experimental Methods

5.2.1 Materials and Storage Conditions

16-Mercaptohexadecanoic acid [HS(CH₂)₁₅COOH] (99.9%), 1-ethyl-3-(3-dimethylaminopropyl)carbodiimide (EDC), *N*-hydroxysuccinimide (NHS), ethanolamine (ETA), phosphate-buffered saline (PBS) pellets, potassium hydroxide (KOH), anhydrous ethanol, human haptoglobin (Hp), and gelatin were purchased from Sigma-Aldrich (St. Louis, MO). Antibody human haptoglobin (aHp) was purchased from Abcam (Cambridge, UK). Desorb kit and gold substrates (SIA kit Au) for SPR were purchased from Cytiva Life Sciences (Marlborough, MA). Gold surfaces (100 nm thick) for XPS and CV measurements were e-beam evaporated onto glass substrates. AFM measurements indicate a root-mean-square surface roughness of 1.17nm (Figure 5.6), consistent with the roughness of other e-beam evaporated Au surfaces in literature.²⁴³

COOH-SAMs were formed as previously described.² In short, the gold surfaces were cleaned with acetone, methanol, and isopropanol rinses followed by an O₂ plasma treatment. The cleaned substrates were incubated in 20 μM ethanolic solutions of 16-mercaptohexadecanoic acid in a N₂ atmosphere for 24 h, sonicated for 5 min in fresh ethanol, and dried via N₂ stream. N₂ atmosphere was provided by a Labstar Pro glovebox (MBRAUN, Germany), with H₂O and O₂ both <1 ppm. For blocked COOH-SAMS, immediately following drying with N₂, the samples were immersed in a solution of 1% gelatin in PBS for 1 hr. When removed from the gelatin solution, the samples were briefly rinsed with DI H₂O and dried via N₂ stream. To limit sample-to-sample variability, COOH-SAMs were batch prepared and stored together.

Samples kept in ambient conditions were placed in a petri dish on the bench, exposed to light. A temperature and humidity monitor (Fisher Scientific) used to monitor the lab space for 2 weeks indicated a temperature range of 21-22°C and a humidity range of 17-58%. Samples kept in N₂ were placed in the Labstar Pro glovebox with O₂ and H₂O both <1ppm, and sealed into a clear plastic box with electrical tape.

5.2.2 X-ray Photoelectron Spectroscopy

XPS was used to track COOH-SAM degradation via oxidation of the S-Au bond to sulfate and sulfite species. XPS measurements were collected with a Thermo Scientific K-Alpha X-ray photoelectron spectrometer system (Waltham, MA) with a monochromatic Al K α source (KE = 1486.6 eV), a 180° double focusing hemispherical analyzer, and a 128-channel detector. High-resolution Au 4f and S 2p spectra were acquired at a pass energy of 50 eV and a spot size of 400 μ m. Because sulfate/sulfite species peaks are difficult to resolve, oxidation was quantified by total peak area above 166 eV, normalized to the substrate Au signal.¹³⁶ Au 4f spectra were fit with 2 peaks (spin-orbit splitting of 3.7 eV, 3:4 area ratio). To aid quantification of S oxidation and avoid fitting noise, S spectra were processed with quadratic Savitzky-Golay smoothing.²⁴⁴ A 10-point window (1 eV), smaller than the peak FWHM, was utilized resulting in <2 % peak height/width distortion.²⁴⁵ An example S 2p spectra before and after smoothing, visually showing limited distortion in peak shape, is shown in Figure 5.1. Shirley-type background was used for all spectra.²⁴⁶ In all summary plots, a total of 5 points were analyzed for each sample type.

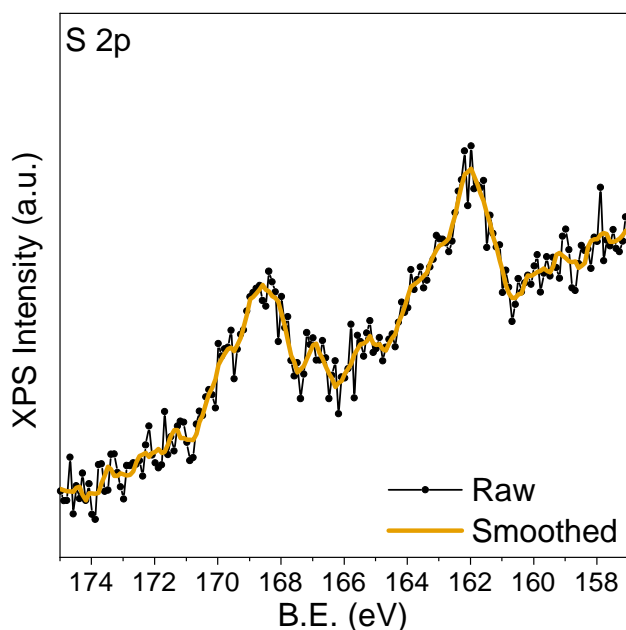


Figure 5.1 – Example S 2p spectrum before and after Savitzky-Golay smoothing.

In many cases, specifically after short storage times, the S oxidation peaks as detected via S 2p XPS are of similar magnitude to the background noise. As such, a standardized method was developed to prevent bias in the determination of peak presence. In this method, after smoothing (Figure 5.1), a Shirley-type background was added to the range corresponding to oxidized S species (166-164 eV), and an unconstrained peak was allowed to optimize in that range. In cases where an obvious peak is present, the results are as expected (Figure 5.2a). However, when the spectra appear essentially flat, the peak may fit to data that appears to be noise (Figure 5.2b). These peak areas are still reported to ensure consistency in the processing of all samples, and thus unoxidized, fresh COOH-SAMs have oxidation signals slightly greater than zero.

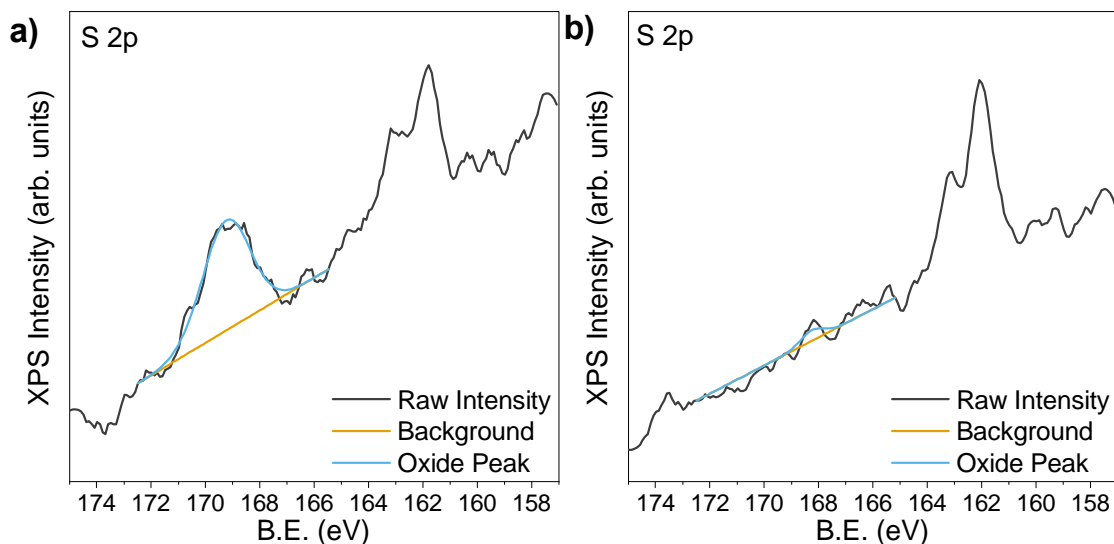


Figure 5.2 – Example S 2p XPS fitting for oxidized signal. a) Peak fitting on a clearly present peak b) non-zero peak fitting on a spectrum that appears flat

5.2.3 Cyclic Voltammetry

Reductive desorption (RD) via cyclic voltammetry (CV) was used to diagnose the state of COOH-SAMs and track changes with time. A Gamry Interface 1000 potentiostat (Warminster, PA) was used for CV measurements. The Gamry was connected to an electrochemical cell (Ametek K0235 Flat Cell) consisting of a Pt-coated mesh counter electrode, dip-in Ag/AgCl reference electrode, and a 1 cm² working electrode area. CV measurements were taken at a scan rate of 20 mV/s from 0 V to -1.3 V vs Ag/AgCl in a 0.5 M aqueous KOH solution.

5.2.4 Surface Plasmon Resonance

SPR was used to demonstrate label-free affinity biosensing on COOH-SAMs over time. A Biacore T200 (Cytiva Life Sciences; Marlborough, MA) was used for SPR data

collection. PBS running buffer and a 30 $\mu\text{L}/\text{min}$ flow rate was used unless otherwise stated. Protein solutions were diluted in PBS. 0.1 M EDC, 0.1 M NHS, and 1 M ETA solutions were prepared with deionized water. Preblocked amine functionalization of aHP is used to modify the COOH-SAMs for selective Hp sensing.² In this method, a 1% solution of gelatin was first introduced to the COOH-SAMs in two 600s-injections, followed by a long 900s rinse to remove any poorly-adsorbed gelatin blocker. Subsequently, a standard amine functionalization method was used, where COOH-groups on the surface were activated with NHS/EDC. After activation, a 600s injection of 1% aHP was introduced to the surface, allowing amide groups on the receptor protein to form amine bonds with the activated COOH-groups. Finally, ETA was used to block any remaining activated COOH-groups. Aged COOH-SAMs were inserted into the SPR without any preceding surface cleaning, and the surfaces were primed with a buffer rinse immediately followed by the functionalization procedure.

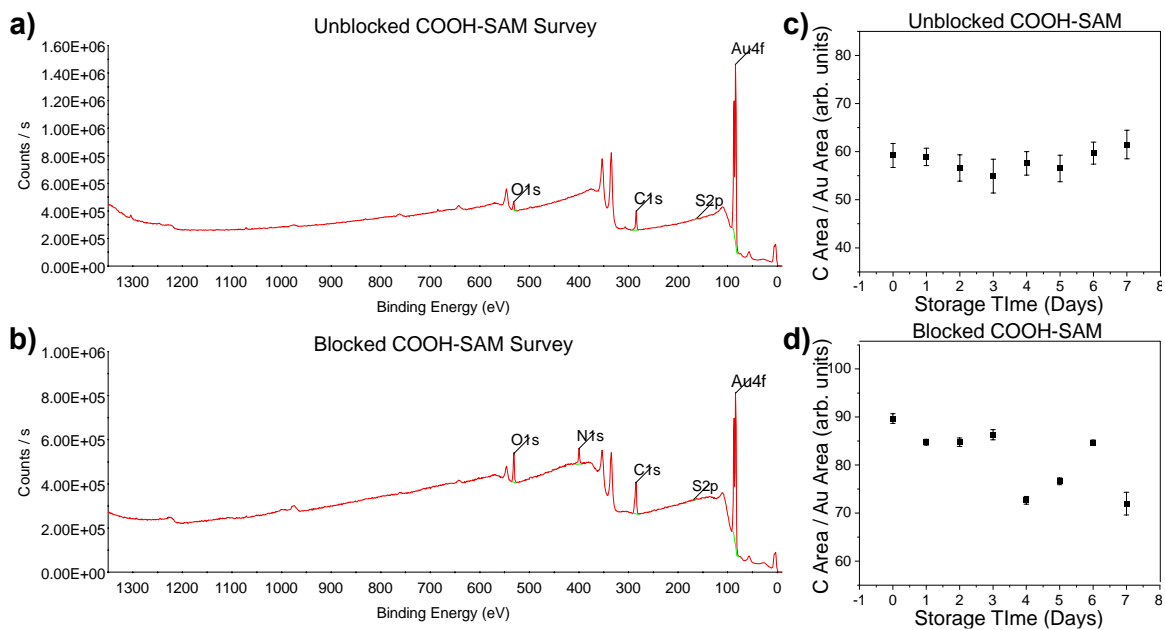


Figure 5.3 – Analysis of C 1s XPS signal. Survey spectra with software-identified peaks for unblocked (a) and blocked (b) COOH-SAMs. Survey C 1s peak area normalized to Au 4f peak area for unblocked (c) and blocked (d) COOH-SAMs during 1 week of storage in ambient conditions.

To check for accumulation of surface contamination during storage, the C 1s signals from survey spectra were analyzed. Survey spectra were acquired at a pass energy of 200 eV and a spot size of 400 μm , and the Thermo Scientific Avantage software was used to identify the elemental composition of survey scans. Figure 5.3a and b show example surveys for unblocked and blocked COOH-SAM samples, respectively. All of the identified elements can be explained by substrate, SAM layer, and blocking protein (N). Figure 5.3c,d show the normalized C Area from the survey spectra for each of the same data points included in Figure 5.5. There is not significant increase in surface

contamination during storage as indicated by C signal for either the blocked nor unblocked sample.

5.3 Results

5.3.1 Degradation of COOH-SAMS in Ambient Conditions

Oxidation of a SAM can be tracked from S 2p XPS, where sulfate and sulfite species (the products of oxidation) are well-resolved from lower binding energy (BE), unoxidized species.¹³⁶ Specifically, oxidized species can be recognized by peaks with BE greater than 166 eV.^{136, 168} To determine whether blocking the COOH-SAM with gelatin inhibits oxidation, XPS was used to monitor oxidation on COOH-SAMs with and without blocking stored in ambient conditions for up to 3 weeks. To limit sample-to-sample variation, all COOH-SAMs were batch prepared in the same solution and stored together on the bench. Additionally, each sample was discarded after XPS measurement, to prevent any influence of ultra-high vacuum or x-ray exposure on oxidation rate. Ambient conditions were chosen due to the ease of implementation of these conditions for point-of-care sensors, as compared to cold storage or inert atmosphere. Figure 5.4a schematically shows the two sample types, where the unblocked COOH-SAM undergoes degradation over time, while the adsorbed gelatin protects the blocked COOH-SAM from the same degradation by physically covering defective areas. Example traces of S 2p spectra over the course of 3 weeks clearly show that, while a visible oxidation peak appears in the S 2p spectra for the unblocked COOH-SAM after only one day, no significant peak is visible after a full 21 days for the blocked COOH-SAM (Figure 5.4b,c).

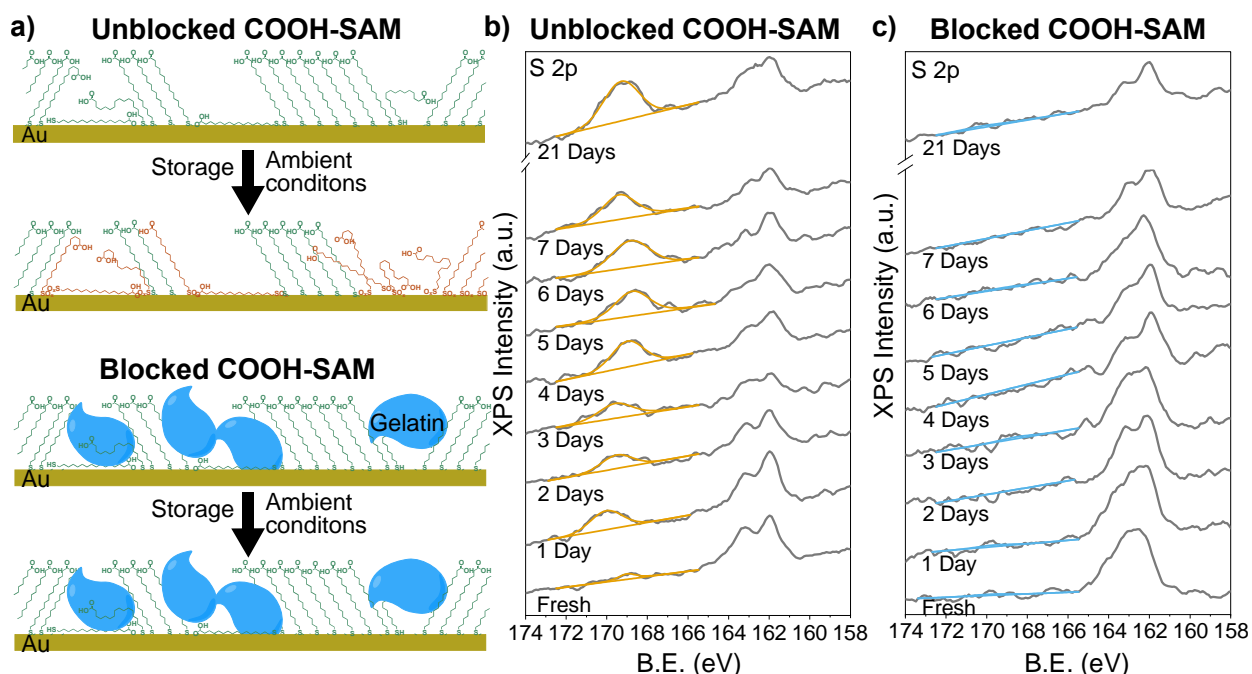


Figure 5.4 – Inhibition of oxidation by gelatin blocking. a) Schematic of COOH-SAM with common defects before and after oxidation in ambient conditions. Gelatin blocks defective regions and prevents oxidation. b) Example S 2p spectra of unblocked COOH-SAM stored in ambient conditions. Orange peak fitting indicates oxidized S species. c) Example S 2p spectra of blocked COOH-SAM stored in ambient conditions. Blue peak fitting illustrates lack of oxidized S species.

The degree of oxidation can further be quantified by finding the oxidation peak area, as shown by the orange and blue peak fitting in Figure 5.4b,c. This area can be normalized to the Au substrate signal and compared across data points; the average and standard deviation of these values for 5 data points of each sample type is presented in Figure 5.5 (3 samples, 1-2 data points each). This quantification confirms what was visually observed in Figure 5.4b,c: while the oxidation of the unblocked COOH-SAM shows a significant amount of oxidation after 1 day and continues to oxidize with time, the

measured oxidation on the blocked COOH-SAM remains unchanged within error after 3 full weeks.

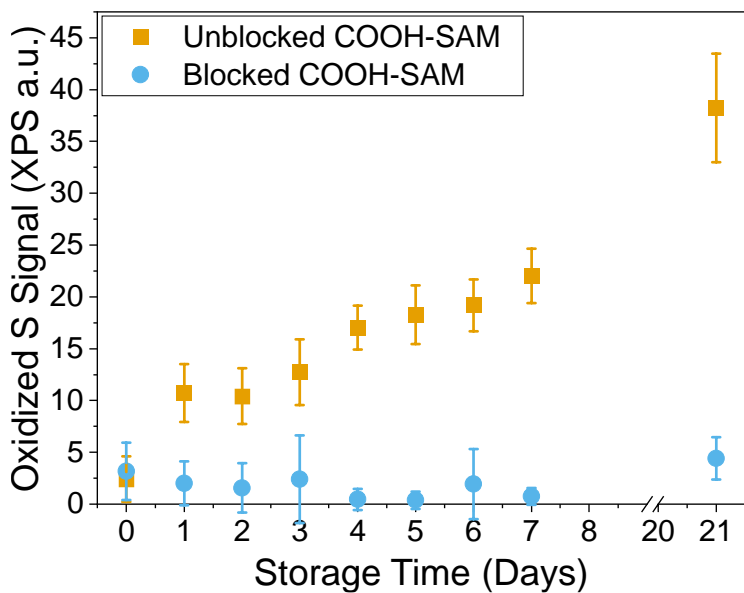


Figure 5.5—Summary of XPS fitting for unblocked COOH-SAM (orange, square) and blocked COOH-SAM (blue, circle) oxidized S peaks.

AFM images of blocked and unblocked COOH-SAMs before and after storage are included in Figure 5.6. Atomic force microscopy (AFM) was performed using a Bruker Icon Scanning Probe Microscope (Billerica, MA) with AppNano (Mountain View, CA) SPM Si probes having a tip radius of <10 nm. AFM images indicate surface roughness is dominated by the polycrystalline Au substrate (Figure 5.6a). The increasing RMS roughness for unblocked COOH-SAM with increasing storage time indicates degradation of surface (Figure 5.6b,c,d). The addition of blocker appears to “smooth out” the surface roughness (Figure 5.6e). The observed roughness of the blocked COOH-SAMs does not increase with storage time (Figure 5.6e,f,g).

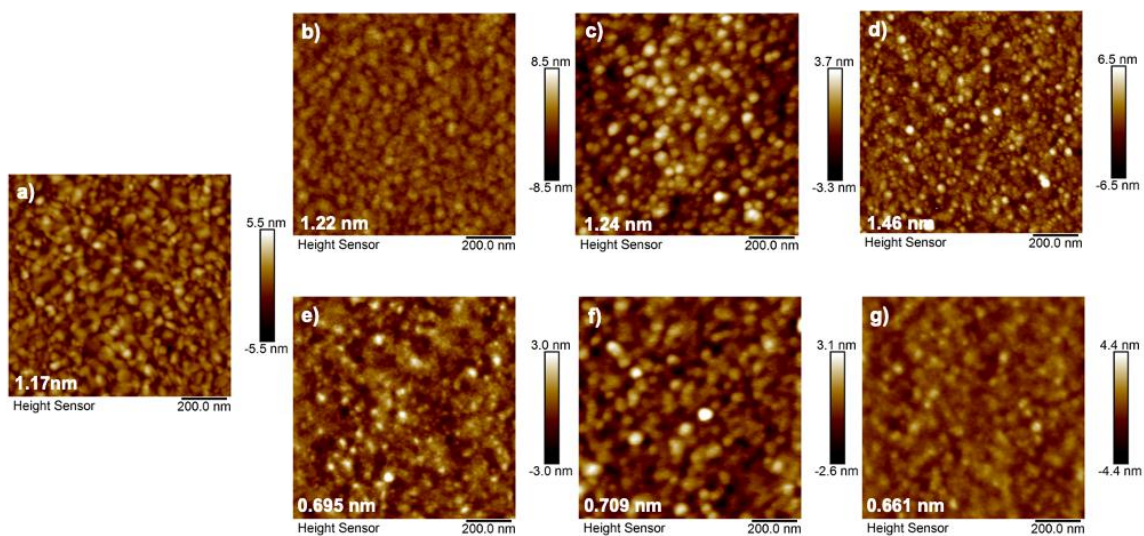


Figure 5.6 – AFM images of functional surfaces on 100 nm Au/SiO₂ chips with inset root-mean-square roughness (in white). a) Plain Au b) unblocked COOH-SAM, freshly prepared c) unblocked COOH-SAM, 1 week storage d) unblocked COOH-SAM, 3 months storage e) blocked COOH-SAM, freshly prepared f) blocked COOH-SAM, 1 week storage g) blocked COOH-SAM, 3 months storage.

Reductive desorption is also a powerful method for diagnosing the state of SAM monolayers via reduction of the S-Au bond.²⁴⁷⁻²⁵⁰ This 1-electron process is shown chemically and schematically in Figure 5.7a, and results in a peak generally reported between -0.7 and -1.1 V vs Ag/AgCl.^{247, 251} The peak position depends on factors including thiol chain length, thiol solubility, and scan rate.²⁴⁷ In these measurements, chain length, solution, scan rate, and preparation conditions are all held constant. Please note, due to interference from charging currents, the RD peak cannot be used to quantify surface coverage, and thus peak integrations are not presented here.^{247, 252} To confirm that the observed peaks are due to the COOH-SAM, a reference scan on plain Au is shown in Figure 5.7b. There are no significant peaks in the bare Au voltammogram, and the

substrate signal is notably flat around -0.9 eV where the COOH-SAM reduction peaks are observed. CV curves for unblocked and blocked COOH-SAMs before and after one week of storage in ambient conditions are shown in Figure 5.7c,d. Voltammograms of each condition were taken in duplicate on separate sensors to illustrate measurement consistency. For a freshly prepared COOH-SAM, the reductive desorption peak is shifted to the left for the blocked COOH-SAM relative to the unblocked COOH-SAM (Figure 5.7c,d). This result is expected, as peak position at a more positive potential (i.e. lower negative voltage) indicates ease of penetration of counterions into the SAM.²⁴⁹ With gelatin present on the surface, penetration of counterions to the sensor surface through less dense, defective regions is encumbered by the blocking protein. This result further indicates that blocking is an effective inhibitor of oxidation; blocking makes the S-Au bond more difficult to oxidize because it is more difficult to access. After a week of storage, the CV curves were measured again and compared to the fresh samples to indicate any changes in the COOH-SAM structure. It is obvious that the unblocked COOH-SAM underwent major chemical and structural changes; the main reductive desorption peak at -0.9V is severely diminished, while several higher potential peaks are now present (Figure 5.7c). These lower-energy interactions have been attributed to physisorbed sulfur (rather than chemisorbed sulfur),^{253, 254} and are most likely due to thiol of various oxidation states interacting weakly with the surface. In contrast, with the blocked COOH-SAM, the CV curves are nearly identical after 1 week of storage, indicating little chemical or structural change has taken place (Figure 5.7d).

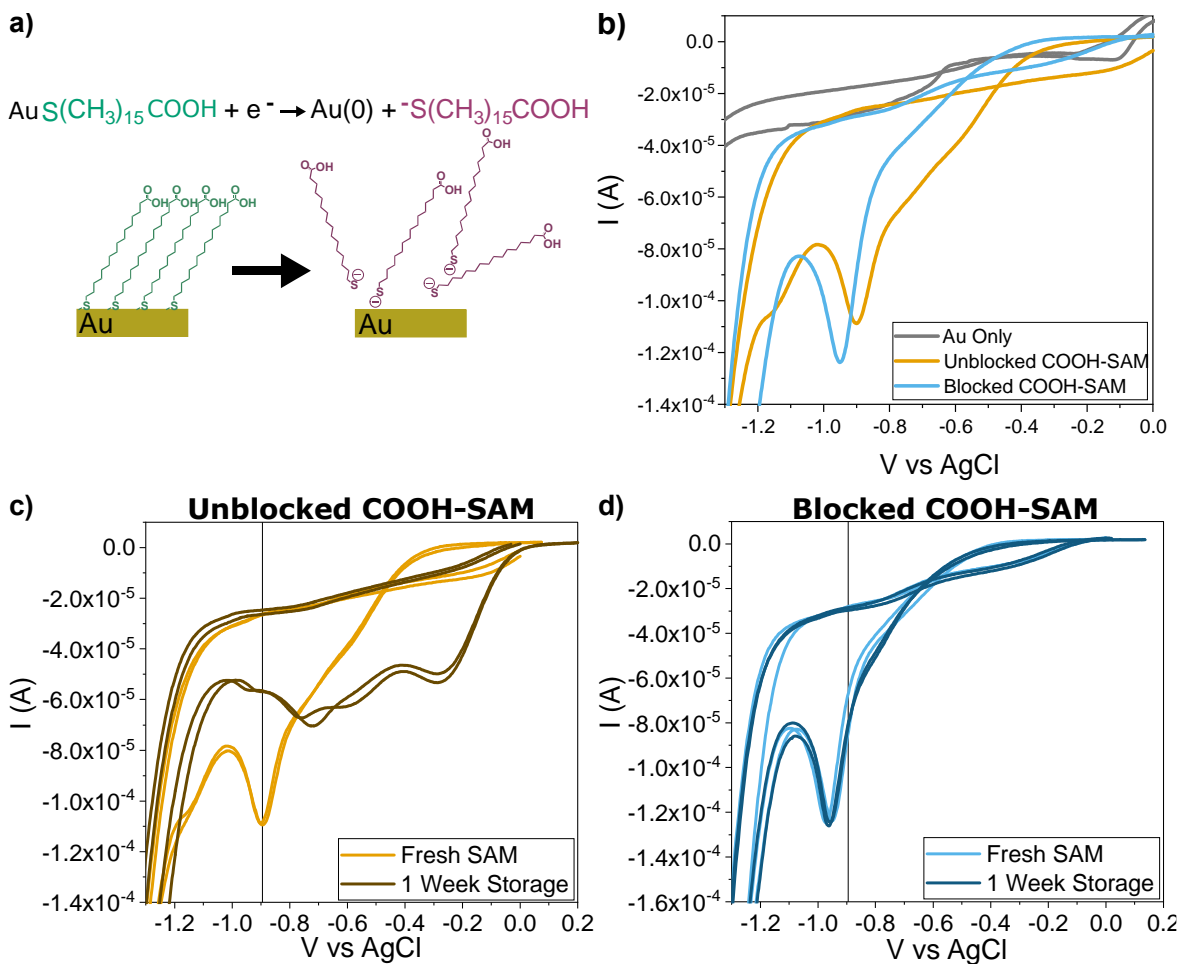


Figure 5.7 – CV curves showing reductive desorption of COOH-SAMs a) chemical reaction and schematic of reductive desorption b) Example CV for bare Au substrate, unblocked COOH-SAM, and blocked COOH-SAM c) CV of unblocked COOH-SAM before and after 1 week storage in ambient conditions d) CV of blocked COOH-SAM before and after 1 week storage in ambient conditions.

5.3.2 Affinity Biosensing after Ambient Storage

While it has previously been shown that oxidation decreases the sensing reliability of a COOH-SAM,²⁴² this result is confirmed through attempted detection of Hp with SPR. Additionally, we compare the sensing results of the oxidized, unblocked COOH-SAM to

both a blocked and fresh COOH-SAM. To compare SPR biosensing on aged COOH-SAMs to a fresh COOH-SAM, preblocking functionalization was used. An example sensorgram of this process is seen in Figure 5.8a, where the preblocker (gelatin, 1% in PBS) is first introduced to the sensor in two 600 s injections, followed by a 900 s wash with PBS. After, the standard amine functionalization is completed, and ETA is used to block leftover activated carboxylic acid groups. Bound receptor is determined by the RU change after flowing aHp, and is summarized in Figure 5.8b. There is a significant reduction in receptor attachment for the unblocked COOH-SAM, indicating degradation of the sensing surface. Post-functionalization drift was also determined by the baseline drift over a 5-min period in PBS after the functionalization procedure was completed (Figure 5.8c). Here, the unblocked SAM shows significantly higher drift than the other 2 sensor types. Since oxidized COOH-SAM is no longer chemisorbed to the sensor, this drift is likely caused by the washing of improperly attached COOH-SAM, receptor, or blocker from the surface.

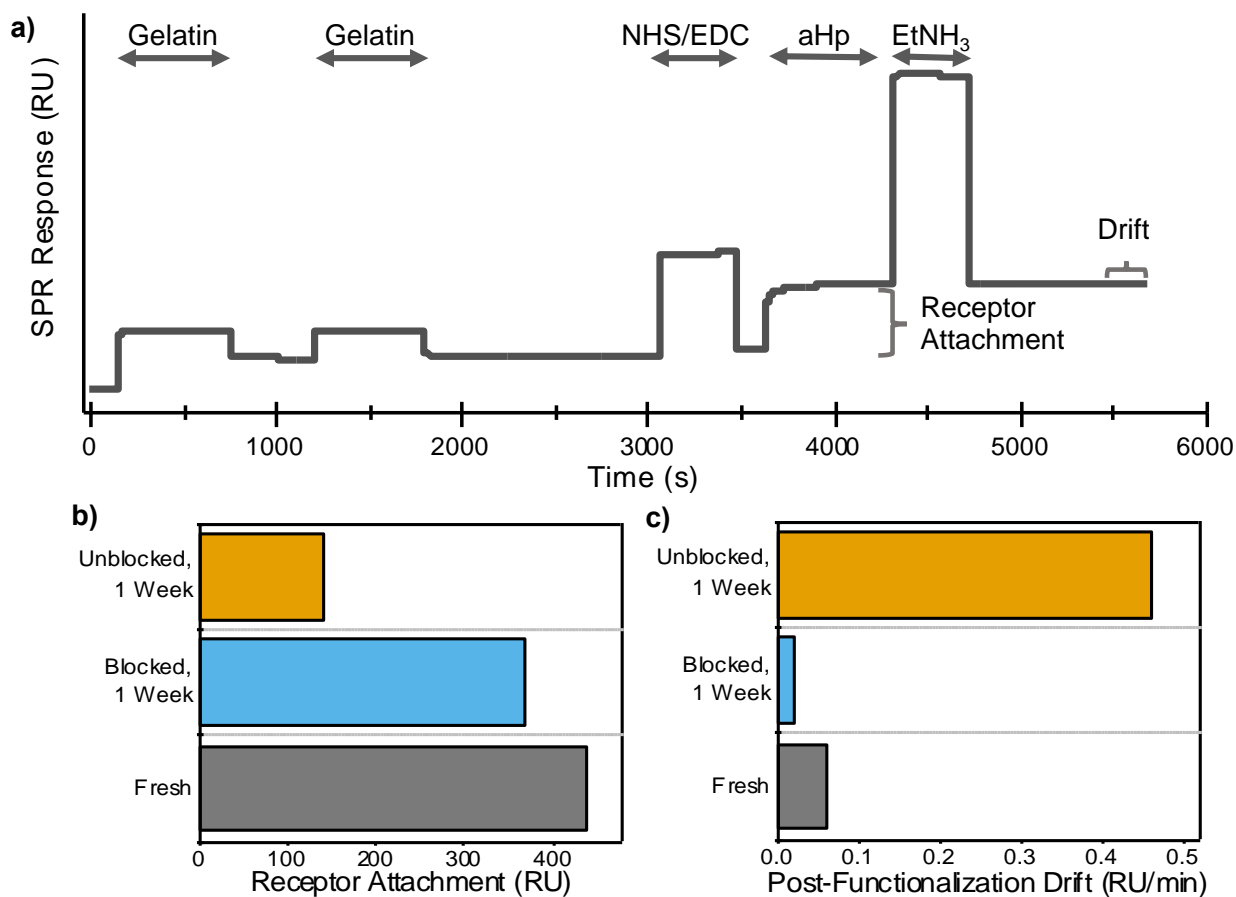
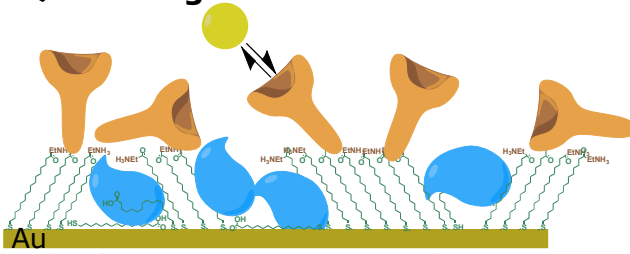


Figure 5.8 – Functionalization parameters for COOH-SAM samples. a) Example functionalization SPR sensorgram with preblocking steps (vertical step changes are due to solution refractive index). b) degree of functionalization on each sample type c) post-functionalization drift of each sample type.

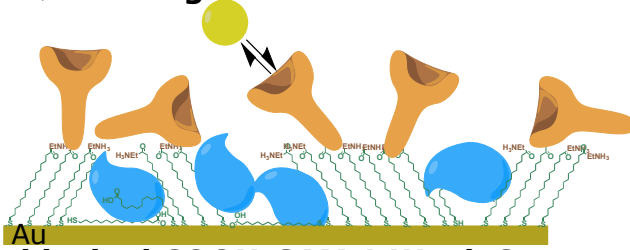
The functionalized fresh, blocked, and unblocked COOH-SAM sensor surfaces are shown schematically in Figure 5.9a. To test Hp sensing, the aHp-functionalized surfaces were introduced to a series of six Hp concentrations (including 0 $\mu\text{g/mL}$) and binding was observed via SPR. The saturated sensor response of each Hp concentration, measured in PBS to exclude solution refractive index effects,²⁵⁵ is shown in Figure 5.9b. For fresh

COOH-SAM, the sensor response follows a Langmuir isotherm, as expected. Langmuir fitting results in a dissociation constant (K_D) value of $10.3 \pm 0.98 \mu\text{g/mL}$ (approximately $6.9 \times 10^{-8} \text{ M}$), which is within the expected affinity range for a commercial IgG antibody.²⁵⁶ The blocked COOH-SAM showed a similar response, with the measured K_D of $11.0 \pm 1.0 \mu\text{g/mL}$, equivalent within error to the fresh COOH-SAM. This result aligns with the lack of oxidation observed for blocked COOH-SAM via XPS and reductive desorption, and confirms that one week of storage in ambient conditions does not negatively affect the sensing outcomes of this sample. However, as expected, the unblocked COOH-SAM, after 1 week storage in ambient conditions, showed completely different binding behavior. The Hp concentration response was approximately linear with respect to target concentration, with a fit K_D value of $311 \pm 111 \mu\text{g/mL}$. This large dissociation constant, indicating extremely low affinity of the Hp with the sensor surface, is inconsistent with an antibody-antigen interaction.²⁵⁷ The apparent linear concentration response is much more likely the result of non-selective interactions of the Hp with the sensor.²⁵⁸ This lack of Hp sensitivity, as well as the functionalization level, post-functionalization drift (Figure 5.8b,c) and unnormalized target response (Figure 5.9b, inset) highlight the lack of stability and sensitivity of the aged device. Together, these results indicate that an unblocked COOH-SAM kept as little as a week in ambient conditions loses all functionality as a biosensing surface.

a) Fresh COOH-SAM
→Blocking and Functionalization



Blocked COOH-SAM, 1 Week Storage
→Blocking and Functionalization



Unblocked COOH-SAM, 1 Week Storage
→Blocking and Functionalization

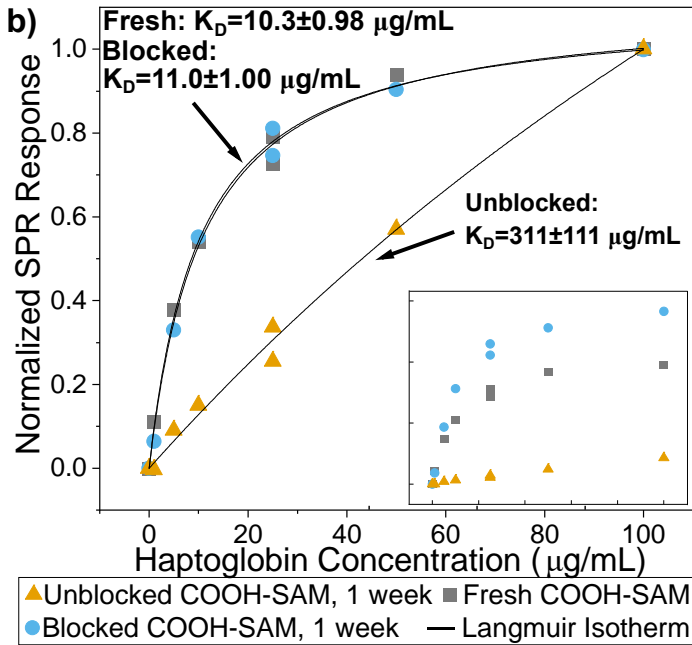
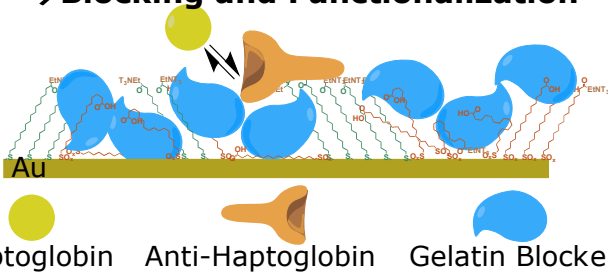


Figure 5.9 – Label-free detection of Hp via SPR with COOH-SAM aHp functionalized sensor. a) schematic representation of functionalized surfaces b) SPR response for each sensor type with Langmuir isotherm fitting. Inset: unnormalized response.

5.3.3 Comparison to Inert Atmosphere Storage

Although storage in ambient conditions does not require any special processing or packaging, other methods can be utilized to minimize degradation due to oxidation. An obvious choice would be the storage of COOH-SAMs in inert gas such as N₂. To compare blocking to N₂ storage, unblocked COOH-SAMs were transferred into a glovebox with O₂ and H₂O both <1ppm, sealed into a clear plastic box with electrical tape, and left inside the glovebox for 2 months. Simultaneously, unblocked and blocked COOH-SAMs were left on the bench in ambient conditions. Figure 5.10a shows CV curves for each sample type after 2 months. As expected, the unblocked COOH-SAM shows significant chemical and structural degradation while the blocked and N₂ COOH-SAMs remain relatively unchanged. It is worth highlighting that, even over the course of 2 months, a blocked COOH-SAM in ambient conditions appears unchanged as measured by RD. Inhibition of oxidation by protein blocking performed as well as an inert atmosphere. Similarly, S oxidation measured by XPS shows significant oxidation of the unblocked COOH-SAM, but only slight increases are observed for both the blocked and N₂ COOH-SAMs when compared to a fresh COOH-SAM (Figure 5.10b). As in Figure 5.5, the average and standard deviation is presented for 5 data points of each sample type (3 samples, 1-2 data points each). It is worth noting the large standard deviation for the N₂ sample; essentially, the N₂-stored COOH-SAM shows oxidation on some, but not all, of the spots surveyed.

Figure 5.10c,d highlights the S 2p traces that correspond to the highest and lowest oxidation values for each sample type, respectively. While both the N₂ and blocked samples had no apparent oxidation on some spots surveyed, the maximum amount of observed oxidation was much higher for the N₂ sample. Since oxidation occurs quickly at highly defective sites, even in a mostly inert atmosphere, defective areas will degrade given a long enough time. In this way, a gelatin blocked COOH-SAM stored in ambient conditions can outperform harder-to-implement storage procedures such as packaging in <1ppm O₂ and H₂O.

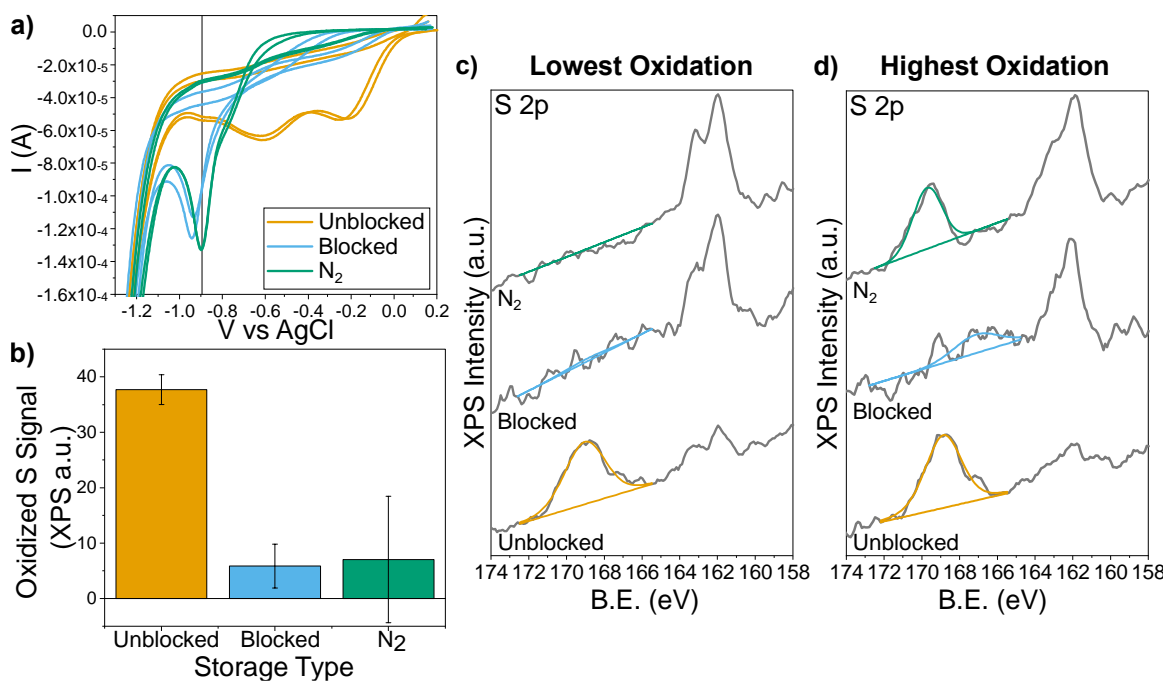


Figure 5.10 – Comparison of COOH-SAM degradation after 2 months storage in ambient and inert (N₂) conditions. a) CV curves for COOH-SAMs b) oxidized S XPS signal for COOH-SAMs. c) XPS S 2p scans with smallest oxidized S signal for each sample type d) XPS S 2p scans with largest oxidized S signal for each sample type.

5.4 Conclusions

Sensor shelf life is a critical consideration for the realization of portable, point-of-care affinity biosensors. While COOH-SAMs have been utilized for the development of label-free sensors across many sensing modalities, little attention has been paid to their shelf life, and therefore their amenability to practical storage conditions. A 16-C COOH-SAM stored in ambient conditions shows significant oxidation in as little as 1 day, and is unusable as a biosensor after 1 week. However, since oxidation begins at defect sites, physical protein blocking serves as an oxidation inhibitor. Unlike an unblocked COOH-SAM, a gelatin-blocked COOH-SAM does not show measurable oxidation via XPS nor RD after 21 days. The blocked COOH-SAM is still a reliable sensor after 1 week, and even outperforms storage in an inert N₂ environment. Moreover, due to the amphiphilic properties of a COOH-SAM, a blocking protein will adsorb selectively to hydrophobic defect sites, leaving hydrophilic COOH-functional groups uncovered. As compared to traditional postblocking, blocking before receptor functionalization protects the COOH-SAM during storage in ambient conditions, but does not limit the flexibility and specificity of the functional layer when used for sensing at a later date. This simple method of protein preblocking allows these sensors to be viable point-of-care devices.

CHAPTER 6. SUBSTRATE MODIFICATION OF GRAPHENE- PROTEIN INTERACTIONS^C

CHAPTER 6 describes how graphene-protein interactions can be influenced by the substrate used to support the atomically thin graphene layer. A brief overview of what is known about graphene-protein interactions, as well as gaps in the existing literature, is described in section 6.1. Section 6.2 details the methods used to investigate protein adhesion to graphene, where the interactions between model small (Lysozyme), medium (Bovine Serum Albumin), and large (Fibrinogen) proteins with monolayer graphene on support substrates of varying hydrophobicity and surface polarity are studied. Ex situ adsorption is measured via ellipsometry. For Au and Si support substrates, in situ adhesion of Lysozyme is measured via quartz crystal microbalance. The results, discussed in section 6.3 indicate that not only the equilibrium attachment, but also the kinetics of interaction, can be affected by the substrate. Overall, a more hydrophobic substrate leads to a larger amount of adsorption to graphene. Moreover, the effect is only observed with monolayer graphene, where no substrate effect is observed with the addition of a second graphene layer. This work indicates that the substrate of a graphene-based biosensor is an important but currently overlooked parameter when understanding and optimizing the performance

^C Adapted with permission from E L Brightbill, K T Young, H F Gezahagne, D S Jin, and E M Vogel. Protein interactions with chemical vapor deposited graphene modified by substrate. *2D Materials* 2021, **8**(2), 025015. Copyright 2021 IOP Publishing Ltd.

of the device. As summarized in section 6.4, the level of non-selective protein adsorption on graphene can be independently engineered through modifying the support substrate without directly modifying the graphene itself.

6.1 Introduction

Due to the range of potential biomedical applications for graphene,^{60, 62, 182-190, 259} understanding the interactions between biomolecules and 2D materials is of high importance.¹⁸² As such, a variety of previous studies offer insight into how biomolecules interact with and adhere to 2D materials. The adsorption of deoxyribonucleic acid (DNA) on graphene has been shown to increase its biostability relative to DNA dispersed in solution.¹⁹³ The DNA-graphene interaction effectively prevents enzymatic cleavage of the DNA by DNase I, but is still weak enough to allow pairing with a complementary strand.¹⁹³ Theoretical and experimental work has shown that proteins can unfold in order to maximize their interaction with graphene, thus denaturing and losing biological activity for sensing.^{120, 192} Hydrophobic, π - π electron interactions, hydrogen bonding, and charge interactions have been used to self-assemble graphene/protein composite materials.¹⁹¹ While studies such as these provide valuable insight into how biomolecules interact with 2D materials, they focus on isolated protein-2D material interactions, generally with both components dispersed in a solvent. Biosensing applications, however, usually require the 2D material, most commonly graphene,^{185, 194-196} to be deposited on a support substrate. Since monolayer graphene is only a single atom thick, protein-graphene interactions may be influenced by the support substrate.

Indeed, it has been shown that the substrate underneath a graphene monolayer can affect the water contact angle of the graphene.²¹⁸ While reports conflict on the degree of wetting transparency, the majority of reports indicate that the substrate's wetting properties at least partially transmit through a graphene monolayer.²¹⁴⁻²¹⁹ A substrate's effect on graphene's hydrophobicity is likely to have a subsequent effect on protein adsorption. It is commonly shown that proteins have a stronger affinity for hydrophobic surfaces than hydrophilic ones.^{79, 119, 220, 221} This increased adsorption can be explained by both the favorable entropic loss of structured water at the substrate and protein surfaces when attachment occurs, as well as a favorable increase in the adsorbing protein's conformational entropy if partial unfolding occurs.^{79, 118, 222} Modification of graphene's contact angle by the substrate therefore suggests that the substrate can modify the affinity of graphene-protein interactions. Indeed, one previous study shows this to be the case, where agglomerations of avidin molecules are observed on graphene when the substrate is modified to be hydrophobic.²²³ This previous study focused on only one biomolecule (avidin) and used small exfoliated graphene flakes. However, for practical sensor applications, large-area chemical vapor deposited (CVD) graphene is required for device fabrication.¹⁸³ It is important to determine whether this finding can be generalized to a wider range of biomolecules and to CVD graphene, where material processing and defects differ. Specifically, CVD graphene is generally transferred from the Cu growth substrate for device fabrication via a poly(methyl methacrylate) (PMMA) scaffold. However, the

PMMA scaffold leaves behind trace residue on the graphene surface, which may impact protein adhesion.²⁶⁰⁻²⁶²

In addition to substrate hydrophobicity, substrate surface polarity may also be important to determine protein adhesion properties to graphene. Kong et al. showed that the polarity of the substrate determines whether or not epitaxial growth is successful across a graphene intermediating layer.²⁶³ More specifically, epitaxial growth on polar GaN was shown to be successful despite the presence of a graphene layer, while epitaxial growth of non-polar Si was not.²⁶³ This indicates that the potential fields of non-polar materials can be screened by a graphene monolayer, while the potential field of an ionic-bonded, polar material generally has the ability to penetrate through a graphene layer. Similarly, substrate polarity may influence the degree to which substrate-protein interactions are able to permeate through the graphene where substrates with larger bond polarity have a larger effect on protein adhesion.

This collection of literature indicates that, while it is generally accepted that substrates can affect properties of a graphene surface, substrate-graphene-solution interactions are largely overlooked. Understanding the impact of substrate contact angle and polarity on graphene-protein interactions is crucial for engineering graphene-based biosensors.

6.2 Experimental Methods

6.2.1 Chemicals and Substrate Cleaning

Phosphate Buffered Saline pellets (PBS), Bovine Serum Albumin (BSA), Fibrinogen, and Lysozyme were purchased from Sigma-Aldrich (St. Louis, MO). Au and Si QCM-D sensors (Q Sensors) were purchased from Biolin Scientific (Gothenburg, Sweden). Si substrates (wafer) were cleaned immediately before use with a 1-min dip in buffered oxide etch to remove native oxide followed by DI rinse. SiO₂ substrates were formed by thermal growth of 280 nm oxide on Si and cleaned immediately before use with an acetone/methanol/isopropyl rinse, dried with N₂, followed by a two-minute O₂/Plasma treatment (200 mTorr, 50 W RF, 25 sccm O₂). 100 nm thick Au surfaces were e-beam evaporated on a substrate consisting of 280 nm of SiO₂ on silicon with a 10 nm W adhesion layer and cleaned as SiO₂. Approximately 280 nm TaN was deposited on Silicon via RF Sputtering of a Ta target (30 min, 5mTorr, 10 sccm Ar, 10 sccm N₂). XPS revealed approximately 10% O content in the TaN film that could not be decreased with deposition parameter optimization. Protein attachment for ellipsometry and XPS measurements was completed by incubating the substrate in a solution of 1% protein in PBS for 1 hour.

6.2.2 X-ray Photoelectron Spectroscopy

Measurements were conducted using a K-Alpha X-ray Photoelectron Spectrometer System (Thermo Scientific, Waltham, MA) with a monochromatic Al K α source (KE = 1486.6 eV), a 180° double focusing hemispherical analyzer, and a 128-channel detector. Spectra were acquired at a pass energy of 50 eV and a spot size of 400 μ m. Au 4f spectra were fit with 2 peaks (spin-orbit splitting of 3.7 eV, 3:4 area ratio). Si 2p spectra were fit with 2 peaks (spin-orbit splitting of 0.63 eV, 1:2 area ratio). Ta 4f spectra were fit with 2

peaks (spin-orbit splitting of 1.92 eV, 3:4 area ratio). N 1s spectra were fit with one peak. C 1s spectra were fit with 5 peaks corresponding graphene and PMMA.^{264, 265} The full-width-half-maximum (FWHM) of all peaks pertaining to one element were constrained to match; a variable Lorenz-Gauss ratio and Shirley-type background were used for all spectra.

6.2.3 Graphene Synthesis and Transfer

Fully coalesced graphene was synthesized via Chemical Vapor Deposition (CVD) on polycrystalline Cu foil for 30 min at 1000°C and 250 mTorr, with CH₄ and H₂ flow rates of 50:15 sccm, respectively. The Cu foil was heavily oxidized before synthesis and enclosed in a physical “pocket” during synthesis resulting in high-quality graphene as previously described.²⁶⁶ Graphene was transferred onto various substrates using a wet transfer process and PMMA scaffold.²⁶⁷ After the removal of PMMA with acetone, the sample was further annealed at 400°C for 1 hour at 2 Torr with N₂ circulating through the furnace to remove any remaining PMMA residue. Raman spectroscopy was performed on samples transferred to SiO₂ using a Renishaw Qontor Dispersive Raman Spectrometer at a wavelength of 488 nm.

6.2.4 Ellipsometry

A Woollam M2000 Ellipsometer was used for all measurements, and CompleteEASE software (J.A. Woollam, Lincoln, NE) was used for all spectra fitting. Software point selection was used to measure the same points on the sample before and after protein solution incubation. CompleteEASE materials database provided Si, TaN, Au,

and Graphite substrate starting properties. Separate layers for native and thermal SiO₂ were added to applicable samples. Graphene was approximated with a B-Spline layer with a thickness of 3.4 Å (6.8 Å for bilayer samples).²⁶⁸ Cauchy layers with a refractive index of 1.45 were used to approximate protein thickness.¹¹⁹ 6 points on each of 3 samples for each sample type were measured, with the exception of graphite, where 12 points on one sample were measured.

6.2.5 Contact Angle

A Ramé-hart Model 250 goniometer was used for contact angle measurements. 0.6 µL drops of DI water were placed on the leveled substrate surface, and the resulting static contact angles were measured by the drop tangent in the Ramé-hart software. Reported values are the average of 3 measurements.

6.2.6 Quartz Crystal Microbalance with Dissipation

A Q-Sense E4 Quartz Crystal Microbalance with Dissipation (Biolin Scientific, Gothenburg, Sweden) at 22° C was used for QCM-D measurements. Si and Au QSensor cleaning methods were the same as those for ellipsometry. A constant flow rate of 75 µL/min was used for all experiments. Frequency and dissipation were measured for each sensor at overtones 1-13. Mass adsorbed to the surface decreases the resonant frequency of the sensor, and the Sauerbrey equation (Equation 9) allows the frequency change (Δf) to be directly converted to mass change (Δm). This relationship is generally accurate when the adsorbed mass is rigid.^{269, 270} C is a constant that depends on the resonant frequency of

the fundamental mode, the piezoelectrically active crystal area, quartz density, and quartz shear modulus; n is the measured overtone.

$$\Delta m = -\frac{C\Delta f}{n} \quad \text{Equation 9}$$

The dissipation, or energy loss in the protein layer, can indicate whether or not using the Sauerbrey approximation is accurate, as well as indicate structural changes in the adsorbed protein layer. Dissipation (D , Equation 10) is described by the ratio of lost (E_{lost}) and stored (E_{stored}) energy. Due to low dissipation, the Sauerbrey approximation is used for all presented QCM-D analysis, allowing the frequency change to be used as a directly proportional analogue for mass change.

$$D = \frac{E_{lost}}{2\pi E_{stored}} \quad \text{Equation 10}$$

6.3 Results

6.3.1 Graphene Transfer and Model System Properties

PMMA scaffolding currently remains the most reliable and commonly used method of graphene transfer, and thus results using this transfer process have the most applicability to current graphene biosensor work. As such, graphene was transferred onto each of the selected substrates via the PMMA process. However, it is well known that this process leaves behind PMMA residue, and since protein interaction with graphene may be impacted by this residue, it is crucial to remove it to the extent possible. Residue removal can be observed via XPS. In Figure 6.2a, peaks corresponding to PMMA can be seen in the C1s spectra even after attempted removal with acetone. However, in Figure 6.2b, those

PMMA peaks are eliminated after anneal, with area comparison indicating that contamination is reduced by 95% compared to pre-anneal graphene. This can also be seen in in Figure 6.2c: after the vacuum anneal process, XPS scans show nearly complete elimination of any non-graphene C 1s signal, with the disappearance of the higher BE peaks as compared to the transferred sample and only a small increase in peak width as compared to as-grown graphene or graphite. This broadening corresponds to an approximately 7% peak area increase, and indicates a trace amount of carbonaceous material (much less than one monolayer) remaining on the surface. This result parallels previous studies that show it is extremely difficult to completely remove all PMMA residue (or, more specifically, carbonaceous residue left from the breakdown of PMMA during annealing). With current methods used in graphene biosensor literature, residue has been eliminated to the extent possible without damaging the graphene.^{60, 259, 260} Thus, our results can be applied directly to graphene biosensors fabricated in this manner. Moreover, the conclusion drawn from the ex situ attachment results (Figure 6.5, Figure 6.6, Figure 6.7) is unchanged even if there happens to be a trace amount of residue remaining on the graphene: protein attachment is driven primarily by the properties of the underlying substrate.

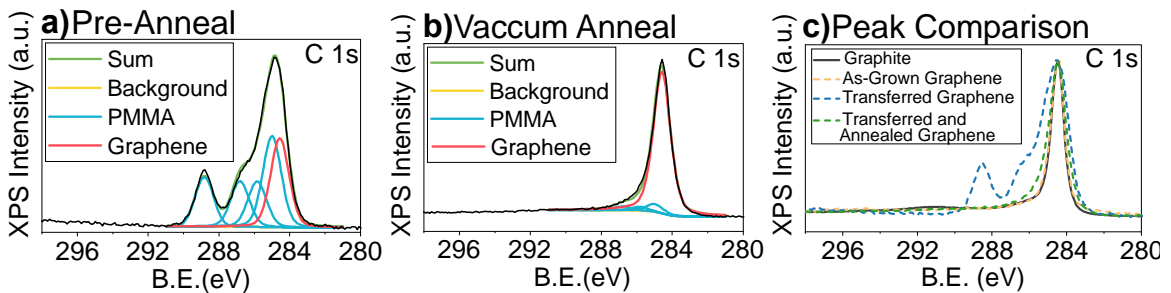


Figure 6.1 – C1s XPS spectra. PMMA fitting before (a) and after (b) post-transfer anneal. c) comparison of C 1s scans of freshly cleaved graphite, as-grown graphene, transferred graphene, and graphene after the transfer and cleaning process.

Raman maps were used to show the graphene layer was continuous with minimum defects across 300 μm x 400 μm scan areas. A representative Raman spectrum of the transferred graphene before and after anneal is shown in Figure 6.2. The Raman spectra after transfer and after anneal both show the representative graphene peaks. The D peak, which indicates defects in the graphene sheet, does not show any significant change after anneal.²⁷¹

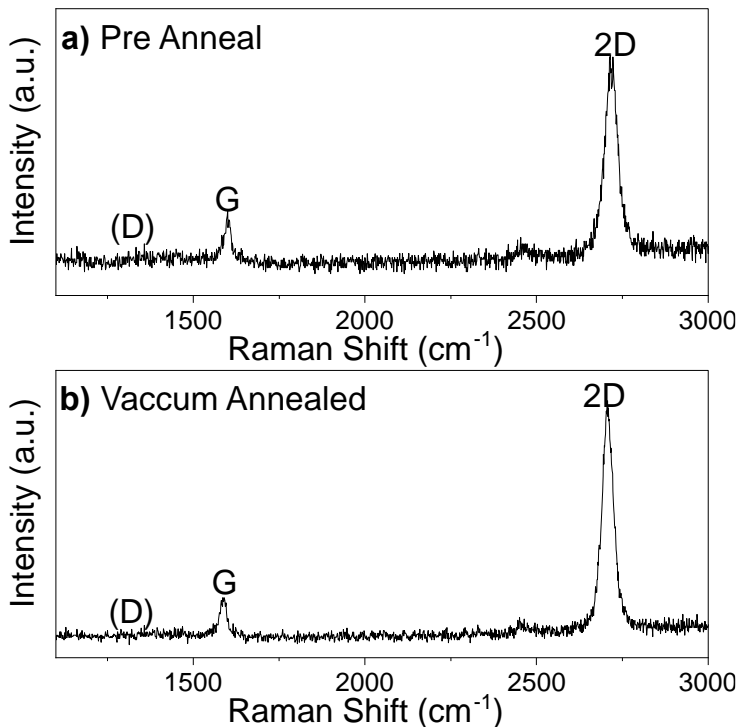


Figure 6.2 – Example Raman of transferred CVD graphene before (a) and after (b) post-transfer anneal.

In order to understand the effect of substrate polarity and hydrophobicity on protein attachment to graphene, substrate materials must be carefully considered. Ideal substrates are those that exhibit differences in both hydrophobicity and polarity^{214, 217, 218, 263} and are amenable to the annealing processes typically used to clean the graphene following transfer. Materials selected based on these criteria are outlined in Table 6.1. SiO₂ and TaN have similar bond polarity, but different water contact angles. Similarly, Si and Au both have zero bond polarity, but different water contact angles. To help ensure applicability of these results to a wide range of proteins, non-specific adsorption (NSA) was measured with three model proteins of very different size, structure and stability: Lysozyme, Bovine Serum Albumin (BSA), and Fibrinogen. Lysozyme (14.4 kDa) is a small protein that is considered to have a high internal stability, indicating that it does not generally denature upon surface adsorption.²⁷² BSA (66.4 kDa) is a moderately sized protein that has a low internal stability, often partially denaturing to maximize interactions with a surface.²⁷² In fact, BSA is commonly known as a “sticky” protein that adsorbs to most surfaces.¹¹⁹ Finally, Fibrinogen (340 kDa) is a large, flexible glycoprotein complex with a variety of hydrophobic and hydrophilic surface areas.²⁷³

Table 6.1 – Parameters of selected graphene substrates.

<i>Substrate Material</i>	<i>Bond Polarity^a</i>	<i>Hydrogen Bonding</i>	<i>DI H₂O Contact Angle^b</i>
SiO₂	1.54	Yes	21°-60°

Si	0	No	32°-80°
Au	0	No	60°-90°
TaN	1.54	Yes	90°-120°

^aBond polarity calculated from element electronegativity ²⁷⁴

^bContact angle range from literature ^{214, 218, 275-278}

Since there is a large degree of variability in contact angle reported in the literature, as well as disagreement over the degree of graphene wetting transparency,^{214, 217, 218} the experimental contact angles for each substrate with and without a transferred graphene layer are shown in Figure 6.3. The clean substrate values correspond to measurements taken quickly after the cleaning methods described, while the graphene measurements were completed after the PMMA removal anneal. All substrate contact angles fall within values reported in literature.^{275, 276, 279} For the substrates selected here, wetting transparency is observed, where the contact angle measured on graphene is strongly influenced by the contact angle of the underlying substrate.^{214, 218} Since the contact angle of the graphene layer changes with substrate, it is expected that protein adhesion will be impacted as well.

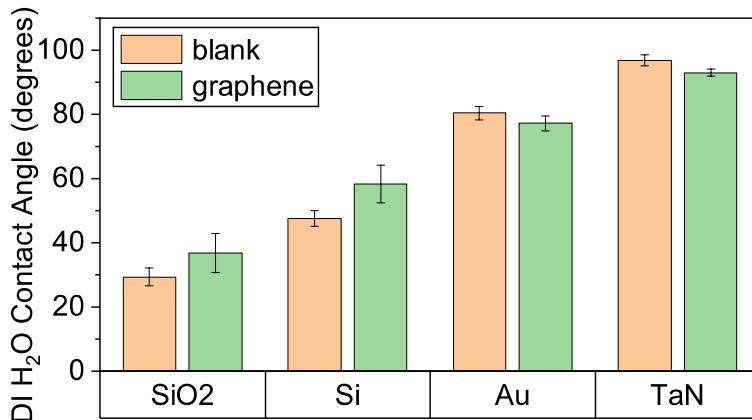


Figure 6.3— DI H₂O contact angles on the prepared substrates with and without a transferred graphene monolayer.

6.3.2 *Ex Situ Protein Adsorption*

In order to assess protein adsorption, unmodified and graphene-coated substrates were analyzed via ellipsometry before and after a 1-hour incubation in a 1% solution of each protein in PBS. During protein attachment, potentials applied to the substrate can alter protein adhesion. However, it is common procedure for a graphene biosensor to be left floating during protein attachment. In order to ascertain if sample electrostatic charge has a measurable effect on protein adsorption, BSA attachment was measured on both Au and Au/Graphene while grounded to a reference electrode and compared to floating samples (Figure 6.4). There was not an observed difference between BSA attachment to Au and Au/Graphene when the substrate was ungrounded in solution vs grounded to a reference electrode (Figure 6.4c). Thus, samples in all following experiments were left ungrounded during incubation.

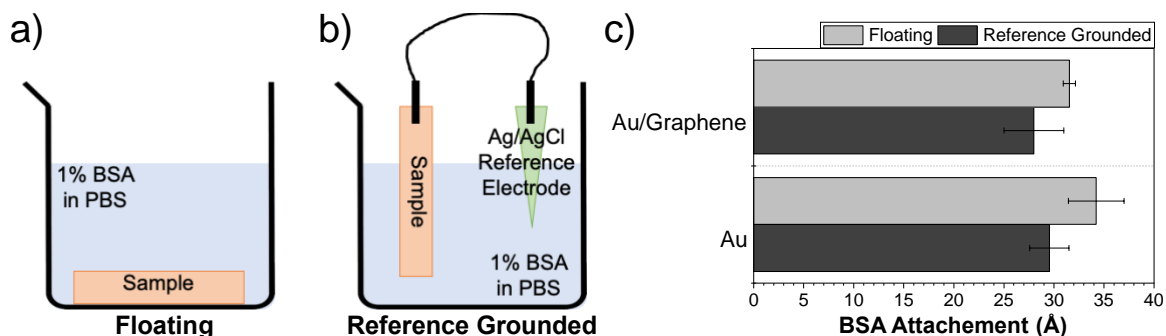


Figure 6.4 – Comparison of BSA attachment on Au and Au with graphene with and without grounding of the substrate during protein adhesion. a) schematic of floating BSA adsorption b) schematic of reference-grounded BSA adsorption c) thickness of BSA layer attachment as measured by ellipsometry.

The measured protein attachment on graphene supported by each selected substrate is summarized in Figure 6.5. Control samples were measured before and after a 1-hour incubation in PBS with no added protein. All control samples showed less than 0.6 nm of signal both before and after incubation, indicating that the measured levels of protein attachment are well above background noise. Additionally, in almost all cases, the level of attachment of a certain protein on a certain substrate is the same regardless of the presence of graphene. This result indicates that the substrate has a profound effect on protein attachment to graphene, to the extent that the properties of graphene itself are largely negligible. Moreover, these results indicate that, similarly to DI wetting behavior on supported graphene, any trace residue from the graphene transfer process does not have a significant effect on protein adsorption, since the graphene adhesion data so closely follows that of the bare substrates.²¹⁸

Protein selection also impacts the degree of observed adsorption. The largest model protein, Fibrinogen, shows a similar level of attachment across all 4 substrates with and without the presence of graphene (Figure 6.5a). Fibrinogen has a wide variety of surface groups²⁸⁰ and can interact with surfaces of varying hydrophilicity.²⁸¹ It has previously been shown that changes in surface charge and hydrophilicity of polyelectrolyte complex surfaces had little effect on equilibrium levels of Fibrinogen adsorption, and minimal differences in Fibrinogen affinity was observed between model hydrophilic (OH) and Hydrophobic (CH₃) self-assembled monolayer surfaces.^{79, 282} Similarly, here, it appears that the studied variation of substrate hydrophilicity and polarity has little effect on adsorption. For Fibrinogen, control of substrate does not have a significant effect of protein adsorption in the range of materials studied.

Lysozyme, the smallest model protein at only 14.4 kDa, shows a difference in adsorption when a graphene monolayer is added to some substrates (Figure 6.5b). More specifically, while the degree of Lysozyme adsorption is approximately the same on the two polar substrates (SiO₂, TaN) regardless of the presence of graphene, the same is not true for the nonpolar substrates (Si, Au). In the latter case, the more hydrophilic substrate appears to show a slight increase in Lysozyme adsorption while the more hydrophobic substrate shows a significant decrease with the presence of graphene. Lysozyme is a small, “hard” protein with high internal stability²⁸³. Since Lysozyme has been shown to largely maintain its native structure even upon adsorption to hydrophobic surfaces,^{117, 284, 285} it is possible that the specific interactions between Lysozyme surface groups and the substrate

surface, rather than the hydrophobic effect, has a significant effect on the degree of adsorption. Therefore, changing the surface atoms through the addition of a graphene layer could have a significant effect. While more work is necessary to determine precisely how this protein adsorption proceeds, Lysozyme shows evidence that the adsorption is not solely determined by the substrate in all systems.

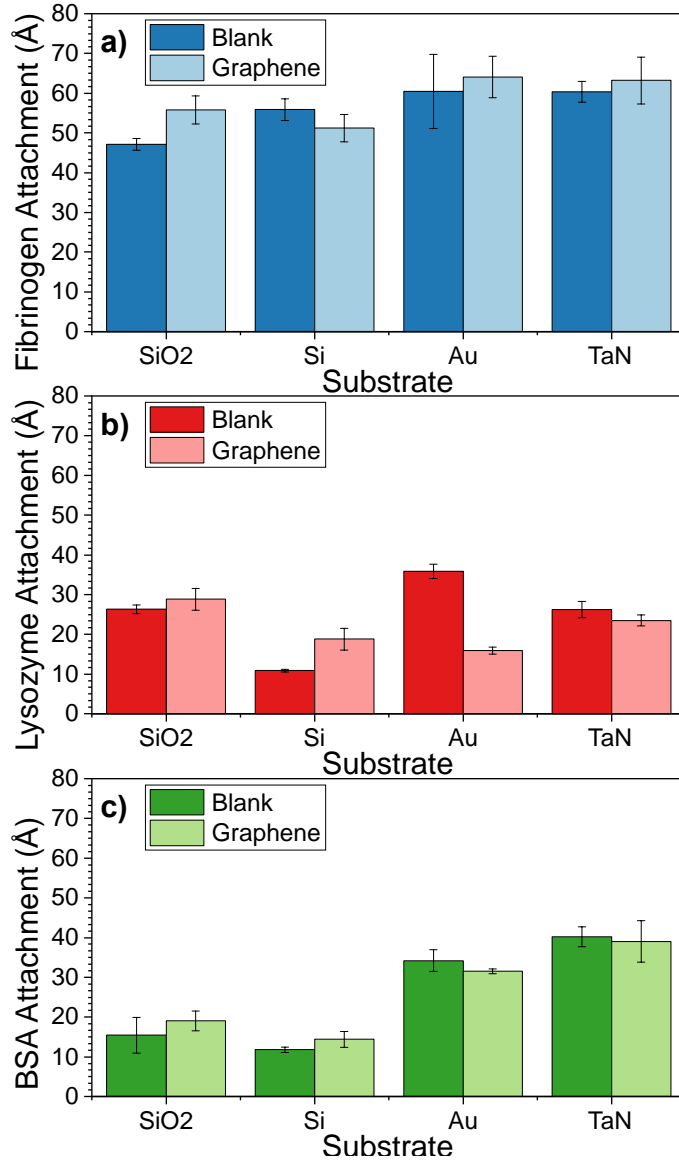


Figure 6.5 – Summary of protein surface layer thickness by ex situ ellipsometry. Fibrinogen (a), Lysozyme (b), and BSA (c), attachment to SiO₂, Si, Au, and TaN substrates with and without a transferred graphene monolayer.

The adsorption of BSA, the intermediate size protein, does not change significantly with the addition of a graphene layer (Figure 6.5c). However, the amount of adsorbed BSA does change with contact angle. As observed in Figure 6.6, there is a general positive trend between measured contact angle and amount of BSA attached. It has previously been shown that the degree of BSA surface adsorption is related to surface hydrophobicity due to entropic stabilization from the hydrophobic effect, and these results indicate that the addition of a graphene monolayer minimally effects this interaction.²²⁰ As a result, the amount of albumin protein adsorption to graphene-based sensors can be maximized or minimized by choosing a support substrate with the proper hydrophilicity.

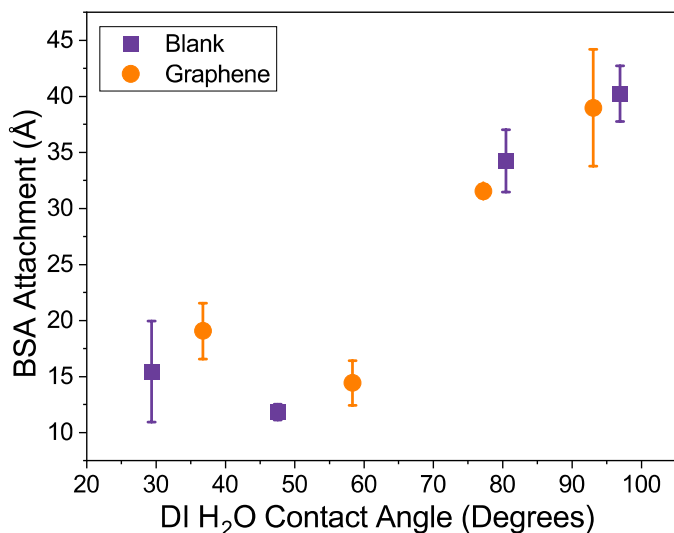


Figure 6.6 – BSA attachment vs measured substrate contact angle. A general positive correlation is seen regardless of the presence of graphene

Since proteins are composed of approximately 16% N, the XPS N 1s signal on N-free substrates can be used to estimate levels of protein adsorption. In the case of TaN, since a large N background was present, the smaller S 2p protein signal was used. As summarized in Figure 6.8, the XPS results provide an independent validation of the ellipsometry data (Figure 6.5) that indicate the degree of protein adsorption to a specific substrate is approximately the same regardless of the presence of graphene. It is important to note that, unlike ellipsometry, results for different proteins and substrates cannot be directly compared to one another since each spectrum is normalized to the substrate background, there is no common reference, and each protein has a different atomic percentage of N and S.

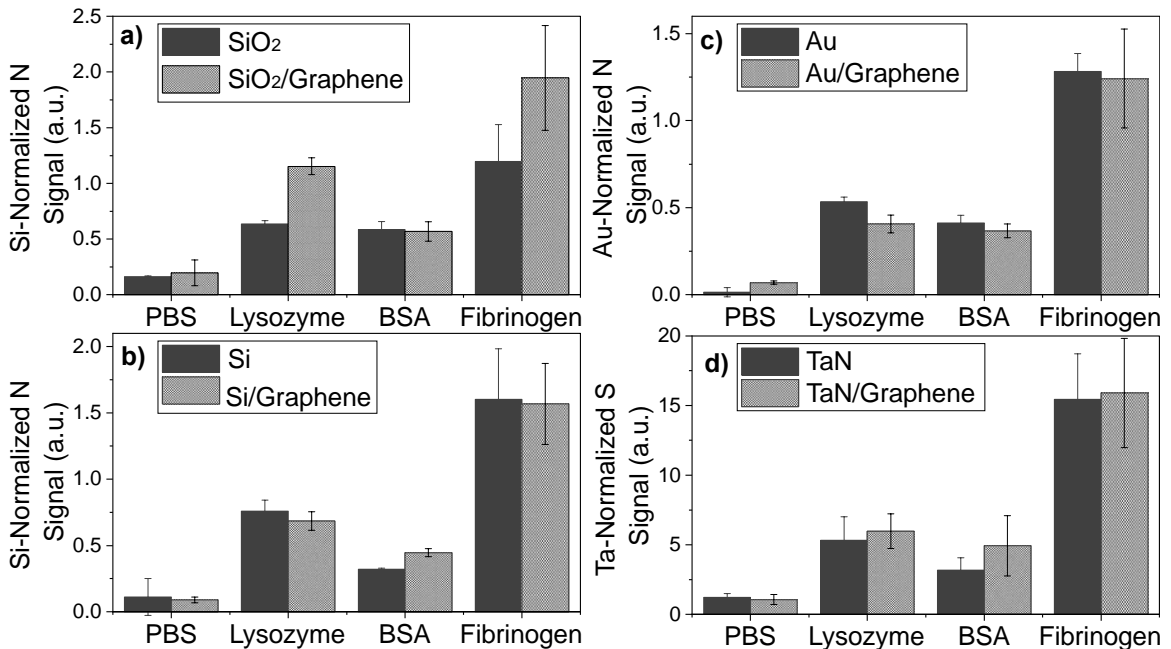


Figure 6.7 – XPS using normalized N 1s or S 2p signal as an indication of protein adsorption levels. Lysozyme, BSA, and Fibrinogen attachment to SiO₂ (a), Si (b), Au (c) and TaN (d) substrates with and without a transferred graphene monolayer.

Since the substrate is expected to influence protein adsorption on graphene due to the atomically thin nature of graphene, a reasonable assumption is that the effect will disappear as additional graphene layers are added to the substrate. Indeed, in Figure 6.8, this is shown to be the case. Although a single layer of graphene on Au results in BSA attachment nearly identical to the Au substrate alone, the addition of a second graphene layer decreases the observed BSA adsorption to the level observed on graphite. This result parallels previous work on substrate influence on graphene's contact angle, where the addition of a second layer of graphene reduced the wetting transparency.²¹⁸ This result also agrees with previous work on the epitaxial growth of materials through graphene, which indicated that potential field fluctuations from non-polar substrates penetrate through a maximum of 1 layer of graphene.²⁶³ Additionally, since each graphene layer was transferred independently, there may be compounding effects that minimize the substrate influence. First, the misalignment of the graphene layers will affect the graphene's electronic properties, and may therefore effect the ability of the substrate to influence graphene.²⁸⁶ Secondly, although the samples were annealed after each transfer, the compounded effect of carbonaceous contamination from the transfer process may quicken the loss of substrate influence.²⁶⁰

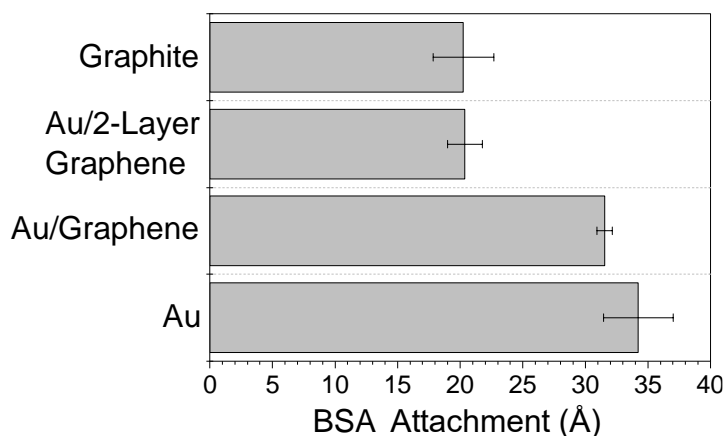


Figure 6.8 – Comparison of BSA attachment on Au/Graphene to Graphite

6.3.3 *In Situ Protein Adsorption*

While ellipsometry can measure *ex situ* protein adsorption, information on protein adsorption kinetics and adsorption reversibility are also valuable in sensor design. To give a more detailed, *in situ* picture of adsorption, quartz crystal microbalance with dissipation (QCM-D) can be used.²⁸⁷ Figure 6.9 shows frequency and dissipation curves for the 5th overtone of the QCM-D measurement for the attachment of Lysozyme to both Au and Si with and without graphene. These samples were selected because, as observed in Figure 6.5, Lysozyme attachment on these surfaces measured by ellipsometry differed when graphene was present. The small changes in dissipation upon protein adsorption (Figure 6.9b,d) indicate that it is reasonable to use the Sauerbrey equation in this context.^{269, 270} However, since steady state is not achieved in all cases, kinetic modelling is necessary to compare equilibrium protein attachment levels.

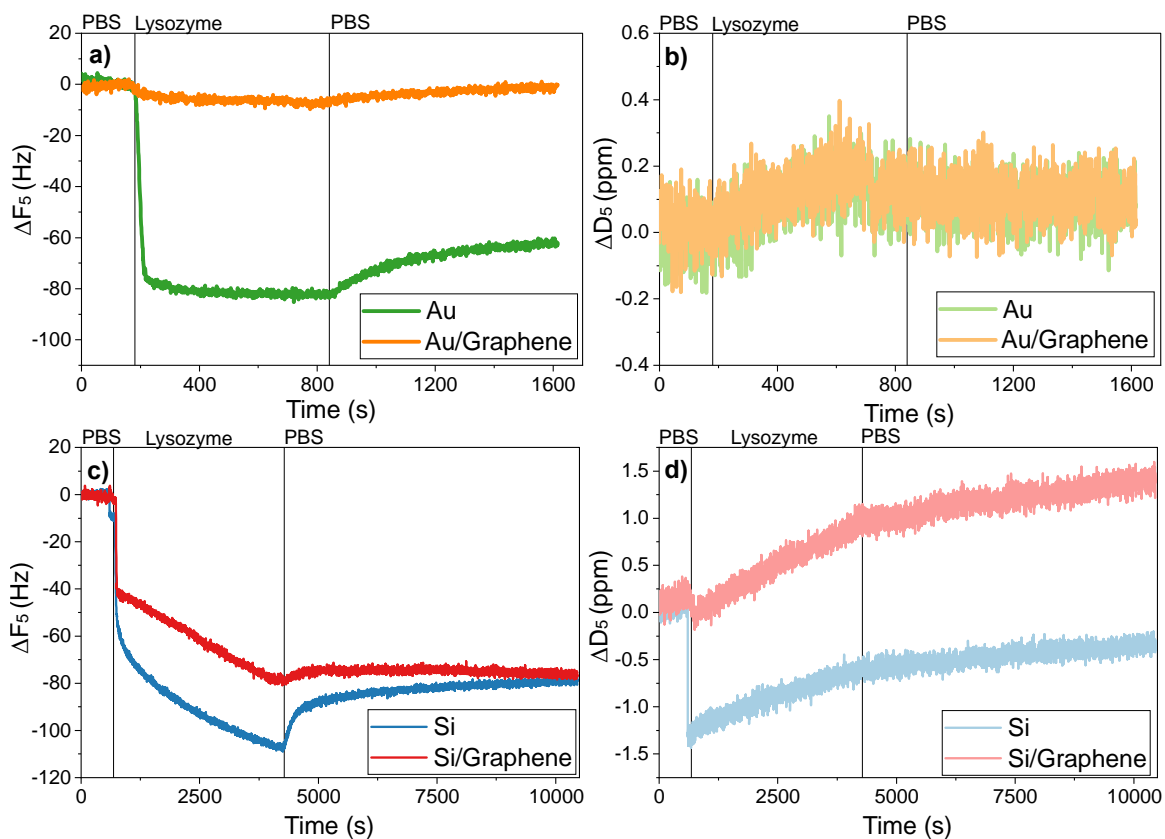


Figure 6.9 – Frequency and Dissipation QCM curves a) frequency overtone 5 and b) dissipation overtone 5 for Lysozyme attachment to Au and Au/graphene sensors. c) frequency overtone 5 and d) dissipation overtone 5 for Lysozyme attachment to Si and Si/graphene

The simplest and most commonly used attachment model is Langmuir adsorption.²⁸⁸ This model assumes adsorption to and desorption from distinct surface sites and ignores adsorbate/adsorbate interactions. For adsorption (Equation 11) the amount of adsorbed protein (q) is determined by the adsorption (k_a) and desorption (k_d) reaction rates as well as the total number of available surface sites (Q), protein concentration (C) and time (t). For desorption only (Equation 12) the expression can be simplified.

$$q(t) = Q(1 - e^{-t(k_a C + k_d)}) \quad \text{Equation 11}$$

$$q(t) = Q(e^{-t k_d}) \quad \text{Equation 12}$$

While Langmuir curves fit the Au and Au/graphene adsorption data with reasonable accuracy, it fails to explain the Si and Si/graphene adsorption curve shapes (Figure 6.10). In this case, it is necessary to employ the more complicated, but still analytically solvable, 2-state model.²⁸⁹ In this model, in addition to the reversible Langmuir adsorption, adsorbed protein can undergo a surface-induced conformational change and attach irreversibly to the surface at some rate s_t . The system of rate equations can be solved (Equation 13) to give adsorption amount (q) over time (t) based on two negative roots (r_1, r_2) and three constants (a_1, a_2, a_3), where a_3 is the saturation coverage of the sensor. r_1 (Equation 14) and r_2 (Equation 15) are functions of all 3 rates (k_a, k_d, s_t) and protein concentration (C). Since these equations contain 3 unknown rates but only 2 fitted roots, the rate values remain unknown when using this analysis.

$$q(t) = a_1 e^{r_1 t} + a_2 e^{r_2 t} + a_3 \quad \text{Equation 13}$$

$$r_1 = -\frac{1}{2}(k_a C + k_d + s_t) + \frac{1}{2}((k_a C + k_d + s_t)^2 - 4s_t k_1 C)^{\frac{1}{2}} \quad \text{Equation 14}$$

$$r_2 = -\frac{1}{2}(k_a C + k_d + s_t) - \frac{1}{2}((k_a C + k_d + s_t)^2 - 4s_t k_1 C)^{\frac{1}{2}} \quad \text{Equation 15}$$

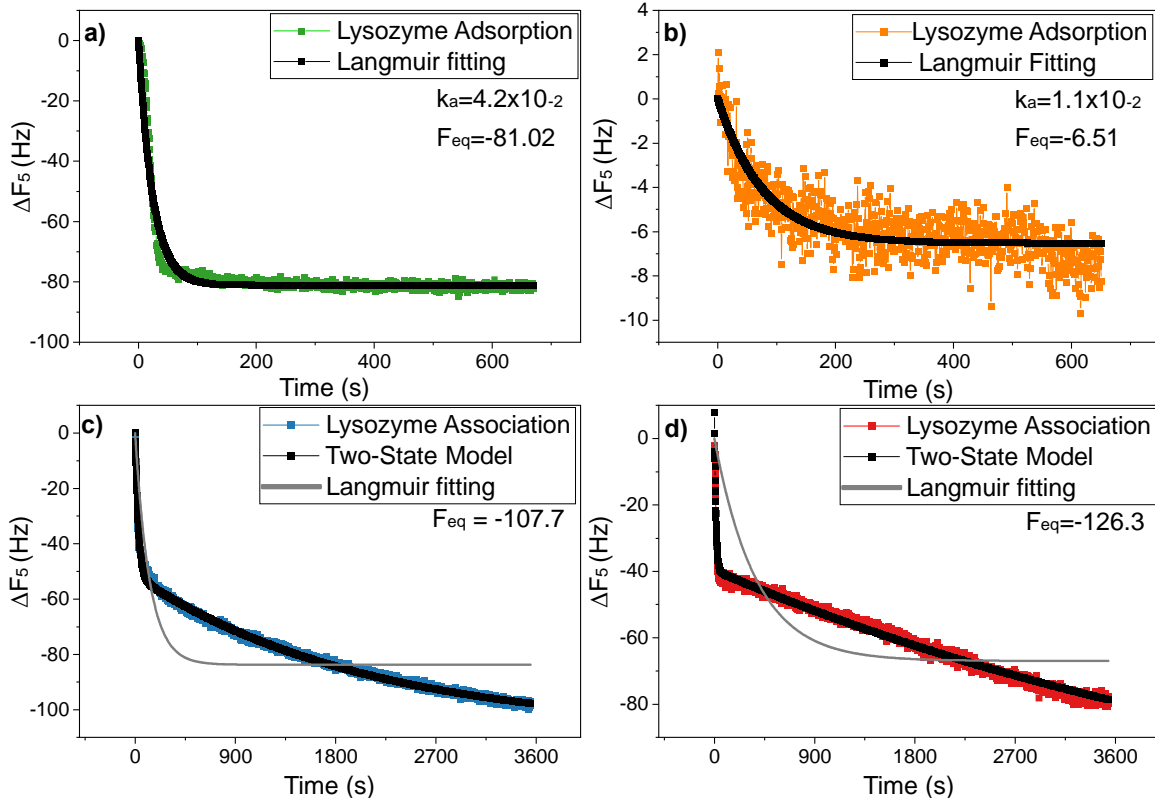


Figure 6.10 – Kinetic fitting of QCM frequency protein attachment curves. Langmuir fitting of Lysozyme adsorption to Au (a) and Au/graphene (b) sensors. Two-state fitting of Lysozyme adsorption to Si (c) and Si/graphene (d) sensors.

Figure 6.10 shows Langmuir and two-state fits on the Au and Si QCM-D frequency curves, respectively. Although the amount of protein adsorption varies in these cases with the presence of graphene, the required protein adsorption model does not change. Using the Sauerbrey equation (Equation 9), the saturation values from the adsorption curves can be converted to attached protein mass density. It is important to note that a lower concentration is used in the QCM-D experiment than the ellipsometry to prevent the initial

protein adsorption from occurring too quickly to fit (0.1 mg/mL and 10 mg/mL, respectively), and thus direct levels of protein attachment should not be compared. However, ellipsometry indicates a decrease in Lysozyme adsorption on Au and an increase on Si with the addition of graphene and the same trend was observed in the QCM-D-measured adsorption. While more work is needed to fully understand the kinetic interactions of Lysozyme, and other proteins, with graphene/substrate materials, this initial QCM-D data indicates that the appropriate kinetic model may be determined by the substrate even in cases where differences in absolute adsorption are observed, further indicating that support substrates have a significant effect on protein adsorption behavior to graphene.

6.4 Conclusions

Together, these protein attachment results reveal a gap in understanding of substrate effects on protein-graphene interactions. The *ex situ* ellipsometry and XPS analysis of protein attachment indicate that the substrate can have a profound impact on protein-graphene interactions, to the extent that twice the BSA attachment to graphene is observed when graphene is supported by TaN rather than Si (Figure 6.5). This stark difference appears to be caused by the significantly different DI H₂O contact angles for the TaN and Si that result in different levels of hydrophobic BSA attachment, and that difference is still apparent after a monolayer of graphene is transferred onto each surface.

While it appears that substrate contact angle is a predictor of graphene-protein equilibrium attachment levels, further studies are needed to fully understand what substrate

properties effect interactions with which classes of proteins. Additionally, the in situ QCM-D measurements of Lysozyme attachment to graphene supported by Si and Au shows that the substrate can not only have an effect on equilibrium attachment, but also attachment kinetics (Figure 6.10). Lysozyme appears to interact with graphene differently on Au than Si, where the first case can be fit by a simple Langmuir curve, while the second adsorption curve indicates a two-state adsorption mechanism is likely. This indicates that careful substrate selection could dictate the difference between biosensing receptors attaching reversibly vs irreversibly to a graphene-based sensor.

Although graphene is finding application in a wide range of biosensor devices, little attention has been given to the substrate used to support the graphene sensor. These results indicate, similarly to previous work on substrate modulation of water contact angle and epitaxial growth, the support substrate influences protein adsorption to graphene. Generally, there is little change between equilibrium protein adsorption to the underlying substrate once a monolayer of transferred graphene is added. As a result, hydrophobic support substrates tend to lead to increased protein adsorption, and thus hydrophilic substrates can decrease biofouling of sensors. Additionally, QCM-D results of Lysozyme attachment indicate that the graphene support substrate can affect the kinetics of how the protein attaches to the surface. Thus, in sensors that attach a bioreceptor to graphene through adsorption, functionalization stability may be increased on certain substrates. Although currently overlooked, the graphene support substrate is an important parameter in sensor design that has a direct effect on the sensor-protein interaction.

CHAPTER 7. SUMMARY AND FUTURE WORK

7.1 Summary

Disease diagnosis, human health and performance monitoring, food safety, environmental monitoring, and drug development all require reliable biomarker sensing. Since the 1960s EIAs have dominated this space, but these assays generally require centralized laboratories and several-day timescales to complete. In contrast, label-free biosensing allows for faster and more flexible biomarker detection, due to the simpler direct detection of the biomolecule of interest. Additionally, label-free electrochemical sensors may be cost-effectively microfabricated and designed as portable point-of-care and field devices. Potentiometric sensors lend themselves to multiplexed, parallel sensing, and are easily integrated with other electronics. However, despite the promise of potentiometric sensors, and label-free sensing in general, device reliability is lacking and precludes successful commercialization.

One large source of potential variability in an affinity biosensor is the surface functional layer that interfaces the sensor with a biological sample. COOH-SAMs, a common method of surface functionalization, are generally adopted in biosensing literature without characterization. These surface layers, however, showed large NSA of proteins across a wide size range. The observed NSA is largely the result of defects in the COOH-SAM that expose hydrophobic surfaces to solution. Best practices to minimize defects during COOH-SAM formation include careful cleaning of the Au surface and incubation

glassware, as well as incubation in a low concentration (20 μM) ethanolic solution of thiol in inert atmosphere for 24 hours.

To further address the use of COOH-SAMs in biosensors, a preblocking procedure was developed. In general, blocking procedures improve the reliability of affinity biosensing by covering sites where the analytical solution may adsorb non-selectively to the sensor, diminishing the selectivity and accuracy of the device. Typically, blocking is completed after receptor functionalization (postblocking). While postblocking the sensor surface does increase the specificity of the sensor, the postblocker can interfere with the activity of the receptor protein, and additionally does not prevent against NSA of the receptor protein itself. Instead, preblocking offers a simple and easily implemented method of stabilizing the chip before covalent functionalization while preserving the activity of the sensing surface and the protein receptors. A protein orthogonal to the system of interest can be used to cover the hydrophobic NSA sites prior to amine functionalization, preventing NSA of the receptor and conserving its activity. Experimentally, the preblocked sensor showed increased receptor activity and decreased baseline drift when compared to the postblocked sensor. In addition to sensor accuracy, preblocking was also shown to improve sensor shelf life. A COOH-SAM stored in ambient conditions showed significant oxidation in as little as 1 day, and was unusable as a biosensor after 1 week. However, since oxidation begins at defect sites, preblocking served as a physical barrier for oxidation. Unlike an unblocked COOH-SAM, a gelatin-blocked COOH-SAM did not show measurable oxidation via XPS nor RD for 21 days. The blocked COOH-SAM was still a

reliable sensor after 1 week, and preblocking even outperformed storage in an inert N₂ environment. Together, the signal stabilization and oxidation protection provided by preblocking allows COOH-SAM-based sensors to be viable point-of-care devices.

In addition to COOH-SAM biosensors, graphene has attracted attention by the scientific community as a potential surface for affinity biosensors. Although a wide range of biosensor devices using graphene have been demonstrated, little attention has been given to the substrate used to support the graphene sensor. This work showed that the support substrate influences protein adsorption to graphene. Generally, there is little change between equilibrium protein adsorption to the underlying substrate once a monolayer of transferred graphene is added. As a result, hydrophobic support substrates tend to lead to increased protein adsorption, and thus hydrophilic substrates can decrease biofouling of sensors. Additionally, QCM-D results of Lysozyme attachment indicated that the graphene support substrate can affect the kinetics of how the protein attaches to the surface. Thus, in sensors that attach a bioreceptor to graphene through adsorption, functionalization stability may be increased on certain substrates. Although currently overlooked, the graphene support substrate is an important parameter in sensor design that has a direct effect on the sensor-protein interaction.

Regardless of the type of sensor surface utilized, some sources of drift and signal instability are universal to all potentiometric biosensors. In the appendices, sensor drift as the result of an unstable reference electrode or reused fluidics was presented. These results highlighted the importance of the entire sensing setup, not just the sensor itself, in the

development of a reliable sensor. Secondly, three methods used to confirm protein binding to a sensor surface were presented. Due to the lack of step-edges on an affinity biosensor, AFM is not easily implemented to confirm target binding. However, ellipsometry and XPS can be used to show attachment of both receptor and target to the sensor. Thirdly, a general model for biomolecule binding to planar and nanowire sensors under the effects of both diffusion and convection was developed. The model approximated experimental binding data under a wide variety of conditions with good accuracy. The model was used to draw comparisons between mass transport under planar and radial diffusion with flow and indicated that the increased mass transport to nanowires due to radial diffusion is negligible given enough flow. Under flow conditions in typical experiments, radial diffusion associated with nanowire sensors is inessential for fast mass transport.

Overall, the work presented in this thesis demonstrated important considerations for reliable control over sensor-solution interfaces used in affinity biosensors. This work provides a step towards the development of stable, accurate, and precise potentiometric biosensors.

7.2 Future Work

While this work makes strides in understanding and controlling the protein-surface interactions necessary for affinity biosensing, there are still gaps in understanding. First of all, while protein interactions were studied with both COOH-SAMs and graphene, there are other sensor-relevant materials that should also be considered. These surfaces include SAMs with different terminal end groups, such as NTA for the selective binding of

Histidine tags,²⁹⁰⁻²⁹³ as well as mixed SAMs.¹⁴⁷ Specifically, some reports indicate that the incorporation of PEG-SAM with COOH-SAM decreases NSA.^{71, 294} In addition to SAMs, electrodeposited layers such as o-aminobenzoic acid are used commonly in EIS sensors.^{31, 295} For each of these surfaces, it should be determined if preblocking can further improve sensing reliability by decreasing NSA and stabilizing drift, as was shown for COOH-SAMs.

For graphene, the support substrate was shown to affect protein interactions with the sensor surface. An obvious expansion of this work would include other 2D materials, particularly those, such as MoS₂, that have been utilized in demonstrated biosensors.²⁹⁶ In addition to semiconducting 2D materials, it is fundamentally interesting to expand research into substrate effects to insulating materials, like hBN. For graphene specifically, the importance of the support substrate should be studied in devices that more closely resemble a final affinity biosensor. While many graphene-based sensors rely on the direct adsorption of the receptor to the graphene surface, others utilize defects in the graphene layer or a linker molecule for a more controlled functionalization procedure.^{201, 202, 205, 207, 212, 213} For instance, if PBASE is utilized to attach an antibody receptor to graphene via pi-stacking interactions, does the substrate still have an effect on the interaction?

Preblocking was demonstrated to improve the outlook of COOH-SAM-based sensors, both by improving signal reliability and protecting against oxidation. However, sensing utilizing preblocking was only demonstrated with SPR. It is useful to directly

demonstrate the applicability of the preblocking technique to other label-free sensing methods, such as potentiometric and EIS.

More generally, while the number of label-free affinity sensors showcased in literature increases daily, few truly portable devices have been demonstrated. The development and field testing of a portable label-free potentiometric sensor is needed to fully realize the potential of this sensing technology.

APPENDIX A. CONSIDERATIONS FOR POTENTIOMETRIC BIOSENSING

APPENDIX A is dedicated to practical considerations for potentiometric biosensing, or more generally any developing label-free biosensing technology. Drift and noise in sensing output directly impact the precision and sensitivity of the platform.^{297, 298} It is therefore critical in sensor design to maximize the signal-to-noise ratio by identifying sources of signal drift and unreliability. This appendix discusses drift due to reference electrodes, drift due to fluidics, multi-channel interference, and voltmeter input impedance.

A.1 Methods

16-Mercaptoundecanoic acid [HS(CH₂)₁₅COOH] (99.9%), 1-Ethyl-3-(3-dimethylaminopropyl) carbodiimide (EDC), N-Hydroxysuccinimide (NHS), ethanolamine (ETA), Phosphate Buffered Saline Pellets (PBS), Acetic Acid (AA), Anhydrous Ethanol, and Bovine Serum Albumin (BSA) were purchased from Sigma-Aldrich (St. Louis, MO). 100 nm thick Gold surfaces were e-beam evaporated on a substrate consisting of 280 nm of SiO₂ on silicon, and patterned via shadow mask. The gold surfaces were cleaned with acetone, methanol, and isopropanol rinses and dried with a N₂ stream, followed by a two-minute O₂/Plasma treatment (200 mTorr, 50 W RF, 25 sccm O₂). The substrates were then placed in 5 mM ethanolic solutions of thiol for 24 hours, sonicated for five minutes in fresh ethanol, and dried in a stream of N₂.

Potentiometric sensing setup is described in Figure A.1.³² Gold strips were individually functionalized and the surface potential was measured with respect to a flow-through reference electrode (Ag/AgCl; Microelectrodes Inc.). The electrical measurements were performed using a semiconductor parameter analyzer (Keithley 4200-SCS and HP 4145A).

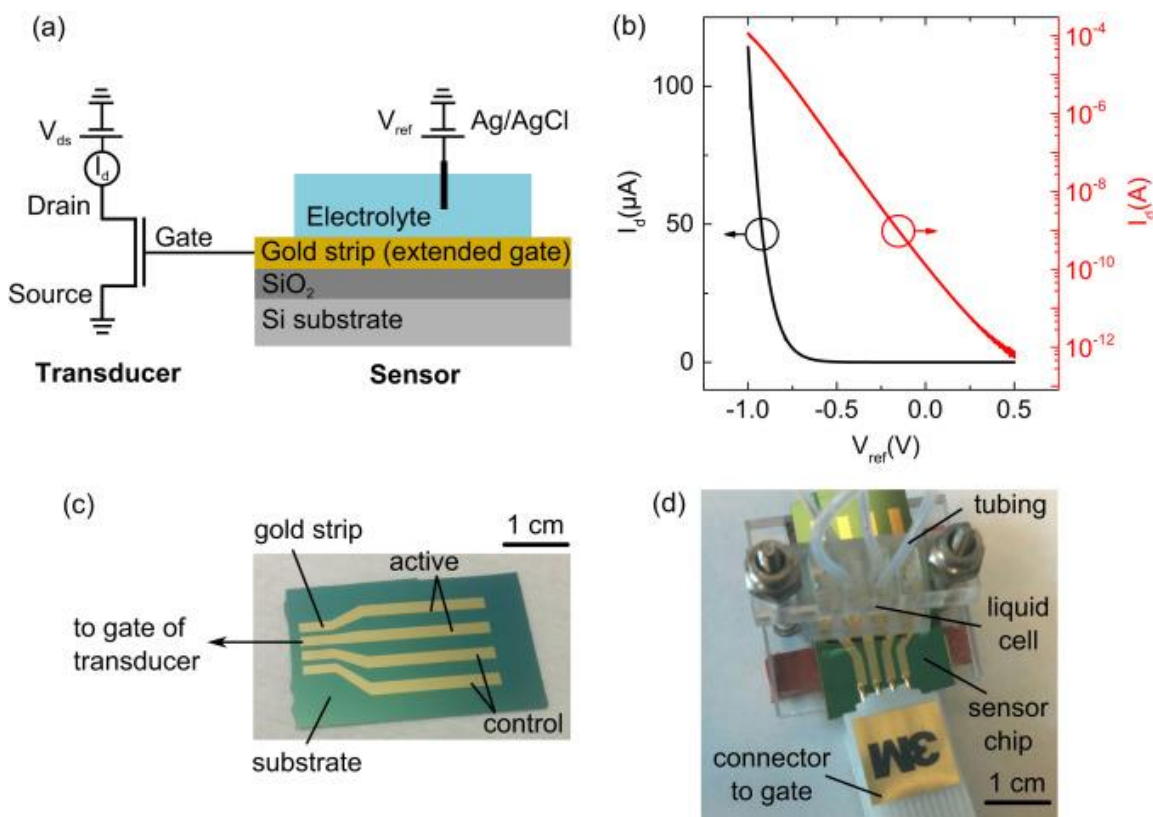


Figure A.1 – EGFET sensor layout and characterization. (a) Schematic of the potentiometric sensing device, consisting of two parts: a sensor for signal generation and a transducer for signal amplification and readout. (b) A typical transistor transfer curve showing that the drain current I_d can be modulated by sweeping the voltage at the reference electrode V_{ref} . The same curve is shown on linear scale (left axis) and semi-log scale (right axis). (c) Image of a disposable sensing chip. (d) sensor chip in contact with solution via PDMS wells and connected using a test clip

shown in to the gate of the transducer. Adapted with permission from A Tarasov, D W Gray, MY Tsai, N Shields, A Montrose, N Creedon, P Lovera, A O'Riordan, M H Mooney, and E M Vogel. A potentiometric biosensor for rapid on-site disease diagnostics *Biosensors and Bioelectronics* 2016, 79, 669-678. Copyright 2016 Elsevier.

A.2 Reference Electrode and Fluidic Tubing

Time-resolved measurements are useful in biosensing devices to detect the real-time attachment kinetics of biomolecules to the sensor surface.⁶³ In time-resolved potentiometric sensing, the gate voltage applied to the reference electrode is held constant while the drain current is monitored over time.^{299, 300} Control of baseline drift during this measurement is crucial to ensuring reliable and sensitive attachment results. Here, the reference electrode and fluidic tubing used for biosensing measurements are identified as significant contributors to baseline drift observed in PBS after amine functionalization of a COOH-SAM-based sensor with BSA (Figure A.2). Specifically, a reference electrode that is not allowed to acclimate to solution for one hour prior to sensing results in an increase in the observed drift. Additionally, re-use of fluidic tubing results in increased drift over time. The fluidic tubing drift is most likely due to biomolecules that have adhered to the interior tubing surfaces over time.³⁰¹

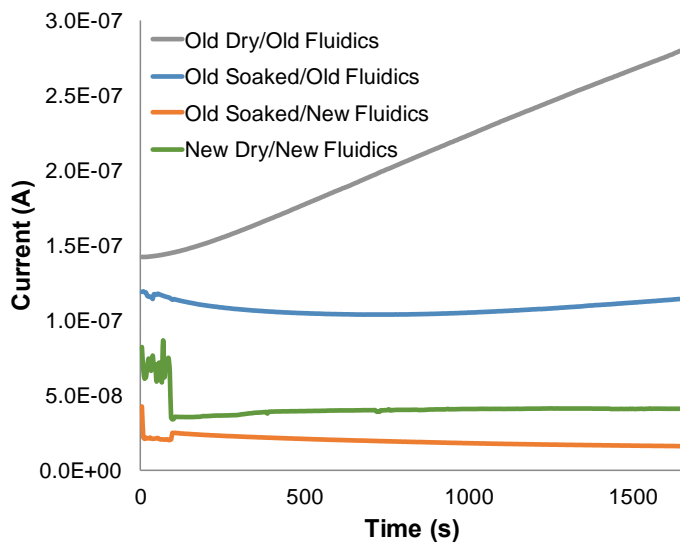


Figure A.2 – Comparison of post-functionalization drift in PBS

A.3 Multi-Channel Detection

Simultaneous detection of a sensor array is advantageous in many applications, where multiple sensors can provide a real-time reference,³⁰² improve sensitivity by reporting an averaged response,³⁰³ or allow simultaneous detection of multiple targets.³⁰⁴ Two important pitfalls of a multiplexed sensor scheme are discussed below.

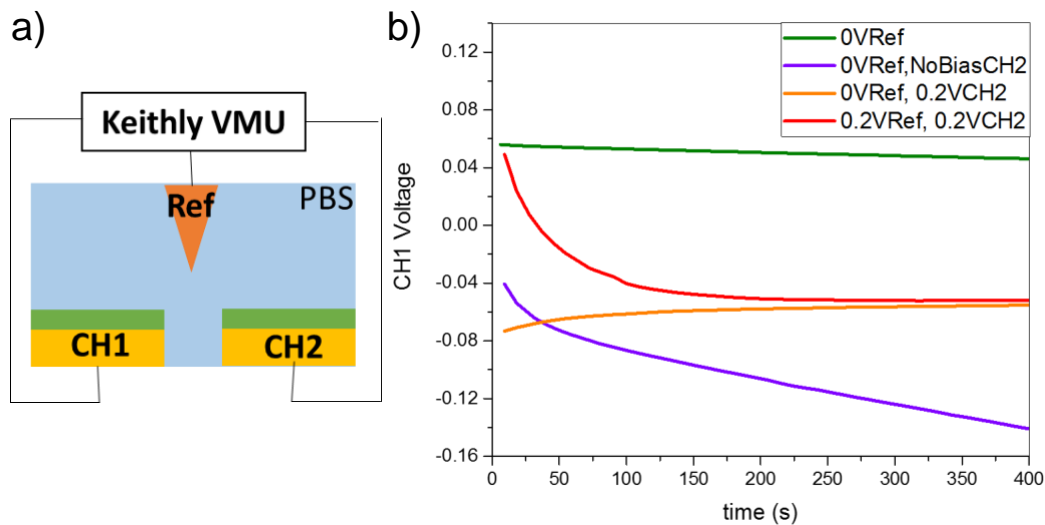


Figure A.3 – Multi-channel sensing interference a) schematic of 2-channel, 1-well sensing b) Measured voltage on CH1 with applied voltages on the reference and CH2

A 2-channel sensor is shown schematically in Figure A.3a. As shown in Figure A.3b, complex coupling occurs when channels share a liquid well, even when the voltage is only being measured on one sensor. When varying voltages are applied to the reference electrode and CH2, the observed voltage on CH1 is affected. Importantly, the effect is not as simple as a translation: the biases can change the shape of the voltage response. This result indicates that care to prevent coupling is required to measure multiple sensors connected by the same electrolyte solution, even if the sensors are measured serially.

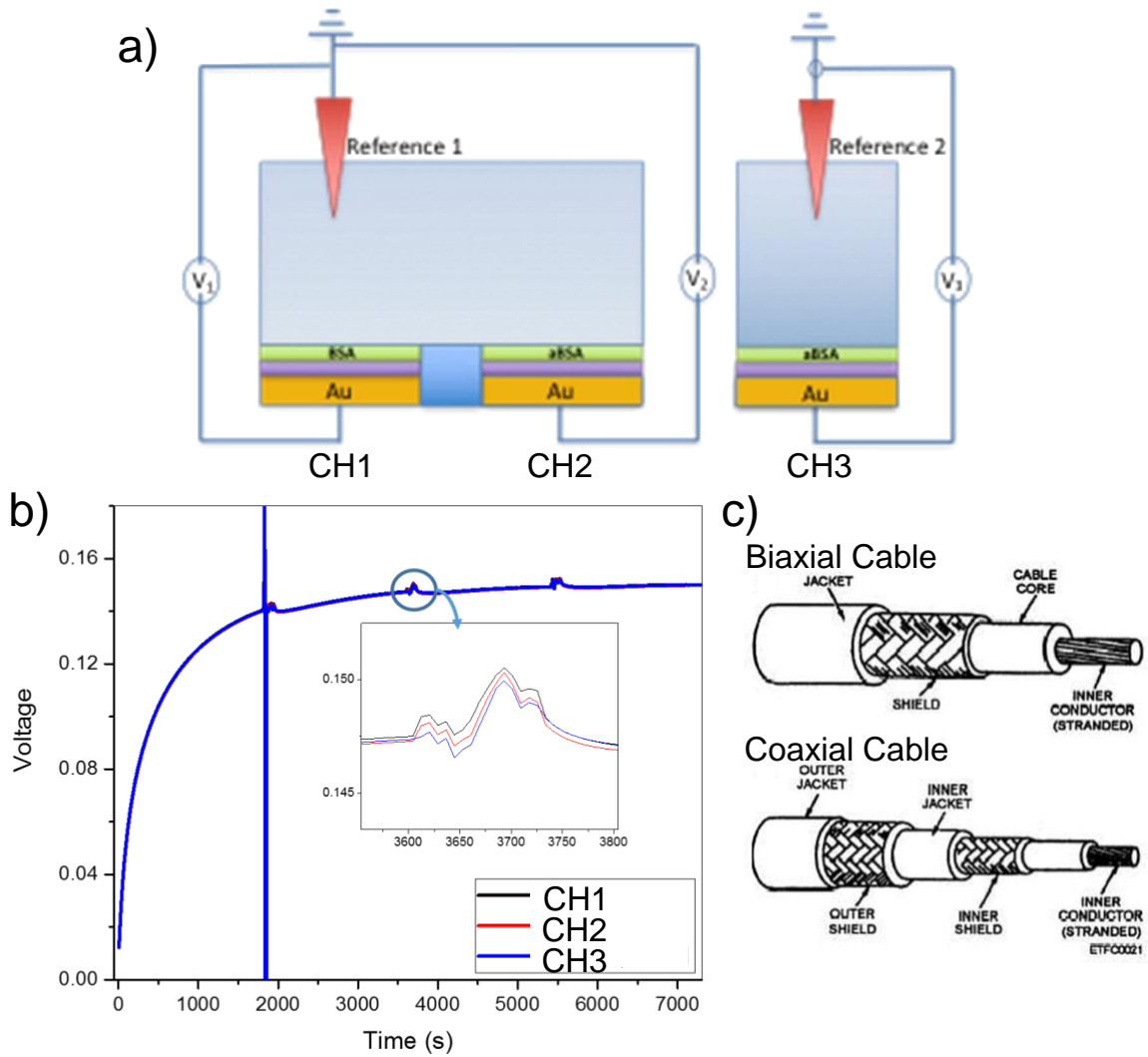


Figure A.4 – Multi-channel coupling from cables a) Schematic of multi-channel sensing b) Coupled response c) Schematic of coaxial and triaxial cables

Incorrect wiring can lead to signal coupling across sensors even when separate solution wells and reference electrodes are utilized. An example sensing setup is shown in Figure A.4a. When all three channels are measured simultaneously, there is coupling between all three sensors, despite the isolation of CH3 in a separate liquid well with a

separate reference electrode (Figure A.4b). In this case, triaxial to coaxial adaptors were to blame, where common adapters short the inner and outer shielding triaxial shielding (Figure A.4c). Completely isolated sensors, both in solution and via wiring, are necessary for simultaneous sensing.

A.4 Direct Voltage Measurements

In most potentiometric sensing configurations, changes in the drain current or gate potential of a FET are monitored and reported as the sensing signal.³⁰⁵ Changes in the FET output are in response to surface potential changes due to a pH change or the binding of charged biomolecules.⁵⁵ Therefore, the same sensing can be accomplished by directly monitoring the voltage of a sensor surface, without an intermediary FET. However, in practice, extremely high impedance is required. When a Keithley 4200 (input impedance $>10^{13} \Omega$) is used for measurement, the expected pH-dependent non-zero voltage difference is observed between the reference electrode and sensor surface (Figure A.5a). However, when surface potential is measured with an HP 4145 or handheld voltmeter (input impedance $> 10^6 \Omega$), no voltage difference between the reference electrode and sensor surface is detected (Figure A.5b). The charge transfer resistance of the sensor is large ($\sim 10^6 \Omega$),⁵⁶ and therefore an even larger impedance is required to maintain a voltage for measurement. Since the input impedance of a commercial FET is very large (in our sensor setup, $>1 \times 10^{13} \Omega$), measurements through the FET are a cost-effective way to monitor the sensor potential (Table A.1).

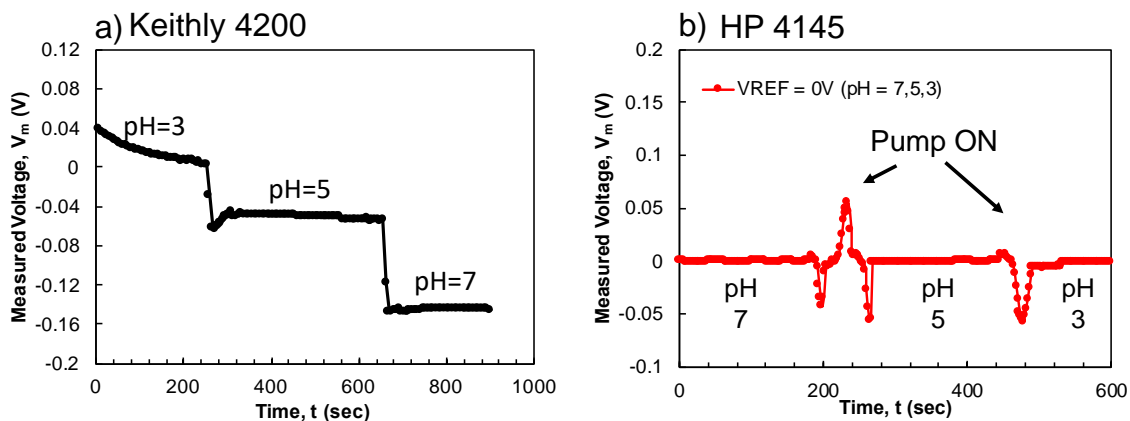


Figure A.5 – Sensor surface voltage changes due to pH measured with high (a, Keithly 4200) and low (b, HP 4245) input impedance instruments. Spikes in (b) due to pump noise.

Table A.1 – Input impedance for selected transducers

Instrument	Input Impedance (Ω)
Keithly 4200	$>1 \times 10^{13}$
HP 4145	1×10^7
Handheld VM	7.8×10^6
FET	$>1 \times 10^{13}$

A.5 Conclusions

This appendix highlighted important sources of drift and sensor signal coupling for potentiometric biosensing. Sensor drift as the result of an unstable reference electrode or reused fluidics was presented. These results highlight the importance of the entire sensing setup, not just the sensor itself, in the development of a reliable sensor. Potential pitfalls

associated with multiplexed sensing and direct voltage measurements were also emphasized.

APPENDIX B. METHODS TO CONFIRM SURFACE-PROTEIN ATTACHMENT

APPENDIX B is dedicated to methods that can independently confirm protein attachment to a label-free sensor. In the development of new label-free biosensing techniques, it is often helpful to confirm observed signal changes are due to the expected antigen binding. In this section, the benefits of three methods of independently confirming antigen binding on a sensor chip, AFM, Ellipsometry, and XPS, are discussed.

For all experiments, 100 nm thick Gold surfaces were e-beam evaporated on a substrate consisting of 280 nm of SiO₂ on silicon. The gold surfaces were cleaned with acetone, methanol, and isopropanol rinses and dried with a N₂ stream, followed by a two-minute O₂/Plasma treatment (200 mTorr, 50 W RF, 25 sccm O₂). The substrates were then placed in ethanolic solutions of thiol in piranha-cleaned (3:1 96% H₂SO₄:H₂O₂) glass petri dishes. After 24 hours, the SAM-covered substrates were sonicated for five minutes in fresh ethanol, followed by drying in a stream of N₂. N₂ atmosphere was provided by a Labstar Pro glovebox (MBRAUN), with H₂O and O₂ both <1ppm.

B.1 Atomic Force Microscopy

Atomic force microscopy (AFM) was performed using a Bruker Icon Scanning Probe Microscope (Billerica, MA) with AppNano (Mountain View, CA) SPM Si probes having a tip radius of <10 nm. COOH-SAMs were formed from 20 μM ethanolic solutions.

AFM images show slight changes in RMS roughness after COOH-SAM formation, preblocking, receptor functionalization, and antigen capture (Figure B.1). The increase in the RMS roughness after COOH-SAM formation compared to bare Au indicates an imperfect SAM surface due to defects reported in the literature.^{135, 153, 161, 162, 164, 165} The addition of pre-blocker appears to “smooth out” the surface roughness. However, other than minor changes in the observed roughness, there is not a clear distinction between the different samples. Most importantly, it would not be accurate to say that the AFM clearly indicates aBSA attachment to the surface between Figure B.1a and b. Since there is no clear step edge to differentiate the different protein layers, it is difficult to use AFM to confirm protein attachment to a sensor.

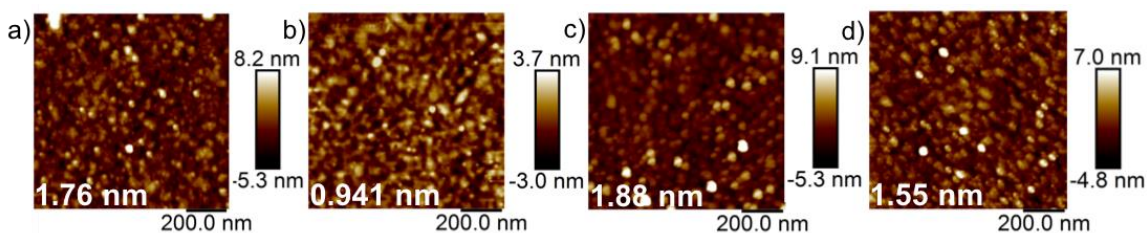


Figure B.1 – AFM images of functional surfaces on 100 nm Au/SiO₂ chips with inset RMS roughness (in white). a) 20 μ M COOH-SAM b) 20 μ M COOH-SAM/Gelatin Preblocking c) 20 μ M COOH-SAM/Gelatin Preblocking/aHp Functionalization d) 20 μ M COOH-SAM/Gelatin Preblocking/aHp Functionalization/50 μ g/mL Hp

B.2 Ellipsometry

A Woollam M2000 Ellipsometer was used for all measurements, and CompleteEASE software (J.A. Woollam, Lincoln, NE) was used for all spectra fitting. Software point selection was used to measure the same points on the sample before and

after protein solution incubation. CompleteEASE materials database provided Au substrate starting properties. Cauchy layers with a refractive index of 1.45 were used to approximate protein thickness.^{119, 306} COOH-SAMs were formed from 20 μM ethanolic solutions.

Figure B.2 shows protein layer thickness as measured by ellipsometry. Au surface with COOH-SAM was used as the baseline reference. After amine functionalization of BSA, a new surface layer with a thickness of approximately 2.9 nm was observed on the sensor. Subsequently, after a 1 hour incubation in 100 $\mu\text{g/mL}$ aBSA, the observed thickness increased to 4.7 nm. In this way, the binding of aBSA to the sensor can be confirmed.

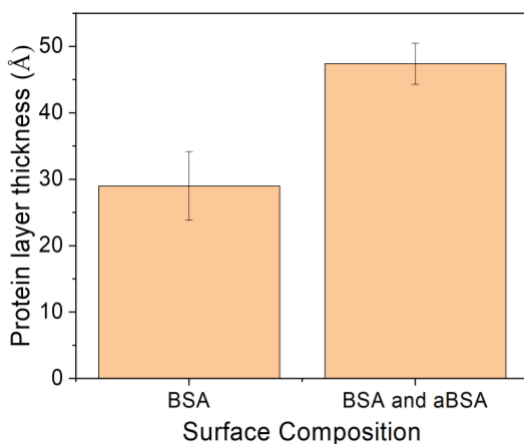


Figure B.2 – Protein layer thickness as measured by ellipsometry.

B.3 X-Ray Photoelectron Spectroscopy

Measurements were conducted using a K-Alpha X-ray Photoelectron Spectrometer System (Thermo Scientific, Waltham, MA) with a monochromatic Al $K\alpha$ source (KE = 1486.6 eV), a 180° double focusing hemispherical analyzer, and a 128-channel detector. Spectra were acquired at a pass energy of 50 eV and a spot size of 400 μm . Au 4f spectra

were fit with 2 peaks (spin-orbit splitting of 3.7 eV, 3:4 area ratio). N 1s spectra were fit with one peak. His-tag functionalization was utilized for HSA capture, with 1% HSA in PBS.²⁹⁰⁻²⁹³ NTA-SAMs were formed from 1 mM ethanolic solutions of 9:1 PEG-thiol:NTA-Thiol. HS-C₁₁EG₃-NTA (NTA-thiol) and HS-C₁₁-EG₃OH (PEG-Thiol) were purchased from Prochimia Surfaces (Gdansk area, Poland). Human Serum Albumin (HSA) and antibody HSA (aHSA) were purchased from abcam (Cambridge, United Kingdom).

Since proteins are composed of approximately 16% N, the XPS N 1s signal can be used to estimate levels of protein adsorption. Step-wise detection of HSA and aHSA binding to the sensor surface via XPS is shown in Figure B.3. Initially, there is a small N 1s signal observed for the NTA-SAM only, due to N in the NTA endgroup. After His-tag functionalization of the HSA, a significant increase in the N 1s signal is observed, corresponding to HSA protein on the sensor surface. Additionally, after 1 hour incubation of the HSA-functionalized sensor in 100 µg/mL aHSA, an additional N signal increase is seen. Via the N signal increase, binding on the aHSA to the sensor chip can be confirmed.

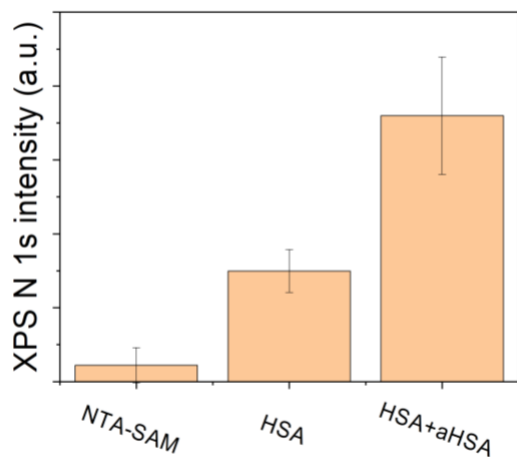


Figure B.3 – N 1S peak intensity of NTA-SAM only, after HSA functionalization, and after aHSA attachment.

B.4 Conclusions

This appendix discussed three methods used to confirm protein binding to a sensor surface. Due to the lack of step-edges on an affinity biosensor, AFM is not easily implemented to confirm target binding. However, both Ellipsometry and XPS can be used to show attachment of both receptor and target to the sensor. Ellipsometry, due to its speed and operation at atmospheric pressure, may be preferred over XPS.

APPENDIX C. MASS TRANSPORT AND SENSOR GEOMETRY^D

APPENDIX C presents a general model for mass transport to a sensor surface, allowing estimation of sensor response time. This work was completed in close collaboration with Decarle Jin, and my contribution to the work focused mainly on diffusion-limited mass transport and experimental validation of the model.

Mass transport to the sensor surface is a critical step in biosensing, often being the factor determining the limit of detection. Modelling transport of the analyte to a surface under convection and diffusion is a challenging task often requiring complex simulation. Herein, we provide a general model for mass transport to planar and nanowire biosensors under flow that is applicable over a wide range of variables. The model is then used to examine the importance of radial diffusion compared with planar diffusion under flow. Only under diffusive transport nanowires are found to have greatly reduced settling times compared with planar sensors due to radial diffusion. However, the presence of flow restricts the growth of the depletion region, resulting in comparable settling times between nanowires and planar sensors of the same size. Under flow conditions in typical experiments, radial diffusion associated with nanowire sensors is inessential for fast mass transport. Instead, the sensor length in the flow direction is the critical parameter as it limits

^D Adapted with permission from D Jin, E L Brightbill, and E M Vogel. General model for mass transport to planar and nanowire biosensor surfaces. *Journal of Applied Physics* 2019, **125**, 114502. Copyright 2019 AIP Publishing.

the concentration drop that can occur as the analyte flows past the sensor. Decreasing the sensor length along the flow direction is found to greatly reduce settling times for both cases of planar and radial diffusion, even approaching the reaction limited case. Similarly, decreasing the channel height decreases the settling time due to restriction of the depletion region, but not as significantly as decreasing the sensor length.

C.1 Theory

C.1.1 Reaction

Reaction between analyte and receptors is modeled as a 1:1 binding interaction.

The rate of conjugation between analyte and receptor is given by

$$\frac{dN}{dt} = k_a(N_0 - N)\rho_s - k_dN \quad \text{Equation 16}$$

where N is the density of conjugated receptors, N_0 is the density of receptors on the sensor surface, ρ_s is the surface concentration of analyte, and k_a and k_d are the association and dissociation rate constant of the analyte respectively. ρ_s is determined by the balance of mass transport toward the sensor surface and the rate of binding of the analyte to the sensor. The faster mass transport can occur, the higher ρ_s is and the faster the analyte can bind. If mass transport can deliver analyte much more quickly than binding can occur, then the binding rate is determined only by the association and dissociation constants of the analyte and the number of receptors available on the sensor surface. This is the reaction-limited case and represents the upper “speed limit” for how quickly binding can occur. Independent

of the rate of mass transport, the equilibrium density of bound receptors is given by $N_{eq} = N_0/(1 + k_a/k_d\rho_0)$ where ρ_0 is the bulk concentration of analyte.

C.1.2 Diffusion

As analyte concentration adsorbs to the sensor surface, it depletes the concentration of analyte near the surface forming a depletion zone of length $\delta_d = \sqrt{2nDt}$, where n is the dimensionality of the sensor ($n=1$ for planar; $n=2$ for nanowire). This concentration gradient drives the diffusion of analyte towards the sensor surface. ρ_s is thus the result of competition between binding depleting the concentration of analyte and diffusion replenishing it. The rate of change of ρ_s can be described by Fick's law of diffusion

$$\frac{d\rho}{dt} = D\nabla^2\rho \quad \text{Equation 17}$$

where D is the diffusion coefficient of analyte in solution. Regardless of the shape or size of the sensor, the solution to Equation 17 at steady state is given by³⁰⁷

$$I = JA_D = C_D(\rho_0 - \rho_s) \quad \text{Equation 18}$$

where I is the integrated flux, J is the incident flux, A_D is the dimension dependent area of the sensor surface, ρ_0 is the bulk concentration and C_D is the diffusion equivalent capacitance. This solution assumes the sensor to be a perfect sink for analyte, i.e. $k_d = 0$. Although no sensor is a perfect sink, this is a good approximation so long as $k_a \gg k_d$, as is commonly true. The incident flux is balanced by the rate of conjugation of analyte to the sensor surface, giving $J = dN/dt$. Equation 16 and Equation 18 can then be solved simultaneously to give

$$\frac{dN}{dt} = -\frac{k_a \rho_0 (N_0 - N) - k_d N}{1 + \frac{k_a (N_0 - N) \frac{C_D(t)}{A_D}}{A_D}} \quad \text{Equation 19}$$

where $C_D(t)/A_D$ depends on the geometry of the sensor (Table C.1). In arriving at this result, we assumed quasi-steady state conditions as described by Alam and Nair.³⁰⁷ A similar assumption is made by Squires et al.³⁰⁸ and in the two-compartment model used in SPR.¹¹⁰ In this assumption, the depletion zone evolves quasi-steadily as analyte is continuously captured. Therefore, the time-dependent response of the biosensor can be considered to be a perturbation of the steady-state solution given by Equation 18. This assumption is valid as long as the time scale for the binding flux to change appreciably is much greater than the time scale for the depletion zone to form,³⁰⁸ i.e. the depletion zone must form well before the sensor surface is saturated. Figure C.1a shows the comparison of our model to previously published numerical solutions³⁰⁷ of the purely diffusive case. The model fits very well in both the nanowire and planar case.

Table C.1 – Dimension dependent parameters used in Equation 19

	A_D	$C_D(t)$
Planar	1	$\frac{D}{\sqrt{2Dt}}$
Radial	$2\pi L$	$\frac{2\pi D}{\log \left[\frac{\sqrt{4Dt} + L}{L} \right]}$

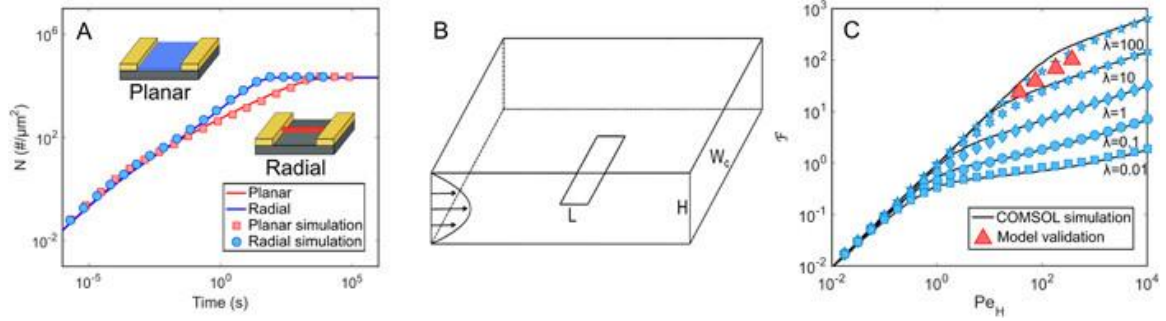


Figure C.1 – (a) Comparison of the model (line) with numerical solutions from the literature (symbols) of the purely diffusive case.³⁰⁷ The inset shows example sensors with planar and radial geometry. (b) Channel geometry. (c) Comparison of the model (blue symbols) to COMSOL simulation data (lines) for the diffusion-convection case.³⁰⁸ The red triangles mark the conditions associated with the model validation provided in Figure C.2.

C.1.3 Convection

In the purely diffusive case, as analyte is continuously adsorbed to the sensor surface, the depletion region will continuously grow while diffusive flux will likewise decrease. The effect of flow is to replenish the depleting analyte, effectively limiting the growth of the depletion region. The effect of convection on the binding rate is included by accounting for its effect on the growth of the depletion region. First, the influence of convection on the depletion region will be established.

In deriving the effects of convection, the fluid is modeled as flowing through a channel with dimensions given in Figure C.1b. Typically, the width of the channel W_c is much greater than its height H , thus the concentration can be assumed to be uniform across the channel (in the H direction) and the system can be treated as two-dimensional. Fluid flows through the channel with velocity

$$u = \frac{6Q}{W_c H^3} z(H - z) \quad \text{Equation 20}$$

which is assumed to be parabolic Poiseuille flow with rate Q . As can be seen, the effect of flow depends on many different dimensional parameters that may vary from system to system. In order to make meaningful comparisons, these systems are often described using dimensionless parameters. First, the Peclet number, $Pe_H = Q/DW_c$, describes the competition between diffusion and convection. When $Pe_H \gg 1$ convection dominates and molecules are swept past the sensor before they can diffuse very far towards the sensor. As a result, only analyte near the sensor surface can be collected, and the flow can be treated as a linear shear flow $u = \dot{\gamma}z$ at a height z above the sensor. The depletion width in this case is limited to δ_f , the distance at which the time for molecules to diffuse towards the sensor (δ_f^2/D) equals the amount of time it takes for them to be swept past the sensor ($L/\dot{\gamma}\delta_f$) The depletion width is thus

$$\delta_f = \frac{L}{Pe_s^{1/3}} \quad \text{Equation 21}$$

where $Pe_s = 6 \left(\frac{L^2}{H^2} \right) Pe_H$ is the shear Peclet number. The incident flux through this depletion width can be estimated as $J_D \sim \frac{D\rho_0}{\delta_f} W_s L$. A dimensionless flux $\mathcal{F} \sim J_D/D\rho_0 W_s$ can also be defined. From this it is clear

$$\delta_f = \frac{L}{\mathcal{F}} \quad \text{Equation 22}$$

The dimensionless flux \mathcal{F} has been determined empirically for high Pe_s ³⁰⁹ and low Pe_s ³¹⁰.

$$\mathcal{F}(Pe_s \gg 1) \approx 0.81Pe_s^{\frac{1}{3}} + 0.71Pe_s^{-\frac{1}{6}} - 0.2Pe_s^{-\frac{1}{3}} \dots \quad \text{Equation 23}$$

$$\mathcal{F}(Pe_s \ll 1) \approx \pi \left(\ln(4/Pe_s^{\frac{1}{2}}) + 1.06 \right)^{-1} \quad \text{Equation 24}$$

Turning to the case where $Pe_H \ll 1$, convection does not dominate. Flow is no longer enough to limit the growth of the depletion region due to diffusion. Instead, the depletion region continues to grow and begins to extend laterally into the channel. In this low flow limit, all molecules that flow towards the sensor are collected such that the diffusive flux, $J_D = \rho_0 HW_c / \delta$, equals the convective flux, $J_c = Q\rho_0$. The dimensionless flux \mathcal{F} in this case equals Pe_H and the depletion width can be defined as

$$\delta_{ch} = \frac{L}{Pe_H} \quad \text{Equation 25}$$

This factor describes the depletion width at the very low flow rates. An effective depletion width due to diffusion and convection can now be established

$$\delta_{eff} = \left(\delta_d^{-1} + (\delta_f + \delta_{ch})^{-1} \right)^{-1} \quad \text{Equation 26}$$

where δ_d is the depletion width of the purely diffusive case. In the first moments of binding, δ_{eff} is determined by δ_d until it approaches δ_f at which point it plateaus. The addition of δ_{ch} ensures \mathcal{F} approaches Pe_H at very low flow rates.

Figure C.1c shows the comparison of our model to COMSOL simulation data in the literature for a planar model in the diffusion-convection case.⁸ The model fits almost exactly with some deviation present at larger λ values, λ being the dimensionless parameter

equal to L/H . Although this comparison only considers the planar geometry, the concepts utilized to account for convection are also applicable to nanowire sensors, and the differences in mass transport to planar and nanowire sensors are assumed to be related to only the differences in diffusive transport.

C.1.4 Model Evaluation

We confirm the validity of the model using simulations and experimental data from literature. Figure C.2a shows our model compared to literature data of reaction limited binding of myoglobin in SPR.³¹¹ In a reaction-limited regime, diffusion and convection are negligible and the binding curve should closely match a simple 1:1 Langmuir binding model. Under conditions without mass transport limitations, our model imitates a 1:1 Langmuir binding model exactly. The model replicates the data very well at all concentrations with some minor deviation at early times. This deviation is due to divergence of the experimental data from ideal 1:1 binding at the initial stages of the experiment. Figure C.2b shows a comparison of our model to simulations of binding in a transport limited regime.¹¹⁰ The model replicates the response exactly at low concentrations, but slightly overestimates the response at increasing concentrations. Figure C.2c and d show a comparison to a simulation of binding at different flow rates with two different binding site densities.³¹² Increasing the number of available binding sites increases the transport limitations present. In the case of low number of binding sites, the model replicates the response almost exactly. With a higher number of binding sites, the binding becomes more mass transport limited, and the model overestimates the binding

response slightly. However, the effect of changing flow rates is reproduced quite well. Figure C.2e shows a comparison of the model to experimental data examining the effect of flow rate on binding. In this case, the diffusivity of the GST-Lcyt-YF protein is unknown. $D_0=5.59 \times 10^{-7} \text{ cm}^2/\text{s}$ was chosen as a good fit to the data. With this diffusivity, the model replicates the data very well. Using the procedure reported by Young et al.³¹³ to estimate diffusivity from molecular weight, an estimate of $7.2 \times 10^{-7} \text{ cm}^2/\text{s}$ is obtained. Given the $\pm 20\%$ error reported by Young when compared to experimental data, our fit diffusivity is reasonable.

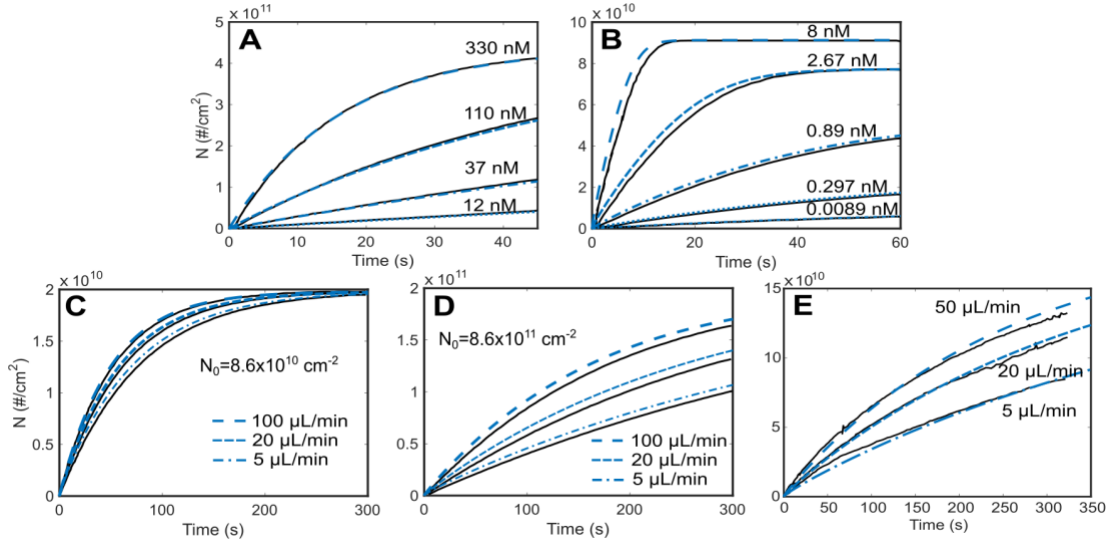


Figure C.2 – Comparison of model to data from literature. (a) SPR data of binding of myoglobin.³¹¹ (b) Data from simulations of binding of a model protein in a transport limited regime.¹¹⁰ (c-d) Data from simulations of binding of a model at different flow rates with $N_0 = 8.6 \times 10^{10} \text{ cm}^{-2}$ and $N_0 = 8.6 \times 10^{11} \text{ cm}^{-2}$.³¹² (e) Experimental SPR data of binding of fusion protein GST-Lcyt-YF at different flow rates.³¹²

C.2 Model Results and Discussion

The model developed here enables simple simulation of a realistic binding response to planar and nanowire sensors over a wide range of flow rates and channel geometries. From modeled binding curves (Figure C.3a), relevant benchmarking metrics can be calculated, such as settling time at different concentrations. To demonstrate the usefulness of this model, settling time is used as a metric to compare the effects of radial diffusion with and without flow. To isolate this effect, all dimensions of the sensors and channels will be kept identical. The nanowire diameter will be the same as the length of the planar sensor. Settling time is defined here as the time required to bind a certain threshold number of molecules $[N(\tau_s) = N_{eq}(1-e^{-1})]$. The advantage of defining settling time in this manner is that it allows us to make consistent, meaningful comparisons over many concentration ranges. If, instead, a static threshold value was chosen, the results may change depending on where along the binding curve this threshold value appears. τ_s defined in this situation plateaus to a constant value at low concentration which is determined solely by k_d , as seen in Figure C.3b. This constant value of τ_s will be the metric for comparison of radial vs planar diffusion. The reaction limited case will also be presented as a “speed limit” to mark when mass transport has no further effect.

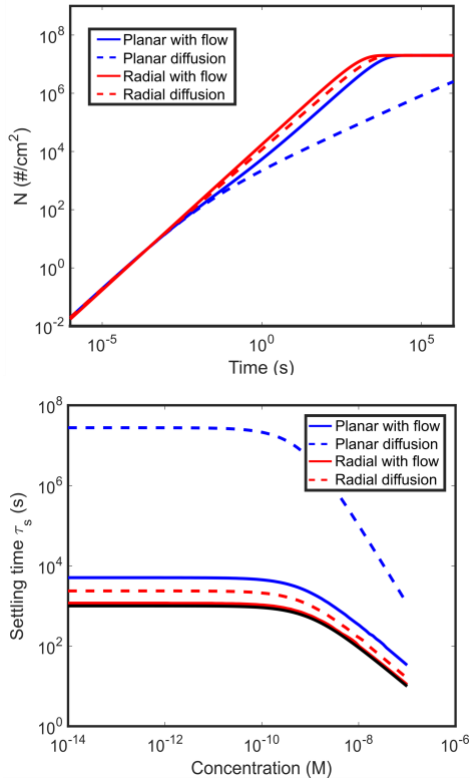


Figure C.3 – Modeling (a) a transient binding curve and (b) settling time at different concentrations to a microplanar and nanowire sensor. $L = 50 \text{ }\mu\text{m}$ (planar), 50 nm (radial), $Q = 10 \text{ }\mu\text{l/min}$, $N_0 = 2 \cdot 10^{12} \text{ cm}^{-3}$, $k_a = 10^6 \text{ M}^{-1}\text{s}^{-1}$, $k_d = 10^{-3} \text{ s}^{-1}$, $c = 10 \text{ fM}$, $D = 10^{-7} \text{ cm}^2/\text{s}$, $H = 100 \text{ }\mu\text{m}$, $W_c = 200 \text{ }\mu\text{m}$

C.2.1 Effect of sensor length (radius) on settling time

Figure C.4a and b show the effect of changing sensor length on the settling time at moderate ($PeH = 1$) and high ($PeH = 100$) flows. Considering first the purely diffusive case, the radial diffusion model has a greatly reduced settling time which decreases with the sensor length in comparison with the planar diffusion model similar to the results by Nair and Alam.³⁰⁷ It should be noted that the planar diffusion model is valid until the depletion region becomes comparable to the length of the sensor. This begins to occur at time L^2/D

in the purely diffusive case,³⁰⁸ after which the depletion region begins to grow radially. At the flow rates investigated here, the depletion region does not grow significantly enough to display radial diffusion, so the effects of radial diffusion do not need to be considered. In the purely diffusive case, the depletion region can grow significantly to the point where radial diffusion becomes significant. The planar diffusion model used here does not account for radial diffusion and most likely overestimates the settling time. However, the focus here is comparing the effects of radial diffusion under flow.

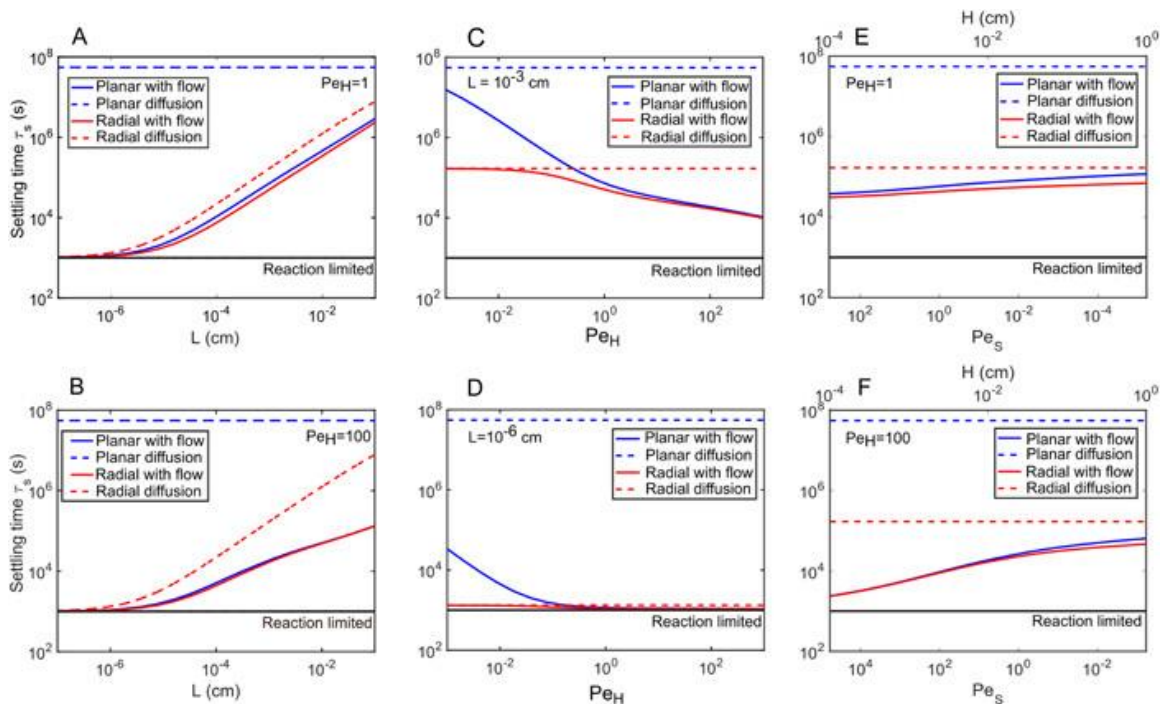


Figure C.4 – (a) and (b) Effect of the sensor length (radius) on the settling time at two different flow rates. (c) and (d) Effect of the flow rate on the settling time at two different sensor sizes. (e) and (f) Effect of the channel height on the settling time at two different flow rates.

When moderate flow rates are included, the settling time of the planar diffusion model drops dramatically, becoming comparable to the radial diffusion model. In contrast,

the radial diffusion model does not see as much enhancement from flow and the relative enhancement decreases with decreasing sensor size in agreement with the theoretical calculations by Sheehan and Whitman³¹⁴ for nanobiosensors. Increasing the flow rate even further decreases the settling times in both cases, and the planar diffusion model replicates the radial diffusion model, demonstrating that the enhancement of radial diffusion is negligible under enough flow.

The decrease in the settling time due to radial diffusion can be understood by considering the growth of the depletion region due to an increase in depletion width of a planar versus a nanowire sensor. The depletion region can be thought of as the region from which analyte can be captured. Increasing the size of this region increases the effective capture area of the sensor. However, increasing the size of the depletion region also increases how far the nearest capturable analyte must travel to reach the sensor. This is the reason diffusion slowdown is observed. For sensors with radial diffusion, the increase in depletion region with depletion width is greater than that for planar sensors. In other words, the relative area from which a nanowire sensor can capture the analyte is greater than a planar sensor at the same depletion widths. The sensor response for cylindrical sensors scales with $\sim t$, while planar sensors scale with $\sim t^{1/2}$.³¹⁵ The effect of flow is to compress the depletion region due to a constant influx of the analyte towards the sensor. Flow has a greater effect on the planar diffusion model because it depletes the solution more rapidly in one dimension, i.e., C_D/A_D decreases with time more rapidly. Conversely, the radial

diffusion model does not deplete the solution as rapidly so the constant influx of the analyte that flow provides has less of an effect.

In both models, the settling time decreases with the sensor size, eventually approaching the reaction limited regime. As the analyte flows past a sensor, it is more likely to first adsorb on the part of the sensor closest to the source. Subsequently, the parts of the sensor further downstream see a lower effective concentration of the analyte. Decreasing the sensor length (along the flow direction) limits the length that this concentration drop can occur and therefore decreases the settling time. These results suggest that, under flow, nanowires will have much lower settling times than purely due to their smaller dimensions. However, this is on a per area basis. Although a smaller sensor reaches a certain #/area of bound molecules more rapidly, a larger sensor has a larger area to capture the analyte.

C.2.2 Effect of flow rate on settling time

Figure C.4c,d shows the effect of the changing flow rate on settling time at two different sensor lengths. In contrast to Figure C.4a,b where the sensor size was varied at two different, static flow rates, the effect of radial diffusion does not change within each individual plot. Similar to changing the sensor radius, increasing the flow rate decreases the settling time for both the planar diffusion and the radial diffusion models, with the planar model benefitting much more from flow. Under moderate flow rates, both models become identical regardless of the sensor size. For the 10 μm sensor, moderate flow rates are needed to see a significant decrease in the settling time for the radial diffusion model, while the planar diffusion model benefits greatly from even minute amounts of flow. As

previously mentioned, the planar diffusion model most likely overestimates the settling time at very low flow rates (below $\sim 0.3 Pe_H$ in these conditions). Neither model approaches the reaction limited regime with even very large flow rates. In contrast, with a 10 nm sensor, the radial diffusion model approaches the reaction limited regime without flow, and the planar diffusion model needs minimal flow to reach the reaction limited regime, further demonstrating the significance of sensor size. These results further demonstrate that enhancement of radial diffusion becomes negligible under flow. This suggests that nanoribbon sensors should possess comparable performance to nanowire sensors under flow, from a mass transport perspective. However, nanoribbon sensors can provide advantages in terms of ease of fabrication.

C.2.3 Effect of changing channel height on settling time

Figure C.4d,e shows the effects of changing the channel height on the settling time at two different flow rates, while holding sensor dimensions constant. Changing the channel height at a constant sensor length and flow lets us examine the effect of changing Pe_s at a constant Pe_H . In other words, changing the channel height under these conditions limits the growth of the depletion region, while the characteristics of the flow with respect to the channel do not change. The effect of channel height in the purely diffusive case is not being considered here. At moderate flows, decreasing the channel height has a limited effect on the settling time, reducing the settling time by less than an order of magnitude over four orders of magnitude of change in height. The effect is much more pronounced at high flow rates, with the settling time approaching the reaction limited limit at low heights.

At both flow rates considered here, the planar diffusion model is comparable to the radial diffusion model.

In the case where $Pe_s \ll 1$, the depletion width is larger than the sensor and δ_f scales with $Pe_s^{-1/2}$. As the height is lowered, the depletion width becomes increasingly smaller, and the flow that the sensor response becomes less parabolic and more linear. For the case where $Pe_s \gg 1$, the depletion width becomes comparable with the sensor size and δ_f scales with $Pe_s^{-1/3}$. When this transition point is reached, the effect of the channel height on the settling time increases noticeably. The overall effect is more pronounced at higher flows because the effect of height on Pe_s is larger at higher flows. From these results, it seems that the reaction limited regime can be reached by simply reducing the channel height regardless of whether radial or planar diffusion is considered. However, decreasing the height to the micrometer scale causes the pressure developed within the channel, at the flow rates used here, to reach extreme values beyond realistic working conditions.

C.3 Conclusions

In this appendix, a general model for binding to planar and nanowire sensors under the effects of both diffusion and convection was developed. The model approximated experimental binding data under a wide variety of conditions quite well. The model was used to draw comparisons between mass transport under planar and radial diffusion with flow and it was found that the increased mass transport to nanowires due to radial diffusion is negligible given enough flow. Moderate flow rates greatly reduced the settling time of planar sensors, whereas nanowire sensors, already possessing rapid mass transport from

radial diffusion, did not benefit as significantly. However, decreasing the sensor size under flow was found to greatly reduce settling times. 10 nm sensors were able to reach the reaction limited regime regardless of the type of diffusion, whereas 10 μm sensors could not under the flow rates used here. Under flow conditions in typical experiments, radial diffusion associated with nanowire sensors is inessential for fast mass transport. Instead, the small sensor length in the flow direction limits the concentration drop that can occur as the analyte flows past the sensor. Similarly, decreasing the channel height decreases the settling time, but to a lesser extent. Although both planar and radial diffusion models were shown to be able to reach the reaction limited regime, this regime may still require incubation time on the order of hours to detect an appreciable response depending on the required number of molecules for detection and diffusion coefficient of the analyte. To further improve the limit of detection of biosensors, it is critical to reduce the number of molecules required for detection or investigate strategies involving increasing k_a , e.g., through electrostatic attraction.³¹⁶ The former may be where nanobiosensors prove to be beneficial.^{317, 318}

REFERENCES

1. Kaisti, M., Detection principles of biological and chemical FET sensors. *Biosensors Bioelectron.* **2017**, *98*, 437-448.
2. Brightbill, E. L.; Hitchcock, B.; Tsai, M.-Y.; Verga, A.; Vogel, E. M., Preblocking Procedure to Mitigate Nonselective Protein Adsorption for Carboxyl-SAMs Used in Biosensing. *The Journal of Physical Chemistry C* **2019**, *123* (27), 16778-16786.
3. Brightbill, E. L.; Gezahagne, H. F.; Jin, D. S.; Brown, B.; Vogel, E. M., Protein blocking inhibits ambient degradation of self-assembled monolayers for affinity biosensing. *Applied Surface Science* **2021**, 149843.
4. Brightbill, E.; Young, K.; Gezahagne, H. F.; Jin, D. S.; Hitchcock, B.; Vogel, E., Protein interactions with chemical vapor deposited graphene modified by substrate. *2D Materials* **2021**.
5. Jin, D. S.; Brightbill, E. L.; Vogel, E. M., General model for mass transport to planar and nanowire biosensor surfaces. *Journal of Applied Physics* **2019**, *125* (11), 114502.
6. Wu, L.; Qu, X., Cancer biomarker detection: recent achievements and challenges. *Chemical Society Reviews* **2015**, *44* (10), 2963-2997.
7. Mishra, G. K.; Barfidokht, A.; Tehrani, F.; Mishra, R. K., Food safety analysis using electrochemical biosensors. *Foods* **2018**, *7* (9), 141.
8. Skelley, A. M.; Scherer, J. R.; Aubrey, A. D.; Grover, W. H.; Ivester, R. H.; Ehrenfreund, P.; Grunthaner, F. J.; Bada, J. L.; Mathies, R. A., Development and evaluation of a microdevice for amino acid biomarker detection and analysis on Mars. *Proceedings of the National Academy of Sciences* **2005**, *102* (4), 1041-1046.
9. Wise, R. A.; Robble, M. A., Dopamine and addiction. *Annual review of psychology* **2020**, *71*, 79-106.
10. Yalow, R. S.; Berson, S. A., Immunoassay of endogenous plasma insulin in man. *The Journal of clinical investigation* **1960**, *39* (7), 1157-1175.
11. Prevention, C. f. D. C. a. Understanding the EIA Test. <https://www.cdc.gov/lyme/diagnosistesting/labtest/twostep/eia/index.html>.

12. Lequin, R. M., Enzyme immunoassay (EIA)/enzyme-linked immunosorbent assay (ELISA). *Clin. Chem.* **2005**, *51* (12), 2415-2418.
13. Boguszewska, K.; Szewczuk, M.; Urbaniak, S.; Karwowski, B. T., immunoassays in DNA damage and instability detection. *Cell. Mol. Life Sci.* **2019**, *76* (23), 4689-4704.
14. Schöning, M. J.; Poghossian, A., *Label-free biosensing: advanced materials, devices and applications*. Springer: 2018; Vol. 16.
15. Rhouati, A.; Catanante, G.; Nunes, G.; Hayat, A.; Marty, J.-L., Label-free aptasensors for the detection of mycotoxins. *Sensors* **2016**, *16* (12), 2178.
16. Kozma, P.; Hámori, A.; Kurunczi, S.; Cottier, K.; Horvath, R., Grating coupled optical waveguide interferometer for label-free biosensing. *Sensors Actuators B: Chem.* **2011**, *155* (2), 446-450.
17. Ouyang, X.; Liu, J.; Li, J.; Yang, R., A carbon nanoparticle-based low-background biosensing platform for sensitive and label-free fluorescent assay of DNA methylation. *Chemical Communications* **2012**, *48* (1), 88-90.
18. Wang, Y.; Yang, F.; Yang, X., Label-free colorimetric biosensing of copper (II) ions with unimolecular self-cleaving deoxyribozymes and unmodified gold nanoparticle probes. *Nanotechnology* **2010**, *21* (20), 205502.
19. Papadopoulou, E.; Bell, S. E., Label-free detection of single-base mismatches in DNA by surface-enhanced Raman spectroscopy. *Angewandte Chemie International Edition* **2011**, *50* (39), 9058-9061.
20. Fan, Z.; Kanchanapally, R.; Ray, P. C., Hybrid graphene oxide based ultrasensitive SERS probe for label-free biosensing. *The Journal of Physical Chemistry Letters* **2013**, *4* (21), 3813-3818.
21. Grist, S. M.; Schmidt, S. A.; Flueckiger, J.; Donzella, V.; Shi, W.; Fard, S. T.; Kirk, J. T.; Ratner, D. M.; Cheung, K. C.; Chrostowski, L., Silicon photonic micro-disk resonators for label-free biosensing. *Optics express* **2013**, *21* (7), 7994-8006.
22. Luchansky, M. S.; Washburn, A. L.; Martin, T. A.; Iqbal, M.; Gunn, L. C.; Bailey, R. C., Characterization of the evanescent field profile and bound mass sensitivity of a label-free silicon photonic microring resonator biosensing platform. *Biosensors Bioelectron.* **2010**, *26* (4), 1283-1291.

23. Chen, S.; Svedendahl, M.; Käll, M.; Gunnarsson, L.; Dmitriev, A., Ultrahigh sensitivity made simple: nanoplasmonic label-free biosensing with an extremely low limit-of-detection for bacterial and cancer diagnostics. *Nanotechnology* **2009**, *20* (43), 434015.
24. Li, X.; Song, S.; Shuai, Q.; Pei, Y.; Aastrup, T.; Pei, Y.; Pei, Z., Real-time and label-free analysis of binding thermodynamics of carbohydrate-protein interactions on unfixed cancer cell surfaces using a QCM biosensor. *Scientific reports* **2015**, *5*, 14066.
25. Yao, C.; Zhu, T.; Tang, J.; Wu, R.; Chen, Q.; Chen, M.; Zhang, B.; Huang, J.; Fu, W., Hybridization assay of hepatitis B virus by QCM peptide nucleic acid biosensor. *Biosensors Bioelectron.* **2008**, *23* (6), 879-885.
26. Wee, K. W.; Kang, G. Y.; Park, J.; Kang, J. Y.; Yoon, D. S.; Park, J. H.; Kim, T. S., Novel electrical detection of label-free disease marker proteins using piezoresistive self-sensing micro-cantilevers. *Biosensors Bioelectron.* **2005**, *20* (10), 1932-1938.
27. Arntz, Y.; Seelig, J. D.; Lang, H.; Zhang, J.; Hunziker, P.; Ramseyer, J.; Meyer, E.; Hegner, M.; Gerber, C., Label-free protein assay based on a nanomechanical cantilever array. *Nanotechnology* **2002**, *14* (1), 86.
28. Nath, N.; Chilkoti, A., Label-free biosensing by surface plasmon resonance of nanoparticles on glass: optimization of nanoparticle size. *Analytical Chemistry* **2004**, *76* (18), 5370-5378.
29. Homola, J., Present and future of surface plasmon resonance biosensors. *Anal. Bioanal. Chem.* **2003**, *377* (3), 528-539.
30. Hu, Y.; Wang, K.; Zhang, Q.; Li, F.; Wu, T.; Niu, L., Decorated graphene sheets for label-free DNA impedance biosensing. *Biomaterials* **2012**, *33* (4), 1097-1106.
31. Tsai, M.-Y.; Creedon, N.; Brightbill, E.; Pavlidis, S.; Brown, B.; Gray, D. W.; Shields, N.; Sayers, R.; Mooney, M. H.; O'Riordan, A., Direct correlation between potentiometric and impedance biosensing of antibody-antigen interactions using an integrated system. *Applied Physics Letters* **2017**, *111* (7), 073701.
32. Tarasov, A.; Gray, D. W.; Tsai, M.-Y.; Shields, N.; Montrose, A.; Creedon, N.; Lovera, P.; O'Riordan, A.; Mooney, M. H.; Vogel, E. M., A potentiometric biosensor for rapid on-site disease diagnostics. *Biosensors Bioelectron.* **2016**, *79*, 669-678.
33. Guo, X., Surface plasmon resonance based biosensor technique: a review. *Journal of biophotonics* **2012**, *5* (7), 483-501.

34. Ritchie, R. H., Plasma losses by fast electrons in thin films. *Physical review* **1957**, *106* (5), 874.
35. Das, G.; Coluccio, M.; Alrasheed, S.; Giugni, A.; Allione, M.; Torre, B.; Perozziello, G.; Candeloro, P.; Di Fabrizio, E., Plasmonic nanostructures for the ultrasensitive detection of biomolecules. *La Rivista del Nuovo Cimento* **2016**, *39*, 547-586.
36. Homola, J.; Yee, S. S.; Gauglitz, G., Surface plasmon resonance sensors. *Sensors Actuators B: Chem.* **1999**, *54* (1-2), 3-15.
37. Sepúlveda, B.; Angelomé, P. C.; Lechuga, L. M.; Liz-Marzán, L. M., LSPR-based nanobiosensors. *nano today* **2009**, *4* (3), 244-251.
38. Pattnaik, P., Surface plasmon resonance. *Appl. Biochem. Biotechnol.* **2005**, *126* (2), 79-92.
39. Nguyen, H. H.; Park, J.; Kang, S.; Kim, M., Surface plasmon resonance: a versatile technique for biosensor applications. *Sensors* **2015**, *15* (5), 10481-10510.
40. Mol, N. J.; Fischer, M. J., *Surface plasmon resonance: methods and protocols*. Springer: 2010.
41. Zijlstra, P.; Paulo, P. M.; Orrit, M., Optical detection of single non-absorbing molecules using the surface plasmon resonance of a gold nanorod. *Nature nanotechnology* **2012**, *7* (6), 379-382.
42. Ritzefeld, M.; Sewald, N., Real-time analysis of specific protein-DNA interactions with surface plasmon resonance. *Journal of amino acids* **2012**, *2012*.
43. Schasfoort, R. B., *Handbook of surface plasmon resonance*. Royal Society of Chemistry: 2017.
44. Goode, J.; Rushworth, J.; Millner, P., Biosensor regeneration: a review of common techniques and outcomes. *Langmuir* **2015**, *31* (23), 6267-6276.
45. Huang, Y.; Zhang, L.; Zhang, H.; Li, Y.; Liu, L.; Chen, Y.; Qiu, X.; Yu, D., Development of a Portable SPR Sensor for Nucleic Acid Detection. *Micromachines* **2020**, *11* (5), 526.
46. Trzaskowski, M.; Napiórkowska, A.; Augustynowicz-Kopec, E.; Ciach, T., Detection of tuberculosis in patients with the use of portable SPR device. *Sensors Actuators B: Chem.* **2018**, *260*, 786-792.

47. Naimushin, A. N.; Soelberg, S. D.; Bartholomew, D. U.; Elkind, J. L.; Furlong, C. E., A portable surface plasmon resonance (SPR) sensor system with temperature regulation. *Sensors Actuators B: Chem.* **2003**, *96* (1-2), 253-260.
48. Wang, S.; Xie, J.; Jiang, M.; Chang, K.; Chen, R.; Ma, L.; Zhu, J.; Guo, Q.; Sun, H.; Hu, J., The development of a portable SPR bioanalyzer for sensitive detection of escherichia coli O157: H7. *Sensors* **2016**, *16* (11), 1856.
49. Zhang, X.-l.; Liu, Y.; Fan, T.; Hu, N.; Yang, Z.; Chen, X.; Wang, Z.-y.; Yang, J., Design and performance of a portable and multichannel SPR device. *Sensors* **2017**, *17* (6), 1435.
50. Walter, J.-G.; Eilers, A.; Alwis, L. S. M.; Roth, B. W.; Bremer, K., SPR biosensor based on polymer multi-mode optical waveguide and nanoparticle signal enhancement. *Sensors* **2020**, *20* (10), 2889.
51. Prabowo, B. A.; Alom, A.; Secario, M. K.; Masim, F. C. P.; Lai, H.-C.; Hatanaka, K.; Liu, K.-C., Graphene-based portable SPR sensor for the detection of Mycobacterium tuberculosis DNA strain. *Procedia Engineering* **2016**, *168*, 541-545.
52. Breault-Turcot, J.; Masson, J.-F., Nanostructured substrates for portable and miniature SPR biosensors. *Anal. Bioanal. Chem.* **2012**, *403* (6), 1477-1484.
53. Capitan-Vallvey, L. F.; Palma, A. J., Recent developments in handheld and portable optosensing—A review. *Anal. Chim. Acta* **2011**, *696* (1-2), 27-46.
54. Bergveld, P., Development, operation, and application of the ion-sensitive field-effect transistor as a tool for electrophysiology. *IEEE Trans. Biomed. Eng.* **1972**, (5), 342-351.
55. Pachauri, V.; Ingebrandt, S., Biologically sensitive field-effect transistors: from ISFETs to NanofETs. *Essays in biochemistry* **2016**, *60* (1), 81-90.
56. Tsai, M.-Y.; Creedon, N.; Brightbill, E.; Pavlidis, S.; Brown, B.; Gray, D.; Shields, N.; Sayers, R.; H. Mooney, M.; O'Riordan, A.; Vogel, E., *Direct correlation between potentiometric and impedance biosensing of antibody-antigen interactions using an integrated system.* 2017; Vol. 111, p 073701.
57. Tarasov, A.; Tsai, M.-Y.; Flynn, E. M.; Joiner, C. A.; Taylor, R. C.; Vogel, E. M., Gold-coated graphene field-effect transistors for quantitative analysis of protein-antibody interactions. *2D Materials* **2015**, *2* (4), 044008.

58. Noor, M. O.; Krull, U. J., Silicon nanowires as field-effect transducers for biosensor development: A review. *Anal. Chim. Acta* **2014**, *825*, 1-25.
59. Zhan, B.; Li, C.; Yang, J.; Jenkins, G.; Huang, W.; Dong, X., Graphene Field-Effect Transistor and Its Application for Electronic Sensing. *Small* **2014**, *10* (20), 4042-4065.
60. Huang, Y.; Dong, X.; Shi, Y.; Li, C. M.; Li, L.-J.; Chen, P., Nanoelectronic biosensors based on CVD grown graphene. *Nanoscale* **2010**, *2* (8), 1485-1488.
61. Tang, X.; Bansaruntip, S.; Nakayama, N.; Yenilmez, E.; Chang, Y.-I.; Wang, Q., Carbon nanotube DNA sensor and sensing mechanism. *Nano Lett.* **2006**, *6* (8), 1632-1636.
62. Lee, J.; Dak, P.; Lee, Y.; Park, H.; Choi, W.; Alam, M. A.; Kim, S., Two-dimensional Layered MoS₂ Biosensors Enable Highly Sensitive Detection of Biomolecules. *Scientific Reports* **2014**, *4*, 7352.
63. Ding, J.; Qin, W., Recent advances in potentiometric biosensors. *TrAC Trends in Analytical Chemistry* **2020**, *124*, 115803.
64. Schasfoort, R. B.; Bergveld, P.; Kooyman, R.; Greve, J., Possibilities and limitations of direct detection of protein charges by means of an immunological field-effect transistor. *Anal. Chim. Acta* **1990**, *238*, 323-329.
65. Park, J.; Nguyen, H. H.; Woubit, A.; Kim, M., Applications of field-effect transistor (FET)-type biosensors. *Applied science and convergence technology* **2014**, *23* (2), 61-71.
66. Hinnemo, M.; Makaraviciute, A.; Ahlberg, P.; Olsson, J.; Zhang, Z.; Zhang, S.-L.; Zhang, Z.-B., Protein sensing beyond the Debye length using graphene field-effect transistors. *IEEE Sensors Journal* **2018**, *18* (16), 6497-6503.
67. Attard, P., Electrolytes and the electric double layer. *Advances in Chemical Physics* **1996**, *92*, 1-160.
68. Stern, E.; Wagner, R.; Sigworth, F. J.; Breaker, R.; Fahmy, T. M.; Reed, M. A., Importance of the Debye screening length on nanowire field effect transistor sensors. *Nano Lett.* **2007**, *7* (11), 3405-3409.
69. Chu, C.-H.; Sarangadharan, I.; Regmi, A.; Chen, Y.-W.; Hsu, C.-P.; Chang, W.-H.; Lee, G.-Y.; Chyi, J.-I.; Chen, C.-C.; Shiesh, S.-C., Beyond the Debye length in high ionic strength solution: direct protein detection with field-effect transistors (FETs) in human serum. *Scientific reports* **2017**, *7* (1), 1-15.

70. Star, A.; Gabriel, J.-C. P.; Bradley, K.; Grüner, G., Electronic detection of specific protein binding using nanotube FET devices. *Nano Lett.* **2003**, *3* (4), 459-463.
71. Gutiérrez-Sanz, Ó.; Andoy, N. M.; Filipiak, M. S.; Haustein, N.; Tarasov, A., Direct, label-free, and rapid transistor-based immunodetection in whole serum. *ACS sensors* **2017**, *2* (9), 1278-1286.
72. Kim, D.-S.; Park, J.-E.; Shin, J.-K.; Kim, P. K.; Lim, G.; Shoji, S., An extended gate FET-based biosensor integrated with a Si microfluidic channel for detection of protein complexes. *Sensors Actuators B: Chem.* **2006**, *117* (2), 488-494.
73. Lin, S.-P.; Pan, C.-Y.; Tseng, K.-C.; Lin, M.-C.; Chen, C.-D.; Tsai, C.-C.; Yu, S.-H.; Sun, Y.-C.; Lin, T.-W.; Chen, Y.-T., A reversible surface functionalized nanowire transistor to study protein-protein interactions. *Nano Today* **2009**, *4* (3), 235-243.
74. Bogomolova, A.; Komarova, E.; Reber, K.; Gerasimov, T.; Yavuz, O.; Bhatt, S.; Aldissi, M., Challenges of electrochemical impedance spectroscopy in protein biosensing. *Analytical Chemistry* **2009**, *81* (10), 3944-3949.
75. Piliarik, M.; Vaisocherová, H.; Homola, J., Surface plasmon resonance biosensing. In *Biosensors and Biodetection*, Springer: 2009; pp 65-88.
76. Ronkainen, N. J.; Halsall, H. B.; Heineman, W. R., Electrochemical biosensors. *Chemical Society Reviews* **2010**, *39* (5), 1747-1763.
77. Benedek, K.; Dong, S.; Karger, B., Kinetics of unfolding of proteins on hydrophobic surfaces in reversed-phase liquid chromatography. *J. Chromatogr.* **1984**, *317*, 227-243.
78. Jungbauer, A.; Machold, C.; Hahn, R., Hydrophobic interaction chromatography of proteins: III. Unfolding of proteins upon adsorption. *J. Chromatogr.* **2005**, *1079* (1-2), 221-228.
79. Roach, P.; Farrar, D.; Perry, C. C., Interpretation of protein adsorption: surface-induced conformational changes. *J. Am. Chem. Soc.* **2005**, *127* (22), 8168-8173.
80. Alberts, B.; Johnson, A.; Lewis, J.; Raff, M.; Roberts, K.; Walter, P., The shape and structure of proteins. In *Molecular Biology of the Cell. 4th edition*, Garland Science: 2002.
81. Meister, A., *Biochemistry of the amino acids*. Elsevier: 2012.

82. Wilson, R. P., Amino acids and proteins. In *Fish nutrition*, Elsevier: 2003; pp 143-179.
83. Gupta, R.; Dey, A.; Vijan, A.; Gartia, B., In Silico Structure Modeling and Characterization of Hypothetical Protein YP_004590319. 1 Present in Enterobacter aerogens. *J Proteomics Bioinform* **2017**, *10*, 152-170.
84. Latour, R. A., Biomaterials: protein-surface interactions. *Encyclopedia of biomaterials and biomedical engineering* **2005**, *1*, 270-278.
85. Petsko, G. A.; Ringe, D., *Protein structure and function*. New Science Press: 2004.
86. Branden, C. I.; Tooze, J., *Introduction to protein structure*. Garland Science: 2012.
87. Onuchic, J. N.; Wolynes, P. G., Theory of protein folding. *Curr. Opin. Struct. Biol.* **2004**, *14* (1), 70-75.
88. Schulz, G. E.; Schirmer, R. H., *Principles of protein structure*. Springer Science & Business Media: 2013.
89. Pratt, L. R.; Chandler, D., Theory of the hydrophobic effect. *The Journal of chemical physics* **1977**, *67* (8), 3683-3704.
90. Walker, C., *The Hydrophobic Effect: Formation of Micelles and Biological Membranes*: by C. Tanford Wiley; Brisbane, Chichester, New York, Toronto, 1980 x+ 233 pages.£ 11.75. Wiley Online Library: 1981.
91. Narten, A.; Danford, M.; Levy, H., X-ray diffraction study of liquid water in the temperature range 4–200 C. *Discussions of the Faraday Society* **1967**, *43*, 97-107.
92. Mark, P.; Nilsson, L., Structure and dynamics of liquid water with different long-range interaction truncation and temperature control methods in molecular dynamics simulations. *Journal of Computational Chemistry* **2002**, *23* (13), 1211-1219.
93. Kusalik, P. G.; Svishchev, I. M., The spatial structure in liquid water. *Science* **1994**, *265* (5176), 1219-1221.
94. Lanza, G.; Chiacchio, M. A., The water molecule arrangement over the side chain of some aliphatic amino acids: A quantum chemical and bottom-up investigation. *International Journal of Quantum Chemistry* **2020**, *120* (9), e26161.

95. Haselmeier, R.; Holz, M.; Marbach, W.; Weingaertner, H., Water dynamics near a dissolved noble gas. First direct experimental evidence for a retardation effect. *The Journal of Physical Chemistry* **1995**, *99* (8), 2243-2246.
96. Djikaev, Y.; Ruckenstein, E., Dependence of the number of hydrogen bonds per water molecule on its distance to a hydrophobic surface and a thereupon-based model for hydrophobic attraction. *The Journal of chemical physics* **2010**, *133* (19), 194105.
97. Lins, L.; Brasseur, R., The hydrophobic effect in protein folding. *The FASEB journal* **1995**, *9* (7), 535-540.
98. Rani, A.; Venkatesu, P., Changing relations between proteins and osmolytes: a choice of nature. *Physical Chemistry Chemical Physics* **2018**, *20* (31), 20315-20333.
99. Padlan, E. A., Anatomy of the antibody molecule. *Mol. Immunol.* **1994**, *31* (3), 169-217.
100. Davies, D. R.; Chacko, S., Antibody structure. *Accounts of chemical research* **1993**, *26* (8), 421-427.
101. Davies, D. R.; Metzger, H., Structural basis of antibody function. *Annu. Rev. Immunol.* **1983**, *1* (1), 87-115.
102. Stevens, N.; Cowin, A., Overcoming the challenges of topical antibody administration for improving healing outcomes: a review of recent laboratory and clinical approaches. *Wound Practice & Research: Journal of the Australian Wound Management Association* **2017**.
103. Zhang, J. X.; Hoshino, K., *Molecular Sensors and Nanodevices: Principles, Designs and Applications in Biomedical Engineering*. Academic Press: 2018.
104. Braden, B. C.; Dall'Acqua, W.; Eisenstein, E.; Fields, B. A.; Goldbaum, F. A.; Malchiodi, E. L.; Mariuzza, R. A.; Schwarz, F. P.; Ysern, X.; Poljak, R. J., Protein motion and lock and key complementarity in antigen-antibody reactions. *Pharmaceutica Acta Helvetiae* **1995**, *69* (4), 225-230.
105. Edwards, P. R.; Gill, A.; Pollardknight, D. V.; Hoare, M.; Buckle, P. E.; Lowe, P. A.; Leatherbarrow, R. J., Kinetics of protein-protein interactions at the surface of an optical biosensor. *Anal. Biochem.* **1995**, *231* (1), 210-217.
106. Guo, H.; Zhou, X.; Zhang, Y.; Gu, C.; Song, B.; Shi, H., Kinetic analysis of a high-affinity antibody/antigen interaction performed by planar waveguide fluorescence immunosensor. *RSC advances* **2016**, *6* (17), 13837-13845.

107. Landry, J. P.; Fei, Y.; Zhu, X., Simultaneous measurement of 10,000 protein-ligand affinity constants using microarray-based kinetic constant assays. *Assay Drug Dev. Technol.* **2012**, *10* (3), 250-259.
108. Liu, Y.; Shen, L., From Langmuir kinetics to first-and second-order rate equations for adsorption. *Langmuir* **2008**, *24* (20), 11625-11630.
109. Langmuir, I., The adsorption of gases on plane surfaces of glass, mica and platinum. *J. Am. Chem. Soc.* **1918**, *40* (9), 1361-1403.
110. Myszka, D. G.; He, X.; Dembo, M.; Morton, T. A.; Goldstein, B., Extending the range of rate constants available from BIACORE: interpreting mass transport-influenced binding data. *Biophys. J.* **1998**, *75* (2), 583-594.
111. Dinh, T. L.; Ngan, K. C.; Shoemaker, C. B.; Walt, D. R., Using antigen-antibody binding kinetic parameters to understand single-molecule array immunoassay performance. *Analytical chemistry* **2016**, *88* (23), 11335-11339.
112. Glaser, R. W., Antigen-antibody binding and mass transport by convection and diffusion to a surface: a two-dimensional computer model of binding and dissociation kinetics. *Anal. Biochem.* **1993**, *213* (1), 152-161.
113. Rabe, M.; Verdes, D.; Seeger, S., Understanding protein adsorption phenomena at solid surfaces. *Advances in colloid and interface science* **2011**, *162* (1-2), 87-106.
114. Andrade, J.; Hlady, V.; Wei, A., Adsorption of complex proteins at interfaces. *Pure and applied chemistry* **1992**, *64* (11), 1777-1781.
115. Norde, W., Driving forces for protein adsorption at solid surfaces. *Biopolymers at interfaces* **2003**, *110*.
116. Norde, W.; Giacomelli, C. E., BSA structural changes during homomolecular exchange between the adsorbed and the dissolved states. *J. Biotechnol.* **2000**, *79* (3), 259-268.
117. Wertz, C. F.; Santore, M. M., Adsorption and reorientation kinetics of lysozyme on hydrophobic surfaces. *Langmuir* **2002**, *18* (4), 1190-1199.
118. Norde, W. In *Driving forces for protein adsorption at solid surfaces*, Macromolecular Symposia, Wiley Online Library: 1996; pp 5-18.
119. Prime, K. L.; Whitesides, G. M., Self-assembled organic monolayers: model systems for studying adsorption of proteins at surfaces. *Science* **1991**, 1164-1167.

120. Raffaini, G.; Ganazzoli, F., Protein adsorption on a hydrophobic surface: a molecular dynamics study of lysozyme on graphite. *Langmuir* **2009**, *26* (8), 5679-5689.
121. Sharp, K. A.; Nicholls, A.; Friedman, R.; Honig, B., Extracting hydrophobic free energies from experimental data: relationship to protein folding and theoretical models. *Biochemistry* **1991**, *30* (40), 9686-9697.
122. Poncin-Epaillard, F.; Vrlinic, T.; Debarnot, D.; Mozetic, M.; Coudreuse, A.; Legeay, G.; El Moualij, B.; Zorzi, W., Surface treatment of polymeric materials controlling the adhesion of biomolecules. *Journal of functional biomaterials* **2012**, *3* (3), 528-543.
123. Krishnan, S.; Weinman, C. J.; Ober, C. K., Advances in polymers for anti-biofouling surfaces. *Journal of Materials Chemistry* **2008**, *18* (29), 3405-3413.
124. Zhang, P.; Lin, L.; Zang, D.; Guo, X.; Liu, M., Designing Bioinspired Anti-Biofouling Surfaces based on a Superwettability Strategy. *Small* **2017**, *13* (4), 1503334.
125. Koutsoukos, P.; Norde, W.; Lyklema, J., Protein adsorption on hematite (α -Fe₂O₃) surfaces. *J. Colloid Interface Sci.* **1983**, *95* (2), 385-397.
126. Bremer, M. G.; Duval, J.; Norde, W.; Lyklema, J., Electrostatic interactions between immunoglobulin (IgG) molecules and a charged sorbent. *Colloids Surf. Physicochem. Eng. Aspects* **2004**, *250* (1-3), 29-42.
127. Demanèche, S.; Chapel, J.-P.; Monrozier, L. J.; Quiquampoix, H., Dissimilar pH-dependent adsorption features of bovine serum albumin and α -chymotrypsin on mica probed by AFM. *Colloids Surf. B. Biointerfaces* **2009**, *70* (2), 226-231.
128. Höök, F.; Rodahl, M.; Brzezinski, P.; Kasemo, B., Measurements using the quartz crystal microbalance technique of ferritin monolayers on methyl-thiolated gold: dependence of energy dissipation and saturation coverage on salt concentration. *J. Colloid Interface Sci.* **1998**, *208* (1), 63-67.
129. Jones, K. L.; O'Melia, C. R., Protein and humic acid adsorption onto hydrophilic membrane surfaces: effects of pH and ionic strength. *J. Membr. Sci.* **2000**, *165* (1), 31-46.
130. Wahlgren, M.; Elofsson, U., Simple models for adsorption kinetics and their correlation to the adsorption of β -lactoglobulin A and B. *J. Colloid Interface Sci.* **1997**, *188* (1), 121-129.
131. Kurrat, R.; Prenosil, J.; Ramsden, J., Kinetics of human and bovine serum albumin adsorption at silica-titania surfaces. *J. Colloid Interface Sci.* **1997**, *185* (1), 1-8.

132. Rabe, M.; Verdes, D.; Zimmermann, J.; Seeger, S., Surface organization and cooperativity during nonspecific protein adsorption events. *The Journal of Physical Chemistry B* **2008**, *112* (44), 13971-13980.
133. Bigelow, W.; Pickett, D.; Zisman, W., Oleophobic monolayers: I. Films adsorbed from solution in non-polar liquids. *Journal of Colloid Science* **1946**, *1* (6), 513-538.
134. Ulman, A., Formation and structure of self-assembled monolayers. *Chemical reviews* **1996**, *96* (4), 1533-1554.
135. Love, J. C.; Estroff, L. A.; Kriebel, J. K.; Nuzzo, R. G.; Whitesides, G. M., Self-Assembled Monolayers of Thiolates on Metals as a Form of Nanotechnology. *Chemical Reviews* **2005**, *105* (4), 1103-1170.
136. Vericat, C.; Vela, M.; Benitez, G.; Carro, P.; Salvarezza, R., Self-assembled monolayers of thiols and dithiols on gold: new challenges for a well-known system. *Chemical Society Reviews* **2010**, *39* (5), 1805-1834.
137. Kim, J.-M.; Baek, C.-W.; Park, J.-H.; Shin, D.-S.; Lee, Y.-S.; Kim, Y.-K., Continuous anti-stiction coatings using self-assembled monolayers for gold microstructures. *Journal of Micromechanics and Microengineering* **2002**, *12* (5), 688.
138. Kane, R. S.; Takayama, S.; Ostuni, E.; Ingber, D. E.; Whitesides, G. M., Patterning proteins and cells using soft lithography. In *The Biomaterials: Silver Jubilee Compendium*, Elsevier: 1999; pp 161-174.
139. Campbell, I.; Kress, J.; Martin, R.; Smith, D.; Barashkov, N.; Ferraris, J., Controlling charge injection in organic electronic devices using self-assembled monolayers. *Applied Physics Letters* **1997**, *71* (24), 3528-3530.
140. Frasconi, M.; Mazzei, F.; Ferri, T., Protein immobilization at gold-thiol surfaces and potential for biosensing. *Anal. Bioanal. Chem.* **2010**, *398* (4), 1545-1564.
141. Dubois, L. H.; Nuzzo, R. G., Synthesis, structure, and properties of model organic surfaces. *Annual review of physical chemistry* **1992**, *43* (1), 437-463.
142. Luo, Y.-R., *Comprehensive handbook of chemical bond energies*. CRC press: 2007.
143. Bain, C. D.; Troughton, E. B.; Tao, Y. T.; Evall, J.; Whitesides, G. M.; Nuzzo, R. G., Formation of monolayer films by the spontaneous assembly of organic thiols from solution onto gold. *J. Am. Chem. Soc.* **1989**, *111* (1), 321-335.

144. Strong, L.; Whitesides, G. M., Structures of self-assembled monolayer films of organosulfur compounds adsorbed on gold single crystals: electron diffraction studies. *Langmuir* **1988**, *4* (3), 546-558.
145. Fischer, M. J., Amine coupling through EDC/NHS: a practical approach. In *Surface plasmon resonance*, Springer: 2010; pp 55-73.
146. O'Shannessy, D. J.; Brigham-Burke, M.; Peck, K., Immobilization chemistries suitable for use in the BIAcore surface plasmon resonance detector. *Anal. Biochem.* **1992**, *205* (1), 132-136.
147. Chaki, N. K.; Vijayamohan, K., Self-assembled monolayers as a tunable platform for biosensor applications. *Biosensors Bioelectron.* **2002**, *17* (1-2), 1-12.
148. Shervedani, R. K.; Mehrjardi, A. H.; Zamiri, N., A novel method for glucose determination based on electrochemical impedance spectroscopy using glucose oxidase self-assembled biosensor. *Bioelectrochemistry* **2006**, *69* (2), 201-208.
149. Subramanian, A.; Irudayaraj, J.; Ryan, T., A mixed self-assembled monolayer-based surface plasmon immunosensor for detection of E. coli O157: H7. *Biosensors Bioelectron.* **2006**, *21* (7), 998-1006.
150. Campuzano, S.; Serra, B.; Pedrero, M. a.; de Villena, F. J. M.; Pingarrón, J. M., Amperometric flow-injection determination of phenolic compounds at self-assembled monolayer-based tyrosinase biosensors. *Anal. Chim. Acta* **2003**, *494* (1-2), 187-197.
151. Duan, C.; Meyerhoff, M. E., Separation-Free Sandwich Enzyme Immunoassays Using Microporous Gold Electrodes and Self-Assembled Monolayer/Immobilized Capture Antibodies. *Analytical Chemistry* **1994**, *66* (9), 1369-1377.
152. Willner, I.; Katz, E.; Riklin, A.; Kasher, R., Mediated electron transfer in glutathione reductase organized in self-assembled monolayers on gold electrodes. *J. Am. Chem. Soc.* **1992**, *114* (27), 10965-10966.
153. Collinson, M.; Bowden, E. F.; Tarlov, M. J., Voltammetry of covalently immobilized cytochrome c on self-assembled monolayer electrodes. *Langmuir* **1992**, *8* (5), 1247-1250.
154. Malem, F.; Mandler, D., Self-assembled monolayers in electroanalytical chemistry: application of omega.-mercapto carboxylic acid monolayers for the electrochemical detection of dopamine in the presence of a high concentration of ascorbic acid. *Analytical Chemistry* **1993**, *65* (1), 37-41.

155. Su, X.-L.; Li, Y., A self-assembled monolayer-based piezoelectric immunosensor for rapid detection of Escherichia coli O157: H7. *Biosensors Bioelectron.* **2004**, *19* (6), 563-574.
156. Caruso, F.; Rodda, E.; Furlong, D. N.; Niikura, K.; Okahata, Y., Quartz crystal microbalance study of DNA immobilization and hybridization for nucleic acid sensor development. *Analytical Chemistry* **1997**, *69* (11), 2043-2049.
157. Spangler, B. D.; Tyler, B. J., Capture agents for a quartz crystal microbalance-continuous flow biosensor: functionalized self-assembled monolayers on gold. *Anal. Chim. Acta* **1999**, *399* (1-2), 51-62.
158. Maehashi, K.; Katsura, T.; Kerman, K.; Takamura, Y.; Matsumoto, K.; Tamiya, E., Label-free protein biosensor based on aptamer-modified carbon nanotube field-effect transistors. *Analytical Chemistry* **2007**, *79* (2), 782-787.
159. Ohno, Y.; Maehashi, K.; Matsumoto, K., Label-free biosensors based on aptamer-modified graphene field-effect transistors. *J. Am. Chem. Soc.* **2010**, *132* (51), 18012-18013.
160. Rickert, J.; Brecht, A.; Göpel, W., Quartz crystal microbalances for quantitative biosensing and characterizing protein multilayers. *Biosensors Bioelectron.* **1997**, *12* (7), 567-575.
161. Arnold, R.; Azzam, W.; Terfort, A.; Wöll, C., Preparation, modification, and crystallinity of aliphatic and aromatic carboxylic acid terminated self-assembled monolayers. *Langmuir* **2002**, *18* (10), 3980-3992.
162. Chidsey, C. E. D.; Loiacono, D. N., Chemical functionality in self-assembled monolayers: structural and electrochemical properties. *Langmuir* **1990**, *6* (3), 682-691.
163. Lee, J. K.; Kim, Y.-G.; Chi, Y. S.; Yun, W. S.; Choi, I. S., Grafting nitrilotriacetic groups onto carboxylic acid-terminated self-assembled monolayers on gold surfaces for immobilization of histidine-tagged proteins. *The Journal of Physical Chemistry B* **2004**, *108* (23), 7665-7673.
164. Wang, H.; Chen, S.; Li, L.; Jiang, S., Improved method for the preparation of carboxylic acid and amine terminated self-assembled monolayers of alkanethiolates. *Langmuir* **2005**, *21* (7), 2633-2636.
165. Schreiber, F., Structure and growth of self-assembling monolayers. *Progress in surface science* **2000**, *65* (5-8), 151-257.

166. Jin, H.; Dong, S.; Wang, D., Measurement of dielectric constant of thin film materials at microwave frequencies. *Journal of Electromagnetic Waves and Applications* **2009**, *23* (5-6), 809-817.
167. Choi, S.; Chae, J., Methods of reducing non-specific adsorption in microfluidic biosensors. *Journal of Micromechanics and Microengineering* **2010**, *20* (7), 075015.
168. Schoenfish, M. H.; Pemberton, J. E., Air stability of alkanethiol self-assembled monolayers on silver and gold surfaces. *J. Am. Chem. Soc.* **1998**, *120* (18), 4502-4513.
169. Yang, G.; Amro, N. A.; Starkewolfe, Z. B.; Liu, G.-y., Molecular-Level Approach To Inhibit Degradations of Alkanethiol Self-Assembled Monolayers in Aqueous Media. *Langmuir* **2004**, *20* (10), 3995-4003.
170. Willey, T. M.; Vance, A. L.; Van Buuren, T.; Bostedt, C.; Terminello, L.; Fadley, C., Rapid degradation of alkanethiol-based self-assembled monolayers on gold in ambient laboratory conditions. *Surface Science* **2005**, *576* (1-3), 188-196.
171. Lee, M.-T.; Hsueh, C.-C.; Freund, M. S.; Ferguson, G. S., Air oxidation of self-assembled monolayers on polycrystalline gold: the role of the gold substrate. *Langmuir* **1998**, *14* (22), 6419-6423.
172. Vericat, C.; Benitez, G. A.; Grumelli, D. E.; Vela, M. E.; Salvarezza, R. C., Thiol-capped gold: from planar to irregular surfaces. *Journal of Physics: Condensed Matter* **2008**, *20* (18), 184004.
173. Novoselov, K. S.; Geim, A. K.; Morozov, S. V.; Jiang, D.; Zhang, Y.; Dubonos, S. V.; Grigorieva, I. V.; Firsov, A. A., Electric Field Effect in Atomically Thin Carbon Films. *Science* **2004**, *306* (5696), 666-669.
174. Gupta, A.; Sakthivel, T.; Seal, S., Recent development in 2D materials beyond graphene. *Progress in Materials Science* **2015**, *73*, 44-126.
175. Butler, S. Z.; Hollen, S. M.; Cao, L.; Cui, Y.; Gupta, J. A.; Gutiérrez, H. R.; Heinz, T. F.; Hong, S. S.; Huang, J.; Ismach, A. F., Progress, challenges, and opportunities in two-dimensional materials beyond graphene. *ACS nano* **2013**, *7* (4), 2898-2926.
176. Mas-Balleste, R.; Gomez-Navarro, C.; Gomez-Herrero, J.; Zamora, F., 2D materials: to graphene and beyond. *Nanoscale* **2011**, *3* (1), 20-30.
177. Revard, B. C.; Tipton, W. W.; Yesypenko, A.; Hennig, R. G., Grand-canonical evolutionary algorithm for the prediction of two-dimensional materials. *Physical Review B* **2016**, *93* (5), 054117.

178. Lebègue, S.; Björkman, T.; Klintenberg, M.; Nieminen, R. M.; Eriksson, O., Two-dimensional materials from data filtering and ab initio calculations. *Physical Review X* **2013**, *3* (3), 031002.
179. Jayakumar, A.; Surendranath, A.; Mohanan, P., 2D materials for next generation healthcare applications. *Int. J. Pharm.* **2018**, *551* (1-2), 309-321.
180. Kurapati, R.; Kostarelos, K.; Prato, M.; Bianco, A., Biomedical uses for 2D materials beyond graphene: current advances and challenges ahead. *Advanced Materials* **2016**, *28* (29), 6052-6074.
181. Chimene, D.; Alge, D. L.; Gaharwar, A. K., Two-dimensional nanomaterials for biomedical applications: emerging trends and future prospects. *Advanced Materials* **2015**, *27* (45), 7261-7284.
182. Xing, W.; Lalwani, G.; Rusakova, I.; Sitharaman, B., Degradation of graphene by hydrogen peroxide. *Particle & Particle Systems Characterization* **2014**, *31* (7), 745-750.
183. Kuila, T.; Bose, S.; Khanra, P.; Mishra, A. K.; Kim, N. H.; Lee, J. H., Recent advances in graphene-based biosensors. *Biosensors Bioelectron.* **2011**, *26* (12), 4637-4648.
184. Holzinger, M.; Le Goff, A.; Cosnier, S., Nanomaterials for biosensing applications: a review. *Frontiers in chemistry* **2014**, *2*, 63.
185. Shao, Y.; Wang, J.; Wu, H.; Liu, J.; Aksay, I. A.; Lin, Y., Graphene based electrochemical sensors and biosensors: a review. *Electroanalysis: An International Journal Devoted to Fundamental and Practical Aspects of Electroanalysis* **2010**, *22* (10), 1027-1036.
186. Serrano, M.; Patino, J.; García-Rama, C.; Ferrer, M.; Fierro, J.; Tamayo, A.; Collazos-Castro, J.; Del Monte, F.; Gutierrez, M., 3D free-standing porous scaffolds made of graphene oxide as substrates for neural cell growth. *Journal of Materials Chemistry B* **2014**, *2* (34), 5698-5706.
187. Yin, W.; Yan, L.; Yu, J.; Tian, G.; Zhou, L.; Zheng, X.; Zhang, X.; Yong, Y.; Li, J.; Gu, Z., High-throughput synthesis of single-layer MoS₂ nanosheets as a near-infrared photothermal-triggered drug delivery for effective cancer therapy. *ACS nano* **2014**, *8* (7), 6922-6933.
188. Zhang, L.; Xia, J.; Zhao, Q.; Liu, L.; Zhang, Z., Functional graphene oxide as a nanocarrier for controlled loading and targeted delivery of mixed anticancer drugs. *small* **2010**, *6* (4), 537-544.

189. Cheng, L.; Liu, J.; Gu, X.; Gong, H.; Shi, X.; Liu, T.; Wang, C.; Wang, X.; Liu, G.; Xing, H., PEGylated WS₂ nanosheets as a multifunctional theranostic agent for in vivo dual-modal CT/photoacoustic imaging guided photothermal therapy. *Advanced materials* **2014**, *26* (12), 1886-1893.
190. Zhang, X.; Xie, X.; Wang, H.; Zhang, J.; Pan, B.; Xie, Y., Enhanced photoresponsive ultrathin graphitic-phase C₃N₄ nanosheets for bioimaging. *J. Am. Chem. Soc.* **2012**, *135* (1), 18-21.
191. Demirel, M. C.; Vural, M.; Terrones, M., Composites of proteins and 2D nanomaterials. *Advanced Functional Materials* **2018**, *28* (27), 1704990.
192. Alava, T.; Mann, J. A.; Théodore, C.; Benitez, J. J.; Dichtel, W. R.; Parpia, J. M.; Craighead, H. G., Control of the Graphene-Protein Interface Is Required To Preserve Adsorbed Protein Function. *Analytical Chemistry* **2013**, *85* (5), 2754-2759.
193. Tang, Z.; Wu, H.; Cort, J. R.; Buchko, G. W.; Zhang, Y.; Shao, Y.; Aksay, I. A.; Liu, J.; Lin, Y., Constraint of DNA on functionalized graphene improves its biostability and specificity. *Small* **2010**, *6* (11), 1205-1209.
194. Justino, C. I.; Gomes, A. R.; Freitas, A. C.; Duarte, A. C.; Rocha-Santos, T. A., Graphene based sensors and biosensors. *TrAC Trends in Analytical Chemistry* **2017**, *91*, 53-66.
195. Wang, L.; Xiong, Q.; Xiao, F.; Duan, H., 2D nanomaterials based electrochemical biosensors for cancer diagnosis. *Biosensors Bioelectron.* **2017**, *89*, 136-151.
196. Song, Y.; Luo, Y.; Zhu, C.; Li, H.; Du, D.; Lin, Y., Recent advances in electrochemical biosensors based on graphene two-dimensional nanomaterials. *Biosensors Bioelectron.* **2016**, *76*, 195-212.
197. McCreery, R. L., Advanced carbon electrode materials for molecular electrochemistry. *Chemical reviews* **2008**, *108* (7), 2646-2687.
198. Wang, J., Carbon-nanotube based electrochemical biosensors: A review. *Electroanalysis: An International Journal Devoted to Fundamental and Practical Aspects of Electroanalysis* **2005**, *17* (1), 7-14.
199. Pumera, M.; Ambrosi, A.; Bonanni, A.; Chng, E. L. K.; Poh, H. L., Graphene for electrochemical sensing and biosensing. *TrAC Trends in Analytical Chemistry* **2010**, *29* (9), 954-965.

200. Pumera, M., The electrochemistry of carbon nanotubes: fundamentals and applications. *Chemistry—A European Journal* **2009**, *15* (20), 4970-4978.
201. Xu, S.; Zhan, J.; Man, B.; Jiang, S.; Yue, W.; Gao, S.; Guo, C.; Liu, H.; Li, Z.; Wang, J., Real-time reliable determination of binding kinetics of DNA hybridization using a multi-channel graphene biosensor. *Nature communications* **2017**, *8* (1), 1-10.
202. Tian, M.; Li, Z.; Song, R.; Li, Y.; Guo, C.; Sha, Y.; Cui, W.; Xu, S.; Hu, G.; Wang, J., Graphene biosensor as affinity biosensors for biorecognition between Guanine riboswitch and ligand. *Applied Surface Science* **2020**, *503*, 144303.
203. Kato, D.; Sekioka, N.; Ueda, A.; Kurita, R.; Hirono, S.; Suzuki, K.; Niwa, O., A nanocarbon film electrode as a platform for exploring DNA methylation. *J. Am. Chem. Soc.* **2008**, *130* (12), 3716-3717.
204. Alwarappan, S.; Liu, C.; Kumar, A.; Li, C.-Z., Enzyme-doped graphene nanosheets for enhanced glucose biosensing. *The Journal of Physical Chemistry C* **2010**, *114* (30), 12920-12924.
205. You, X.; Pak, J. J., Graphene-based field effect transistor enzymatic glucose biosensor using silk protein for enzyme immobilization and device substrate. *Sensors Actuators B: Chem.* **2014**, *202*, 1357-1365.
206. Pumera, M., Electrochemistry of graphene: new horizons for sensing and energy storage. *The Chemical Record* **2009**, *9* (4), 211-223.
207. Lin, C. T.; Loan, P. T. K.; Chen, T. Y.; Liu, K. K.; Chen, C. H.; Wei, K. H.; Li, L. J., Label-Free Electrical detection of DNA hybridization on graphene using Hall Effect measurements: revisiting the sensing mechanism. *Advanced Functional Materials* **2013**, *23* (18), 2301-2307.
208. Wu, L.; Chu, H.; Koh, W.; Li, E., Highly sensitive graphene biosensors based on surface plasmon resonance. *Optics express* **2010**, *18* (14), 14395-14400.
209. Janegitz, B. C.; Silva, T. A.; Wong, A.; Ribovski, L.; Vicentini, F. C.; Sotomayor, M. d. P. T.; Fatibello-Filho, O., The application of graphene for in vitro and in vivo electrochemical biosensing. *Biosensors Bioelectron.* **2017**, *89*, 224-233.
210. Matsumoto, K.; Maehashi, K.; Ohno, Y.; Inoue, K., Recent advances in functional graphene biosensors. *Journal of Physics D: Applied Physics* **2014**, *47* (9), 094005.
211. Navakul, K.; Warakulwit, C.; Yenchitsomanus, P.-t.; Panya, A.; Lieberzeit, P. A.; Sangma, C., A novel method for dengue virus detection and antibody screening using

a graphene-polymer based electrochemical biosensor. *Nanomed. Nanotechnol. Biol. Med.* **2017**, *13* (2), 549-557.

212. Pandey, A.; Gurbuz, Y.; Ozguz, V.; Niazi, J. H.; Qureshi, A., Graphene-interfaced electrical biosensor for label-free and sensitive detection of foodborne pathogenic *E. coli* O157: H7. *Biosensors Bioelectron.* **2017**, *91*, 225-231.

213. Peña-Bahamonde, J.; Nguyen, H. N.; Fanourakis, S. K.; Rodrigues, D. F., Recent advances in graphene-based biosensor technology with applications in life sciences. *Journal of nanobiotechnology* **2018**, *16* (1), 1-17.

214. Shih, C.-J.; Wang, Q. H.; Lin, S.; Park, K.-C.; Jin, Z.; Strano, M. S.; Blankschtein, D., Breakdown in the wetting transparency of graphene. *Physical review letters* **2012**, *109* (17), 176101.

215. Li, Z.; Wang, Y.; Kozbial, A.; Shenoy, G.; Zhou, F.; McGinley, R.; Ireland, P.; Morganstein, B.; Kunkel, A.; Surwade, S. P., Effect of airborne contaminants on the wettability of supported graphene and graphite. *Nature materials* **2013**, *12* (10), 925.

216. Kozbial, A.; Li, Z.; Conaway, C.; McGinley, R.; Dhingra, S.; Vahdat, V.; Zhou, F.; D'Urso, B.; Liu, H.; Li, L., Study on the surface energy of graphene by contact angle measurements. *Langmuir* **2014**, *30* (28), 8598-8606.

217. Raj, R.; Maroo, S. C.; Wang, E. N., Wettability of graphene. *Nano Lett.* **2013**, *13* (4), 1509-1515.

218. Rafiee, J.; Mi, X.; Gullapalli, H.; Thomas, A. V.; Yavari, F.; Shi, Y.; Ajayan, P. M.; Koratkar, N. A., Wetting transparency of graphene. *Nature materials* **2012**, *11* (3), 217.

219. Taherian, F.; Marcon, V.; van der Vegt, N. F.; Leroy, F., What is the contact angle of water on graphene? *Langmuir* **2013**, *29* (5), 1457-1465.

220. Jeyachandran, Y.; Mielczarski, J.; Mielczarski, E.; Rai, B., Efficiency of blocking of non-specific interaction of different proteins by BSA adsorbed on hydrophobic and hydrophilic surfaces. *J. Colloid Interface Sci.* **2010**, *341* (1), 136-142.

221. Tangpasuthadol, V.; Pongchaisirikul, N.; Hoven, V. P., Surface modification of chitosan films.: Effects of hydrophobicity on protein adsorption. *Carbohydrate Research* **2003**, *338* (9), 937-942.

222. Pace, C. N., Contribution of the hydrophobic effect to globular protein stability. *J. Mol. Biol.* **1992**, *226* (1), 29-35.

223. Kamiya, Y.; Yamazaki, K.; Ogino, T., Protein adsorption to graphene surfaces controlled by chemical modification of the substrate surfaces. *J. Colloid Interface Sci.* **2014**, *431*, 77-81.
224. Kong, W.; Li, H.; Qiao, K.; Kim, Y.; Lee, K.; Nie, Y.; Lee, D.; Osadchy, T.; Molnar, R. J.; Gaskill, D. K., Polarity governs atomic interaction through two-dimensional materials. *Nature materials* **2018**, *17* (11), 999.
225. Golan, Y.; Margulis, L.; Rubinstein, I., Vacuum-deposited gold films: I. Factors affecting the film morphology. *Surface Science* **1992**, *264* (3), 312-326.
226. Shaporenko, A.; Terfort, A.; Grunze, M.; Zharnikov, M., A detailed analysis of the photoemission spectra of basic thioaromatic monolayers on noble metal substrates. *Journal of electron spectroscopy and related phenomena* **2006**, *151* (1), 45-51.
227. Heister, K.; Zharnikov, M.; Grunze, M.; Johansson, L., Adsorption of alkanethiols and biphenylthiols on Au and Ag substrates: a high-resolution X-ray photoelectron spectroscopy study. *The Journal of Physical Chemistry B* **2001**, *105* (19), 4058-4061.
228. Heister, K.; Zharnikov, M.; Grunze, M.; Johansson, L.; Ulman, A., Characterization of X-ray induced damage in alkanethiolate monolayers by high-resolution photoelectron spectroscopy. *Langmuir* **2001**, *17* (1), 8-11.
229. Duwez, A.-S., Exploiting electron spectroscopies to probe the structure and organization of self-assembled monolayers: a review. *Journal of Electron Spectroscopy and Related Phenomena* **2004**, *134* (2-3), 97-138.
230. Bourg, M.-C.; Badia, A.; Lennox, R. B., Gold– sulfur bonding in 2D and 3D self-assembled monolayers: XPS characterization. *The Journal of Physical Chemistry B* **2000**, *104* (28), 6562-6567.
231. Waske, P. A.; Meyerbröker, N.; Eck, W.; Zharnikov, M., Self-assembled monolayers of cyclic aliphatic thiols and their reaction toward electron irradiation. *The Journal of Physical Chemistry C* **2012**, *116* (25), 13559-13568.
232. Vericat, C.; Vela, M.; Benitez, G.; Gago, J. M.; Torrelles, X.; Salvarezza, R., Surface characterization of sulfur and alkanethiol self-assembled monolayers on Au (111). *Journal of Physics: Condensed Matter* **2006**, *18* (48), R867.
233. Techane, S. D.; Gamble, L. J.; Castner, D. G., X-ray photoelectron spectroscopy characterization of gold nanoparticles functionalized with amine-terminated alkanethiols. *Biointerphases* **2011**, *6* (3), 98-104.

234. NIST X-ray Photoelectron Spectroscopy Database. In *National Institute of Standards and Technology*, 2000 ed.; Gaithersburg MD, 20899, Vol. NIST Standard Reference Database Number 20.
235. Wagner, C., Sensitivity factors for XPS analysis of surface atoms. *Journal of electron spectroscopy and related phenomena* **1983**, *32* (2), 99-102.
236. Laibinis, P. E.; Whitesides, G. M.; Allara, D. L.; Tao, Y. T.; Parikh, A. N.; Nuzzo, R. G., Comparison of the structures and wetting properties of self-assembled monolayers of n-alkanethiols on the coinage metal surfaces, copper, silver, and gold. *J. Am. Chem. Soc.* **1991**, *113* (19), 7152-7167.
237. Love, J. C.; Wolfe, D. B.; Haasch, R.; Chabinyc, M. L.; Paul, K. E.; Whitesides, G. M.; Nuzzo, R. G., Formation and structure of self-assembled monolayers of alkanethiolates on palladium. *J. Am. Chem. Soc.* **2003**, *125* (9), 2597-2609.
238. Asghar, W.; Yuksekkaya, M.; Shafiee, H.; Zhang, M.; Ozen, M. O.; Inci, F.; Kocakulak, M.; Demirci, U., Engineering long shelf life multi-layer biologically active surfaces on microfluidic devices for point of care applications. *Scientific reports* **2016**, *6* (1), 1-10.
239. Lee, S.-H.; Lin, W.-C.; Kuo, C.-H.; Karakachian, M.; Lin, Y.-C.; Yu, B.-Y.; Shyue, J.-J., Photooxidation of amine-terminated self-assembled monolayers on gold. *The Journal of Physical Chemistry C* **2010**, *114* (23), 10512-10519.
240. Ang, X.; Lin, A.; Li, J.; Wei, J.; Chen, Z.; Wong, C. In *Stability of self-assembled monolayers on gold for MEMs/NEMs applications*, ASME International Mechanical Engineering Congress and Exposition, 2008; pp 5-10.
241. Moulton, S.; Barisci, J.; Bath, A.; Stella, R.; Wallace, G., Investigation of protein adsorption and electrochemical behavior at a gold electrode. *J. Colloid Interface Sci.* **2003**, *261* (2), 312-319.
242. Jans, K.; Bonroy, K.; De Palma, R.; Reekmans, G.; Jans, H.; Laureyn, W.; Smet, M.; Borghs, G.; Maes, G., Stability of mixed PEO– thiol SAMs for biosensing applications. *Langmuir* **2008**, *24* (8), 3949-3954.
243. Lepage, D.; Carrier, D.; Jiménez, A.; Beauvais, J.; Dubowski, J. J., Plasmonic propagations distances for interferometric surface plasmon resonance biosensing. *Nanoscale research letters* **2011**, *6* (1), 1-7.
244. Cumpson, P., Guide to smoothing in AES and XPS. **1998**.

245. Seah, M.; Dench, W., Smoothing and the signal-to-noise ratio of peaks in electron spectroscopy. *Journal of electron spectroscopy and related phenomena* **1989**, *48* (1), 43-54.
246. Repoux, M., Comparison of background removal methods for XPS. *Surface and interface analysis* **1992**, *18* (7), 567-570.
247. Kakiuchi, T.; Usui, H.; Hobara, D.; Yamamoto, M., Voltammetric properties of the reductive desorption of alkanethiol self-assembled monolayers from a metal surface. *Langmuir* **2002**, *18* (13), 5231-5238.
248. Hobara, D.; Miyake, K.; Imabayashi, S.-i.; Niki, K.; Kakiuchi, T., In-situ scanning tunneling microscopy imaging of the reductive desorption process of alkanethiols on Au (111). *Langmuir* **1998**, *14* (13), 3590-3596.
249. Widrig, C. A.; Chung, C.; Porter, M. D., The electrochemical desorption of n-alkanethiol monolayers from polycrystalline Au and Ag electrodes. *Journal of electroanalytical chemistry and interfacial electrochemistry* **1991**, *310* (1-2), 335-359.
250. Rojas, M. T.; Koeniger, R.; Stoddart, J. F.; Kaifer, A. E., Supported monolayers containing preformed binding sites. Synthesis and interfacial binding properties of a thiolated. beta.-cyclodextrin derivative. *J. Am. Chem. Soc.* **1995**, *117* (1), 336-343.
251. Imabayashi, S.-i.; Iida, M.; Hobara, D.; Feng, Z. Q.; Niki, K.; Kakiuchi, T., Reductive desorption of carboxylic-acid-terminated alkanethiol monolayers from Au (111) surfaces. *Journal of Electroanalytical Chemistry* **1997**, *428* (1-2), 33-38.
252. Schneider, T. W.; Buttry, D. A., Electrochemical quartz crystal microbalance studies of adsorption and desorption of self-assembled monolayers of alkyl thiols on gold. *J. Am. Chem. Soc.* **1993**, *115* (26), 12391-12397.
253. Byloos, M.; Al-Maznai, H.; Morin, M., Formation of a self-assembled monolayer via the electrospreeding of physisorbed micelles of thiolates. *The Journal of Physical Chemistry B* **1999**, *103* (31), 6554-6561.
254. Mohtat, N.; Byloos, M.; Soucy, M.; Morin, S.; Morin, M., Electrochemical evidence of the adsorption of alkanethiols on two sites on Ag (111). *Journal of Electroanalytical Chemistry* **2000**, *484* (2), 120-130.
255. Tang, Y.; Zeng, X.; Liang, J., Surface plasmon resonance: an introduction to a surface spectroscopy technique. *Journal of chemical education* **2010**, *87* (7), 742-746.
256. Goding, J. W., *Monoclonal antibodies: principles and practice*. Elsevier: 1996.

257. Nisonoff, A.; Hopper, J. E.; Spring, S. B., *The antibody molecule*. Academic Press: 2014.
258. Ohno, Y.; Maehashi, K.; Yamashiro, Y.; Matsumoto, K., Electrolyte-gated graphene field-effect transistors for detecting pH and protein adsorption. *Nano Lett.* **2009**, *9* (9), 3318-3322.
259. Kwak, Y. H.; Choi, D. S.; Kim, Y. N.; Kim, H.; Yoon, D. H.; Ahn, S.-S.; Yang, J.-W.; Yang, W. S.; Seo, S., Flexible glucose sensor using CVD-grown graphene-based field effect transistor. *Biosensors Bioelectron.* **2012**, *37* (1), 82-87.
260. Lin, Y.-C.; Lu, C.-C.; Yeh, C.-H.; Jin, C.; Suenaga, K.; Chiu, P.-W., Graphene annealing: how clean can it be? *Nano Lett.* **2012**, *12* (1), 414-419.
261. Pirkle, A.; Chan, J.; Venugopal, A.; Hinojos, D.; Magnuson, C.; McDonnell, S.; Colombo, L.; Vogel, E.; Ruoff, R.; Wallace, R., The effect of chemical residues on the physical and electrical properties of chemical vapor deposited graphene transferred to SiO₂. *Applied Physics Letters* **2011**, *99* (12), 122108.
262. Her, M.; Beams, R.; Novotny, L., Graphene transfer with reduced residue. *Physics Letters A* **2013**, *377* (21-22), 1455-1458.
263. Kong, W.; Li, H.; Qiao, K.; Kim, Y.; Lee, K.; Nie, Y.; Lee, D.; Osadchy, T.; Molnar, R. J.; Gaskill, D. K., Polarity governs atomic interaction through two-dimensional materials. *Nature materials* **2018**, *17* (11), 999-1004.
264. Louette, P.; Bodino, F.; Pireaux, J.-J., Poly (methyl methacrylate)(PMMA) XPS reference core level and energy loss spectra. *Surface science spectra* **2005**, *12* (1), 69-73.
265. Ferrah, D.; Renault, O.; Petit-Etienne, C.; Okuno, H.; Berne, C.; Bouchiat, V.; Cunge, G., XPS investigations of graphene surface cleaning using H₂-and Cl₂-based inductively coupled plasma. *Surface and interface analysis* **2016**, *48* (7), 451-455.
266. Young, K. T.; Phillips, S. S.; Coley, J. T.; Perini, C. J.; Hitchcock, D. A.; Serkiz, S. M.; Vogel, E. M., The impact of defect density, grain size, and Cu orientation on thermal oxidation of graphene-coated Cu. *Applied Surface Science* **2019**, *478*, 959-968.
267. Chan, J.; Venugopal, A.; Pirkle, A.; McDonnell, S.; Hinojos, D.; Magnuson, C. W.; Ruoff, R. S.; Colombo, L.; Wallace, R. M.; Vogel, E. M., Reducing extrinsic performance-limiting factors in graphene grown by chemical vapor deposition. *ACS nano* **2012**, *6* (4), 3224-3229.

268. Weber, J.; Calado, V.; Van De Sanden, M., Optical constants of graphene measured by spectroscopic ellipsometry. *Applied Physics Letters* **2010**, *97* (9), 091904.
269. Kankare, J., Sauerbrey equation of quartz crystal microbalance in liquid medium. *Langmuir* **2002**, *18* (18), 7092-7094.
270. Latif, U.; Can, S.; Hayden, O.; Grillberger, P.; Dickert, F. L., Sauerbrey and anti-Sauerbrey behavioral studies in QCM sensors—Detection of bioanalytes. *Sensors Actuators B: Chem.* **2013**, *176*, 825-830.
271. Malard, L.; Pimenta, M.; Dresselhaus, G.; Dresselhaus, M., Raman spectroscopy in graphene. *Physics reports* **2009**, *473* (5-6), 51-87.
272. Nakanishi, K.; Sakiyama, T.; Imamura, K., On the adsorption of proteins on solid surfaces, a common but very complicated phenomenon. *J. Biosci. Bioeng.* **2001**, *91* (3), 233-244.
273. Fuss, C.; Palmaz, J. C.; Sprague, E. A., Fibrinogen: structure, function, and surface interactions. *Journal of Vascular and Interventional Radiology* **2001**, *12* (6), 677-682.
274. book, a.
275. Wei, Q.; Becherer, T.; Mutihac, R.-C.; Noeske, P.-L. M.; Paulus, F.; Haag, R.; Grunwald, I., Multivalent anchoring and cross-linking of mussel-inspired antifouling surface coatings. *Biomacromolecules* **2014**, *15* (8), 3061-3071.
276. Shen, D.; Zou, G.; Liu, L.; Wu, A.; Duley, W. W.; Zhou, Y. N., Investigation of impact and spreading of molten nanosized gold droplets on solid surfaces. *Appl. Opt.* **2018**, *57* (9), 2080-2086.
277. Mitra, S.; Gunda, N. S. K.; Mitra, S. K., Wetting characteristics of underwater micro-patterned surfaces. *RSC advances* **2017**, *7* (15), 9064-9072.
278. Xu, J.; Wang, C.; Wang, T.; Wang, Y.; Kang, Q.; Liu, Y.; Tian, Y., Mechanisms for low-temperature direct bonding of Si/Si and quartz/quartz via VUV/O₃ activation. *RSC advances* **2018**, *8* (21), 11528-11535.
279. Fan, C.-W.; Lee, S.-C., Effects in surface free energy of sputter-deposited TaN_x films. *IEEE transactions on advanced packaging* **2008**, *31* (2), 394-398.
280. Doolittle, R. F., Fibrinogen and fibrin. *Annu. Rev. Biochem.* **1984**, *53* (1), 195-229.

281. Wertz, C. F.; Santore, M. M., Fibrinogen adsorption on hydrophilic and hydrophobic surfaces: Geometrical and energetic aspects of interfacial relaxations. *Langmuir* **2002**, *18* (3), 706-715.
282. Schmitt, A.; Varoqui, R.; Uniyal, S.; Brash, J.; Pusineri, C., Interaction of fibrinogen with solid surfaces of varying charge and hydrophobic—hydrophilic balance: I. Adsorption isotherms. *J. Colloid Interface Sci.* **1983**, *92* (1), 25-34.
283. Carré, A.; Mittal, K. L., *Surface and interfacial aspects of cell adhesion*. CRC Press: 2011.
284. Robeson, J. L.; Tilton, R. D., Spontaneous reconfiguration of adsorbed lysozyme layers observed by total internal reflection fluorescence with a pH-sensitive fluorophore. *Langmuir* **1996**, *12* (25), 6104-6113.
285. Su, T.; Lu, J.; Thomas, R.; Cui, Z.; Penfold, J., The effect of solution pH on the structure of lysozyme layers adsorbed at the silica– water interface studied by neutron reflection. *Langmuir* **1998**, *14* (2), 438-445.
286. Neto, A. C.; Guinea, F.; Peres, N. M.; Novoselov, K. S.; Geim, A. K., The electronic properties of graphene. *Reviews of modern physics* **2009**, *81* (1), 109.
287. Phan, H. T.; Bartelt-Hunt, S.; Rodenhausen, K. B.; Schubert, M.; Bartz, J. C., Investigation of bovine serum albumin (BSA) attachment onto self-assembled monolayers (SAMs) using combinatorial quartz crystal microbalance with dissipation (QCM-D) and spectroscopic ellipsometry (SE). *PLoS one* **2015**, *10* (10).
288. Lee, R. G.; Kim, S. W., Adsorption of proteins onto hydrophobic polymer surfaces: adsorption isotherms and kinetics. *Journal of biomedical materials research* **1974**, *8* (5), 251-259.
289. Krisdhasima, V.; McGuire, J.; Sproull, R., Surface hydrophobic influences on β -lactoglobulin adsorption kinetics. *J. Colloid Interface Sci.* **1992**, *154* (2), 337-350.
290. Wegner, S. V.; Schenk, F. C.; Spatz, J. P., Cobalt (III)-Mediated Permanent and Stable Immobilization of Histidine-Tagged Proteins on NTA-Functionalized Surfaces. *Chemistry—A European Journal* **2016**, *22* (9), 3156-3162.
291. Chu, R.; Reczek, D.; Brondyk, W., Capture-stabilize approach for membrane protein SPR assays. *Scientific reports* **2014**, *4* (1), 1-9.

292. Sigal, G. B.; Bamdad, C.; Barberis, A.; Strominger, J.; Whitesides, G. M., A self-assembled monolayer for the binding and study of histidine-tagged proteins by surface plasmon resonance. *Analytical Chemistry* **1996**, *68* (3), 490-497.
293. Nieba, L.; Nieba-Axmann, S. E.; Persson, A.; Hämäläinen, M.; Edebratt, F.; Hansson, A.; Lidholm, J.; Magnusson, K.; Karlsson, Å. F.; Plückthun, A., BIACORE analysis of histidine-tagged proteins using a chelating NTA sensor chip. *Anal. Biochem.* **1997**, *252* (2), 217-228.
294. Al-Ani, A.; Boden, A.; Al Kobaisi, M.; Pingle, H.; Wang, P.-Y.; Kingshott, P., The influence of PEG-thiol derivatives on controlling cellular and bacterial interactions with gold surfaces. *Applied Surface Science* **2018**, *462*, 980-990.
295. Taleat, Z.; Cristea, C.; Marrazza, G.; Mazloum-Ardakani, M.; Săndulescu, R., Electrochemical immunoassay based on aptamer–protein interaction and functionalized polymer for cancer biomarker detection. *Journal of Electroanalytical Chemistry* **2014**, *717*, 119-124.
296. Kalantar-zadeh, K.; Ou, J. Z., Biosensors based on two-dimensional MoS₂. *Acs Sensors* **2016**, *1* (1), 5-16.
297. Feuerstein, D.; Parker, K. H.; Boutelle, M. G., Practical methods for noise removal: applications to spikes, nonstationary quasi-periodic noise, and baseline drift. *Analytical chemistry* **2009**, *81* (12), 4987-4994.
298. Shrivastava, A.; Gupta, V., Methods for the determination of limit of detection and limit of quantitation of the analytical methods. *Chronicles of young scientists* **2011**, *2* (1), 21-21.
299. Ding, J.; Wang, X.; Qin, W., Pulsed galvanostatic control of a polymeric membrane ion-selective electrode for potentiometric immunoassays. *ACS applied materials & interfaces* **2013**, *5* (19), 9488-9493.
300. Chen, Y.; Ding, J.; Qin, W., Potentiometric determination of trypsin using a polymeric membrane polycation-sensitive electrode based on current-controlled reagent delivery. *Bioelectrochemistry* **2012**, *88*, 144-147.
301. Rebeski, D. E.; Winger, E. M.; Shin, Y.-K.; Lelenta, M.; Robinson, M. M.; Varecka, R.; Crowther, J. R., Identification of unacceptable background caused by non-specific protein adsorption to the plastic surface of 96-well immunoassay plates using a standardized enzyme-linked immunosorbent assay procedure. *J. Immunol. Methods* **1999**, *226* (1-2), 85-92.

302. Ding, J.; Lei, J.; Ma, X.; Gong, J.; Qin, W., Potentiometric aptasensing of *Listeria monocytogenes* using protamine as an indicator. *Analytical chemistry* **2014**, *86* (19), 9412-9416.
303. Turgeon, R. T.; Bowser, M. T., Improving sensitivity in micro-free flow electrophoresis using signal averaging. *Electrophoresis* **2009**, *30* (8), 1342-1348.
304. Dai, H.; Zhang, S.; Hong, Z.; Lin, Y., A potentiometric addressable photoelectrochemical biosensor for sensitive detection of two biomarkers. *Analytical chemistry* **2016**, *88* (19), 9532-9538.
305. Koncki, R., Recent developments in potentiometric biosensors for biomedical analysis. *Anal. Chim. Acta* **2007**, *599* (1), 7-15.
306. Porter, M. D.; Bright, T. B.; Allara, D. L.; Chidsey, C. E., Spontaneously organized molecular assemblies. 4. Structural characterization of n-alkyl thiol monolayers on gold by optical ellipsometry, infrared spectroscopy, and electrochemistry. *J. Am. Chem. Soc.* **1987**, *109* (12), 3559-3568.
307. Nair, P.; Alam, M., Performance limits of nanobiosensors. *Applied physics letters* **2006**, *88* (23), 233120.
308. Squires, T. M.; Messinger, R. J.; Manalis, S. R., Making it stick: convection, reaction and diffusion in surface-based biosensors. *Nat. Biotechnol.* **2008**, *26* (4), 417-426.
309. Newman, J., The fundamental principles of current distribution and mass transport in electrochemical cells. **1973**.
310. Ackerberg, R.; Patel, R.; Gupta, S., The heat/mass transfer to a finite strip at small Péclet numbers. *Journal of Fluid Mechanics* **1978**, *86* (1), 49-65.
311. Roden, L. D.; Myszka, D. G., Global analysis of a macromolecular interaction measured on BIAcore. *Biochem. Biophys. Res. Commun.* **1996**, *225* (3), 1073-1077.
312. Sigmundsson, K.; Másson, G.; Rice, R.; Beauchemin, N.; Öbrink, B., Determination of active concentrations and association and dissociation rate constants of interacting biomolecules: an analytical solution to the theory for kinetic and mass transport limitations in biosensor technology and its experimental verification. *Biochemistry* **2002**, *41* (26), 8263-8276.
313. Young, M.; Carroad, P.; Bell, R., Estimation of diffusion coefficients of proteins. *Biotechnol. Bioeng.* **1980**, *22* (5), 947-955.

314. Sheehan, P. E.; Whitman, L. J., Detection limits for nanoscale biosensors. *Nano Lett.* **2005**, *5* (4), 803-807.
315. Nair, P. R.; Alam, M. A., Dimensionally frustrated diffusion towards fractal adsorbers. *Physical review letters* **2007**, *99* (25), 256101.
316. Wallis, R.; Moore, G. R.; James, R.; Kleanthous, C., Protein-protein interactions in colicin E9 DNase-immunity protein complexes. 1. Diffusion-controlled association and femtomolar binding for the cognate complex. *Biochemistry* **1995**, *34* (42), 13743-13750.
317. Rajan, N. K.; Routenberg, D. A.; Reed, M. A., Optimal signal-to-noise ratio for silicon nanowire biochemical sensors. *Applied physics letters* **2011**, *98* (26), 264107.
318. Gao, X. P.; Zheng, G.; Lieber, C. M., Subthreshold regime has the optimal sensitivity for nanowire FET biosensors. *Nano Lett.* **2010**, *10* (2), 547-552.